Broadly tunable self-oscillating antenna based on negative immittance conversion

Vincelj, Leo

University of Zagreb

FACULTY OF ELECTRICAL ENGINEERING AND COMPUTING

Leo Vincelj

BROADLY TUNABLE SELF-OSCILLATING ANTENNA BASED ON NEGATIVE IMMITTANCE CONVERSION

DOCTORAL THESIS

Zagreb, 2021

University of Zagreb

FACULTY OF ELECTRICAL ENGINEERING AND COMPUTING

Leo Vincelj

BROADLY TUNABLE SELF-OSCILLATING ANTENNA BASED ON NEGATIVE IMMITTANCE CONVERSION

DOCTORAL THESIS

Supervisor: Professor Silvio Hrabar, PhD

Zagreb, 2021

Sveučilište u Zagrebu

FAKULTET ELEKTROTEHNIKE I RAČUNARSTVA

Leo Vincelj

ŠIROKOPOJASNO UGODIVA SAMOOSCILIRAJUĆA ANTENA TEMELJENA NA NEGATIVNOJ PRETVORBI IMITANCIJE

DOKTORSKI RAD

Mentor: prof. dr. sc. Silvio Hrabar

Zagreb, 2021.

Doctoral thesis was made at the University of Zagreb, Faculty of Electrical Engineering and Computing, Department of Communication and Space Technologies.

Supervisor: Professor Silvio Hrabar, PhD

Number of pages: 134

Doctoral thesis No.: _____

About the Supervisor

Silvio Hrabar received Dipl.Ing. and M.Sc. degrees from the University of Zagreb Faculty of electrical engineering, and a Ph.D. from the Brunel University of West London, UK, in 1986, 1991 and 1999, respectively. In the past, he worked at the Institute of Radio Industry Zagreb, on the development of UHF transceivers and antenna systems, at the Brunel University of West London, on electromagnetic compatibility, numerical electromagnetics, electrostatics, and microwave tube design. Currently, he is employed at the University of Zagreb Faculty of electrical engineering and computing as a full professor, and has been a visiting professor and lecturer at several universities in America, Europe and Asia. His research interests include applied electromagnetics, electromagnetic compatibility, antennas, as well as radio frequency and microwave electronics. He has made a couple of important contributions in the field of metamaterials: theoretical explanation and experimental verification of sub-wavelength propagation in metamaterial waveguide, as well as first experimental demonstrations of a sub-wavelength resonator and broadband non-Foster active metamaterial in the world. He is the author and co-author of many papers in scientific journals, book chapters, conference papers and technical studies, and is a reviewer for a dozen of scientific journals. In 2012, he was awarded the "Award for Outstanding Achievement in Research and Innovation, for his contribution to the understanding of physics of electromagnetic metamaterials and development of their engineering applications".

O mentoru

Silvio Hrabar diplomirao je i magistrirao na Elektrotehničkom fakultetu Sveučilišta u Zagrebu, a doktorirao na Brunel University of West London, Velika Britanija, 1986., 1991. i 1999. godine. Radio je na Institutu Radio Industrije Zagreb, na razvoju UHF primopredajnika i antenskih sustava, na Brunel University of West London, na istraživanju elektromagnetske kompatibilnosti, numeričkom elektromagnetizmu, elektrostatici te dizajnu mikrovalnih cijevi. Trenutno je zaposlen na Sveučilištu u Zagrebu Fakultetu elektrotehnike i računarstva, na mjestu redovitog profesora u trajnom zvanju, a bio je gostujući profesor i predavač na više sveučilišta u Americi, Europi i Aziji. Njegov istraživački interes uključuje primijenjeni elektromagnetizam, elektromagnetsku kompatibilnost, antene, radiofrekvencijsku i mikrovalnu elektroniku. Polučio je nekoliko važnih doprinosa u području metamaterijala: teoretsko objašnjenje i prvu eksperimentalnu verifikaciju subvalne propagacije u metamaterijalnom valovodu, prvu eksperimentalnu demonstraciju subvalnog rezonatora i širokopojasnog aktivnog nefosterovskog metamaterijala na svijetu. Autor je i koautor mnogih radova u znanstvenim časopisima, poglavlja u knjigama, konferencijskih priopćenja i tehničkih studija te je recenzent za desetak znanstvenih časopisa. 2012. godine nagrađen je "Nagradom za iznimno postignuće u istraživanju i inovacijama, a posebno za doprinos razumijevanju fizike elektromagnetskih metamaterijala i razvoju njihovih inženjerskih primjena".

For those who are never completely sure
what they want with their life...

"A greater task than to feel secure
is to be able to tolerate insecurity."
- Erich Fromm

I wish to express my sincerest gratitude and warm appreciation to the following people who had contributed much to my PhD study.

My parents, Danica and Srećko, for bringing me to this place of wonder. I appreciate all the support and effort.

My sister Ana-Marija, brother-in-law Jura and niece Elina. You were always caring and supporting.

My work buddies, J. Lo, Ante, Dario, Marko B., Jurica, Žane, Jakov, Ivana, Jelena, Fix, J. Vu, Leonard and Marko Š., for without you this journey wouldn't be the same. You are great friends and I owe you for improving me both as a researcher and a person.

My supervisor, professor Silvio Hrabar, for mentoring me through both graduate and post-graduate education.

Professors and associates at the Department of Communication and Space Technologies. Your advices and lectures helped me a lot.

Professor Igor Krois for all the technical support and invested time.

Professor Richard W. Ziolkowski from the University of Technology Sydney for the collaboration and help regarding Chapter 5 of the thesis.

My hiking group for all the good time we spent finding relaxation in the nature.

All my other friends and family for the infinite tolerance and support.

Abstract

The thesis deals with the investigation of the concept of a broadly tunable self-oscillating antenna (antenna-transmitter). Such an antenna is based on immittance conversion of a first electromagnetic (EM) radiator into its 'negative image'. This 'negative image' is further connected to a second, identical EM radiator, creating a frequency agile self-oscillating system. Expected application of such an antenna system is related to future self-oscillating reflective metasurfaces. The basic electronic circuit used in described self-oscillating antenna is a negative impedance converter (NIC). Therefore, NIC's behaviour in the case of both ideal and realistic active elements, as well as EM radiators, is analysed both analytically and numerically. The analysis is focused on the influence of dispersion and non-linearity. Analytical models of NIC are derived in order to investigate the influence of non-idealities on the NIC input immittance. Analytical results were verified by measurements on the experimental demonstrators. Demonstrators comprise a NIC based on ultra-fast operational amplifiers, and crossed dipoles or elemental Huygens' EM radiators. Measurement results revealed the tuning range of 1:3 for the prototype with dipole-like antennas, and 1:2 for the prototype with Huygens' radiators. Finally, the implementations of various additional features such as injection locking and modulation, were discussed.

Keywords: negative impedance converter, non-Foster networks, self-oscillating antenna, dispersion, non-linearity, Huygens' radiator

Širokopojasno ugodiva samooscilirajuća antena temeljena na negativnoj pretvorbi imitancije

U radu je istražen koncept širokopojasno ugodive samooscilirajuće antene (antene-odašiljača). Takva antena temelji se na pretvorbi imitancije prvog elektromagnetskog (EM) radijatora u njegovu 'negativnu sliku'. Ta 'negativna slika' radijatora je zatim spojena na drugi identični EM radijator, stvarajući tako širokopojasno ugodivi samooscilatorni prilagođeni sustav. Očekivana primjena navedenog antenskog sustava je u budućim samooscilirajućim rekonfigurabilnim metapovršinama. Kako je osnovni sklop korišten u samooscilirajućoj anteni negativni pretvornik impedancije (NIC), analitički i numerički je istražen njegov rad u slučaju idealnih i realnih aktivnih elemenata, s posebnim naglaskom na utjecaj disperzije i nelinearnosti. U svrhu toga izveden je matematički model NIC-a i napravljena analiza utjecaja neidealnosti na ulaznu imitanciju. Također, napravljen je dizajn te su provedene numeričke simulacije elektromagnetskih radijatora korištenih u samooscilirajućem sustavu. Rezultati teorijske analize verificirani su mjerenjima na eksperimentalnim demonstratorima, odnosno prototipima. Demonstratori su temeljeni na negativnom pretvorniku impedancije sa ultra-brzim operacijskim pojačalima te ukrižanim dipolu sličnim antenama, odnosno Huygensovim elementarnim EM radijatorima. Ostvaren je raspon ugađanja frekvencije od 1:3 u slučaju dipolu sličnih antena te 1:2 u slučaju Huygensovih antena. Razmatrana je mogućnost modulacije i sinkronizacije samooscilirajuće antene vanjskim radiofrekvencijskim izvorom.

Disertacija je podijeljena u sedam poglavlja, pri čemu se svako sljedeće nadovezuje na ono prethodno. Uvodno (1.) poglavlje objašnjava potrebu za korištenjem električki kratkih antena te ističe njihova fundamentalna ograničenja. Tri osnovna ograničenja su niska efikasnost zračenja, mali dobitak i veliki faktor dobrote. U praksi, veliki faktor dobrote, odnosno visoka reaktivnost električki kratkih antena uzrokuje gotovo totalnu refleksiju elektromagnetskog vala od antene natrag prema radiofrekvencijskom izvoru. U svrhu ostvarenja prihvatljivih razina zračenja koriste se prilagodne mreže, koje se spajaju između radiofrekvencijskog izvora i antene. Njihov zadatak je minimizirati koeficijent refleksije od nekog mjesta prijenosnog sustava nadalje. Međutim, fundamentalni problem pasivnih prilagodnih mreže je uskopojasnost. Zbog toga su se počeli koristiti negativni elementi kao sastavni dio aktivnih prilagodnih mreža. Negativni elementi posjeduju disperzivna svojstva upravo suprotna onima pozitivnih reaktivnih elemenata, stoga otvaraju mogućnost širokopojasnog prilagođenja. Sama ideja korištenja negativnih elemenata za prilagođenje električki kratkih antena ustvari potječe iz relativno novog područja unutar elektromagnetizma, područja metamaterijala. Metamaterijali i metapovršine su posebno projektirane rezonantne strukture koje na makroskopskoj razini omogućuju ostvarenje elektromagnetskih svojstava rijetko viđenih u prirodi (primjerice negativne permitivnost i permeabilnost). Negativni elementi implementirani u strukturama metamaterijala i metapovršina

omogućuju ostvarivanje svojstava poput rekonfigurabilnosti, pojačanja, ugodivosti i oblikovanja valne fronte elektromagnetskog vala. U praksi, negativni elementi se mogu realizirati korištenjem elektroničkog sklopa koji se naziva negativni pretvornik impedancije. Negativni pretvornik impedancije (NIC) je ustvari pojačalo pojačanja većeg od jedan, s pozitivnom povratnom vezom. Iako negativni elementi imaju širok spektar potencijalnih primjena, zbog prisutnosti pozitivne povratne veze su u praksi često uzrok nestabilnosti. Dva su moguća pristupa problemu nestabilnosti. Cilj prvog od njih je pronaći odgovarajuće kriterije stabilnosti za mreže s negativnim elementima, dok je cilj drugog pristupa iskoristiti inherentnu nestabilnost te projektirati oscilatorni sustav. U ovom radu, bavit ćemo se potonjom metodom.

Poglavlje broj dva (2.) iznosi ideju o uporabi negativnih elemenata za prilagođenje antena, ali u nestabilnom (samooscilirajućem) sustavu. Ideja samooscilirajuće antene temeljene na negativnoj pretvorbi imitancije detaljno je objašnjena u idealnom slučaju. Sustav se sastoji od dvije identične ortogonalno postavljene antene, negativnog pretvornika impedancije i titrajnog kruga. Ideja je razvijena od samooscilirajuće antene s jednim radijatorom i nadomjesnom mrežom antene u povratnoj vezi NIC-a do samooscilirajuće antene s dva radijatora. Jedan od radijatora je pretvoren u svoju 'negativnu sliku' putem negativnog pretvornika impedancije te spojen s drugim 'pozitivnim' radijatorom. Poboljšanja koja dolaze korištenjem dvije antene umjesto jedne antene i nadomjesne mreže su veća razina izračene snage te širi pojas ugađanja. Predložen uređaj uspoređen je s klasičnom aktivnom antenom i istaknute su glavne razlike. Osnovna prednost predloženog uređaja u odnosu na klasičnu samooscilirajuću aktivnu antenu je potencijalno mnogo veća širina pojasa ugađanja. Generalno, kombinacija 'pozitivnog' radijatora i njegove 'negativne slike' omogućava teoretski beskonačno široko poništavanje imitancije i generiranje oscilacija. Ugađanje frekvencije moguće je pritom ostvariti paralelnim ili serijskim spajanjem jednostavnog titrajnog kruga. Neminovna posljedica samooscilacija ovakvog sustava je zračenje elektromagnetske energije, budući da tereti nisu električke komponente već antene. Također, utvrđeni su kriteriji za stabilnost radne točke koji osiguravaju gašenje bilo kakve perturbacije u frekvenciji ili amplitudi. Nadalje, predložena je uporaba samooscilirajuće antene temeljene na negativnoj pretvorbi imitancije kao jedinične ćelije samooscilirajuće reflektivne metapovršine. U takvoj konfiguraciji, metapovršina je osvijetljena elektromagnetskim valom te radi u modu nelinearne sinkronizacije, pri čemu se svaka jedinična ćelija sinkronizira na frekvenciju vanjskog radiofrekvencijskog izvora, a kombinirani učinak periodičke strukture donosi pojačanje snage upadnog vala.

U poglavlju broj tri (3.) izvedeni su matematički modeli negativnog pretvornika impedancije i analiziran je utjecaj neidealnosti na ulaznu imitanciju negativnog pretvornika impedancije. Uspoređene su dvije različite konfiguracije negativnog pretvornika impedancije ostvarene pomoću operacijskih pojačala, uzemljeni i plivajući tip. Uzemljena konfiguracija NIC-a je nešto jednostavnija jer sadrži samo jedno operacijsko pojačalo s pozitivnom povratnom vezom, no

plivajuća konfiguracija omogućava potpuno odvojeno i simetrično povezivanje antena što minimizira međuimpedanciju između antena. Prvi matematički model uzima u obzir utjecaj disperzije i konačnih dimenzija pojačala, dok drugi model opisuje utjecaj nelinearnosti. Utvrđeno je da pogreška u preslikavanju NIC-a zbog disperzije ovisi o faktoru dobrote tereta. U slučaju preslikavanja električki kratke antene pogreška je izražena pretežito u realnom dijelu ulazne imitancije. S druge strane, nelinearnost ima jednak utjecaj na realni i imaginarni dio ulazne imitancije te pogreška preslikavanja ne ovisi o faktoru dobrote tereta. Konačno, napravljena je dinamička analiza samooscilirajuće antene koja uzima u obzir sve navedene neidealnosti te su razmatrani uvjeti početka oscilacija u realnom slučaju. Razvijen je pripadajući trodimenzionalni dijagram koji ilustrira dinamiku oscilacija. U tom slučaju, aktivni element (negativni pretvornik impedancije s antenom u pozitivnoj povratnoj vezi) predstavljen je plohom u trodimenzionalnom prostoru. Sjecište između plohe aktivnog elementa i parametarske krivulje koja predstavlja pasivni element (druga antena i titrajni krug) predstavlja stacionarno stanje oscilatora, pomoću kojeg je moguće predvidjeti amplitudu i frekvenciju generiranih titraja.

Četvrto poglavlje (4.) obuhvaća numeričku analizu i realizaciju prototipa samooscilirajuće antene temeljene na negativnoj pretvorbi imitancije s ukrižanim dipolu sličnim antenama. Prvo su napravljene numeričke simulacije te konstruirani prototipi s nadomjesnim mrežama antene temeljeni na uzemljenom tipu NIC-a. Zatim su dizajnirane i numerički simulirane antene korištenjem računalnog elektromagnetskog simulatora (CST^{TM}). Proces je ponovljen za tri različita tipa antena s dipolu sličnim dijagramom zračenja, ukrižane dipole, kapacitivno opterećene dipole i ukrižane 'bow-tie' antene. Ostali rezultati simulacija dobiveni su korištenjem računalnog simulatora električnih krugova (ADS^{TM}). Također, određeni rezultati simulacija uspoređeni su s analitičkim rezultatima iz prethodnog poglavlja. Nadalje, razvijeni su prototipi s antenama (izrađeni od tankog aluminijskog sloja na podlozi od stiropora) radi testiranja osnovne ideje. Rezultati mjerenja su uspoređeni s rezultatima simulacija i ostvareno je zadovoljavajuće poklapanje. Sve simulacije i mjerenja provedeni su na elektroničkim sklopovima s uzemljenim negativnim pretvornikom impedancije, temeljenim na ultra-brzom operacijskom pojačalu THS4304, u nižem radiofrekvencijskom pojasu (do 50 MHz-a). Zbog velikih dimenzija antena (postavljene su u kvadrat dimenzija 1m x 1m), sva mjerenja obavljena su u bliskom polju. Eksperimentalno su potvrđeni pojasi ugađanja od 1:2 u slučaju ukrižanih kapacitivno opterećenih dipola te 1:3 u slučaju ukrižanih 'bow-tie' antena.

Poglavlje broj pet (5.) donosi proširenje osnovne ideje samooscilirajuće antene na samooscilirajući Huygensov radijator. Huygensov radijator moguće je ostvariti spregnutim parom električnog i magnetskog dipola, u svrhu ostvarenja jednosmjernog (kardioidnog) dijagrama zračenja. Za realizaciju jednosmjernog dijagrama zračenja s elementarnim radijatorima na niskim frekvencijama potrebno bi bilo ukomponirati uzemljenu ravninu prilično velikih dimenzija. Zbog svoje kompaktnosti, Huygensova antena predstavlja vrlo dobru alternativu anteni

s uzemljenom ravninom. Dizajn Huygensove antene napravljen je u elektromagnetskom simulatoru (CST^{TM}), a cijeli samooscilirajući sustav testiran je u simulatoru električnih krugova (ADS^{TM}). Simulacije predviđaju širinu pojasa ugađanja od 1:2.3 te područje ostvarenja kardioidnog dijagrama zračenja između 60 i 70 MHz. Naime, za kardioidni dijagram zračenja je potrebno zadovoljiti uvjete jednakih magnituda i 90° faznog razmaka između struja kroz petlju i dipol. Zbog različitih frekvencijskih ovisnosti struja kroz petlju i dipol, te uvjete je moguće zadovoljiti samo u relativno uskom frekvencijskom pojasu. U petom poglavlju je također objašnjena problematika rada negativnog pretvornika impedancije u slučaju preslikavanja rezonantnog tereta, primjerice antene. Zbog promjene predznaka pogreške preslikavanja, samooscilirajuća antena temeljena na negativnoj pretvorbi imitancije ne može ostvariti uvjet za stabilne oscilacije u blizini rezonancije. Predloženo je rješenje koje se sastoji od spajanja kapaciteta u seriju sa svakom antenom, što pomiče rezonantnu frekvenciju prema višim frekevencijama, te promjene pojačanja pojačala, što omogućuje ostvarenje zadovoljavajućeg koeficijenta konverzije. Pokazano je da je implementacijom ta dva koraka moguće postići održive samooscilacije u blizini rezonancije te obuhvatiti cjelokupan frekvencijski pojas kardioidnog dijagrama zračenja. Izrađen je prototip samooscilirajućeve Huygensove antene i prezentirani su rezultati mjerenja u nižem radiofrekvencijskom pojasu (do 70 MHz-a). Eksperimentalno je potvrđen pojas ugađanja od 1:2.

Šesto poglavlje (6.) se podrobnije dotiče pitanja izračene snage i prilagođenja samooscilirajuće antene temeljene na negativnoj pretvorbi imitancije. Analizirane su tri vrste efikasnosti samooscilirajućeg antenskog sustava. Identificirano je da je postignuta vrsta prilagodbe kod koje je generator prilagođen na teret, odnosno prilagodbe kod koje je unutarnja impedancija generatora jednaka impedanciji tereta. Teret u tom slučaju predstavlja 'pozitivnu' antenu, generator je naponski upravljano pojačalo (NIC) koje mijenja smjer ulazne struje, dok je unutarnja impedancija generatora antena u povratnoj vezi NIC-a. Za razliku od konjugirane prilagodbe kod koje se ostvaruje maksimalni prijenos snage s generatora na teret, no pritom maksimalna efikasnot iznosi svega 50%, prilagodba u slučaju samooscilirajuće antene osigurava da sva raspoloživa snaga bude izračena. Nedostatak takve prilagodbe je u tome što se raspoloživa snaga generatora mijenja u ovisnosti o ulaznom naponu NIC-a te o impedanciji antena. Drugim riječima, raspoloživa snaga je ovisna o frekvenciji. Kao solucija tog problema predlažu se dva koraka. Kao prvo, koristiti pojačalo s osjetno većim hodom napona, te drugo, koristiti samooscilirajući sustav u frekvencijskom opsegu u kojem je promjena impedancija antena minimalna. Implementacijom ta dva koraka, hod radne snage je smanjen na 5 dB u frekvencijskom rasponu 1:2. Nadalje, navode se neke od mogućih aplikacija samooscilirajuće antene temeljene na negativnoj pretvorbi imitancije. Jedna aplikacija podrazumijeva prisutnost vanjskog sinkronizirajućeg izvora. U tom slučaju samooscilirajuća antena funkcionira bez titrajnog kruga i frekvencija oscilacija ovisi samo o vanjskom signalu. Glavna prednost navedene konfiguracije

leži u mogućnosti vrlo širokopojasnog pojačanja relativno slabog pobudnog signala. Druga aplikacija samooscilirajuće antene sastoji se u implementaciji FSK modulacije, što je od koristi za potencijalne komunikacijske svrhe. FSK modulacija ostvarena je promjenom frekvencije titrajnog kruga naponski upravljanim kapacitetom.

Sedmo poglavlje (7.) zaključuje disertaciju ističući ostvarene znanstvene doprinose i otvarajući vidike za buduća istraživanja. Kao tri glavna smjera budućih istraživanja predlažu se izvedba samooscilirajuće antene u mikrovalnom području korištenjem mikroelektroničke tehnologije radi smanjenja dimenzija jedinične ćelije, eksperimentalna verifikacija sinkronizacije samooscilirajuće antene vanjskim radiofrekvencijskim izvorom te provedba istraživanja samooscilirajuće metapovršine koja bi se sastojala od većeg broja jediničnih ćelija.

Ključne riječi: negativni pretvornik impedancije, nefosterovske mreže, samooscilirajuća antena, disperzija, nelinearnost, Huygensova antena

Contents

Chapter 1

Introduction

In today's world the use of wireless devices is widespread. Almost any electronic device, gadget, vechicle or instrument supports wireless connectivity via bluetooth, WiFi or radio in general, and in some cases even through satellite connection. For that reason, the importance of progress in the field of applied electromagnetics is not a dilemma [1].

Main parts of any communication system are transmitter and receiver. As the name says itself, the goal of transmitter is to transform useful information into signal, which can then be transmitted via medium (free space), all the way to the receiving point. At the receiving point (receiver), signal is accepted and transformed back into the information understandable to the recipient [2]. This transformation is usually performed in three steps. Firstly, useful information is directly converted into electrical signal, then the signal is adapted in a way which is more appropriate for free space propagation (signal is modulated), and finally, modulated electrical signal is converted into electromagnetic energy via antenna. The same transformation happens at the receiver, but in the reverse order. Electromagnetic wave containing the information is registered by the antenna and there converted into electrical signal. Then, the signal is demodulated, and displayed as a useful information [2].

Each of those parts of receiver and transmitter have their requirements, which are defined by users and manufacturers. However, some requirements are limited by fundamental physical constraints. Users generally want a fast, stable connection, using a device which is compact in dimensions and energy efficient. Configurability and ease of use are also demands in various applications. In some cases though, electromagnetic wave has to be transmitted in the lower radio frequency range (up to few hundred MHz), meaning that transmitting and receiving antennas could potentially be electrically small [3]. From the manufacturers' point of view, only goal is to actually realize given user demands, with as little cost (money and time) as possible or with the greater overall benefit.

This thesis tends to make a contribution in the field of applied electromagnetics regarding three common user demands for wireless communication devices. It deals with electrically

small antennas, energy efficiency and configurability. The goal is to design a broadly tunable device comprising an electrically small antenna, with a beneficial distribution of energy.

1.1 Limitations of electrically small antennas

The requirement for small physical dimensions of a wireless device is related to many fundamental constraints. The problem lies within the nature of the radiating element (antenna) [4, 5]. Basically, the absolute dimensions do not specifically represent a difficulty. Constraints are related to relative dimensions of the antenna, regarding to the operating wavelength (λ) [4].

There are several criteria by which an antenna can be defined as electrically small [4, 6, 7]. Generally, size of the antenna (a) has to be much smaller than the operating wavelength ($a \ll \lambda$). Size a is in that case defined as the radius of the smallest sphere encircling the radiating element, as shown in Fig. 1.1.

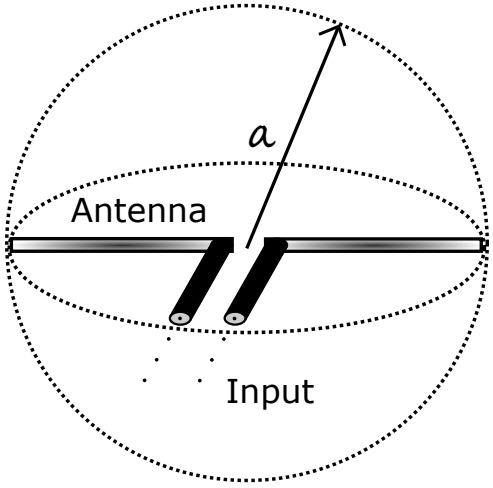

Figure 1.1: Definition of the antenna size a as a radius of the smallest sphere containing the antenna structure.

Many years ago, with the use of spherical wave functions to describe electromagnetic fields, Chu defined the limit for electrically small antennas as [6]:

$$\frac{2\pi a}{\lambda} \ll 1. \tag{1.1}$$

The first constraint of electrically small antennas is their low radiation efficiency [5]. Briefly, power at the antenna consists of three parts, radiated power (P_{RAD}), dissipated power (P_{LOSS}) and reactive power (P_{STORED}). Therefore, using circuit theory, an antenna impedance can be modelled using three circuit elements. In Fig. 1.2, a representation of antenna impedance is shown, comprising of radiation resistance (R_{RAD}), conduction losses (R_{LOSS}) and antenna reactance (X_{ANT}). Current that flows through the circuit will develop power at each of those elements, which is equivalent to the actual power flow at the antenna [3].

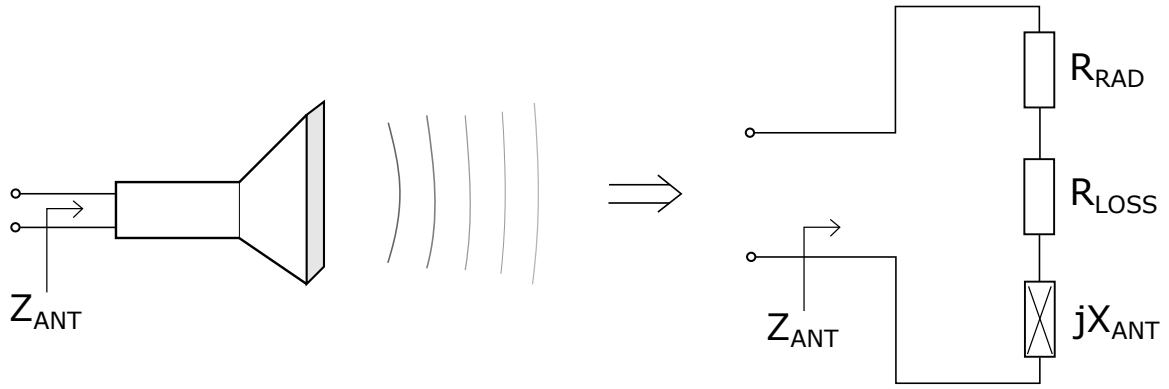

Figure 1.2: Equivalent circuit model of an antenna comprising radiation resistance (R_{RAD}), losses (R_{LOSS}) and reactance (X_{ANT}).

Accordingly, radiation efficiency (η_{RAD}) can be defined as a ratio between the radiated power (P_{RAD}) and total active power accepted by the antenna ($P_{ACCEPTED}$):

$$\eta_{RAD} = \frac{P_{RAD}}{P_{ACCEPTED}} = \frac{P_{RAD}}{P_{RAD} + P_{LOSS}}. \tag{1.2}$$

Low radiation efficiency is caused by the high density of current associated with small dimensions of conductors used for antenna construction. Such disproportion thus results in high values of dissipated power. This drawback is closely related to materials from which an antenna is constructed and it can be improved by the careful choice of materials, but only to some extent.

There are some successful methods that overcome the low radiation efficiency. To point out, one may consider the use of near field parasitic elements (NFRP) [8–10]. The idea is to introduce an electrically small resonant parasitic object into the near field of the radiator [9]. By tailoring of its characteristics it is possible to improve the efficiency, but the method is generally effective only at the narrow frequency band. The problem of radiation efficiency is not easily solved, and it will not be the main concern of this thesis.

Secondly, antennas can only have limited gain (G). In 1948., Chu derived criterion for the maximum antenna gain regarding the antenna dimensions [6]. It turns out that antenna gain is proportional to dimensions of the antenna (a), and reversely proportional to the wavelength (λ):

$$G \approx \frac{4\pi}{\lambda^2} \cdot A_{eff} = \frac{4\pi}{\lambda^2} \cdot a^2\pi = \left(\frac{2a\pi}{\lambda}\right)^2. \tag{1.3}$$

Again, a stands for radius of the smallest sphere comprising the antenna, as shown in Fig. 1.1, while A_{eff} stands for the effective antenna surface. As well as efficiency, gain of an electrically small antenna can also be improved to some extent, but unfortunately at the cost of narrow relative operational bandwidth. For example, in [11], it was shown that resonant Huygens' source elements (crossed electric and magnetic dipoles) forming an electrically small two-element parasitic array can theoretically have a free-space gain as high as 9 dB.

The third limitation of electrically small antennas comes from their highly reactive nature, and it is causally linked to the gain constraint. Reactive behaviour is best described by the antenna quality factor (Q), which can be defined as a ratio between the mean stored (E_{Stored}) and mean lost energy (E_{Lost}) at the antenna per cycle [3, 12]:

$$Q = 2\pi \cdot \frac{\overline{E_{Stored}}}{\overline{E_{Lost}}}. \tag{1.4}$$

Chu established the limit on Q for a linearly polarized antenna [6], which was later on extended by Harrington, for a circularly polarized antenna [13]. Equation (1.5) sets the limit on a minimum achievable Q for an antenna [13]:

$$Q \geq \frac{1}{ka} + \frac{1}{(ka)^3}. \tag{1.5}$$

Here, a is the antenna radius, and k is defined as the wave number, which can be calculated as follows:

$$k = \frac{2\pi}{\lambda}. \tag{1.6}$$

If the antenna dimensions are small comparing to the wavelength, then Q is fairly large ($Q \gg 10$). Moreover, Q is reversely proportional to the relative bandwidth of the antenna, which can be defined as a ratio of frequency bandwidth at which return loss drops by 3 dB (Δf), and frequency with the highest value of return loss (f_0):

$$B = \frac{\Delta f}{f_0} = \frac{1}{Q}. \tag{1.7}$$

Equation (1.7) states that the antennas with high quality factor will inevitably be narrowband ($B < 0.1$) [12]. High Q factor can also be interpreted as if an antenna equivalent impedance consists of a small resistance ($R_{RAD} + R_{LOSS}$), and a very high reactance (X_{ANT}). Nature of the reactance depends on the specific antenna which is used. For example, small dipole antenna is capacitive, while a small loop antenna is inductive [3]. Using the definition with circuit elements, antenna quality factor (Q_{ANT}) can be derived as:

$$Q_{ANT} = \frac{X_{ANT}}{R_{RAD} + R_{LOSS}}. \tag{1.8}$$

Nevertheless, in a most general radio frequency system where the characteristic impedance (Z_0) is equal to 50 Ω, magnitude of the antenna reflection coefficient ($|\Gamma_L|$) of an electrically small antenna, will be close to unity. It means that most of the input power will be reflected back to the generator (in a case of a transmitting system). Very similar behaviour occurs with the antenna at the receiving point (signal power accepted by the receiving antenna will mostly be reflected back, instead of being delivered to the receiver) [2, 14].

1.2 Antenna matching networks

To overcome the problem of large reflected energy and increase radiated energy as well as efficiency, additional reactive networks are inserted between the generator and antenna, both at the transmitting and receiving side. Those are called matching networks [2, 14, 15]. Their main purpose is to transform the input impedance seen from the generator towards the antenna to the system impedance (usually 50Ω). In such case, magnitude of the input reflection coefficient ($|\Gamma_{IN}|$) is close to zero and most of the invested (incident) power is radiated or received. An example of a transmitting system comprising an RF generator, a transmission line, an antenna and a matching network, is shown in Fig. 1.3.

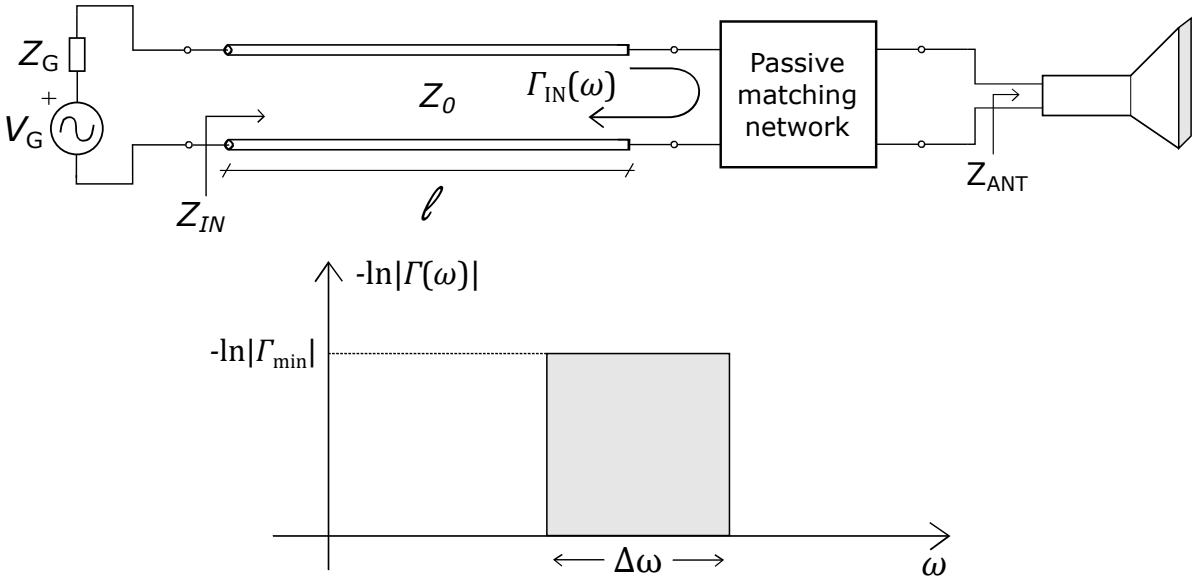

Figure 1.3: Upper: diagram of transmitting system comprising an RF generator, segment of transmission line, passive matching network and antenna. Bottom: dependence of input reflection coefficient with frequency of an antenna matched with passive matching network.

Matching networks can be synthesized in various ways. Most commonly, they are implemented as standard reactive networks that comprise either lumped reactive components (capacitors and inductors) or by using segments of transmission lines [2]. However, it can be shown that any load can be matched with some predetermined magnitude of reflection coefficient ($|\Gamma_{min}|$) only within a limited bandwidth. This limitation is known as Bode-Fano criterion [15]):

$$\int_0^{\infty} \ln \frac{1}{|\Gamma_{IN}(\omega)|} d\omega \leq \frac{\pi}{RC}. \tag{1.9}$$

In (1.9), R and C stand for the equivalent shunt resistance and capacitance of a load (antenna). An illustration of the frequency limitation of passive matching networks, described by Bode-Fano criterion, is shown in the bottom part of Fig. 1.3 [15]. Fundamentally, reason for such narrowband behaviour lies in the passive nature of both load (antenna) and matching network. Their dispersion characteristics follow the same principle (Fig. 1.4), which is

in accordance with Foster's reactance theorem [16], valid for all passive lossless reactive networks. Due to the monotonically increasing behaviour of reactances of passive elements [16], dispersion cancellation occurs only at a narrow band around the resonant frequency (Fig. 1.4).

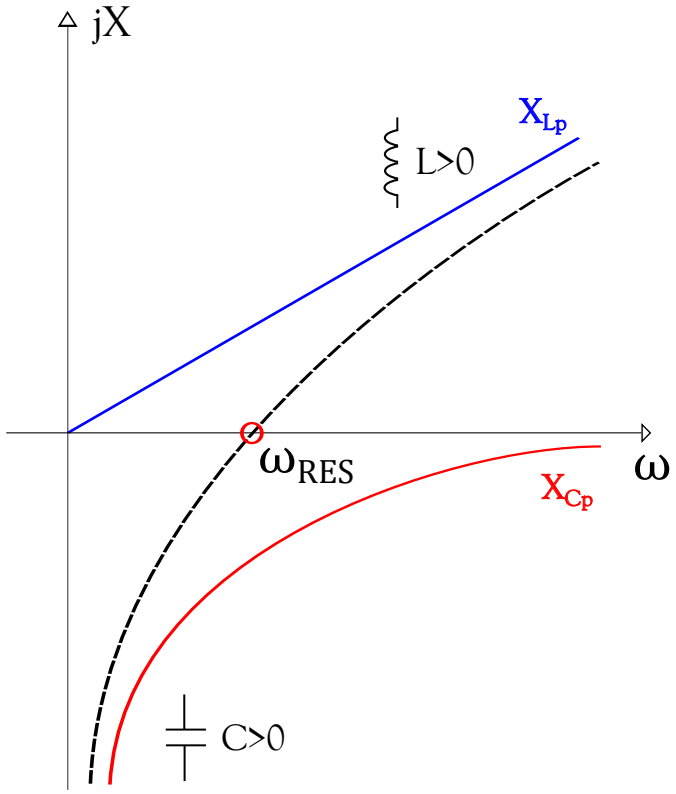

Figure 1.4: Antenna matching using passive reactive networks. Blue solid: reactance of positive inductance; Red solid: reactance of positive capacitance; Black dashed: reactance of series LC circuit.

In this context, engineers came up with some new ideas with a view of broadband matching, which were based on negative capacitors and inductors, i.e. negative elements [17, 18]. Those are hypothetical elements that possess dispersion properties which are inverse to those of ordinary passive reactive elements (positive capacitors and inductors). In another words, slope of the imaginary part of negative element's input immittance (reactance or susceptance) with regards to the frequency, is negative (Fig. 1.5). Such behaviour is the inverse of that described in Foster's reactance theorem [16], so negative elements are popularly called non-Foster elements.

However, decrease of reactance and susceptance with frequency is physically possible only by adding additional energy to the circuit [19]. That means that negative elements are inevitably realized with active elements.

Reactance characteristics of ideal positive and negative elements are shown in Fig. 1.5. If combined, positive and negative elements cancel each other's reactances or susceptances. Therefore, broadband matching is, at least in principle, possible [20].

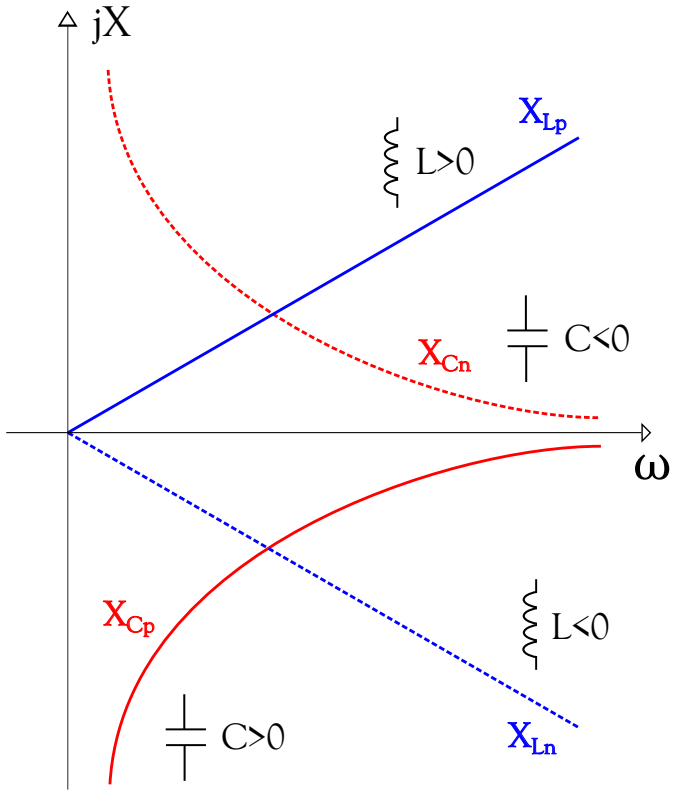

Figure 1.5: Dispersion characteristics of positive and negative capacitance and inductance. Solid: reactance of positive elements; Dotted: reactance of negative elements.

1.3 Metamaterials and metasurfaces

The idea of matching of electrically small antennas with negative elements came with the development of a new research field within electromagnetics, the field of metamaterials. Briefly, metamaterials are engineered composites, structured in a way that enables beneficial control of electromagnetic waves and acquisition of electromagnetic properties which are rarely seen in the nature [21].

First developed metamaterials were completely passive structures that comprised different types of periodic inclusions (usually realized as resonant structures) [21–23]. By definition, dimensions of such inclusions are a very small fraction of the operating wavelength [23]. The idea is that the composite gains its electrical properties from its structure, rather than inheriting them directly from the materials it is composed of [21].

An example of a volumetric metamaterial is shown in Fig. 1.6. When an electromagnetic wave impinges on such structure, the field scattered from the inclusions modifies the original field distribution in a way similar to the mechanism of polarization or magnetization in continuous materials. Therefore, the structure behaves as a hypothetical continuous material with new (homogenized) values of constitutive parameters (permittivity ε and permeability μ) [24].

On a macroscopic scale, metamaterials offer realization of exciting properties such as negative permittivity and/or permeability, permittivity or permeability near zero, negative refractive

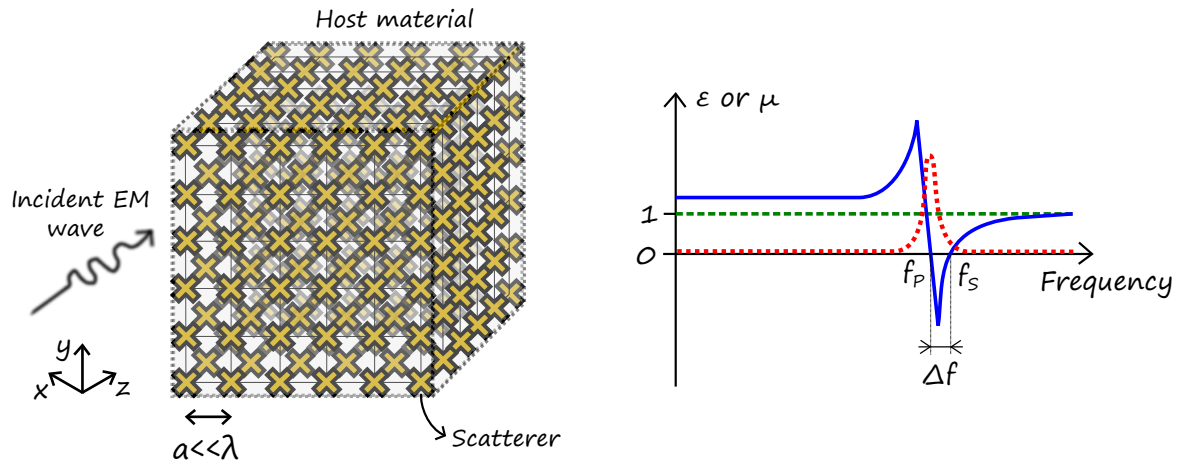

Figure 1.6: Left: concept of a 3-dimensional metamaterial with periodic scatterers (inclusions); Right: Lorentz dispersion model of relative permittivity or permeability of passive materials. Blue solid: real part of relative permittivity/permeability; Red dotted: imaginary part of relative permittivity/permeability; Green dashed: dispersion-less material.

index, electromagnetic invisibility, etc [25–30]. The inclusions from Fig. 1.6 behave as a resonator, in which the energy is constantly redistributed. Energy redistribution from the electric field into magnetic field causes a decrease of effective permittivity to a value of less than unity or negative. Similarly, energy redistribution from the magnetic field into electric field causes a decrease of effective permeability [24]. It can be considered that passive metamaterials obey Lorentz' dispersion model, as it is shown in Fig. 1.6, with parallel and series resonance (f_P and f_S). Between those two resonant frequencies values of permittivity or permeability are negative. Due to their resonant nature, passive metamaterials are inherently narrowband [23] and they introduce high losses. Consequently, the most of the properties mentioned above have not reached the point where they could be used for practical, real-word engineering applications [19].

On the other hand, a subdivision of metamaterials which is nowadays reaching maturity and bringing some successful results are so-called metasurfaces. Metasurfaces are thin sheets of material containing resonant periodic inclusions, dimensions of which are much smaller than the wavelength [31]. They can be considered as two-dimensional metamaterials. In metasurfaces, constitutive parameters (permittivity and permeability) are replaced with surface admittance and impedance parameters, which are associated with equivalent electric and magnetic surface currents. Practical advantage of such two-dimensional approach is a smaller number of scatterers, which also results in lower losses, and a simple fabrication technique that uses printed circuit boards [24]. However, passive metasurfaces, the same as metamaterials, comprise ordinary passive materials (dielectric slab with metallic pattern), which means that they are also restrained by energy-dispersion relations. In another words, they do not solve the problem of relatively narrow operating bandwidth.

So far, passive metasurfaces were successfully engineered to achieve optical lenses, polar-

ization converters, phase manipulators and many other applications [31–36]. Moreover, there are successful realizations of active metasurfaces, which contain active electronic elements [37–39]. Properties that could be achieved with active metasurfaces are wave amplification, tunability, reconfigurability and wavefront shaping. Some of the realizations of active metasurfaces are based on negative elements [19].

1.4 Realization and application of negative elements

Negative (non-Foster) elements are implemented using a negative impedance converter (NIC) or a negative impedance inverter (NIV) [40–42]. An ideal NIC is an active electronic circuit that transforms given load immittance into its negative image, regardless of the operating frequency [18, 40]. NIC comprises either an amplifier (usually voltage or current amplifier), configured to have a positive feedback loop with a load to be converted (Fig. 1.7) [40–42]. On the other hand, a negative impedance inverter can be used to realize a negative dual of any given immittance [43]. For instance, NIV can transform a positive inductance into a negative capacitance. This thesis deals only with negative impedance converters due to the more widespread use and simplicity. A simple analysis of a voltage-inversion NIC (VNIC, Fig. 1.7), and a current-inversion NIC (INIC, Fig. 1.7) leads to the expressions for the input immittance [44, 45]:

$$Y_{VNIC} = Y_L \cdot (1 - A_V), Z_{INIC} = \frac{Z_L}{1 - A_I}. \tag{1.10}$$

Here, Y_L and Z_L stand for the admittance and impedance of the load, while A_V and A_I are voltage and current gain of the NIC amplifier, respectively. A common choice in practice is $A_V = 2$ (or $A_I = 2$). This choice leads to unitary negative conversion of a load admittance (or impedance) into its negative image: $Y_L \rightarrow -Y_L$, $Z_L \rightarrow -Z_L$. If a load has a purely reactive character (capacitance or inductance), an input port of a NIC will behave as a negative capacitor or negative inductor.

Although the idea of infinitely broadband matching with negative elements sounds fascinating, variety of problems can occur in reality. First of all, there is no realistic amplifier whose gain can maintain a constant value across infinite bandwidth. Limited bandwidth is related to system poles, which in turn introduce a NIC conversion error. In the case of a negative capacitance, there is a generation of parasitic conductance, connected in parallel to negative capacitance. In order to minimize this unwanted phenomenon, one should use a super-fast amplifier with a very high cutoff frequency (tens or even hundreds GHz) [19].

Possibly the simplest way to realize a NIC is by using an operational amplifier (OPAMP) [46], and the fastest OPAMPs can operate up to the frequency of a few GHz. For higher RF and microwave frequencies, amplifiers based on discrete bipolar transistors (BJTs) or field effect transistors (FETs), are needed [41, 42]. However, the use of OPAMPs is quite good for con-

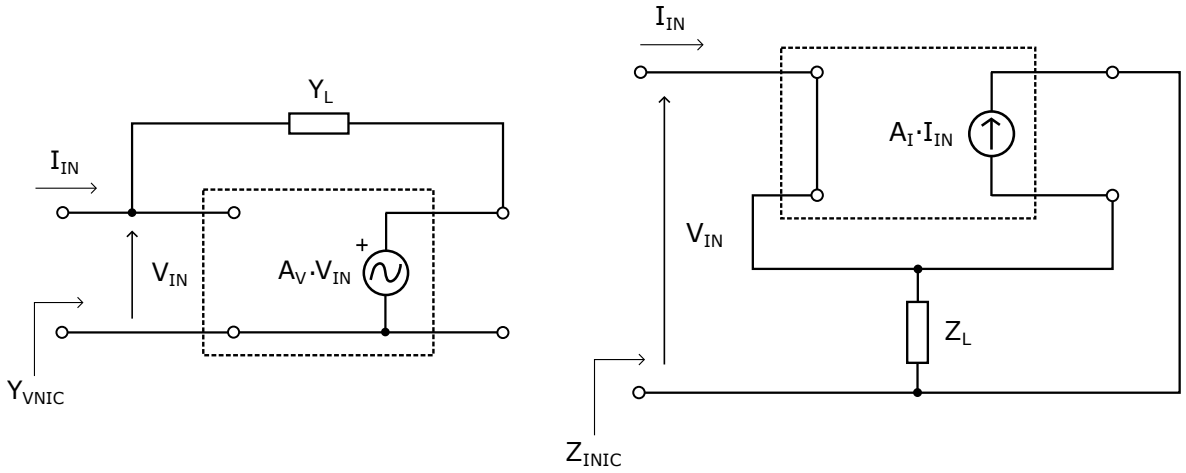

Figure 1.7: Voltage-inverting (VNIC, left) and current-inverting (INIC, right) negative impedance converters.

struction of prototypes in the lower RF regime. There were several successful realizations of negative inductors and negative capacitors [19, 20, 47–50], but all of them behaved as expected just within a limited frequency range. One of the most successful OPAMP-based approaches spans the band from 100 kHz to 700 MHz [49].

Another big challenge is the assurance of stable behaviour. By the widely accepted definition of stability (BIBO stability), system is stable if any bounded input signal yields a bounded output. It turns out that a continuous time LTI (linear time independent) system with impulse response $h(t)$ is BIBO stable if and only if [51]:

$$\int_{-\infty}^{\infty} |h(t)|dt < \infty, \tag{1.11}$$

meaning that the impulse response of a stable system is absolutely integrable.

When being part of a larger radio frequency system, networks with negative elements often show instability, and thus tend to oscillate. Stability of networks with negative elements has been investigated since 1960s [52–55]. One of the fundamental factors that contributes to instability is the inevitable presence of a positive feedback loop in the NIC circuits. It is very important to predict the possible instability, i.e. to find appropriate stability criteria in order to ensure appropriate operation of networks with negative elements [56–59].

For instance, necessary stability condition for a parallel combination of ideal positive (C_P) and negative (C_N) lumped capacitance is that their sum is positive ($C_P + C_N > 0$) [57]. The same condition applies when connecting ideal positive (L_P) and negative (L_N) lumped inductance in series, sum of inductances must be positive ($L_P + L_N > 0$) [57]. In more realistic case, when amplifier dispersion and transmission line theory is taken into account, stability criteria becomes a lot more complicated [59–62].

Even from this very brief observation it can be seen that it is actually impossible to achieve

perfect matching, along with assuring stable behaviour, using negative elements. However, constructed active matching networks have still brought many improvements comparing to passive matching networks, and definitely broadened the horizons for antenna engineers [11, 20, 63–72]. To point out a few, in [20], measurements on the constructed receiver demonstrated up to 20 dB improvement in S/N over 20 to 120 MHz range, as well as two times better power efficiency of the transmitter over 5% relative bandwidth. In [67], measurement results showed 25 MHz 10 dB bandwidth around 300 MHz, for an electrically small antenna augmented with negative elements, which is about four times greater than measured values of bandwidth of the original passive design.

Besides antenna matching, various different applications of negative elements have been attempted so far [19]. There were attempts to construct waveguides with superluminal transmission [73, 74], tunable phase shifters [75], and to prototype a variety of different wideband applications [76–78]. One example is a transmission line periodically loaded with series negative inductors and shunt negative capacitors, which is actually one-dimensional variant of active metamaterial that exhibits negative permittivity [79]. The idea was to artificially decrease distributed inductance and capacitance of the transmission line and allow so-called superluminal wave propagation [79]. Authors reported that both superluminal phase and group velocities were measured [79]. Of course, velocity of energy propagation is always lower than the velocity of light c.

Another interesting application of negative elements could be broadening of the amplifier bandwidth. The goal is to artificially decrease inherent parasitic capacitances of the amplifier by introducing additional negative capacitances, connected in parallel to parasitic positive capacitances [80].

One of the most intriguing ideas in the field of metamaterials and negative elements is a so-called cloak of invisibility. First experimental attempts included just passive elements [28, 29], but recent simulations with active (negative) elements on a thin cylindrical cloak offered significantly increased bandwidth comparing to passive cloaking [81, 82]. As interesting as it sounds, only theoretical analysis was made so far without any successful experiments. The problem of practical realization is requirement for large number of unit cells that should obtain stable operation.

Not many experiments that dealt with two-dimensional or three-dimensional problems have been made so far. One two-dimensional experiment that could be pointed out was an array of small antennas loaded with negative capacitors, inserted between a parallel-plate capacitor [48]. Antennas that were used were vertical dipoles operating in the low frequency range (up to 50 MHz). Again, the idea was to decrease the equivalent permittivity and achieve superluminal phase and group velocities.

Some three-dimensional structures have also been proposed theoretically [49], but no suc-

cessful prototypes were built to this moment. More attempts were focused on metasurfaces. Interesting applications of metasurfaces with negative elements include artificial magnetic conductors [83], broadband absorbers [84], materials with tunable refractive index [27].

Finally, some other theoretical studies attempted to include manipulation of bianisotropy [85], construction of artificial atoms [86], non-linear shaping of the waveform of electromagnetic excitation signal [86]. Also, some digital as well as high-power applications were investigated [87–89].

On the positive side, due to their unusual dispersion properties, negative elements have a lot of potential with regard to expanding the bandwidth of existing applications and broadband antenna matching. However, stability is still an unresolved issue, and there are technological constraints (for instance, finite dimensions and dispersion of an amplifier cause phase delay and distortion of signal [90]) present in practical realizations. Having that in mind, the question arises as to whether benefits gained from using negative elements exceed currently accepted solutions to such a degree that it pays of dealing with potential difficulties.

This thesis tends to unite the potential of networks with negative elements, regarding broadband matching of electrically small antennas, with their inherent instability. From that perspective, newly conceptualised antenna and matching network will be considered as an integrated self-oscillating system.

1.5 Organization of the thesis

The thesis is organized into seven chapters that generally build on each other. The introductory chapter provides a context for the use of electrically small antennas and indicates their fundamental limitations. Moreover, it provides a brief review of the field of metamaterials in electromagnetics, which is closely related to possible future applications of the research. Most difficulties of electrically small antennas are caused by their highly reactive nature and relatively low efficiency. In order to achieve better power efficiency, matching networks are inserted between the RF generator and antenna. Drawback of passive matching networks though, is that they are fundamentally narrowband. For that reason, negative elements started to be used as essential components of active matching networks. Negative elements have dispersion characteristics that are an inverse of those of ordinary positive reactive elements, so they open up the possibility of a broadband dispersion cancellation, i.e. broadband matching. However, negative elements are in practice realized using an amplifier with a positive feedback loop, which is often the cause of instability. There are two approaches to the problem of instability. One of them deals with derivation of proper stability criteria, while the other one tends to make use of the instability in a broadly matched self-oscillating system.

Chapter 2 elaborates the idea of using negative elements for antenna matching in an unsta-

ble (self-oscillating) system. Concept of a self-oscillating antenna based on negative immittance conversion is thoroughly explained in an ideal case. Briefly, in its barest form, envisioned system is comprised of two identical antennas and a NIC. One of the radiators is negatively converted via NIC, and connected to a second identical radiator. Due to the identical dispersive properties of both positive and negated antenna, admittance cancellation occurs across the infinite frequency range. Frequency tuning (selection) can be achieved either by adding a simple tank circuit or with an external synchronizing signal. The proposed device is compared to a classical active antenna and main differences are stressed out. The idea is expanded from a self-oscillating antenna with one radiator and antenna emulating network to a self-oscillating antenna with two orthogonal radiators. Main improvement of the above idea comparing to present electrically small antenna systems is frequency agile operation with theoretically higher efficiency.

In chapter 3, mathematical models of a negative impedance converter are derived, and influence of non-idealities on NIC input immittance is discussed. Models are based on two different types of NIC comprising operational amplifiers, grounded and floating version. First mathematical model takes dispersion and finite length of the amplifier into account, while the second model considers non-linearity. Finally, all of the non-idealities are taken into account for the analysis of dynamic behaviour and oscillating conditions of a self-oscillating antenna. Associated three-dimensional diagram of oscillation dynamics is developed for prediction of the amplitude and frequency of self-oscillations.

Chapter 4 focuses on the numerical analysis and experimental demonstration of a self-oscillating antenna based on negative immittance conversion with orthogonal dipole-like antennas, in the lower RF range (up to 50 MHz). Electronic part of the circuit comprises OPAMP realization of NIC (based on THS4304 OPAMP) as well as a parallel tank circuit. Antenna design and numerical calculations are conducted using a full-wave electromagnetic simulator (CST^{TM}), and a circuit theory simulator (ADS^{TM}). The process is repeated for three different types of antennas with a dipole-like radiation pattern, crossed dipoles, capacitively loaded dipoles and bow-tie antennas. Measurements on a constructed prototype are compared with obtained SPICE-based simulation results, and with theoretical analysis from Chapter 3.

Chapter 5 offers an extension of the basic idea of self-oscillating antenna to a self-oscillating Huygens' radiator. Briefly, Huygens' radiator or antenna is a coupled pair of electric and magnetic dipole, combined to achieve a unidirectional radiation pattern. Because of their low profile and compactness, planar Huygens' antennas represent a solid alternative to an antenna with ground plane. Design of an Huygens' antenna is made in full-wave electromagnetic simulator (CST^{TM}), while the whole self-oscillating system is tested in circuit theory simulator (ADS^{TM}). Simulation results as well as measurements on a developed experimental demonstrator in the lower RF range (up to 70 MHz), are presented and compared.

Chapter 6 addresses the issues of radiation efficiency, bandwidth and matching properties of a self-oscillating antenna based on negative immittance conversion. Furthermore, it covers some of its possible applications. One of the applications includes the use of an external synchronizing source. In such case, self-oscillating antenna operates without the tuning circuit and the waveform of oscillations depends only on the external signal. The main advantage of such configuration is a very broadband amplification of relatively small injected signal (similar to the concept of broadband reflection amplifier). Another application considers the implementation of FSK modulation, which is useful for communication purposes. FSK modulation is achieved using a voltage controlled capacitance for the change of frequency of the tank circuit.

Chapter 7 concludes the thesis by distinguishing the achieved contributions and pointing out the possible direction of related future work.

Chapter 2

Self-oscillating antenna based on negative immittance conversion - Main idea

The vast majority of applications of negative elements, mentioned in Chapter 1, deals with stable networks. Here, we investigate a quite different approach [24, 91–93]. The proposed device can be seen both as an oscillator (from the circuit theory perspective) and as a radiating system (from the antenna theory), similar to a well known concept of active antennas [94]. The idea is to make use of the instability which easily occurs in networks with negative elements, and also embed their matching potential [93].

The base of device are two identical antennas, and a negative impedance converter (NIC) [92]. Antennas are located at the same position in space (they have the same phase centre), while their polarizations are orthogonal in order to minimize mutual impedance, i.e. to minimize cross coupling. Additional tuning block for frequency selection is placed between the two antennas, and its realization depends on the particular application. If device is used as an integrated self-oscillating antenna, frequency tuning is achieved with an insertion of a simple tank circuit (Fig. 2.1). On the other hand, device can also be used to amplify the signal of small amplitude, injected by an external radio frequency source [24]. In that case, tuning block (tank circuit) is replaced by some kind of signal injecting circuit. For now, we will concentrate on the realization with tank circuit, as depicted in Fig. 2.1. The application with an external source will be described in chapter 6 in more details.

The working principle is as follows. Immittance (either impedance or admittance, depending on the NIC type) of the first antenna is converted into its negative image via negative impedance converter, and cancelled by an unchanged (positive) immittance of the second identical antenna (Fig. 2.1) [92]. In an ideal case, the immittances of both antennas change in the same manner with the change of the operating frequency, thus enabling very broadband immittance cancellation. The addition of an LC tank circuit, connected between the positive and negated antenna, causes resonant behaviour (sinusoidal exchange of energy between the

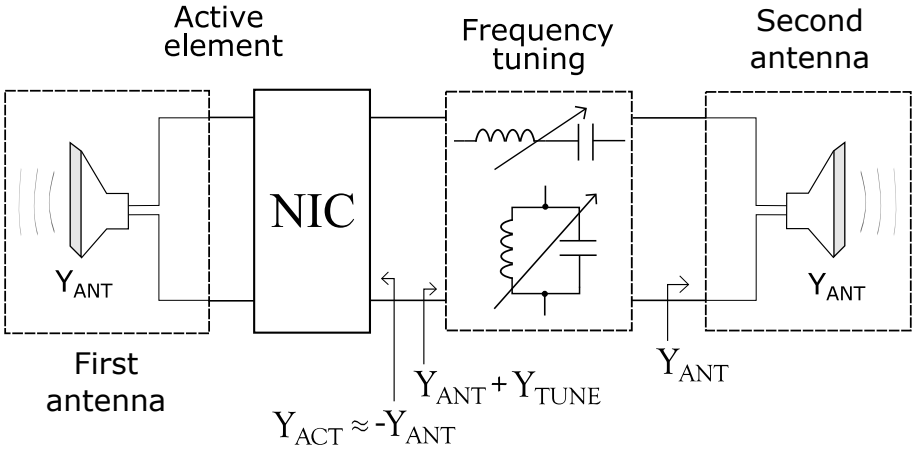

Figure 2.1: Simplified block schematic of a self-oscillating antenna based on negative immittance conversion [93].

capacitance and inductance), i.e. generation of self-oscillations. From the circuit theory point of view, total net immittance of such circuit will always be zero. It can be seen as if an active element (NIC) is capable of covering the losses in both the antenna and the tank circuit (if they are present) at any given operating frequency, which is, accordingly, solely defined by the LC resonant circuit. Ideally, it is an infinitely broadband frequency agile system [92].

The main benefit of the system lies in the fact that none of the available power is lost due to the mismatch of generator and load. Both immittance of the load and internal immittance of the generator represent actual antennas, which are chosen to be identical [93]. In another words, system is source-load matched.

Namely, the circuit behaves as an oscillator, in which an oscillating signal is created as the result of energy transformation, from DC to alternating current. In such configuration, NIC can be seen as a source or a generator with an internal immittance, which is equal to the immittance in the positive feedback loop (antenna immittance). Load immittance is defined by the second identical antenna. That means that internal immittance of the generator and load immittance are matched. Consequently, total active power is either radiated or, due to inevitable losses, dissipated at the antennas. The ratio between the radiated and dissipated power is determined by the antenna efficiency. Primary aim of the study is verification of a novel ideal of self-oscillating antenna based on negative immittance conversion. Thus, the optimization of efficiency is out of research scope, and is left out for future efforts.

From the above observation, one can derive associated equivalent circuit of a self-oscillating antenna (Fig. 2.2). In the left part of Fig. 2.2, each of the components of self-oscillating system is replaced by its circuit theory equivalent, while right part of Fig. 2.2 depicts the behaviour in steady state. Impedance Z_{ACT} represents the input impedance of NIC, while Z_{ANT} stands for the impedance of the load. Using oscillator theory [95], one can conclude that self-oscillations will occur at the resonant frequency defined by the tank circuit ($\omega_0 = \frac{1}{\sqrt{L_0 C_0}}$), without any source

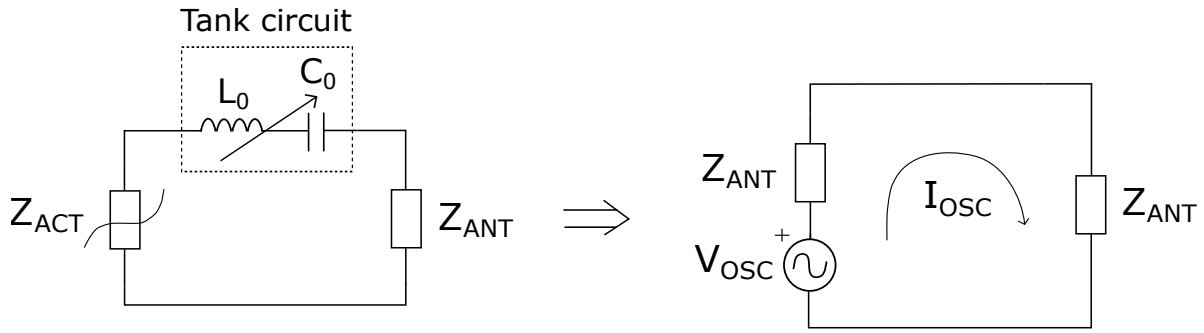

Figure 2.2: Left: representation of components of self-oscillating antenna with their circuit theory equivalents; Right: equivalent circuit of self-oscillating antenna in steady state.

present. In order to maintain the stable amplitude of self-oscillations, circuit has to comprise an active element, which will cover inherent losses of tank circuit and load [95]. If this is achieved, current of magnitude I_{OSC} will continuously flow through both antennas (loads).

It is important to mention that voltage (V_{OSC}) and current (I_{OSC}) of generated self-oscillations vary, and their magnitudes and phases depend on several different parameters. The most impact comes from the immittance of the antenna as well as gain, voltage swing and frequency characteristics of the active element. On the other hand, frequency of oscillations is mostly determined by the parameters of the tank circuit [95].

2.1 Classical active antenna versus self-oscillating antenna based on negative immittance conversion

A transmitting system, similar to a self-oscillating antenna based on negative immittance conversion, can already be found in microvawe electronics textbooks and many research studies. It is called an active antenna [2, 14, 94]. Active antennas have been investigated for many years ago. However, the device described in this thesis offers improvements regarding tunability. In this section, main working principles as well as differences between those two devices, will be promptly described and pointed out.

A classical self-oscillating (active) antenna (Fig. 2.3) [94] can be thought of as a one-port oscillator. Let us suppose for now that all of the elements are connected in parallel. In that case it is easier to conduct an analysis using admittances than using impedances. An active antenna comprises an active element with non-linear negative conductance, an admittance transformation network, and an antenna (Fig. 2.3) [94].

An equivalent circuit of this system (Fig. 2.4) is a simple parallel combination of transformed active element admittance (Y_{ACT}) and the antenna admittance (Y_{ANT}). Since Y_{ACT} describes active non-linear element, it is a function of both signal amplitude (V) and signal frequency (ω) [95]. On the contrary, Y_{ANT} describes passive antenna and it is only a function of

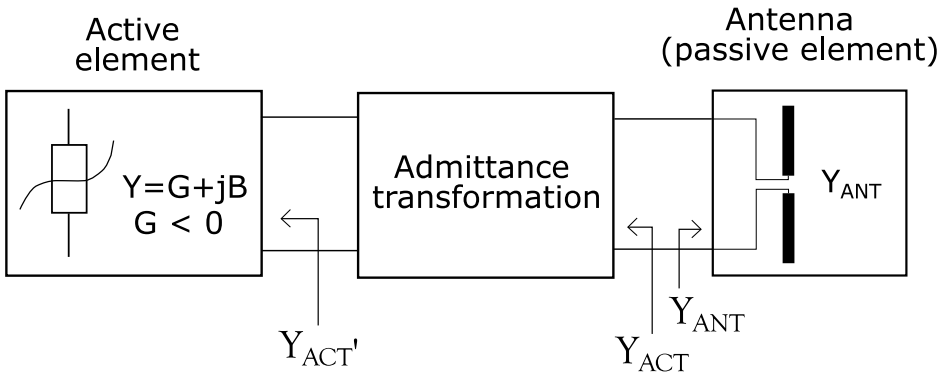

Figure 2.3: Simplified block schematic of a classical active antenna.

signal frequency (ω). Kirchhoff's voltage law relates the voltage of the only node to the mesh admittance as:

$$V(Y_{ACT}(V,\omega)+Y_{ANT}(\omega))=0. \tag{2.1}$$

A non-trivial solution ($V \neq 0$) of 2.1 leads to a well-known oscillating condition of a one-port oscillator [96]:

$$Y_{ACT}(V,\omega)=-Y_{ANT}(\omega). \tag{2.2}$$

Since most active antennas are narrowband, it is a common practice to neglect the variation of the admittance of an active element on the frequency. Thus, one can introduce simplification $Y_{ACT}(V,\omega)\sim Y_{ACT}(V)$, which allows the use of very intuitive graphical interpretation from basic oscillator theory (Fig. 2.5) [97]. A locus of the active element is located in the left hand side of a complex admittance plane, usually close to the origin (majority of active devices possess relative low negative conductance, modulus of which is significantly lower than the antenna admittance). Due to this, the modulus of an active element admittance is usually transformed to a higher value [94]. It can be achieved by incorporating a separate transforming/tuning network. The modulus of a negated transformed admittance of an active element ($-Y_{ACT}(V)$) decreases

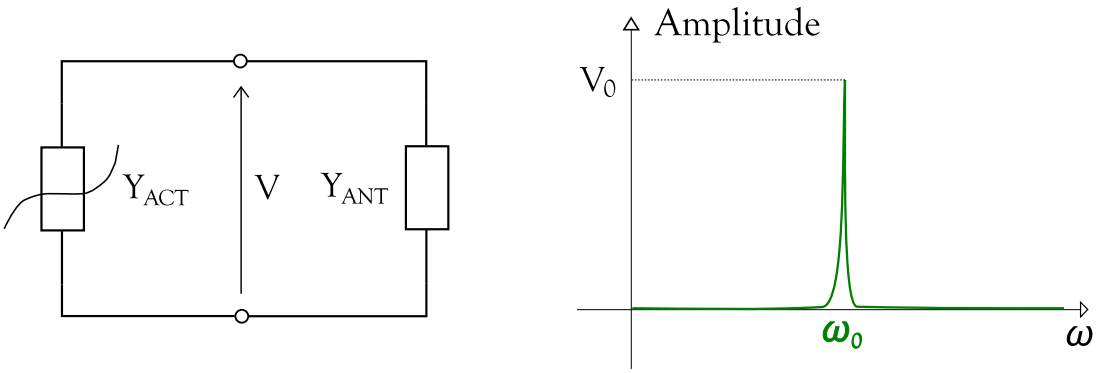

Figure 2.4: Equivalent circuit of a classical active antenna and representation of its spectrum [93].

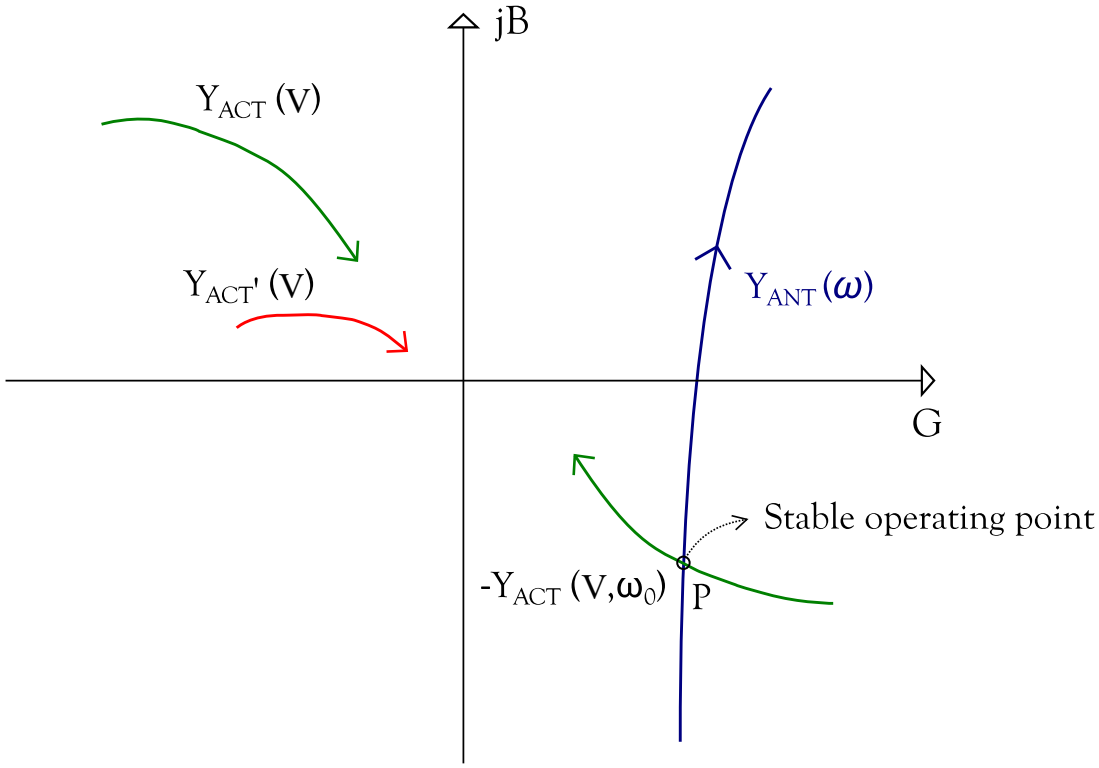

Figure 2.5: Admittance loci of a classical active antenna and process of reaching a stable operating point (V_0, ω_0). Red solid: active element; Green solid: active element with admittance transformation network; Blue solid: antenna.

during the oscillation growth. Finally, the locus of $-Y_{ACT}(V)$ intersects the locus of a passive load (an antenna, Y_{ANT}) at the operating point that determines both the amplitude and frequency of oscillations (V_0, ω_0) [97].

However, the intersection between the admittance loci of active (Y_{ACT}) and passive (Y_{PASS}) element (condition from (2.2)) is not enough to ensure stable state of oscillations. Stability requires that any perturbation in voltage or frequency will be damped out, returning the oscillator to its original state [2]. Considering the effect of a small change in voltage δV, and a small change δs in complex frequency $s = \sigma + j\omega$, one can write a Taylor series for total net admittance $Y_T(V,s) = Y_{ACT}(V,s) + Y_{PASS}(s)$ around the operating point (V_0,ω_0):

$$Y_T(V,s) = Y_T(V_0,s_0) + \left.\frac{\partial Y_T}{\partial V}\right|_{V_0,s_0} \delta V + \left.\frac{\partial Y_T}{\partial s}\right|_{V_0,s_0} \delta s = 0. \tag{2.3}$$

Here, $s_0 = j\omega_0$ stands for the complex frequency at the operating point, while total net admittance Y_T must be zero if oscillations are occurring. Taking into account that $Y_T(V_0,s_0)$=0, and that $\partial Y_T/\partial s = -j(\partial Y_T/\partial \omega)$, one can solve (2.3) for $\delta s = \delta\sigma + j\delta\omega$ [2]:

$$\delta s = \delta\sigma + j\delta\omega = \left.\frac{-\partial Y_T/\partial V}{\partial Y_T/\partial s}\right|_{V_0,s_0} \delta V = \frac{-j(\partial Y_T/\partial V)(\partial Y_T^*/\partial \omega)}{|\partial Y_T/\partial \omega|^2}\delta V. \tag{2.4}$$

In order to ensure stable operating point, transient caused by δV and $\delta\omega$ has to vanish, which

means that $\delta\sigma < 0$ when $\delta V > 0$. Equation (2.4) then requires that:

$$\frac{\partial G_T}{\partial V}\frac{\partial B_T}{\partial \omega} - \frac{\partial B_T}{\partial V}\frac{\partial G_T}{\partial \omega} > 0, \tag{2.5}$$

which is known in literature as Kurokawa's condition [97].

In the case of an active antenna shown in Fig. 2.3, $\partial G_{PASS}/\partial V = \partial B_{PASS}/\partial V = 0$, so condition (2.5) comes down to:

$$\frac{\partial G_{ACT}}{\partial V}\frac{\partial}{\partial \omega}(B_{ACT} + B_{PASS}) - \frac{\partial B_{ACT}}{\partial V}\frac{\partial}{\partial \omega}(G_{ACT} + G_{PASS}) > 0. \tag{2.6}$$

Usually, $\partial G_{ACT}/\partial V > 0$, which yields that (2.6) can be satisfied if $\partial(B_{ACT} + B_{PASS})/\partial\omega \gg 0$, implying that a high-Q circuit results in maximal frequency stability of an active antenna [2].

Now, let us analyse a possibility of using the principle of active antenna for construction of an electrically small, broadly tunable, transmitting system. Electrically small radiating elements are inevitably highly reactive, which would require a high transformation ratio of associated passive network (Fig. 2.3) and, consequently, would lead to a narrow tuning range. Indeed, a narrow tuning range is a common property of active antennas that use the same electromagnetic device (such as patch antenna), both for admittance transformation and radiation [94].

One possible solution to the problem could be a different selection of the active element. For instance, one could use an active element for which a negated admittance locus ($-Y_{ACT}$) is similar to the admittance locus of a radiating element, across a broad range of frequencies. If this is a case, no additional admittance transformation would be needed and oscillating frequency could be tuned across a broader bandwidth [93].

Antenna is a passive element and its susceptance increases with frequency ($\partial B/\partial\omega > 0$), except at the narrow frequency band around the resonance (anomalous dispersion) [3]. On the other hand, real part of the antenna admittance is very small when the antenna is electrically small, and it increases approximately with ω^2 [3]. Presuming aforementioned similarity between the two loci (Y_{ANT} and $-Y_{ACT}$), one finds that the susceptance (reactance) of the active element should decrease with frequency ($\partial B/\partial\omega < 0$), while conductance of the active element should always be negative ($G_{ACT} < 0$). So, one may think of a required active element as an ordinary passive admittance that was transformed into its negative image. The conclusion leads us exactly to networks with negative elements, realized using a negative impedance converter. Consequently, frequency agile active antenna is actually the device investigated in the thesis, a self-oscillating (active) antenna based on negative immittance conversion.

2.2 Self-oscillating antenna with a negatively converted antenna emulating network

The simplest idea of self-oscillating antenna comprising negative elements is sketched in Fig. 2.6 [91]. It is similar to the case of an ordinary active self-oscillating antenna from Fig. 2.3, but the admittance transformation network is replaced with a tuning network in the form of a simple tank circuit. Required decrease of susceptance of active element with frequency, is achieved by NIC loaded with a series RC network that (approximately) mimics an admittance of a short dipole antenna [91]. Namely, equivalent circuit of a very short dipole ($l < \frac{\lambda}{10}$) consists of a relatively small radiation resistance ($R_{RAD} \leq 2\Omega$) and highly capacitive reactance ($C \leq 4$pF) [3]. Active element can be considered as a negated antenna equivalent circuit (emulating network).

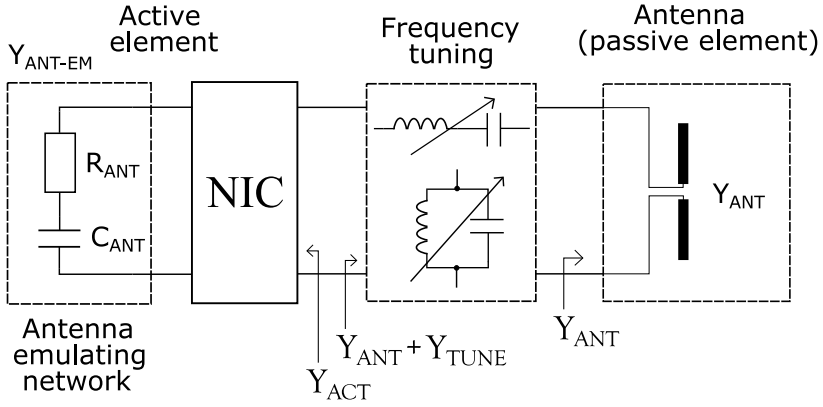

Figure 2.6: Simplified block schematic of a self-oscillating antenna based on negative immittance conversion with antenna emulating network [93].

In an ideal case, the NIC input admittance is a negative image of a load admittance (a series RC circuit, Fig. 2.7). This behaviour presumes a fixed conversion ratio of the NIC circuit at some optimal signal amplitude V_0 ($Y_{ACT}(V_0) \approx -Y_{ANT}$). A similarity between those two admittances occurs across the whole frequency band, in which the approximation of a self-admittance of a short dipole with a series RC circuit is valid ($Y_{ACT}(V_0, \omega) \approx -Y_{ANT}(\omega)$), assuming ideal NIC.

As it will be shown later, the dependence of NIC admittance on the signal amplitude occurs due to gain compression [98, 99]. During the growth of signal amplitude, before the stable operating point is reached, the NIC amplifier may be driven into a non-linear regime. This effect changes a conversion ratio and causes a decrease of the modulus of negated active element admittance ($-Y_{ACT}(V, \omega_0)$), which is shown in Fig. 2.8. Hence, the admittance of an active element (a NIC loaded with an RC circuit) is a function of both amplitude and frequency. Those effects form a family of $Y_{ACT}(V, \omega)$ curves (and $Y_{ACT}(V, \omega)$ curves) in a complex plane (Fig. 2.8). In an ideal case, only one among $Y_{ACT}(V, \omega)$ curves will coincide with the part of the antenna admittance curve ($Y_{ANT}(\omega)$), across some finite bandwidth $\Delta\omega$ (Fig. 2.8). A common

part of the $-Y_{ACT}(V,\omega)$ and $Y_{ANT}(\omega)$ loci defines the tuning range. Of course, the existence of common part is a consequence of the fact that RC circuit mimics an admittance of a short dipole. Due to pronounced similarity of two curves, a tuning range is inherently broader than the tuning range of an ordinary active antenna (Fig. 2.5). Indeed, at some point within this range, the system will have stable self-oscillations [24].

In order to find an operating point, it is necessary to include the admittance of an LC tuning circuit ($Y_{TUNE}(\omega)$) into the analysis. The tuning circuit is connected in parallel to $Y_{ANT}(\omega)$, forming a new admittance curve $Y_{ANT}(\omega)+Y_{TUNE}(\omega)$ (Fig. 2.8). This new curve is approximately perpendicular to the negated curve of the active element ($Y_{ACT}(V,\omega)$) and intersects it at an operating point, defining the amplitude and frequency of oscillations (V_0,ω_0). The frequency of oscillations (ω_0) is approximately equal to the resonant frequency of the tuning LC circuit. At this frequency, the admittance of an LC circuit ($Y_{TUNE}(\omega_0)$) is equal to zero. The change of the resonant frequency of the LC circuit changes the intersection between the $Y_{ANT}(\omega)+Y_{TUNE}(\omega)$ and $-Y_{ACT}(V,\omega)$ curve and, therefore, changes the frequency of oscillations ω_0 (Fig. 2.8). The condition for stability of an operating point is the same as in the case of a classical active antenna. Equation (2.6) has to be satisfied, which can be achieved with a high-Q resonant circuit.

There are two drawbacks of the system from Fig. 2.6. First, a dipole equivalent circuit (antenna mimicking network) that comprises only one resistor and only one capacitor is a very crude approximation, valid only within the narrow bandwidth [100]. Dipoles are naturally resonant elements, and their radiation resistance varies with ω^2 [3]. Thus, in practice, the tuning bandwidth with nearly perfect matching will be narrower than predicted. Secondly, the RF power dissipated in a resistor of an antenna mimicking network does not contribute to radiation. If a VNIC (left part of Fig. 1.7) is used for negative admittance conversion, the current through the antenna mimicking network is equal to the current through the antenna. Conversely, in the case of INIC (right part of Fig. 1.7), the voltage across the antenna mimicking network is equal to the voltage across the antenna. In both cases, the power dissipated within the antenna mimicking network is (in an ideal case) equal to the radiated power.

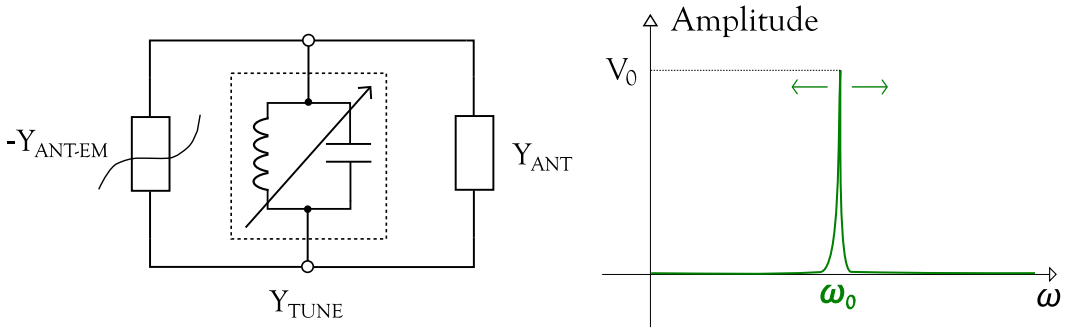

Figure 2.7: Equivalent circuit of a self-oscillating antenna based on negative immittance conversion with antenna emulating network. Representation of the spectrum for arbitrary operating frequency.

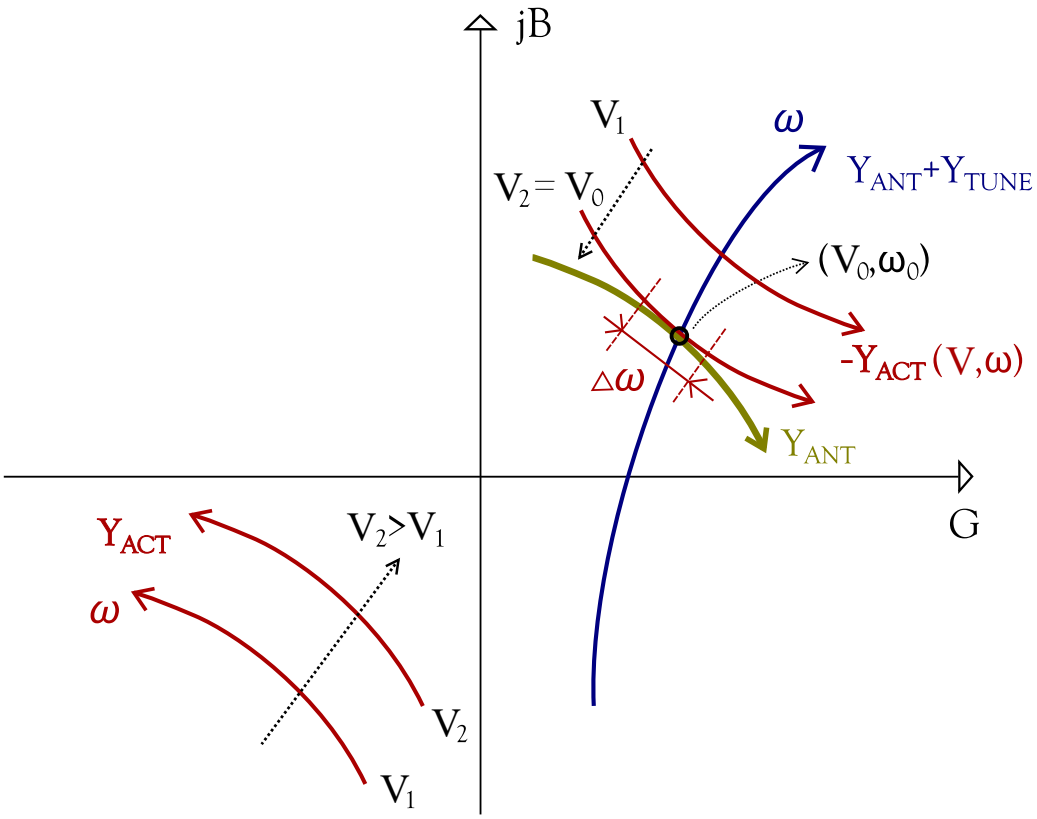

Figure 2.8: Admittance loci of a self-oscillating antenna based on negative immittance conversion with antenna emulating network. Red solid: active element (NIC); Green solid: antenna; Blue solid: antenna with tuning network [93].

2.3 Self-oscillating antenna with two radiators

In order to overcome the bandwidth problem one could construct a more complicated antenna network that mimics admittance of a short dipole more accurately. There are broadband antenna admittance models that show high accuracy within a frequency bandwidth larger than one decade, using just five elements [100]. It is clear that every antenna admittance model must contain some resistor, dissipation at which models the radiated power. However, a half of the RF energy generated by self-oscillating antenna will be dissipated again.

A better solution is a replacement of the emulating network with the second antenna that is identical to the first antenna (Fig. 2.1, [92]). By doing so, NIC input admittance would be equal to the negative image of the input admittance of the first antenna at any frequency (Fig. 2.9).

In an ideal case, the tuning bandwidth would be infinite. In reality, the tuning bandwidth will be limited by the bandwidth in which the NIC accurately converts antenna admittance into its negative image. This is the bandwidth in which the $-Y_{ACT}(V,\omega)$ and $Y_{ANT}(\omega)$ curves in a middle part of Fig. 2.10 coincide ($\Delta\omega$). Clearly, this tuning bandwidth is larger than the tuning bandwidth of a self-oscillating antenna with an antenna emulating network from Fig. 2.6. As in the case of a system from Fig. 2.6, the operating point (V_0, ω_0) is given by the resonant frequency of an LC circuit, i.e. by the intersection of a negated curve of the active element

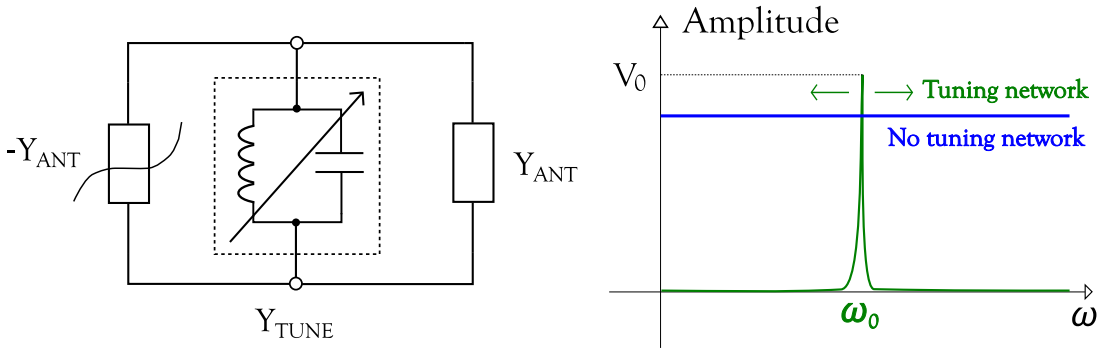

Figure 2.9: Equivalent circuit of a self-oscillating antenna based on negative immittance conversion with two radiating elements. Representation of spectrum with and without the tuning network.

$-Y_{ACT}(V,\omega)$, and $Y_{ANT}(\omega)+Y_{TUNE}(\omega)$ curve (Fig. 2.10) [97].

The intersection between the admittance curve of active and passive element indeed represents a stable operating point if a condition from (2.5) is satisfied. In the case of an ideal self-oscillating antenna with two identical radiators, where $Y_{ACT}(V_0,\omega) \equiv -Y_{ANT}(\omega)$, and neglecting the frequency dependence of losses in the tuning circuit ($\partial G_{TUNE}/\partial\omega \approx 0$), (2.5) reduces to:

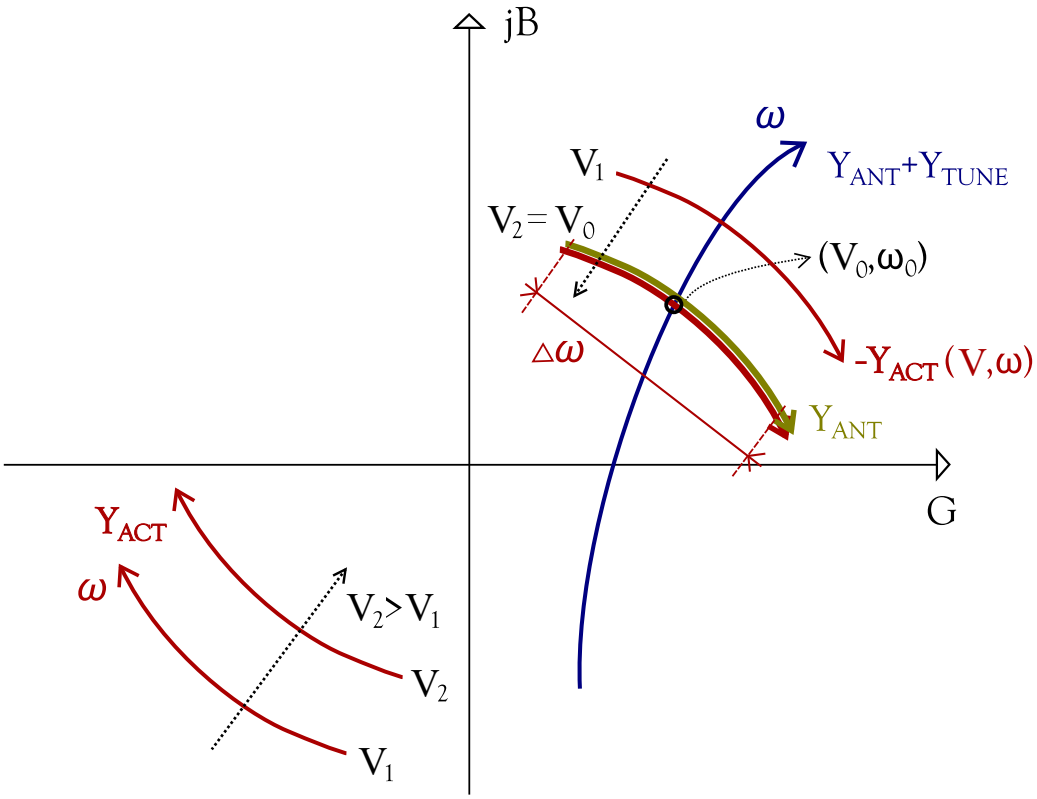

Figure 2.10: Admittance loci of a self-oscillating antenna based on negative immittance conversion with two radiating elements. Red solid: active element (NIC); Green solid: antenna; Blue solid: antenna with tuning network [93].

$$\frac{\partial G_{ACT}}{\partial V}\frac{\partial B_{TUNE}}{\partial \omega} > 0. \tag{2.7}$$

Due to the passive reactive nature of the tuning circuit, $\partial B_{TUNE}/\partial\omega$ is always positive, while non-linear analysis, which will be presented in Chapter 3.3, reveals that $\partial G_{ACT}/\partial V$ in the case of VNIC, is also positive. In another words, condition (2.7) for frequency stability is satisfied.

In the system from Fig. 2.1, both antennas equally contribute to radiation. The radiated power is theoretically 3dB higher than the power in the system from Fig. 2.6. This is related to the fact that the currents (or voltages, depending on the type of NIC) at both antennas are equal. Entire discussion of improved self-oscillating antenna based on negative immittance conversion presumed that there is no mutual coupling between two antennas. One possible way of approaching this idealized scenario in practice is the use of crossed dipoles with orthogonal polarizations [92]. Such realization is illustrated in Fig. 2.11.

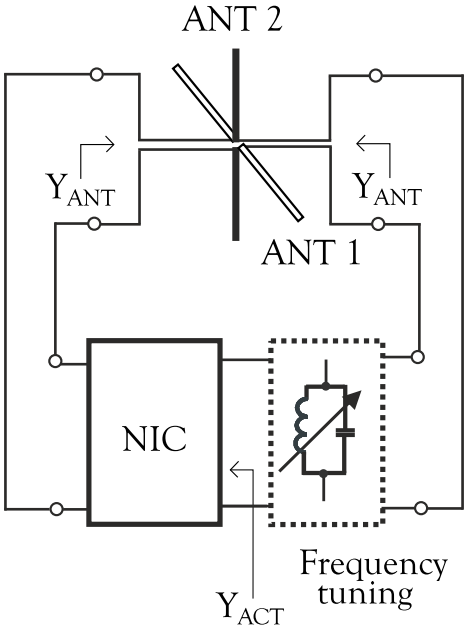

Figure 2.11: Block schematic of a self-oscillating antenna with two orthogonally polarized dipole antennas [93].

In order to numerically investigate the working principle of an ideal self-oscillating antenna based on negative immittance conversion, circuit theory simulations were made in commercial circuit simulator ADS^{TM}. The circuit diagram used in simulations is shown in Fig. 2.12.

The antennas were modelled with lumped elements (RC equivalent circuit comprised of a radiation resistance and capacitance), while NIC was modelled with an ideal voltage controlled voltage source as a voltage inverting NIC (Z_{IN}->∞, Z_{OUT}->0, ω_{POLE}->∞). The transfer parameter of a controlled source (voltage gain of the amplifier) was set to 2. These models were used in transient simulations, excited by a narrow current pulse. The simulation outputs were waveform and spectrum of a self-oscillating signal [101]. For the given circuit one would expect

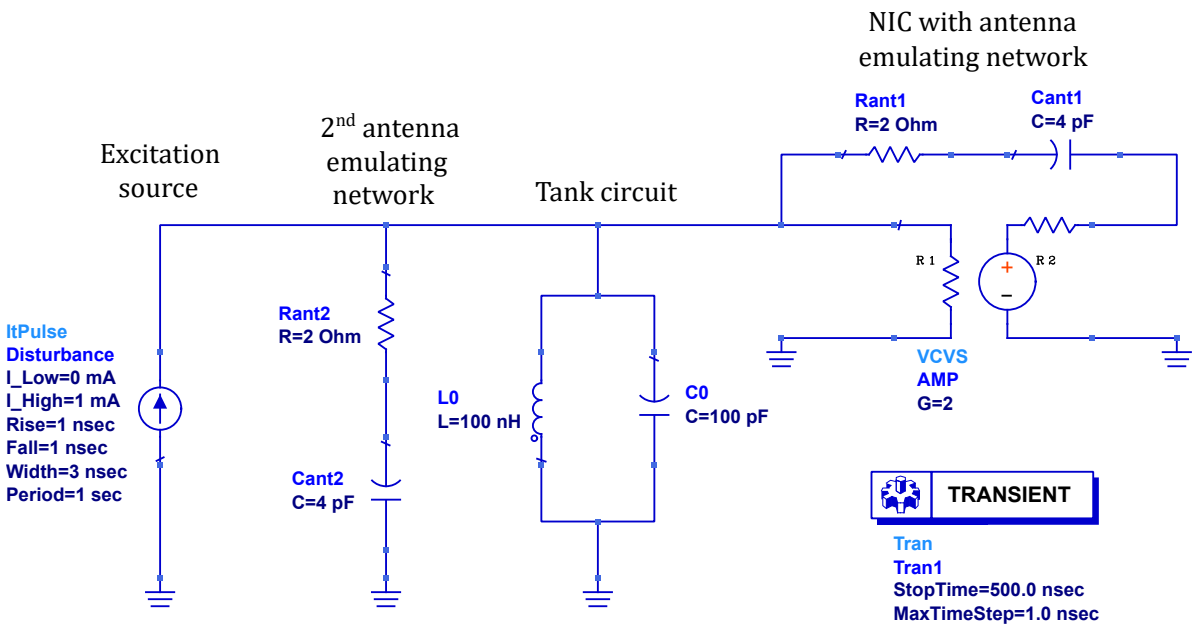

Figure 2.12: Circuit diagram of simulated self-oscillating antenna with RC antenna equivalent networks from ADS^{TM}.

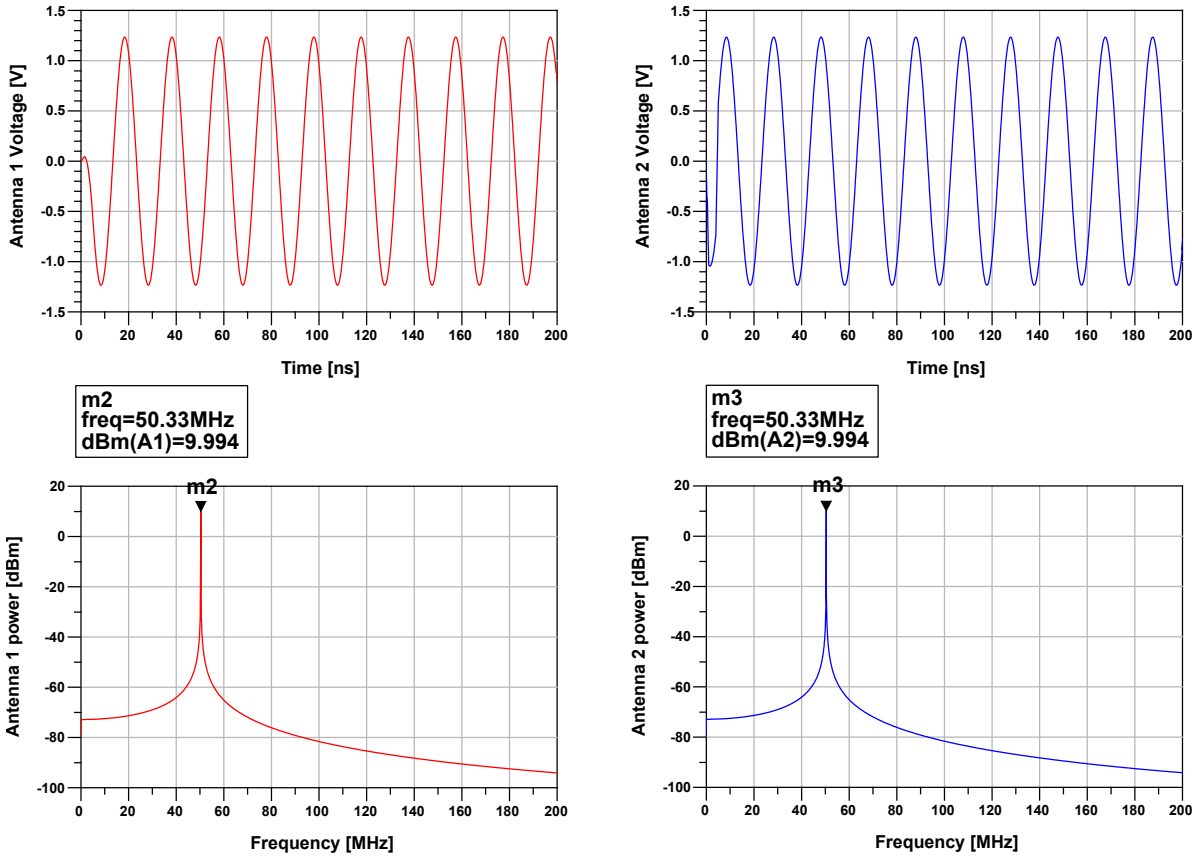

Figure 2.13: Waveforms (upper part) and spectra (lower part) of a generated self-oscillating signal at the first (left) and the second (right) antenna. Ideal self-oscillating radiating system based on negative immittance conversion.

the occurrence of self-oscillations with the frequency determined only by the parameters of the tank circuit. In Fig. 2.13, the waveforms of voltage signals and power spectra across both of the antennas are shown, and frequency of oscillations is compared with the theoretical value (L_0=100nH, C_0=100pF, f_0=$\frac{1}{2\pi\sqrt{L_0C_0}}$=50.33$MHz$).

Left part of the figure shows waveform and spectrum of the signal at the first antenna, while the right part represents waveform and spectrum of the signal at the second antenna. It can be seen that voltage magnitudes across the first and the second antenna are identical. The only difference is a phase difference of approximately 180°. Of course, this is a direct consequence of used voltage type of NIC (VNIC) [44]. Furthermore, the fundamental frequency (obtained using Fourier transform) perfectly corresponds with the calculated one. Absence of spurious components in spectra indicate that the oscillator operates in a "quasi-linear" regime. In this regime non-linearity is very week, which does not cause significant signal distortion. At the same time, non-linear effects are of the level that is enough to stabilize the amplitude of oscillations [101].

The analysis described in Figs. 2.10 and 2.13 indicates that an ideal self-oscillating antenna with two identical radiators inherently has an infinite number of potential operating points and seemingly does not need non-linearity [93]. Negated admittance locus of an active element perfectly coincides with the admittance locus of the antenna (Fig. 2.10), thus theoretically infinitely broadband oscillations are possible. However, such conclusion comes by considering only steady state analysis, and it does not take into account the process of reaching the stable operating point, i.e. the onset of oscillations and damping out the perturbations. In reality, negative resistance oscillators are designed in such a way that the amplitude of the oscillating signal has to rise to the point where the intersection between the active and passive admittance locus exists. Furthermore, any perturbation in voltage or frequency needs to be damped out, returning the oscillator to stable state. With that specific amplitude and frequency, the oscillator has reached a stable operating point, and such behaviour is possible only in the non-linear regime [95, 97].

Another very interesting property of an improved self-oscillating antenna (Fig. 2.1) is operation without the tuning LC circuit. If the LC circuit is not present, the antenna admittance will cancel the negative image of a second antenna at any given frequency (presuming identical antennas and ideal NIC). The waveform of the oscillating signal will solely depend on the waveform of an external initial disturbance [24]. For example, if one injects a small CW signal with an external generator, the device will oscillate with the same waveform, and the antennas will be perfectly matched due to admittance cancellation achieved by NIC. This situation is very similar to a classical injection locking of one-port oscillator, described by Adler's equation [102]. The lock-in range of classical oscillator is given by several parameters, including the inverse value of external Q factor of a resonator [102]. A bare self-oscillating antenna from Fig.

2.1 does not comprise a resonator (an LC circuit), hence, in ideal case, the lock-in range would be infinite [93]. If the external disturbance is just noise, the self-oscillating antenna without tuning LC circuit will generate signal with uniform spectral distribution (similar to white noise) [24].

This effect could be used for external tuning of envisaged self-oscillating metasurface, sketched in Fig. 2.14. Such metasurface would behave similarly to familiar grid oscillators [103, 104], but with a larger tuning bandwidth and better matching properties [93]. It could, along with external tuning based on injection locking, support even beam steering functionality, and preferably be combined with other tunable and reconfigurable metasurfaces [31]. Self-oscillating antenna without the tank circuit would in that case be considered as a unit cell [93]. In reality, the lock-in range would primarily be limited by the non-idealities of NIC, its finite operational bandwidth, limited conversion accuracy and non-linear properties.

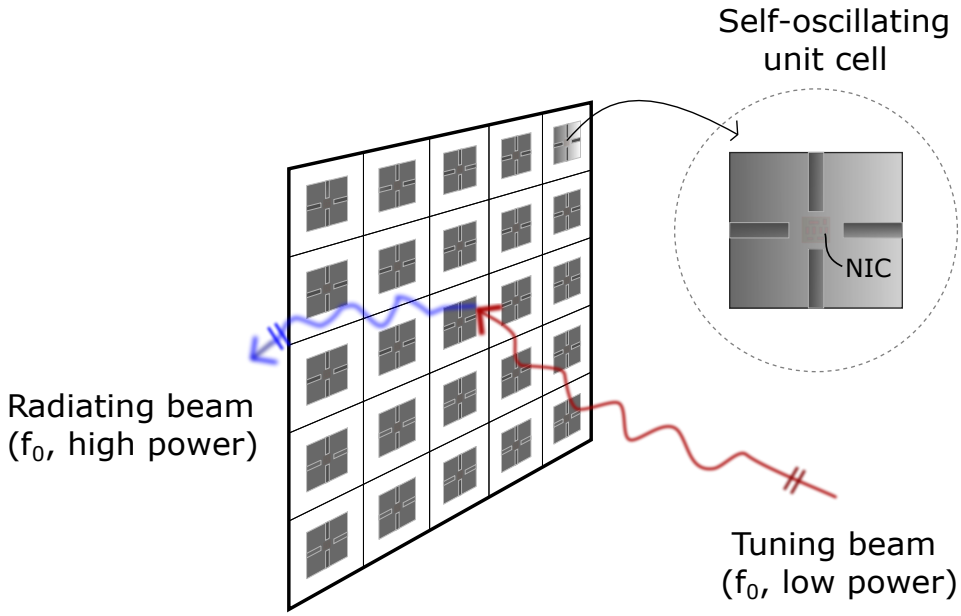

Figure 2.14: Self-oscillating metasurface comprised of self-oscillating antennas as unit cells [93].

Chapter 3

Theoretical analysis of self-oscillating antenna based on negative immittance conversion

In order to predict the behaviour of a self-oscillating antenna based on negative immittance conversion one should first derive appropriate mathematical models. Essential parts of a system from Fig. 2.1 are two identical antennas, tuning circuit and a negative impedance converter. Antennas are electromagnetic components, while tuning circuit is an electrical network, but they both have passive, linear properties. Due to that, their circuit theory modelling is performed straightforwardly using well known analytical equations [3]. Negative impedance converter, on the other hand, is based on an amplifier which necessarily comprises active components [40]. Active components are inherently non-linear and they always need some additional DC source which ensures proper operation (biasing). Behaviour of active electronic components has also been analysed for a long time (almost hundred years [105]) and the most important equations are already available. However, influence of physical phenomena as dispersion and non-linearity is not yet thoroughly investigated in basic NIC configurations.

Generally, analysis in the thesis considers only negative impedance converters based on operational amplifiers (OPAMPs), due to simplicity and practical purposes. Two possible types of NIC regarding the conversion mechanism (VNIC and INIC, Fig. 1.7) were already mentioned in section 1.4, but without going into much details. In this chapter, two different implementations of VNIC (grounded and floating version) based on OPAMPs, are discussed and analysed. Dispersive and finite length model, both for grounded and floating version of NIC, is derived. Moreover, a non-linear model, which is independent on the actual realization, is also derived.

3.1 Grounded vs. floating negative impedance converter

First, let us analyse how both grounded and floating versions of OPAMP based NIC convert the load immittance in a linear, dimensionless case with no dispersion. In such case, amplifier's gain is a constant value, regardless of the input signal magnitude or frequency of operation [46]. We introduce the following simplifications for the operational amplifier: $A_{OL} \to \infty$, $Z_{IN} \to \infty$, $Z_{OUT} \to 0$, $\omega_P \to \infty$. A_{OL} stands for the open loop gain, Z_{IN} and Z_{OUT} stand for the input and output impedance of the OPAMP, while ω_P stands for the angular frequency of the first pole of the OPAMP [46].

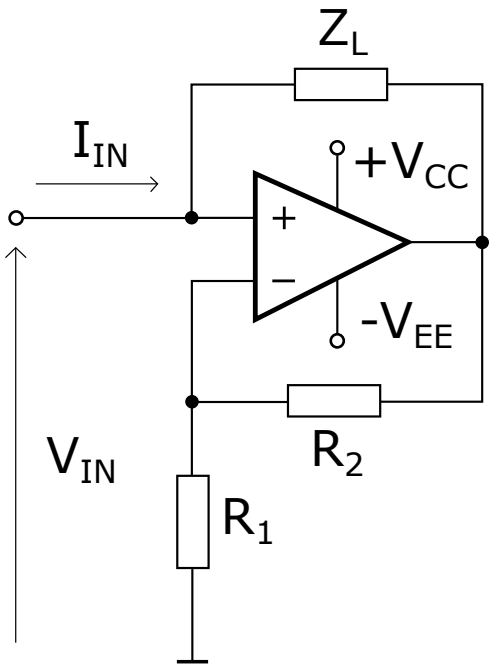

Figure 3.1: Schematic diagram of grounded negative impedance converter (NIC) based on operational amplifier.

Now, let us derive the equation for the input impedance of a grounded type NIC (Fig. 3.1). Due to the infinite open loop gain, one can write [46]:

$$V_+ = V_- = V_{OUT} \cdot \frac{R_1}{R_1 + R_2}. \tag{3.1}$$

Furthermore:

$$A_0 = \frac{V_{OUT}}{V_{IN}} = 1 + \frac{R_2}{R_1}. \tag{3.2}$$

Here, linear voltage gain for the OPAMP configuration from Fig. 3.1 (non-inverting amplifier with additional positive feedback loop) was named A_0.

The input current can be calculated as:

$$I_{IN} = \frac{V_{IN} - V_{OUT}}{Z_L} = (V_{IN} - V_{OUT}) \cdot Y_L. \tag{3.3}$$

Finally, one gets the NIC input admittance:

$$Y_{IN} = \frac{I_{IN}}{V_{IN}} = \frac{(V_{IN} - A_0 \cdot V_{IN}) \cdot Y_L}{V_{IN}} = (1 - A_0) \cdot Y_L = -\frac{R_2}{R_1} \cdot Y_L. \tag{3.4}$$

It can be seen that resistors R_1 and R_2, which form a negative feedback loop of the OPAMP, are used to set the gain as well as NIC conversion ratio. Z_L and Y_L are impedance and admittance of the load to be converted, respectively. The reason for expressing the input admittance (Y_{IN}) instead of input impedance (Z_{IN}) is following. NIC from Fig. 3.1 is a voltage inverting type (VNIC), where voltage is used as an excitation and current as a response. If there is no excitation, circuit is shorted at the input, which leads to stable behaviour [54]. Such circuit is referred to as short circuit stable (SCS) [52]. However, if one would use impedance function, where current is excitation and voltage is response, zero excitation would lead to open circuit at the input, which is in this case unstable. In addition, the equivalent input immittance of VNIC can be represented with a parallel combination of two elements (conductance and susceptance), so it is indeed more natural to calculate the input admittance [106]. On the other hand, for the current inverting type of NIC (INIC), with open circuit stability (OCS), it is required to observe the input impedance (Z_{IN}) [106].

For the case in which resistors R_1 and R_2 are of same values ($R_1 = R_2$), using the equation (3.2), one gets $A_0 = 2$, and inserting into (3.4) the input admittance turns out to be $Y_{IN} = -Y_L$.

Now, let us look at the floating version of NIC based on OPAMPs (Fig. 3.2). Floating version consists of two OPAMPs which are connected similarly to an instrumentation amplifier (Fig. 3.2) [107]. Again, this is a voltage inverting type of NIC, with short circuit stability, so it is required to investigate the input admittance (Y_{IN}). The difference comparing to the grounded version (Fig. 3.1) is the position of the load (Z_L). The load is connected between the inverting input terminals of associated OPAMPs. Also, the floating version of NIC is symmetrical. The input voltage is measured between the two non-inverting input terminals of OPAMPs, rather than between the single input terminal and predetermined reference level (ground), as it is the case with grounded NIC [107]. Let us derive the equation for the input admittance (Y_{IN}) in the floating version.

The floating version consists of two OPAMPs which are connected in series. Feedback resistors of both OPAMPs should be of the same values to get a symmetrical circuit ($R_1 = R_3, R_2 = R_4$), which is our point of interest. In that case the analysis can be made just for one half of the circuit, and then be replicated to the other half. In order to do so, the load impedance Z_L has to be divided into two identical impedances in series, with values $\frac{Z_L}{2}$. Using Kirchoff's laws as in (3.2) one can express linear voltage gain (A_0) of the OPAMPs from Fig. 3.2 as [46]:

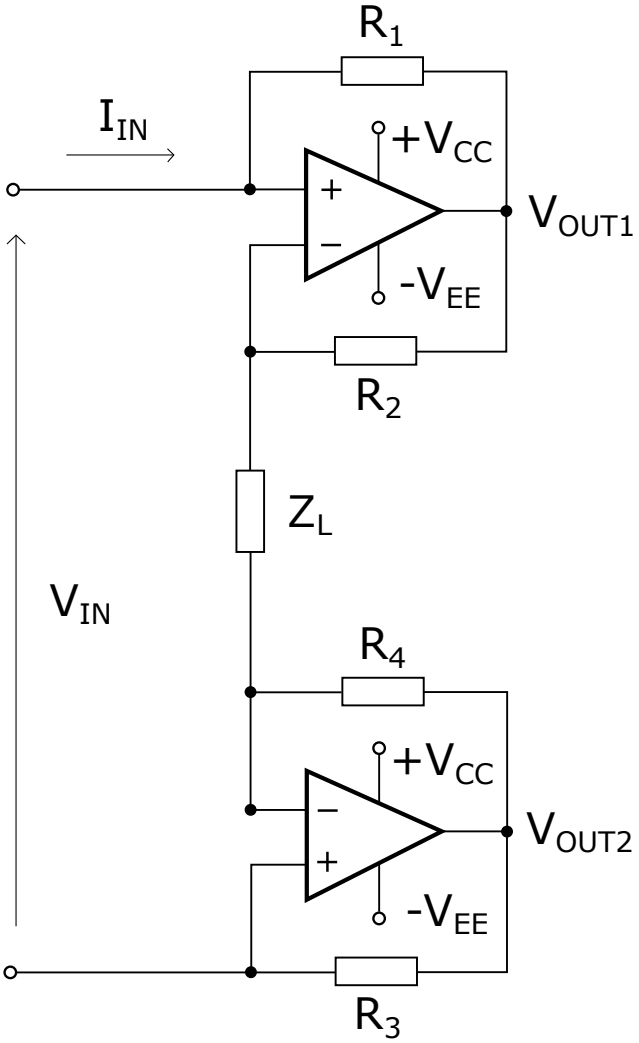

Figure 3.2: Schematic diagram of floating negative impedance converter (NIC) based on operational amplifiers.

$$A_0 = A_{01} = A_{02} = \frac{V_{OUT1,2}}{V_+} = 1 + \frac{R_2}{\frac{Z_L}{2}} = 1 + 2R_2 \cdot Y_L. \tag{3.5}$$

$V_{OUT1,2}$ stands for the output voltages of OPAMPs (Fig. 3.2) with respect to the reference level (ground). Reference level is here defined by the hypothetical line of symmetry that separates the load impedance (Z_L) into two halves. Output voltage levels are identical due to symmetry. Consequently, one gets for the half of the input impedance (Z'_{IN}):

$$Z'_{IN} = \frac{V_+}{I_{IN}} = \frac{V_+ \cdot R_1}{V_+ - A_0 \cdot V_+} = \frac{R_1}{1 - A_0}. \tag{3.6}$$

Inserting (3.5) into (3.6) gives:

$$Z'_{IN} = \frac{R_1}{1 - 1 - \frac{2R_2}{Z_L}} = -\frac{R_1}{2R_2} \cdot Z_L. \tag{3.7}$$

Finally, given that the total NIC input impedance is twice the value of the individual OPAMP

input impedance, we get:

$$Z_{IN} = 2 \cdot Z'_{IN} = -\frac{R_1}{R_2} \cdot Z_L. \tag{3.8}$$

From there, the NIC input admittance for the floating type NIC can be simply derived as:

$$Y_{IN} = -\frac{R_2}{R_1} \cdot Y_L. \tag{3.9}$$

Even though the final equations for the NIC input admittance are the same for both grounded and floating versions of NIC, there are a few important differences between the two. From (3.2) it is evident that the linear voltage gain in the grounded version is constant and it depends only on the ratio $\frac{R_2}{R_1}$. On the other hand, linear voltage gain of the floating version also depends on the admittance of the load (Y_L). Clearly, in the case of a complex load Y_L, gain will be frequency dependent. Maximal voltage swing of the floating NIC is twice as large as in the grounded version, due to the use of two OPAMPs. Finally, the floating version allows symmetrical connection of the load and external network, unlike in the grounded version. Symmetrical connection is a big advantage for the self-oscillating applications with crossed planar antennas, because it enables balanced feeding of the antennas, and minimization of mutual impedance.

3.2 Dispersive finite-length model of negative impedance converter

First realistic effect we will take into consideration is dispersive behaviour of an amplifier. It is caused by inherent parasitic capacitances and finite propagation path of a signal. There is a difference between the analysis in the case of a grounded and floating version of NIC. Firstly, grounded NIC (Fig. 3.1) has a constant value of voltage linear gain, regardless of the load to be converted (Y_L), while in the case of a floating NIC (Fig. 3.2), the gain changes with the admittance of the load. And, secondly, floating version consists of two amplifiers, which in reality can have slightly different characteristics. That can also affect the conversion accuracy. For the sake of simplicity, in our analysis we will consider both of the OPAMPs in the floating type NIC to be identical.

A model (block schematic) of a dispersive finite length NIC, which is independent on the NIC realization, is shown in Fig. 3.3 [90, 93]. Dispersion is modelled with a well known single pole approximation, where ω_P stand for the angular frequency of the first pole [46]. Pole frequency is inversely proportional to the time constant (τ) of the OPAMP ($\omega_P = \frac{1}{\tau}$) [46]. On the other hand, signal propagation path is interpreted as phase delay (ϕ) that manifests as a segment of transmission line ($e^{-j\phi}$) [2].

The correlation between the amplifier length (Δl) and phase delay (ϕ) is given by the fol-

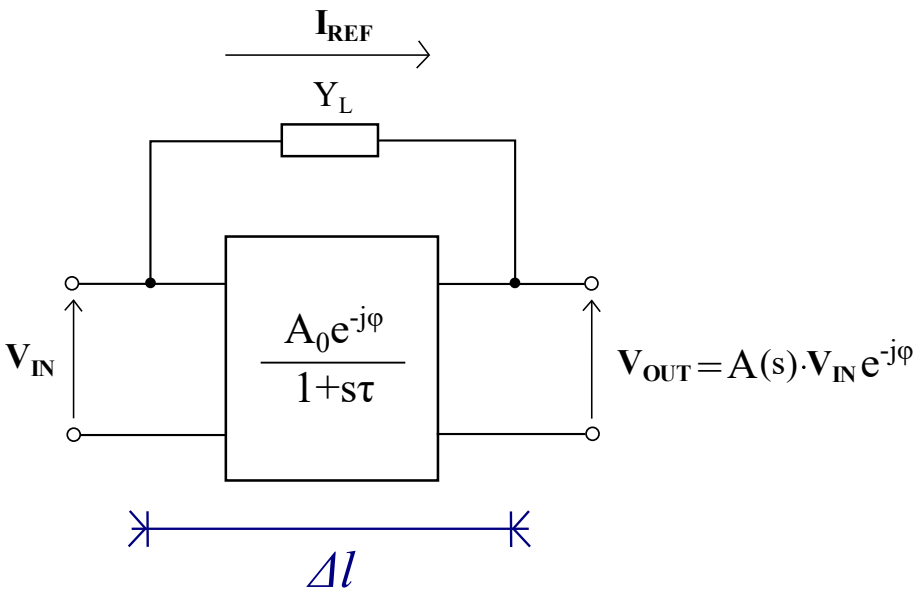

Figure 3.3: Single pole finite-length model of a NIC.

lowing equation [2]:

$$\phi = \phi(\omega) = \beta\Delta l = \frac{\omega\Delta l}{c}, \tag{3.10}$$

where β is phase constant (imaginary part of the wave propagation constant), and c is the velocity of light ($c = 3 \cdot 10^8$ m/s). How phase delay and presence of pole affect the signal in time domain, is shown in Fig. 3.4. The example is based on a simple voltage pulse. The voltage signal at the output is amplified, but distorted due to dispersion, and delayed in time because of finite propagation distance [105].

Also, it is common to observe the effect of dispersion in the frequency domain (ω). In Fig. 3.5 it is shown what a single pole (ω_P) does to the voltage gain (A). Gain starts to drop with a 20 dB per decade slope [46]. It would be even more precise to include more than one pole in the analysis. However, introduction of several poles significantly complicates the equations for NIC input admittance, without revealing new information of interest. All of the conclusions obtained by the single pole model of OPAMP are perfectly valid and sufficient for our application.

On the other hand, influence of phase delay can be illustrated using phasor diagrams as in Fig. 3.6 [24]. Phasors of currents and voltages are based on NIC, block schematic of which is given in the upper part of Fig. 3.6. NIC comprises a parallel combination of conductance (G_L), and capacitance (C_L), in the positive feedback loop. I_{REF} stands for the reference current, and by definition it flows from the NIC input toward the output. Due to the higher electric potential at the amplifier output (point B) than at the input (point A), real direction of current is from the output toward the input, and that current is labelled as I_{IN}. Current I_{IN} is divided into currents I_G and I_C, because of the parallel combination of G_L and C_L. I_G is in phase with the voltage difference between the input and output terminal of NIC ($V_{AB} = V_{IN} - V_{OUT}$), while I_C precedes

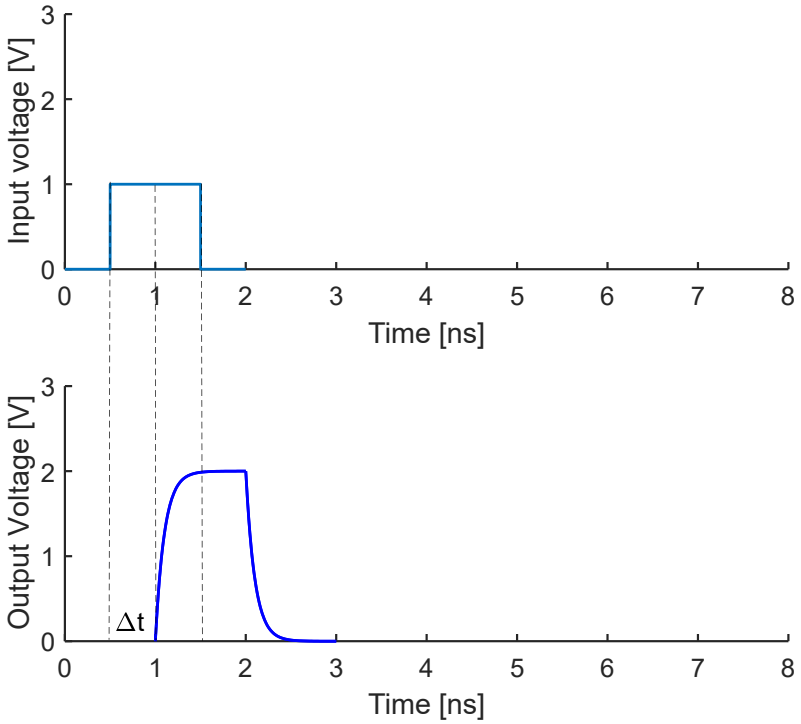

Figure 3.4: Voltage at the input (upper graph) and output (lower graph) of NIC for a dispersive finite-length NIC model.

by 90°. The analysis for the parallel combination of conductance and inductance would be analogue, but the current at the inductance would have 90° delay comparing to I_G.

It can be seen that phase delay ϕ, due to finite amplifier length, causes the shift of current I_{IN}, represented with the angle α. However, using geometry, one can conclude that the angle α is actually equal to phase delay ϕ. Finally, phase shift of current I_{IN} will cause the same phase shift (α or ϕ) of the NIC input admittance, because the input admittance is given with the equation:

$$\mathbf{Y_{IN}} = \frac{\mathbf{I_{IN}}}{\mathbf{V_{IN}}} = \frac{|I_{IN}|\angle\phi}{\mathbf{V_{IN}}}. \tag{3.11}$$

The influence on the input admittance is illustrated in Fig. 3.7 [24]. Two different cases are shown, for two different loads in the positive feedback loop. Left graph in Fig. 3.7 represents the influence of phase delay on conversion of a low-Q load ($\frac{B_L}{G_L} \approx 1$), while right graph represents conversion of a low-Q load ($\frac{B_L}{G_L} \gg 1$).

It is evident that in both cases phase delay causes offset of the real and imaginary part of the input admittance. However, signs of offsets (δG and δB) are opposite, and they depend on the nature of the load (inductive or capacitive):

$$Y_{IN} = G_{IN} + jB_{IN} = -(G_L + \delta G) - j(B_L - \delta B). \tag{3.12}$$

Most importantly, relative errors of input conductance and susceptance ($\frac{\delta G}{G_{IN}}$ and $\frac{\delta B}{B_{IN}}$) depend

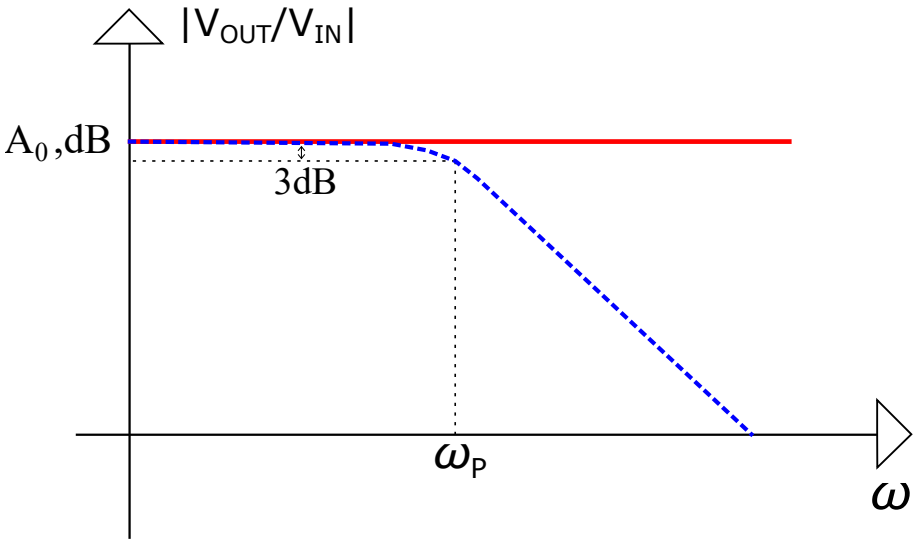

Figure 3.5: Gain-frequency characteristic of a single pole amplifier. Red solid: ideal dispersion-less amplifier; Blue dashed: single pole amplifier.

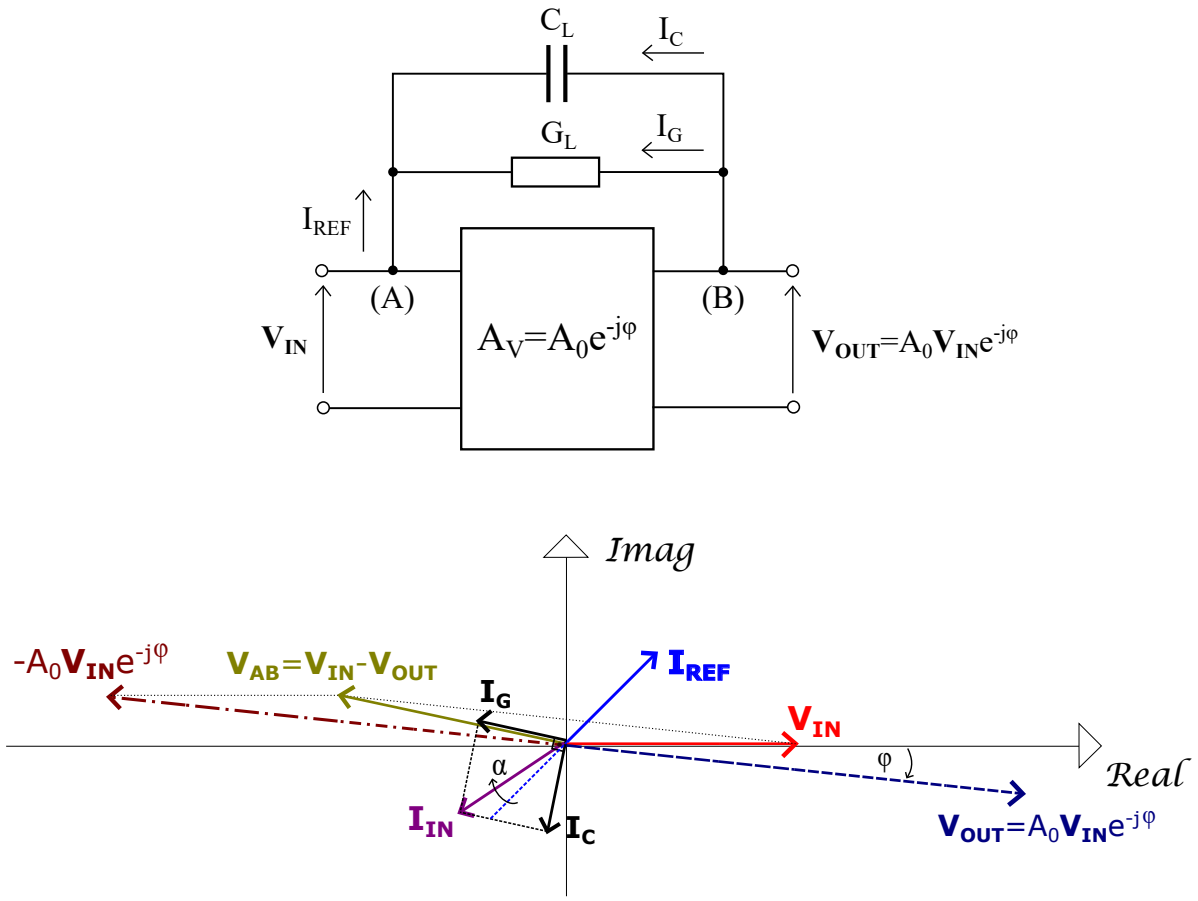

Figure 3.6: Upper: block schematic of a finite-length NIC with parallel combination of conductance and capacitance in the positive feedback loop; Bottom: phasor diagram of currents and voltages in negative impedance converter with a present phase delay. Red solid: NIC input voltage; Blue solid: input reference current; Purple dashed: NIC output voltage; Brown dot-dashed: negated output voltage; Solid green: differential voltage; Black solid: conductance and capacitance currents; Purple solid: actual input current.

on the quality factor of the load ($Q = \frac{B_L}{G_L}$) [90]. For instance, load which has approximately same magnitude of conductance and susceptance (left part of Fig. 3.7) will exhibit proportional errors. On the other hand, load with much greater imaginary part of the admittance will exhibit greater error of the input conductance, and vice versa.

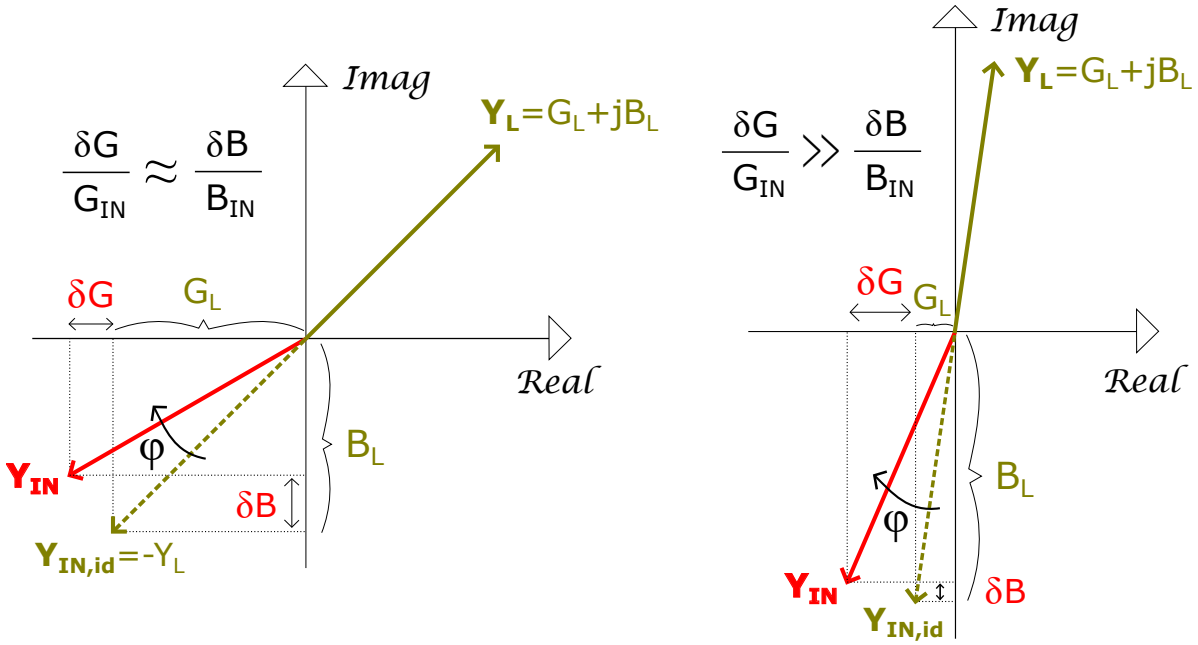

Figure 3.7: Phasor diagram of load and input admittances of negative impedance converter with a present phase delay. Left graph: low-Q load; Right graph: high-Q load. Green: load admittance and ideal conversion; Red: realistic conversion.

Let us now derive the equations for NIC input admittance, for the grounded version of NIC (Fig. 3.1), with an admittance Y_L in the positive feedback loop. As shown in Fig. 3.3, gain-transfer function of an amplifier can be expressed as [46]:

$$A = \frac{A_0 e^{-j\phi}}{1 + \frac{s}{\omega_P}}. \tag{3.13}$$

By inserting (3.13) into (3.4), with the substitution $A_0 \to A$, and by using simplification $e^{-j\phi} \to \cos\phi - j\sin\phi$, the equation comes down to:

$$Y_{IN} = Y_L \left(\frac{1 + \frac{s}{\omega_P} - A_0 \cos\phi + jA_0 \sin\phi}{1 + \frac{s}{\omega_P}} \right). \tag{3.14}$$

However, (3.14) does not provide intuitive information about the influence of dispersion on the NIC conversion. For the most cases of interest, steady state analysis is sufficient, and therefore, one can substitute a complex variable s with the angular frequency ($s \to j\omega$). Also, let us suppose that load admittance consists of arbitrary conductance and susceptance ($Y_L = G_L + jB_L$). The NIC input admittance now reads as:

$$Y_{IN} = (G_L + jB_L)\left(\frac{1 + j\frac{\omega}{\omega_P} - A_0\cos\phi + jA_0\sin\phi}{1 + j\frac{\omega}{\omega_P}}\right). \tag{3.15}$$

Finally, by rewriting the equation and separating the real and imaginary parts of the input admittance, one gets:

$$Real\{Y_{IN}\} = \frac{G_L(1 - A_0\cos\phi) - A_0B_L\sin\phi + (A_0G_L\sin\phi - A_0B_L\cos\phi)\frac{\omega}{\omega_P} + G_L(\frac{\omega}{\omega_P})^2}{1 + (\frac{\omega}{\omega_P})^2}, \tag{3.16}$$

$$Imag\{Y_{IN}\} = \frac{B_L(1 - A_0\cos\phi) + A_0G_L\sin\phi + (A_0B_L\sin\phi + A_0G_L\cos\phi)\frac{\omega}{\omega_P} + B_L(\frac{\omega}{\omega_P})^2}{1 + (\frac{\omega}{\omega_P})^2}. \tag{3.17}$$

It can be seen that the NIC input admittance Y_{IN} is not a scaled negative image of Y_L, as it was in the ideal case ($Y_{IN} = Y_L(1 - A_0)$). Now, both real and imaginary parts of Y_{IN} are functions of angular frequency (ω), indicating that the accuracy of NIC conversion is limited (they are also a function of phase shift ϕ, but ϕ is dependent only on the angular frequency, $\phi = const \cdot \omega$).

A careful inspection of (3.16), (3.17) reveals that the value of NIC conversion error depends both on the properties of the amplifier (pole frequency ω_P and length of the amplifier Δl), and on the Q factor of the load to be converted (ratio $\frac{B_L}{G_L}$) [90, 93]. Physically, the error occurs because the input voltage is not precisely a negative version of the load voltage ($V_L = V_{IN} - V_{OUT}$), as it would be the in ideal case. Inevitable phase shift of the output voltage and parasitic capacitance of the amplifier cause the conversion offset at low frequencies as well as perturbations at frequencies close to the pole frequency ($\omega \approx \omega_P$), and above. If a load (Y_L) has a large Q factor, ratio of currents flowing through B_L and G_L is inherently large. In this case, a small phase shift will introduce a small relative change of the current through B_L but, at the same time, a large relative change of the current through G_L. Thus, a conversion error of the real part of Y_L will be more pronounced [90, 93].

The most complex situation occurs when converting a load, real and imaginary parts of which are a complicated function of the operating frequency. Such load can be a dipole antenna, which is here modelled with a broadband numerically obtained five-element equivalent circuit, containing capacitances, inductances, and a resistance [100]. Specified antenna equivalent circuit, which is actually modified Chu's model of electrically small dipole, is shown in Fig. 3.8. For the dipole of length l=1.5m, values of circuit elements are L_1=47.25nH, L_2=1.335μH, C_1=0.625pF, C_2=1.95pF, R=8992Ω.

Antenna is a load, admittance of which considerably changes with the operating frequency.

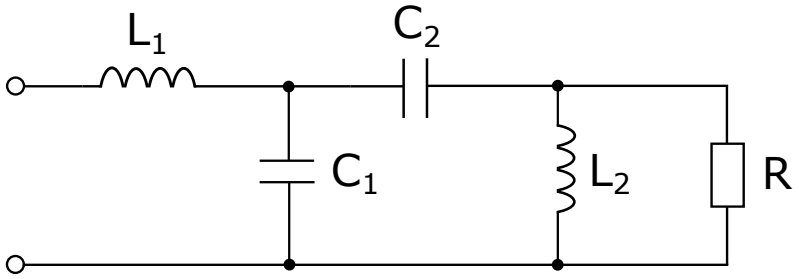

Figure 3.8: Broadband 5-element equivalent circuit model of dipole antenna [100].

At some frequencies it can be considered a high-Q load ($l \lessapprox \frac{\lambda}{5}$), while at other frequencies it behaves as a low-Q load ($\frac{\lambda}{5} \lessapprox l \gtrapprox \frac{\lambda}{2}$) [3]. In this example, antenna is 1.5m long, making it a $\lambda/2$ dipole at the frequency $\omega = \frac{\omega_P}{10}$.

Based on (3.16), (3.17), a series of calculations of relative conversion error was performed and some of the representative results are given in Figs. 3.9, 3.10, 3.11, and 3.12. The first set of results displays NIC conversion ratio for three different loads in the positive feedback loop [90]. Fig. 3.9 represents conversion ratio of the real part of the input admittance ($\frac{G_{IN}}{G_L}$), while Fig. 3.10 represents the conversion ratio of the imaginary part of the admittance ($\frac{B_{IN}}{B_L}$).

On the graphs, ideal NIC conversion is represented with a dot dashed green line ($\frac{Y_{IN}}{Y_L} = -1$), conversion of a low-Q load (series RC circuit with R=2Ω, C=100pF) with a dashed blue line, conversion of a high-Q load (series RC circuit with R=2Ω, C=4 pF) with a dotted red line, and conversion of a five-element equivalent circuit of a 1.5m long dipole antenna (numerically

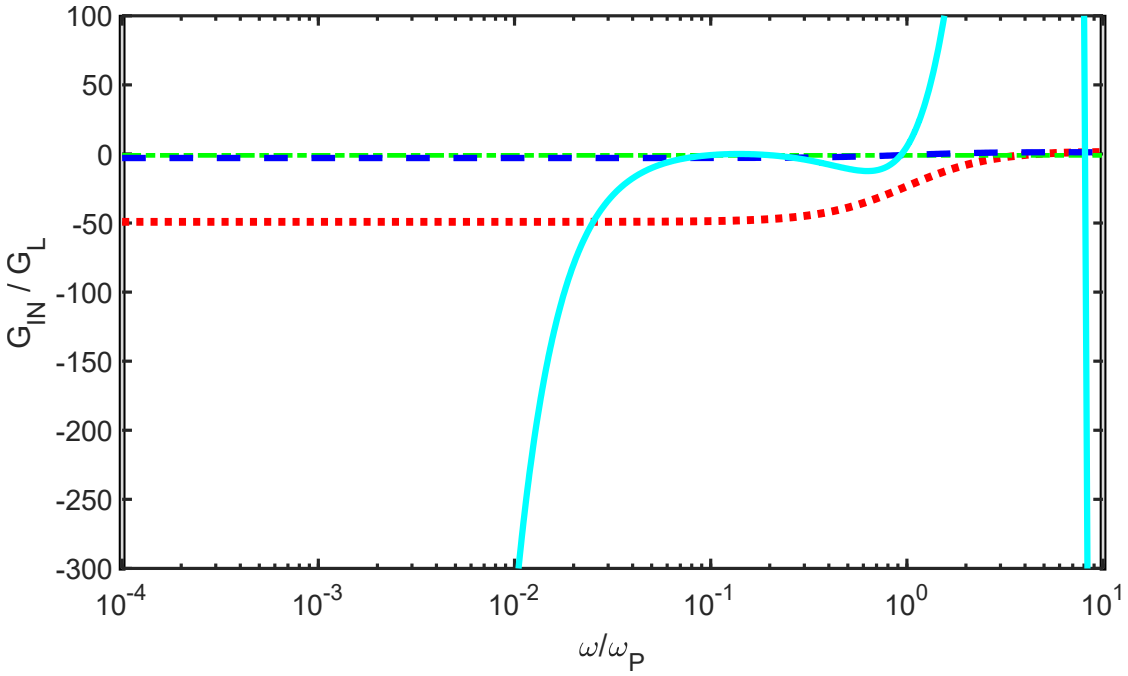

Figure 3.9: Conversion ratio of the real part of the NIC input admittance for three different loads for the grounded version of NIC. Green dot-dashed: ideal conversion; Blue dashed: low-Q load; Red dotted: high-Q load; Cyan solid: 5-element dipole antenna model.

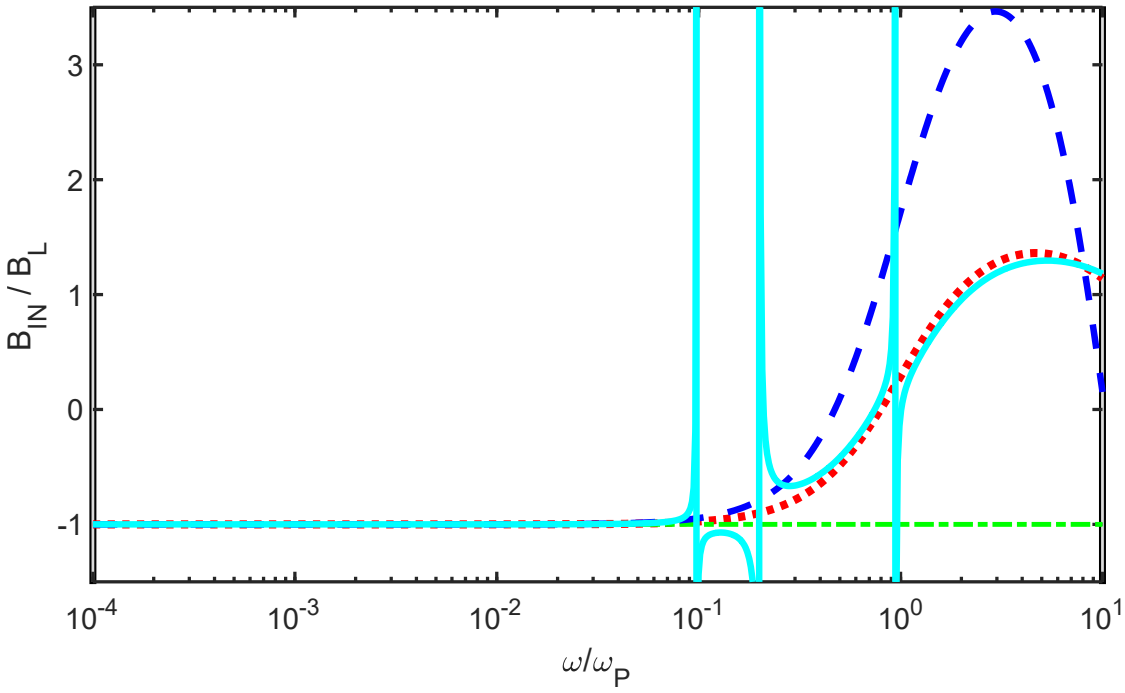

Figure 3.10: Conversion ratio of the imaginary part of the NIC input admittance for three different loads for the grounded version of NIC. Green dot-dashed: ideal conversion; Blue dashed: low-Q load; Red dotted: high-Q load; Cyan solid: 5-element dipole antenna model.

obtained model [100]) is represented with a solid cyan line. In all calculations pole frequency was set to $\omega_P = 2\pi \cdot 10^9$rad/s, while amplifier length Δl was 1cm.

One can immediately notice that the conversion accuracy depends not only on the characteristics of the NIC, but also on the load to be converted [90]. The effect on the real part of the input admittance is much more pronounced than the effect on the imaginary part of the admittance. In the case of a low-Q load, both real and imaginary parts of the admittance are converted almost ideally up to the frequency $\frac{\omega_P}{10}$. At that point, phase starts to decrease and it reaches -45° at the frequency $\omega = \omega_P$. The phase characteristics affects the conversion and gradually shifts conversion ratio towards positive values.

However, in the case of a high-Q load, conversion error of the real part of the admittance occurs even at frequencies well below the frequency $\frac{\omega_P}{10}$. The error manifests itself as an offset independent on the frequency. The reason for such offset can be found with careful analysis of (3.16). To be precise, the third term in (3.16), in the cases where G_L or B_L are inversely proportional to the frequency ω, cancels out with the part $\frac{\omega}{\omega_P}$. Therefore, the third term becomes independent of the operating frequency. The value of the offset depends on the value of the equivalent capacitance or inductance of the load. For example, for capacitive loads with C_{EQ} =4pF (dashed red line in Figs. 3.9, 3.10) the offset is approximately 20 times larger than for the capacitive loads with C_{EQ} =100pF.

It can be seen in Fig. 3.9 that conversion ratio of the real part of the admittance of dipole antenna equivalent circuit, for frequencies approximately below $\frac{\omega_P}{25}$, is 50 times larger than in

the ideal case. At those frequencies, length of the antenna is smaller than $\frac{\lambda}{5}$ and antenna can be considered as a high-Q load. For frequencies between $\frac{\omega_P}{25}$ and $\frac{\omega_P}{10}$, where the antenna length is between $\frac{\lambda}{5}$ and $\frac{\lambda}{2}$, antenna can be considered as a low-Q load and the conversion error is acceptable for most applications.

Again, the imaginary part of the input admittance is converted almost ideally up to the frequency $\frac{\omega_P}{10}$ (Fig. 3.10). Irregularities at higher frequencies are caused by the resonant nature of the antenna.

Let us now separately investigate the influence of dispersion and phase shift of the amplifier on the NIC input admittance [90]. The load is now the same for all cases, it is a high-Q network (series RC circuit with R=2Ω, C=4pF, a rough approximation of a small dipole antenna). Again, the pole frequency was set to $\omega_P = 2\pi \cdot 10^9$rad/s, while amplifier length Δl was 1cm. The dot dashed green line represents an ideal conversion ($\frac{Y_{IN}}{Y_L} = -1$), dashed blue line represents only the influence of amplifier finite dimensions, dotted red line represents only the influence of dispersion, while combined effect of both length and dispersion is shown with solid black line. Results for the conversion ratio of real and imaginary parts of the admittance are shown in Figs. 3.11, 3.12.

It can be seen that both dispersion and finite length cause conversion offset of the real part of the admittance at low frequencies. Conversion ratio due to phase shift is around 10 times greater than the one from ideal case, while dispersion causes even 40 times greater conversion ratio comparing to the envisaged one. Combined influence results in about 50 times greater

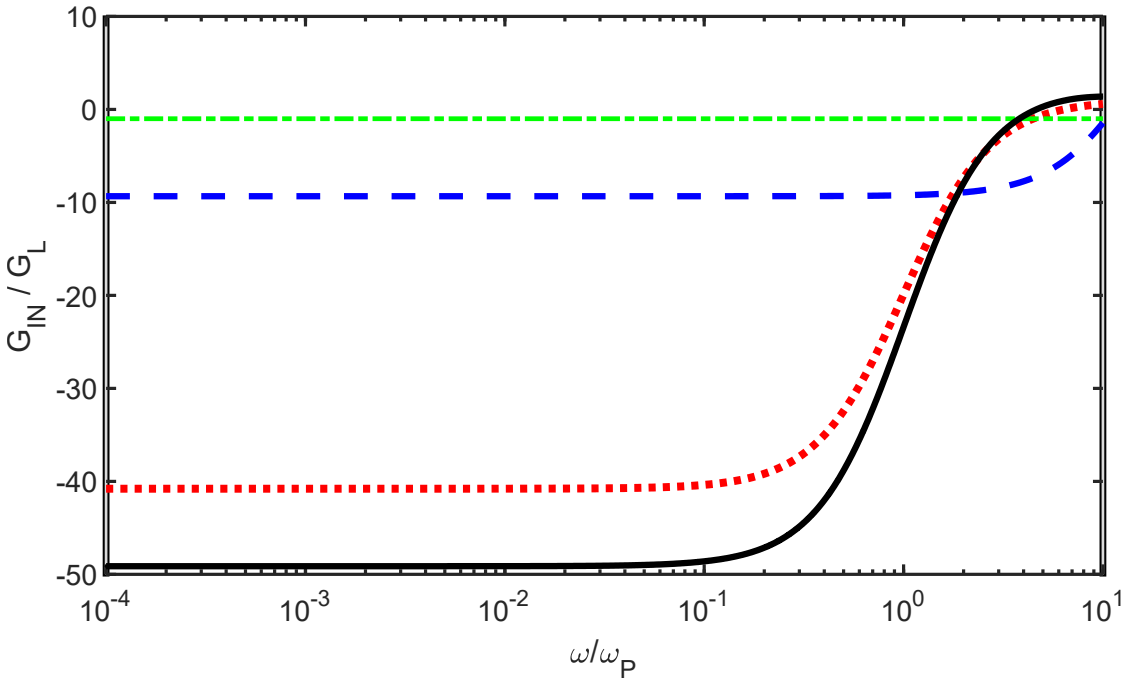

Figure 3.11: Influence of different physical mechanisms on the conversion ratio of the real part of the NIC input admittance. Green dot-dashed: ideal conversion; Blue dashed: influence of phase delay; Red dotted: influence of dispersion; Solid black: combined effect.

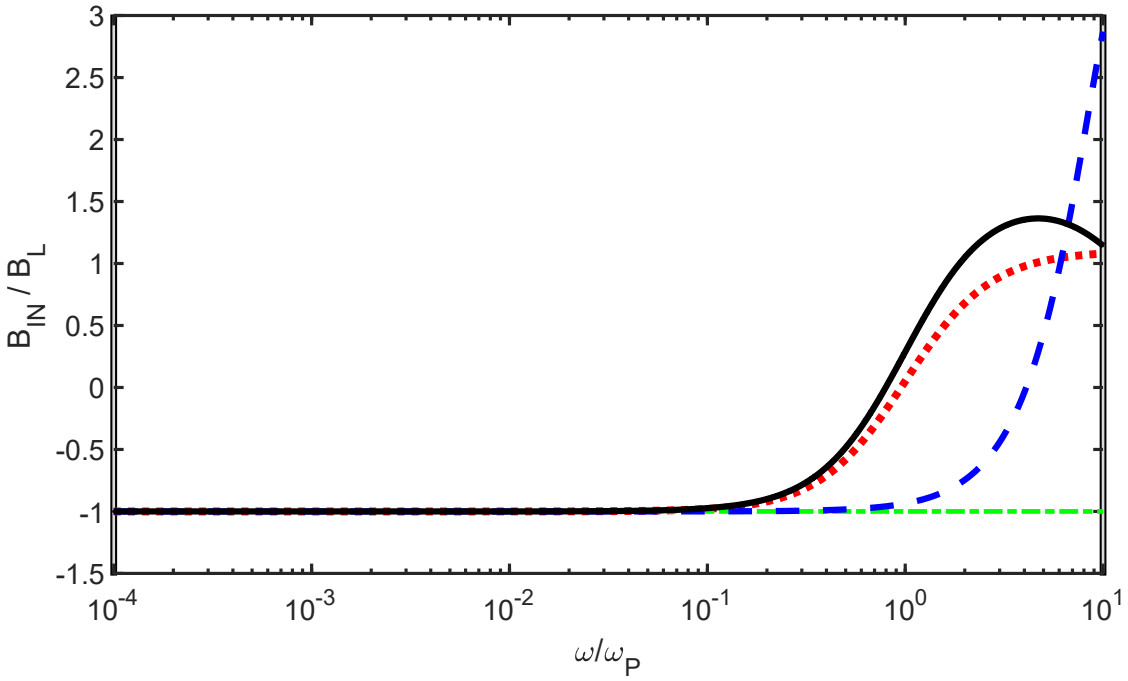

Figure 3.12: Influence of different physical mechanisms on the conversion ratio of the imaginary part of the NIC input admittance. Green dot-dashed: ideal conversion; Blue dashed: influence of phase delay; Red dotted: influence of dispersion; Solid black: combined effect.

conversion ratio than in the ideal case (Fig. 3.11). Imaginary part of the admittance for any load is very close to the one from ideal case, at low frequencies (Fig. 3.12). At higher frequencies, both the influence of the pole, and dimensions, cause the conversion ratios to approach positive values, i.e. the OPAMP can no longer be used for negative conversion. Discrepancy between the real and imaginary parts of the NIC input admittance is caused by high Q factor of the load to be converted [90].

Similar, but not identical effects occur when dealing with floating version of NIC. The same NIC model from Fig. 3.3 can be used for the analysis, but A_0 is not defined the same as in the grounded version. Also, it is very important to stress out that the pole frequency (ω_P) of the floating type of NIC is no longer constant, but rather a function of frequency itself. This statement is related to a fact that pole frequency depends on the OPAMP gain, and is connected with gain through the gain bandwidth product (*GBP*) [46]:

$$\omega_P = \frac{2\pi \cdot GBP}{A_0}. \tag{3.18}$$

In the case of a floating NIC, where A_0 is derived in (3.5), the pole frequency is:

$$\omega_P = \frac{2\pi \cdot GBP}{1 + 2R_2 \cdot Y_L}. \tag{3.19}$$

That means that equations (3.16) and (3.17) should be modified. Let us start the analysis by inserting (3.13) in the expression (3.6) for the half of the input impedance of floating NIC from

Fig. 3.2:

$$Z'_{IN} = \frac{R_1}{1-A_0} = \frac{R_1}{1-\frac{A_0 e^{-j\phi}}{1+s\tau}} = \frac{R_1(1+s\tau)}{1+s\tau-A_0 e^{-j\phi}}. \tag{3.20}$$

Given that the total input impedance is twice the value of Z'_{IN} in the symmetrical case, and using that the input admittance is the inverse of the impedance, one gets:

$$Y_{IN} = \frac{1+s\tau-A_0 e^{-j\phi}}{2R_1(1+s\tau)}. \tag{3.21}$$

The linear voltage gain of the OPAMP in floating configuration was given in (3.5), so combining it with (3.21) one can write for Y_{IN}:

$$Y_{IN} = \frac{1+s\tau-(1+2R_2\cdot Y_L)e^{-j\phi}}{2R_1(1+s\tau)}. \tag{3.22}$$

Equation (3.22) displays the influence of dispersion and dimensions of both amplifiers in the floating type NIC. However, it is not clearly evident how those effects influence the NIC conversion ratio of the real and imaginary parts of the admittance. In order to get a clearer picture, one should introduce following substitutions: $s \to j\omega$, $e^{-j\phi} \to \cos(\phi) - j\sin(\phi)$, $Y_L = G_L + jB_L$. Furthermore, for the unitary conversion, one should set all of the resistors in the feedback loops to the same value ($R_1 = R_2 = R_3 = R_4$). After all the substitutions and simplification, real and imaginary parts of (3.22) become:

$$Real\{Y_{IN}\} = \frac{1-\cos\phi-2R_2(G_L\cos\phi+B_L\sin\phi)+2R_2\frac{\omega}{\omega_P}(G_L\sin\phi-B_L\cos\phi)+\frac{\omega}{\omega_P}\sin\phi+(\frac{\omega}{\omega_P})^2}{2R_1(1+(\frac{\omega}{\omega_P})^2)}, \tag{3.23}$$

$$Imag\{Y_{IN}\} = \frac{\sin\phi+2R_2(G_L\sin\phi-B_L\cos\phi)+2R_2\frac{\omega}{\omega_P}(G_L\cos\phi+B_L\sin\phi)+\frac{\omega}{\omega_P}\cos\phi}{2R_1(1+(\frac{\omega}{\omega_P})^2)}. \tag{3.24}$$

Again, we can notice that real and imaginary parts of the NIC input admittance are not a scaled image of load admittance Y_L, but rather quite complicated functions of the operating frequency ω. Also, we have to bear in mind that pole frequency (ω_P) is a function of the operating frequency, as well. In order to illustrate the effects, several graphs of conversion ratio based on (3.23), (3.24) were plotted. On the first two graphs (Fig. 3.13, 3.14), there is a comparison of NIC conversion ratio for three different loads, a low-Q load (series RC circuit with R=2Ω, C=100pF, dashed blue curve), a high-Q load (series RC circuit with R=2Ω, C=4 pF, dotted red curve), and equivalent circuit of a 1.5m long dipole antenna (solid cyan curve). The results are also compared to those associated with an ideal conversion ratio ($\frac{Y_{IN}}{Y_L} = -1$), which

is shown with a dot dashed green line. Conversion ratios of the real part of the admittance are shown in Fig. 3.13, while conversion ratios of the imaginary part of the admittance are shown in Fig. 3.14.

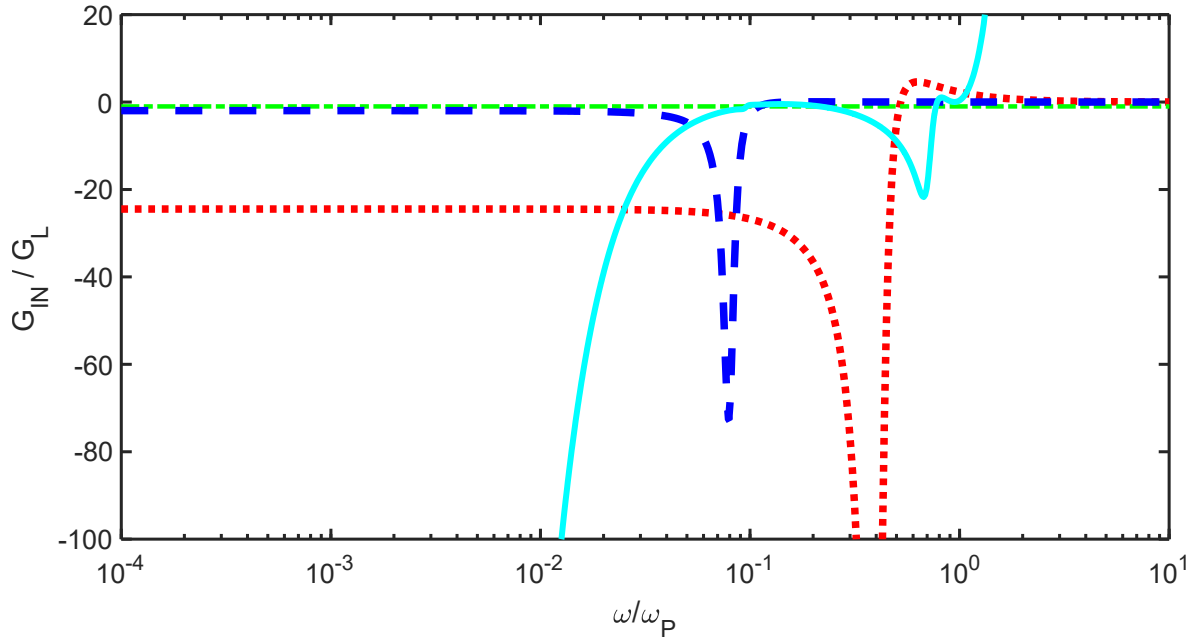

Figure 3.13: Conversion ratio of the real part of the NIC input admittance for three different loads for the floating version of NIC. Green dot-dashed: ideal conversion; Blue dashed: low-Q load; Red dotted: high-Q load; Cyan solid: 5-element dipole antenna model [100].

Results for conversion ratio of the real part of the admittance are similar to those for the grounded version of NIC (Fig. 3.9). In Figs. 3.13, 3.14 frequency ω is normalized to the pole frequency of grounded type NIC for easier comparison. Again, in the cases of a high-Q and a low-Q load there is an offset present at low frequencies. In the case of a high-Q load the offset is much more pronounced. The biggest difference in conversion of high-Q and low-Q loads, comparing to grounded NIC, is an indentation in the frequency characteristic of the input conductance (relatively narrow drop, Fig. 3.13). After the drop, amplifier no longer provides a negative conversion. From the frequency shift at which the drop occurs, it is clear that the pole frequency for high-Q load is higher than the pole frequency in the case of a low-Q load. When converting an equivalent circuit of a dipole antenna, the results are again very similar to those with the grounded version of NIC. Slight difference occurs at frequencies close to the antenna resonance ($\omega \approx \frac{\omega_P}{10}$), due to the change of sign of the complex load (from capacitive to inductive).

The most important observation from the graphs in Fig. 3.13 deals with the fact that the pole frequency (ω_P) is no longer a constant. It depends on the amplifier gain, and as such on the load immittance. For example, it can be seen that the conversion of a low-Q load starts deteriorating at the frequency which is approximately 5 times lower than the one for a high-Q load. Such behaviour gives the advantage of the use of grounded NIC for low-Q loads, and the

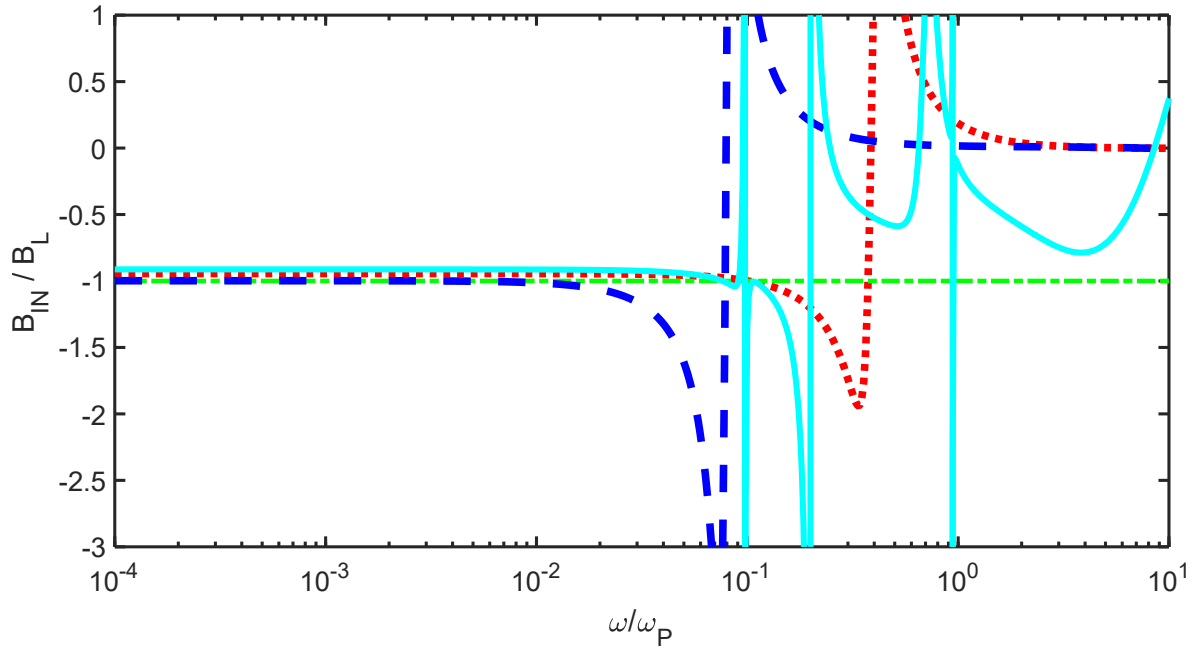

Figure 3.14: Conversion ratio of the imaginary part of the NIC input admittance for three different loads for the floating version of NIC. Green dot-dashed: ideal conversion; Blue dashed: low-Q load; Red dotted: high-Q load; Cyan solid: 5-element dipole antenna model.

use of floating NIC for high-Q loads.

Conversion ratio of the imaginary part of the admittance is much closer to the one from ideal case. The offset at low frequencies is still present. Conversion error is not so pronounced in the imaginary part as it is in the real part of the admittance, but it can still represent a drawback in some applications. Again, as in the real part of the admittance, conversion of the imaginary part of the admittance starts deteriorating at lower frequencies for the low-Q load than for the high-Q load.

The following two graphs (Figs. 3.15, 3.16) show direct comparison of admittance conversion ratios between the grounded and floating type of NIC. The comparison is made for two different loads, a high-Q load, and equivalent circuit of a dipole antenna. The purpose of the comparison is to highlight the advantages and disadvantages of both NIC realizations.

On the graphs, conversion of the high-Q load for grounded NIC is represented with dashed red curve, high-Q load for floating NIC with dot dashed green curve, dipole antenna for grounded NIC with dashed blue curve, and dipole antenna for floating NIC with solid cyan curve. Frequency ω is normalized to the pole frequency of the grounded type NIC. Firstly, one can notice that at low frequencies, real part of the admittance is converted more accurately with floating type NIC, for both loads (Fig. 3.15). For instance, conversion ratio of a high-Q load for floating NIC is around -25, while for the grounded NIC the ratio is -50. In another words, floating version brings an improvement of exactly two times. Such better accuracy can be of significant importance regarding construction of a self-oscillating antenna with electrically small radiators. High frequency behaviour ($\omega > \frac{\omega_p}{10}$) is somewhat different in the case of a high-Q load than it is

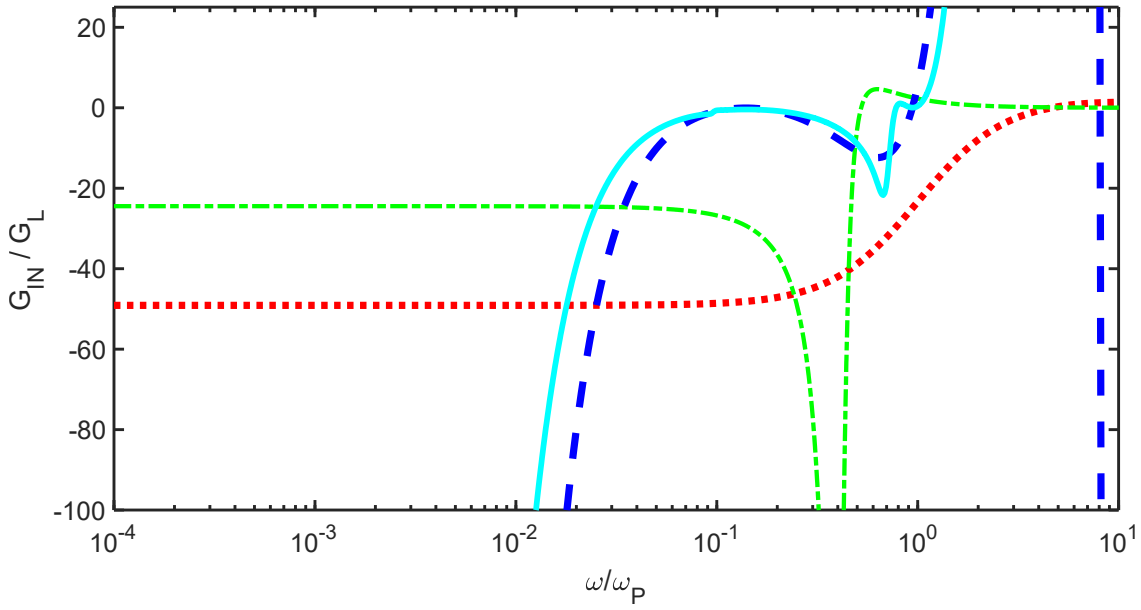

Figure 3.15: Comparison of the conversion ratios of the real part of the NIC input admittance between the grounded and floating type NIC, for two different loads. Red dotted: high-Q load with grounded NIC; Green dot-dashed: high-Q load with floating NIC; Blue dashed: 5-element dipole antenna model with grounded NIC; Solid cyan: 5-element dipole antenna model with floating NIC.

in the case of a dipole antenna. In the case of a generic high-Q load, there is a notch in the curve of input conductance ratio, in the region $\frac{\omega_p}{10} < \omega < \omega_P$, for floating NIC. On the other hand, transition of conversion ratio toward the positive values is smooth for the grounded NIC. In the case of a dipole antenna, both NICs give positive values of conversion ratio for frequencies above ω_P, and thereby disable possible NIC operation in that region. In the case of a floating NIC, a notch in the curve of input conductance ratio occurs slightly before the frequency $\omega = \omega_P$.

Regarding the conversion ratio of the imaginary part of the admittance (Fig. 3.16), grounded version of NIC offers slightly better results at low frequencies. For example, in the case of a dipole antenna, conversion ratio obtained with grounded NIC is very close to -1, while floating NIC gives conversion ratio of approximately -0.9, which is equivalent to an error of 10%. At frequencies above $\frac{\omega_P}{10}$ both versions of NIC start approaching positive values of conversion ratio.

Few conclusions can be drawn from the given results. Even though the floating type of NIC contains two OPAMPs, both of which are dispersive and of finite length, the quality of conversion is very similar to the quality of conversion achieved with grounded type of NIC. Considering the real part of the admittance, conversion at low frequencies is even more accurate when using floating type NIC.

However, the imaginary part of the admittance is converted slightly better with grounded NIC, both in the case of a dipole antenna and in the case of a generic high-Q load. For frequencies above $\frac{\omega_P}{10}$, the conversion ratio starts approaching positive values in both NIC realizations, for any given load. Thereby, NIC conversion error of the imaginary part of the admittance is rapidly increasing above $\frac{\omega_P}{10}$. Which of the NIC realizations should be used, depends on the

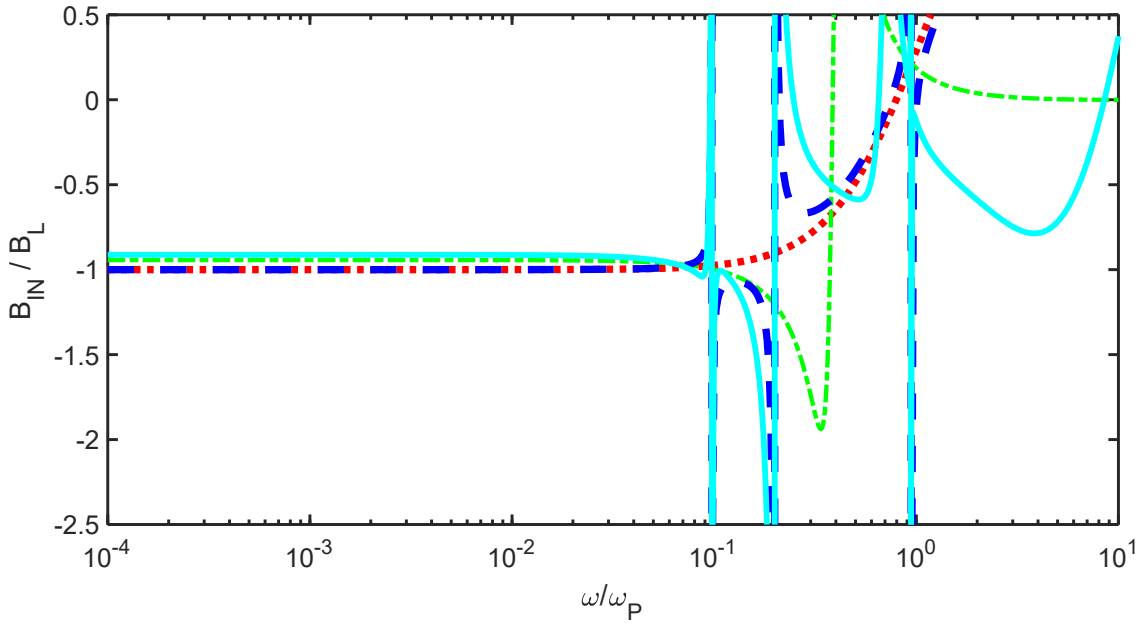

Figure 3.16: Comparison of the conversion ratios of the imaginary part of the NIC input admittance between the grounded and floating type NIC, for two different loads. Red dotted: high-Q load with grounded NIC; Green dot-dashed: high-Q load with floating NIC; Blue dashed: 5-element dipole antenna model with grounded NIC; Solid cyan: 5-element dipole antenna model with floating NIC.

actual application. Both of them have their advantages and drawbacks. However, one should bear in mind that due to dispersion and finite signal propagation time, NIC conversion error always exists. Furthermore, it highly depends on the quality factor of the load to be converted.

3.3 Non-linear model of negative impedance converter

Next phenomenon which is present in realistic NIC circuits is non-linearity. Oscillators are inevitably non-linear devices [95], comprising electronic elements, so the influence of saturation will be of great importance for our application. So far in the analysis, amplifiers used in NIC realizations have been considered perfectly linear and DC gain A_0 was a constant. In practical situation, both a voltage gain (A_V) and a current gain (A_I) decrease when the input signal drives circuit into a non-linear regime (this is manifested as gain compression [105]), Fig. 3.17.

Neglecting gain dependence on the frequency for a moment, one can take a simple inspection of (1.10) in the region of compression. It reveals a decrease of either input admittance (Y_{IN}) in the case of VNIC or decrease of the input impedance (Z_{IN}) in the case of INIC. Formally, the input immittance can be described by generalized non-linear curves of negative elements introduced in [24] (Fig. 3.18). Briefly, these curves are extension of the familiar concept of 'N' and 'S' curves for differential conductance and resistance from microwave engineering [2]. Generalized curves describe effective differential capacitance ($C(v) = \frac{\partial Q_e}{\partial v}$) and effective differential inductance ($L(i) = \frac{\partial Q_m}{\partial i}$). In those definitions, v and i stand for voltage and current,

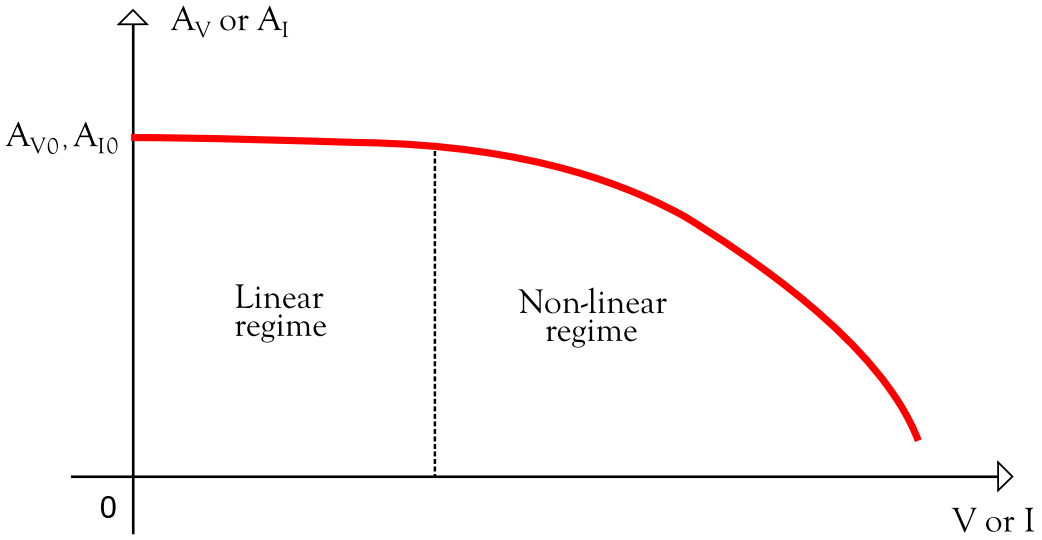

Figure 3.17: Illustration of the effect of non-linearity on the amplifier gain (compression).

while Q_e and Q_m are equivalent electric and magnetic charges, respectively. It can be shown that non-linear properties of VNIC and INIC (Fig. 1.7) are described by 'N' and 'S' curves (Fig. 3.18) [24].

In order to predict a decrease of VNIC input admittance caused by the gain compression, a mathematical model of non-linear transfer function of a NIC was derived [99]. Block schematic of non-linear NIC is shown in Fig. 3.19.

It should be stressed that this non-linear model is independent on the actual realization of VNIC. Only parameters of the model are dependent on the implementation. Similar analysis could be made for INIC. The most general non-linear behaviour of VNIC can be described with the help of electronic engineering. Very convenient choice (that can easily be applied for most

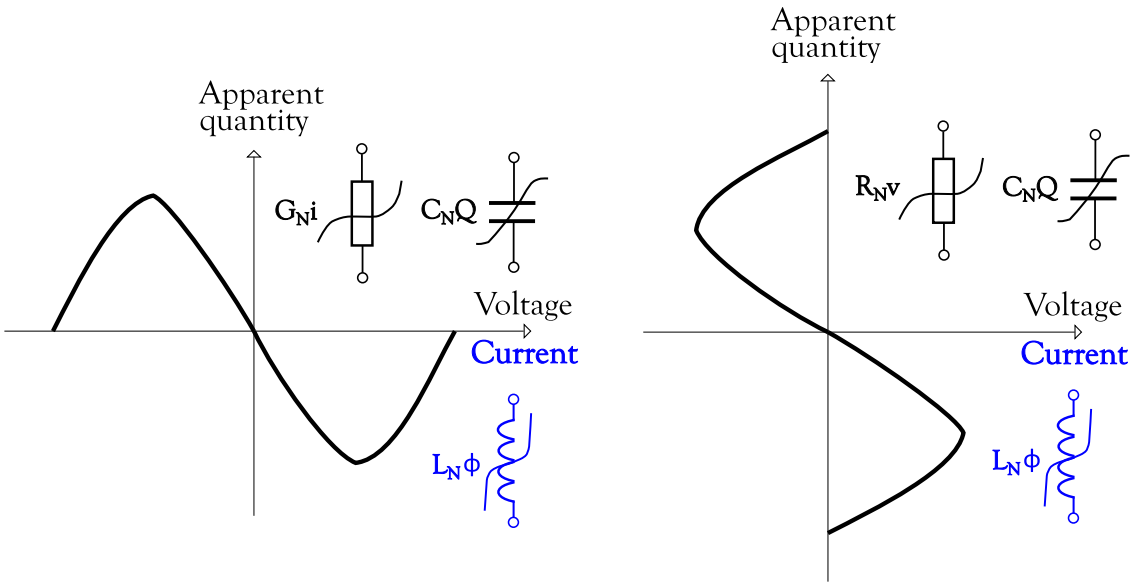

Figure 3.18: Generalized 'N' (left graph) and 'S' (right graph) curves for NIC loaded with resistance, capacitance, inductance or conductance [93].

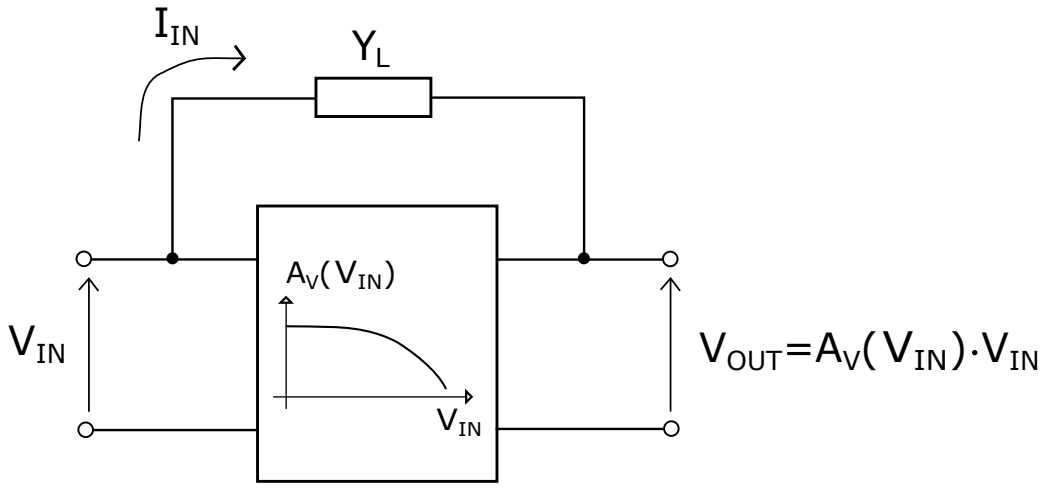

Figure 3.19: Block schematic of a non-linear model of negative impedance converter.

standard NIC designs) is a voltage transfer function of a differential amplifier [105]:

$$v_{OUT} = \frac{2V_{SAT}}{1+\exp(-\frac{v_{IN}}{V_T})} - V_{SAT}, \tag{3.25}$$

where V_{SAT} stands for the output saturation voltage, while V_T represents the voltage equivalent of temperature (25mV). The expression was simplified in such a manner that the output voltage has no DC offset, which is the case with symmetrically biased operational amplifiers [46]. Simplifying (3.25) one gets:

$$v_{OUT} = V_{SAT} \cdot \frac{1-\exp(-\frac{v_{IN}}{V_T})}{1+\exp(-\frac{v_{IN}}{V_T})} = V_{SAT} \cdot \tanh(\frac{v_{IN}}{2V_T}). \tag{3.26}$$

Furthermore, in order to ensure a constant value of gain in the linear operating region, one should incorporate a negative feedback loop in addition to a positive one. This negative feedback loop is here defined by a feedback factor A_{V0} (linear gain). Now, the transfer function becomes:

$$v_{OUT} = V_{SAT} \cdot \tanh\left[\frac{1}{2V_T}(v_{IN} - \frac{1}{A_{V0}} \cdot v_{OUT})\right]. \tag{3.27}$$

This is a transcendental function and it cannot be expressed explicitly. However, (3.27) can be plotted using dedicated computer software such as $Mathematica^{TM}$, and then one could use some of the available basic fitting options. In this particular case we used a simple polynomial fitting. Coefficients of the polynomial can be extracted, and voltage transfer function can now be explicitly expressed as [99]:

$$v_{OUT} = a_n \cdot {v_{IN}}^n + a_{n-1} \cdot {v_{IN}}^{n-1} + ... + a_1 \cdot v_{IN} + a_0 = \sum_{n=0}^{\infty} a_n \cdot {v_{IN}}^n. \tag{3.28}$$

Furthermore, voltage transfer characteristic has an odd parity so all the even coefficients (a_{2n})

are relatively small and can be neglected. Function of output voltage comes down to following Maclaurin series:

$$v_{OUT} = \sum_{n=0}^{\infty} a_{2n+1} \cdot {v_{IN}}^{2n+1}. \tag{3.29}$$

Analogue to that, one can also express voltage gain function of a NIC based on operational amplifiers as:

$$A(V_{IN}) = \frac{v_{OUT}}{v_{IN}} = \sum_{n=0}^{\infty} a_{2n+1} {v_{IN}}^{2n}. \tag{3.30}$$

Coefficients of the polynomial (a_{2n+1}) can be obtained numerically for the specific amplifier used in the practical realization. In Fig. 3.20, three different voltage transfer characteristics are compared. Transfer characteristic of an ideal linear amplifier is shown with dotted black line, the exact non-linear transfer characteristic based on expression (3.27) is shown with solid blue curve, while polynomial fitting up to 7^{th} degree of the function from (3.27) is represented with dashed red curve [99].

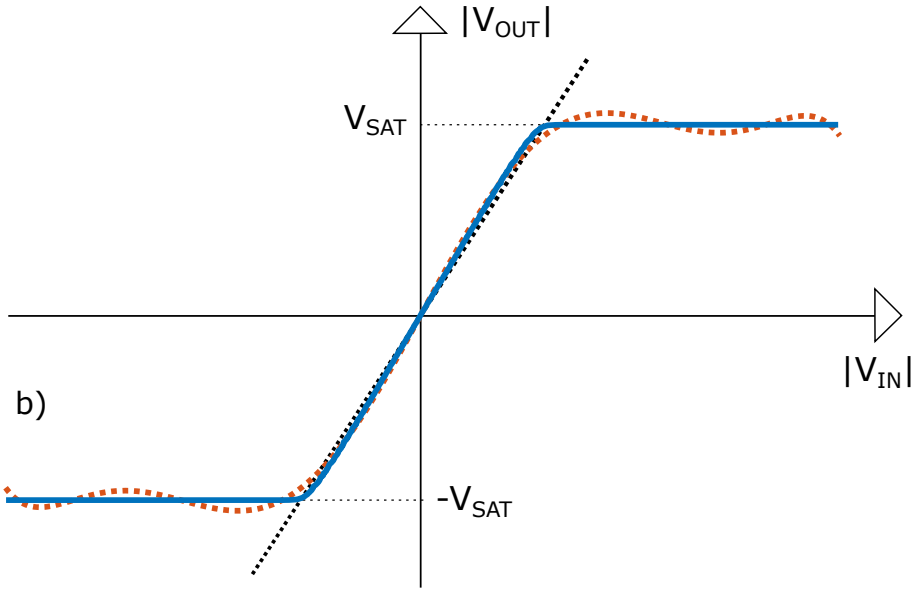

Figure 3.20: Comparison of voltage transfer characteristics of an amplifier. Black dotted: ideal linear amplifier; Blue solid: OPAMP; Red dashed: 7^{th} degree polynomial fit of an OPAMP characteristic.

Even though one could take arbitrary number of terms in the Maclaurin series, it is evident from Fig. 3.20 that 7^{th} order polynomial is already a good approximation of the transfer characteristic. In the next step, we assumed a single-tone (harmonic) excitation at the frequency ω_0, the amplitude of which (V_{IN}) was set into a non-linear part of transfer function from Fig. 3.20:

$$v_{IN} = V_{IN} \cos(\omega_0 \cdot t). \tag{3.31}$$

By inserting (3.31) into (3.29) one gets for the output voltage:

$$v_{OUT} = \sum_{n=0}^{\infty} a_{2n+1} \cdot {V_{IN}}^{2n+1} \cos(\omega_0 \cdot t)^{2n+1}. \tag{3.32}$$

If we limit the series to a 7^{th} degree polynomial (which is more than enough for most calculations), and by using trigonometric identities, output voltage can be easily written as:

$$\begin{aligned} v_{OUT} = &\cos(\omega_0 \cdot t) \left[\frac{35}{64} a_7 {V_{IN}}^7 + \frac{5}{8} a_5 {V_{IN}}^5 + \frac{3}{4} a_3 {V_{IN}}^3 + a_1 V_{IN} \right] \\ &+ \cos(3\omega_0 \cdot t) \left[\frac{21}{64} a_7 {V_{IN}}^7 + \frac{5}{16} a_5 {V_{IN}}^5 + \frac{1}{4} a_3 {V_{IN}}^3 \right] \\ &+ \cos(5\omega_0 \cdot t) \left[\frac{7}{64} a_7 {V_{IN}}^7 + \frac{1}{16} a_5 {V_{IN}}^5 \right] \\ &+ \cos(7\omega_0 \cdot t) \left[\frac{1}{64} a_7 {V_{IN}}^7 \right]. \end{aligned} \tag{3.33}$$

It can be seen that higher harmonics will be generated at the output as a direct consequence of non-linearity. Each harmonic has different amplitude, which is dependent only on the coefficients of the transfer function and amplitude of the input signal. However, in the first approximation, one can limit the observation only to a fundamental frequency. In such case, using (3.30), voltage gain at the fundamental frequency can be derived as:

$$A_{\omega_0}(V_{IN}) = \frac{35}{64} a_7 {V_{IN}}^6 + \frac{5}{8} a_5 {V_{IN}}^4 + \frac{3}{4} a_3 {V_{IN}}^2 + a_1. \tag{3.34}$$

Aforementioned analysis simplifies the problem of non-linearity of negative impedance converters to a simple expression for non-linear gain at the fundamental frequency [99]. Also, from the equation (3.33) for output voltage, one can estimate magnitudes of generated higher harmonics.

Now, let us use a developed model to predict the influence of non-linearity of VNIC on the conversion error. We consider the situation where positive feedback loop of the NIC is composed of the arbitrary complex admittance ($Y_L = G_L + jB_L$). Using (1.10) and (3.34), for gain at the fundamental frequency, one can write the following equation for the NIC's input admittance:

$$Y_{IN,\omega_0}(V_{IN}) = Y_L(1 - A_{\omega_0}) = (G_L + jB_L)(1 - \frac{35}{64} a_7 {V_{IN}}^6 - \frac{5}{8} a_5 {V_{IN}}^4 - \frac{3}{4} a_3 {V_{IN}}^2 - a_1). \tag{3.35}$$

It should be stressed that above equation is valid only for observation at the fundamental frequency. Such quantity is called a harmonic admittance [95]. It can be seen that real and imaginary parts of the input admittance are now independent of each other, as they are only a

function of the input voltage magnitude (V_{IN}). We calculated a conversion ratio of the real and imaginary parts of the input admittance for the arbitrary load using (3.35), and the results as shown in Fig. 3.21. The coefficients of the polynomial fit from (3.29) were calculated for the specific operational amplifier THS4304, by Texas Instruments [108].

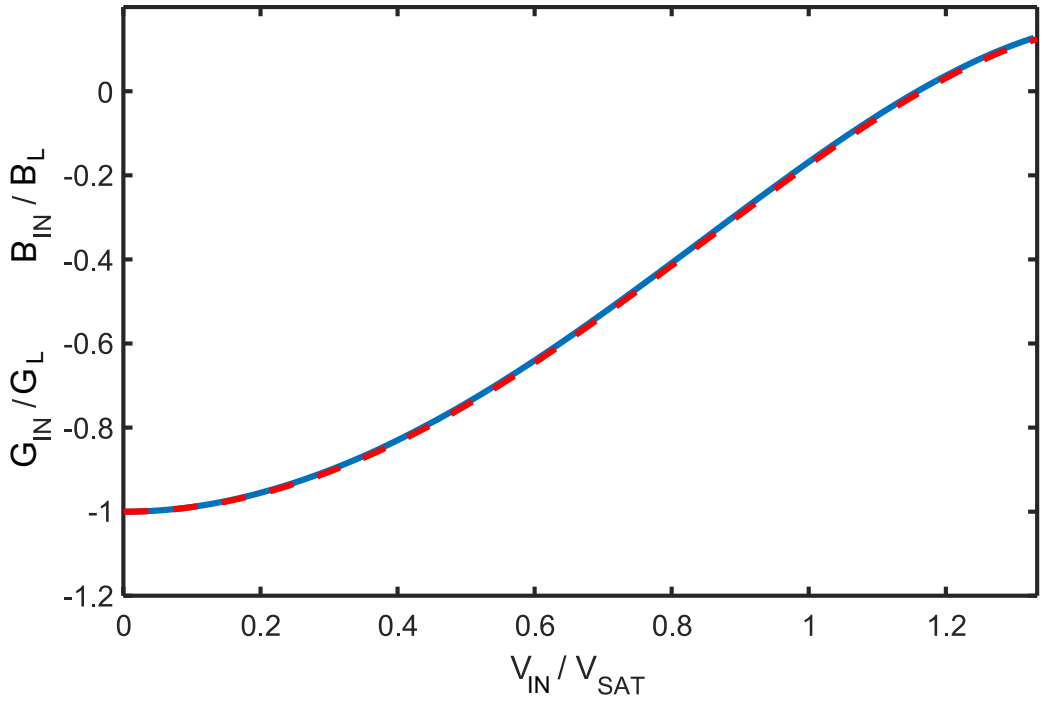

Figure 3.21: Conversion ratio of NIC input admittance with respect to the input voltage amplitude, for an arbitrary network in the positive feedback loop. Blue solid: input conductance ratio; Red dashed: input susceptance ratio.

From Fig. 3.21 it is visible that both the input conductance and susceptance have the same behaviour [99]. When the signal amplitude is infinitesimally small (linear regime), NIC does an ideal conversion ($Y_{IN} = -Y_L$). As the signal amplitude grows, modulus of the input conductance and susceptance starts to decrease. If the amplitude of the input voltage (V_{IN}) reaches the value of saturation voltage (V_{SAT}), input admittance conversion ratio, and also the input admittance itself, becomes zero ($Y_{IN} = 0$). For the signals, amplitude of which is larger than V_{SAT}, gain A_{ω_0} becomes lower than 1. In such case, the input admittance is positive, and negative conversion phenomenon is ceased. Of course, this is not a desirable behavior, as it would among other things disable operation of a self oscillating antenna (negative immittance oscillator). Going back to the equation (3.35) and Fig. 3.21, one finds that the conversion error introduced by non-linear operation of NIC affects equally the real and imaginary part of the input admittance. Thus, this type of the conversion error is independent on the quality factor of the load to be converted.

3.4 Dynamic behaviour of self-oscillating antenna based on negative immittance conversion

In practice, negative elements based on NICs will always be dependent both on the frequency and amplitude of the input signal. In previous sections, the influence of dispersion, finite amplifier length and non-linearity was investigated separately. Here, we combine all of these effects (non-idealities) in order to explain the oscillating process of a realistic self-oscillating antenna based on negative immittance conversion (negative immittance oscillator) [101]. Using equation (3.13) and considering that gain is also dependent on the voltage magnitude, one can write:

$$A(V_{IN}, s, \phi) = \frac{A(V_{IN})e^{-j\phi}}{1+s\tau}. \tag{3.36}$$

Here, we considered a grounded version of NIC. Similar analysis can be made with the floating version. However, the effect on the input admittance in both versions is very similar and conclusion one draws are valid in both cases. The load in the positive feedback loop of NIC is now an actual antenna ($Y_L = Y_{ANT}$), so combining (1.10) and (3.36) one can write for the input admittance of NIC [101]:

$$Y_{IN} = Y_{ACT} = Y_{ANT}\frac{1+s\tau - A(V_{IN})e^{-j\phi}}{1+s\tau}. \tag{3.37}$$

It can be seen from (3.37) that in the realistic case Y_{IN} becomes a function of three variables (V_{IN}, s and ϕ). Thus, it is quite complicated to calculate it analytically. We can simplify the problem by neglecting the real component of the complex variable s (s->$j\omega$), and using the relation (3.10) as in the Chapter 3.2. Thus, Y_{IN} becomes a function of only two variables (V_{IN}, ω). Analysis in Chapter 3.2, describing the influence of amplifier dispersion on the input admittance, revealed that the NIC conversion error depends on the Q factor of the load to be converted. In the case of a high Q load, error will be more noticeable in the real part of the input admittance and it results in pronounced negative values of the input conductance. Unfortunately, electrically small antennas fundamentally have high Q factor, and therefore they introduce larger conversion error. On the other hand, in the Chapter 3.3 we concluded that non-linearity has the same effect on both real and imaginary parts of the input admittance, regardless of the load's Q factor. Having that in mind, we construct admittance loci of active and passive components of a realistic self-oscillating antenna (Fig. 3.22) and analyse the process of reaching a stable operating point [101].

Admittance locus of an ideal 'negative antenna' is shown with dashed green line ($Y_{ACT,ID}$). For high Q loads dispersion causes relatively large conversion error in the real part of the input admittance. Hence, it causes the admittance locus of the active element to shift to the left. In addition, we obtain a solid red curve located in the third quadrant of the coordinate system in

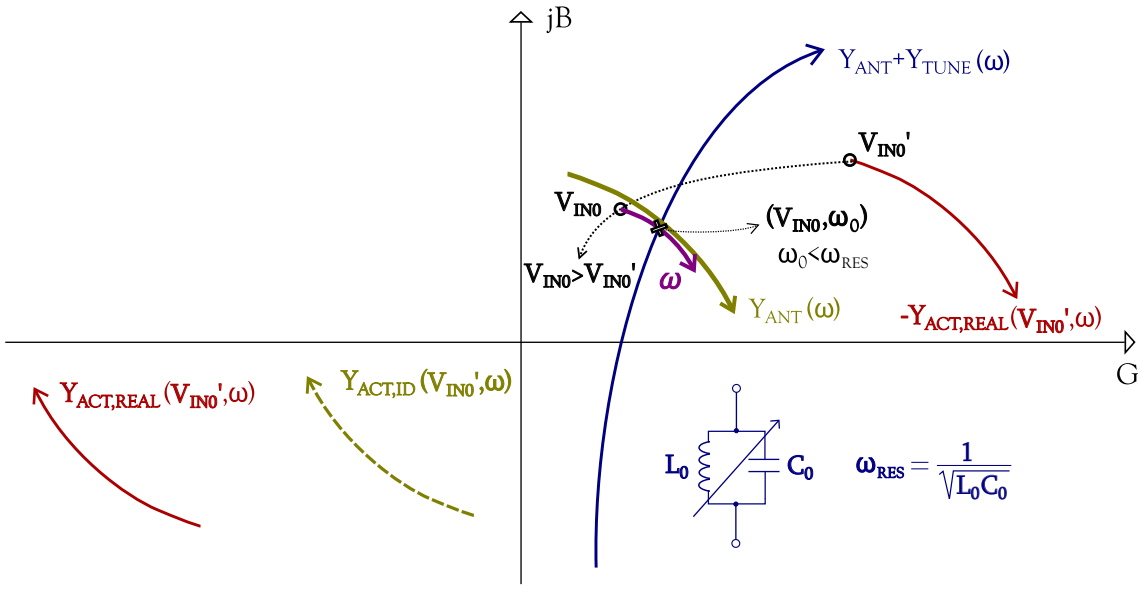

Figure 3.22: Admittance loci of active and passive elements of a realistic self-oscillating antenna based on negative immittance conversion. Green dashed: ideal active element; Solid green: antenna; Solid red: realistic active element; Solid blue: antenna with tuning network; Solid purple: active element in non-linear regime.

Fig. 3.22 ($Y_{ACT,REAL}$). In oscillator analysis it is common to multiply the admittance locus of the active element by -1 in order to find the intersection with the curve of the passive element (drawn with a solid blue line (Y_{ANT}+Y_{TUNE})). However, in our case there is no intersection due to the very large conversion error caused by dispersion. Because of that, amplitude of the oscillating signal has to rise and amplifier needs to enter a non-linear regime which causes its negated admittance locus to 'shrink' and move left towards the admittance locus of the passive element ($-Y_{ACT,REAL}$) [93].

When the admittance locus has moved enough to create an intersection between the two curves at the certain operating frequency (ω_0), amplitude of the signal will stop increasing. Thus, the oscillator will stabilize itself at the operating point (V_{IN0}, ω_0). It can be seen that a growth of the amplitude results in a somewhat lower operating frequency comparing to the resonant frequency of the tank circuit (ω_0<ω_{RES}). Due to the conversion error caused by the non-idealities of NIC, negated admittance of the active element is different than the admittance of the antenna, so the admittance of tank circuit has to cover this difference [93]. Clearly, it is possible only if the oscillating frequency is different than the resonant frequency of the tank circuit. Stable state of oscillations is ensured by satisfying the condition in equation (2.5), which can be achieved by using a high-Q resonant circuit.

The analysis of a realistic self-oscillating antenna based on negative immittance conversion can also be performed numerically (for this purpose we used $MATLAB^{TM}$). The main goal is to construct a graphical tool that will enable the prediction of the amplitude and the fundamental

frequency of the oscillating signal [101].

The first step is to rewrite the simplified gain function from (3.36) and calculate the coefficients from (3.30) for the specific amplifier. By doing that we obtain the expression for Y_{ACT}, which is now a function of two variables (V_{IN}, ω) and can be plotted as a surface in a three-dimensional space (Fig. 3.23) defined by conductance (G), susceptance (B) and the angular frequency (ω). The next step is to plot the admittance locus of the passive element (Y_{ANT}+Y_{TUNE}), which is now a parametric curve in 3D space, dependent only on the frequency ω. The intersection between the curve of the passive element and the surface (describing the behaviour of the negated active element) directly represents the operating point of the oscillator (V_{IN0}, ω_0).

Knowing the operating frequency (ω_0) we can isolate a single curve on the surface, which is dependent only on the amplitude of the oscillating signal (red solid line), and track down the growth of oscillations. The analysis described in Fig. 3.23 was based on a self-oscillating antenna comprising two electrically small dipoles ($Q \approx 100$) [93]. NIC was realized as a single pole (ω_P=2πGHz) non-linear model, mimicking commercially available THS4304 operational amplifier [108]. Furthermore, the results were compared with ADS^{TM} transient simulations based on the full SPICE model of the used OPAMP [109], and a good agreement was found.

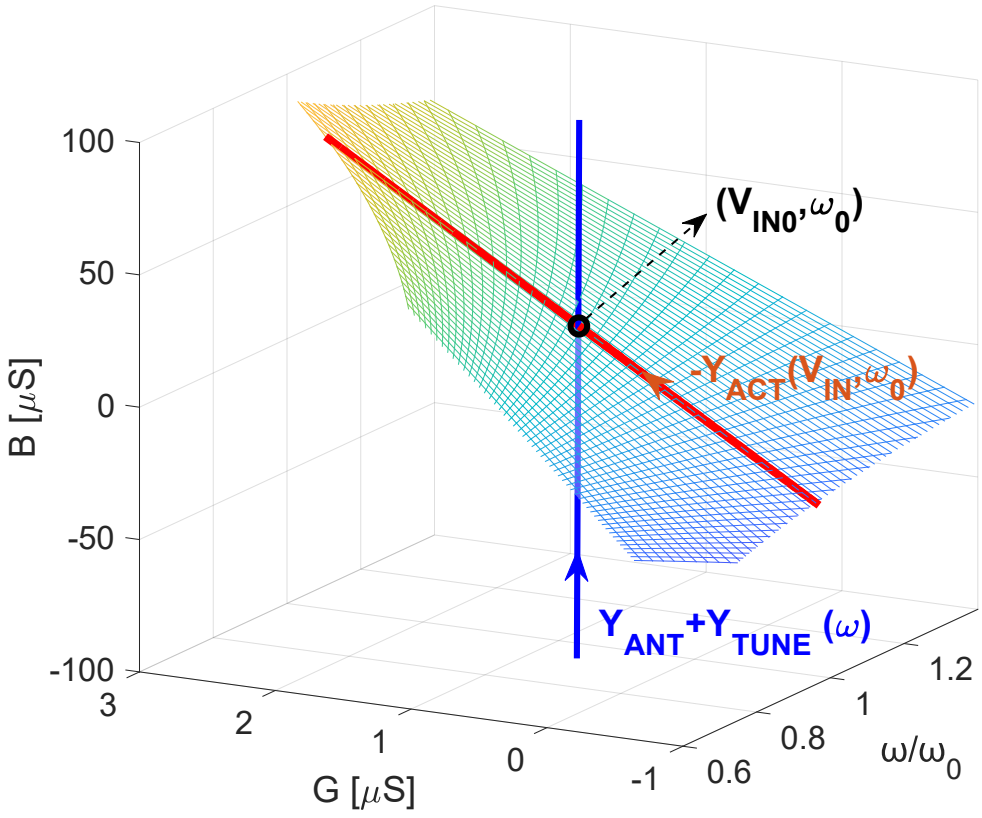

Figure 3.23: Intersection of admittance loci of active and passive elements of a self-oscillating antenna based on negative immittance conversion in 3D space. Surface: active element; Red solid: active element at the operating frequency; Blue solid: antenna with tuning network [101].

Chapter 4

Experimental demonstration of self-oscillating antenna with dipole-like radiation pattern

In order to test the feasibility of the basic idea of a self-oscillating antenna based on negative immittance conversion, several devices were designed and tested. Devices were tested numerically, which was followed by measurements on constructed prototypes. All of the circuits where designed for the low radio frequency range (up to 50 MHz). In this frequency band, the problem of parasitic capacitances and inductances is not so pronounced and it is possible to use tunable prototypes based on low-cost commercial electronic components. Among them, high-speed operational amplifiers have been found as particularly convenient for construction of different NIC based RF structures and devices (active metamaterials [49], negative elements for antenna matching [20], absorbers based on negative elements [84]). Downsides of high-speed OPAMPs are their poor noise properties, and relatively small output voltage swing (limited by the relatively low-voltage DC supply) [46]. However, these drawbacks are not important for the construction of a proof-of-concept RF demonstrator.

All of the designed devices are based on high-speed operational amplifier THS4304 [108], configured as voltage converting NIC (VNIC) [44]. Segment of the THS4304 technical datasheet [108], revealing some of the most important OPAMP characteristics, is shown in Fig. 4.1. For instance, nominal bandwidth of the OPAMP is 3 GHz, while slew rate is as high as 830 V/μs. Those two characteristics indicate fairly broadband amplifier operation, without any specific restrictions for applications in the lower RF range (up to few hundreds MHz).

We have tested two types of design that follow the basic principle from Fig. 2.1. The first design is based on a grounded type NIC with an operational amplifier, and its circuit diagram is shown in Fig. 4.2 [93]. The tuning circuit (parallel capacitance C_0 and inductance L_0) was used for tuning of the oscillating frequency (ω_0). In the grounded version of oscillator (Fig.

TEXAS INSTRUMENTS
www.ti.com

THS4304

SLOS436A–MARCH 2004–REVISED JULY 2004

Wideband Operational Amplifier

FEATURES

- Wide Bandwidth: 3 GHz
- High Slew Rate: 830 V/μs
- Low Voltage Noise: 2.4 nV/√Hz
- Single Supply: 5 V, 3 V
- Quiescent Current: 18 mA

APPLICATIONS

- Active Filter
- ADC Driver
- Ultrasound
- Gamma Camera
- RF/Telecom

Figure 4.1: Segment of the THS4304 datasheet, taken from [108].

4.2), resistors R_1 and R_2 were set to the same value in order to achieve voltage gain (A_V) of 2 ($A_V = 2$), which, in an ideal case, leads to unitary conversion ($Y_{IN} = -Y_{ANT}$). Here, Y_{ANT} stands for the equivalent admittance of the antenna. Both of the antennas are identical, so in the case of ideal NIC conversion, their admittances cancel out at any operating frequency.

Due to DC power supply voltage of ±2.5V, maximal (undistorted) effective output voltage is limited to approximately 1.5V. In turn, it limits the maximal voltage at the antenna terminals to 0.75 V (with $A_V = 2$).

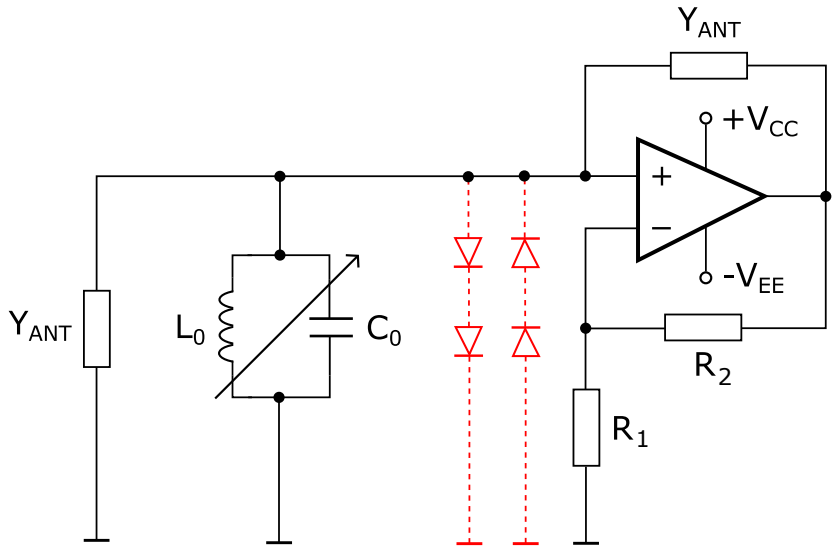

Figure 4.2: Circuit diagram of a self-oscillating antenna based on grounded type NIC with two identical antennas. Optional diode limiter is sketched with dashed red lines [93].

Drawbacks of the grounded version of self oscillating antenna from Fig. 4.2 are a common terminal (non-inverting OPAMP input) for connection of the antennas, and a constant value of gain (which reduces available voltage swing at the antennas). A common terminal can lead to higher mutual impedance between the antennas, which can in turn increase NIC conversion error. In addition, one of the antennas is grounded, while the other one is connected between

the input and output of OPAMP. That means that antennas are connected asymmetrically, and require additional device to transform a balanced feed to an unbalanced one (balun [110]). Improper antenna feed can be the cause of unwanted interference, and therefore, signal distortion and noise. On the other hand, due to the constant value of gain in grounded type of NIC, oscillator is in some cases unable to reach a stable operating point without highly non-linear behaviour. In another words, amplifier gain is compressed to a value below unity, which results in deterioration of matching properties. The purpose of diode-based limiter network (dashed red part in Fig. 4.2) is to limit the magnitude of self-oscillating signal at the NIC input and disable high gain compression. Even though limiter ensures proper NIC operation, it also reduces available voltage swing at the antennas, and therefore, decreases available active power.

The second design uses two OPAMPs (again THS4304) in the form of a differential floating NIC (Fig. 4.3). Such configuration enables up to two times higher level of signal at the antennas' terminals, and in turn, higher radiated power [93]. Additional (perhaps even more important) feature of this design is that it avoids the need of a common connection point between the two antennas. This assures symmetrical (balanced) excitation of the antennas and minimizes eventual unwanted effects of mutual impedance on the operation of a self-oscillating antenna, as explained earlier. Again, the NIC is loaded with two identical antennas (represented by their self-admittance Y_{ANT}) and a parallel tuning circuit (L_0C_0). As in the grounded version of self-oscillating antenna, diode-limiter can be used at NIC input, in order to limit the magnitude of self-oscillating signal, but at the cost of reduced voltage swing at the antennas.

4.1 Numerical SPICE-based analysis of NIC with complex load

Before investigating the whole self-oscillating system, we performed SPICE-based simulations in commercial circuit simulator ADS^{TM}. NIC with a complex load in the positive feedback loop was investigated alone, without the antennas and tank circuit. The goal was to compare the obtained numerical results to those from theoretically derived model in Chapter 3, and predict the behaviour of a self-oscillating antenna. All of the simulations in this section investigated both grounded and floating versions of NIC.

Firstly, it was analysed how the properties of NIC depend on the operating frequency, and this part was done using S-parameters simulations in ADS^{TM}. Simulations, results of which are presented below, were made for high-Q load, low-Q load, as well as for dipole antenna equivalent network. The same as in Chapter 3, a high-Q load was implemented as a series RC circuit with R=2Ω and C=4pF, and a low-Q load as a series RC circuit with R=2Ω and C=100pF. A 1.5m long dipole was modelled as a 5-element equivalent network with lumped elements, which uses extended Chu's model [100]. The values of used elements were numerically obtained us-

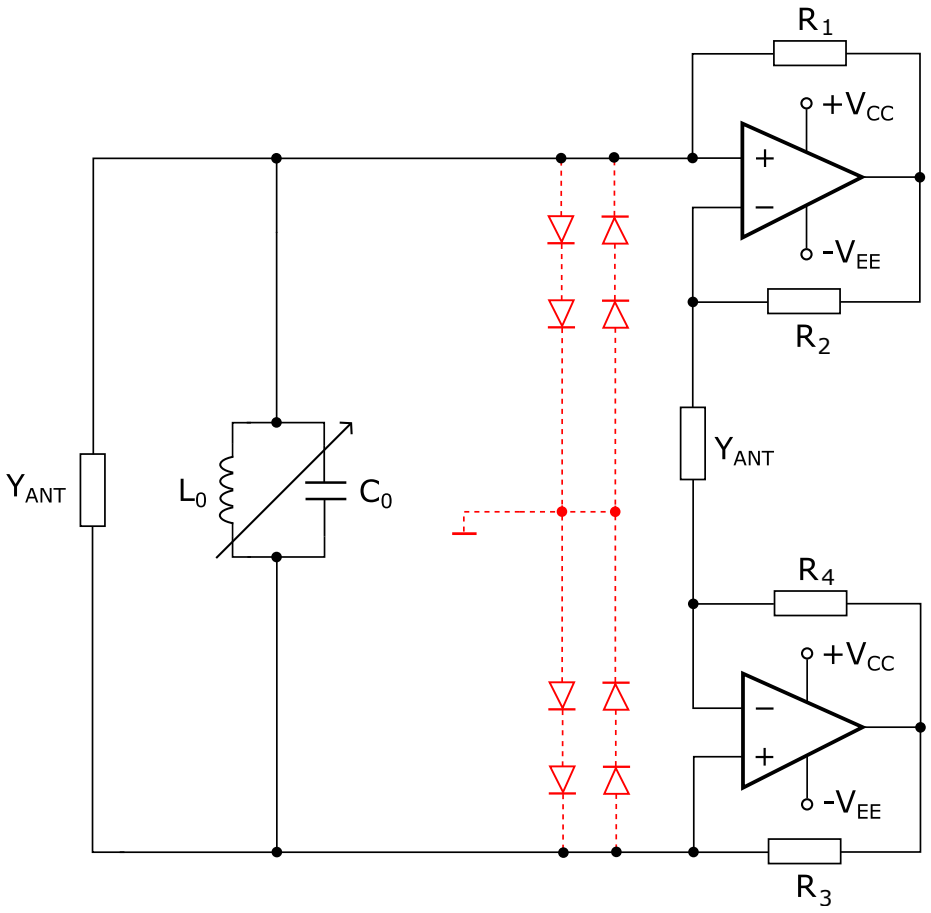

Figure 4.3: Circuit diagram of a self-oscillating antenna based on floating type NIC with two identical antennas. Optional diode limiter is sketched with dashed red lines [93].

ing empirical methods [100]. In the grounded version of NIC, resistors R_1 and R_2 were set to the same value ($R_1 = R_2 = 250\Omega$) to achieve the voltage gain value of 2. In the floating version, all of the feedback resistors were also set to the same value in order to achieve a unitary negative conversion. Results of S-parameter simulations for grounded version of NIC based on THS4304 OPAMP are shown in Figs. 4.4, 4.5.

In associated graphs, ideal conversion is represented with dot dashed green line, conversion of a high-Q load with dotted red curve, conversion of a low-Q load with dashed blue curve, and conversion of a dipole antenna with solid cyan curve. Due to the use of negative feedback loop and the fact that voltage gain value is set to 2, first pole of the OPAMP is located at the frequency of approximately 1GHz [108].

As expected, the most accurate results are obtained in the case of a low Q load. Both real and imaginary parts are converted very close to the ideal value of -1, up to the frequency of around 300MHz. In the case of a high Q load and antenna equivalent model, quite interesting behaviour occurs at frequencies below 2MHz. For those loads, conversion ratio actually starts with high positive values, and reaches expected values only at frequencies above 2MHz. Such phenomenon was not predicted in the theoretical analysis.

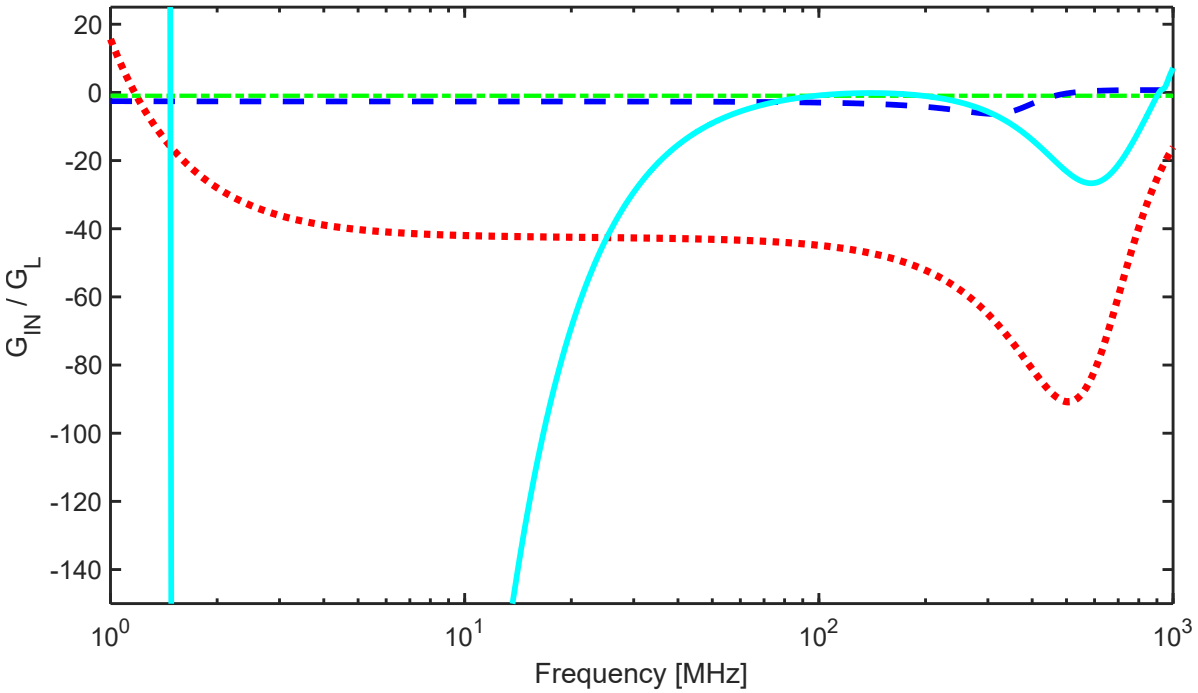

Figure 4.4: Simulated conductance conversion ratio of grounded NIC based on SPICE model of THS4304 OPAMP for three different loads. Green dot-dashed: ideal conversion; Blue dashed: low-Q load; Red dotted: high-Q load; Cyan solid: 5-element dipole antenna model.

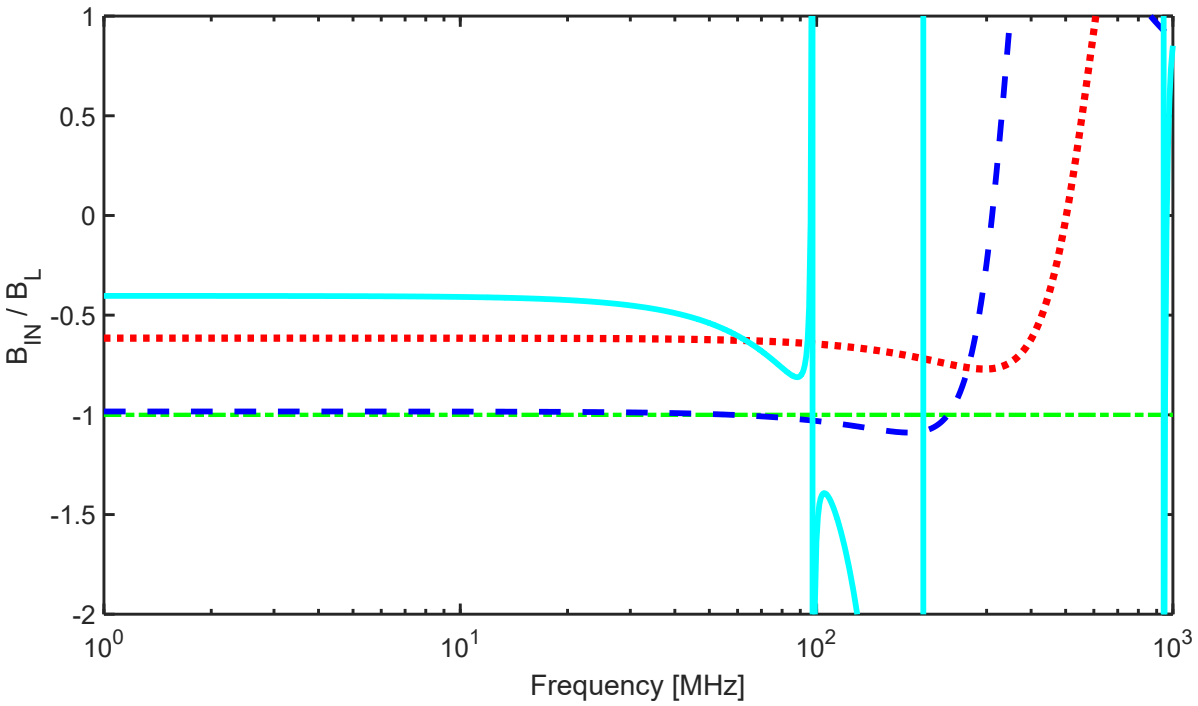

Figure 4.5: Simulated susceptance conversion ratio of grounded NIC based on SPICE model of THS4304 OPAMP for three different loads. Green dot-dashed: ideal conversion; Blue dashed: low-Q load; Red dotted: high-Q load; Cyan solid: 5-element dipole antenna model.

The reason for such behaviour can be found if one carefully examines the datasheet of the OPAMP [108]. Namely, THS4304 is based on bipolar transistors, meaning that the input impedance of OPAMP is not as high as if it were in the case of FET-based OPAMPs. To be more

precise, input capacitance from each of terminals of OPAMP to the ground has a value of 1.5pF, which is certainly comparable to 4pF capacitance of a high Q load, and the low equivalent capacitance of a dipole antenna model. It results in relatively high positive values of input conductance at low frequencies. As expected, conversion ratio of the imaginary part is much more accurate for every given load, up to the frequency of approximately $\frac{f_{POLE}}{10}$.

The next set of simulations dealt with S-parameter analysis of floating type NIC based on THS4304. Again, investigation was made for high Q load, low Q load, and dipole antenna equivalent network. Simulation results for real and imaginary parts of the input admittance are shown in Figs. 4.6, 4.7. Ideal conversion is represented with dot dashed green line, conversion of a high-Q load with dotted red curve, conversion of a low-Q load with dashed blue curve, and conversion of an equivalent circuit model of dipole antenna with solid cyan curve.

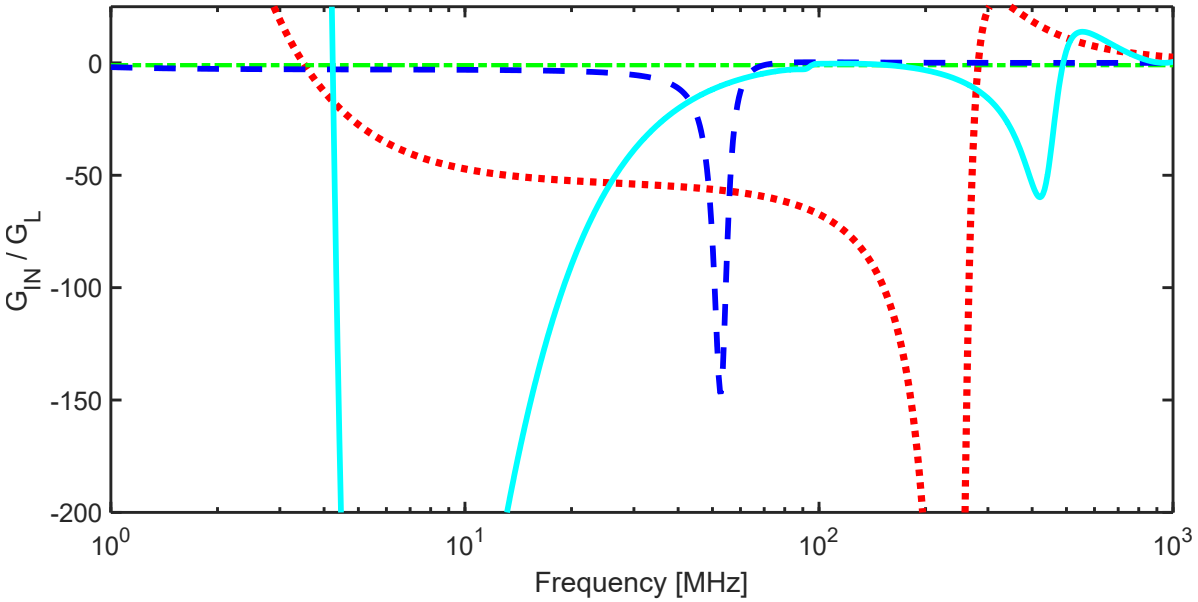

Figure 4.6: Simulated conductance conversion ratio of floating NIC based on SPICE model of THS4304 OPAMP for three different loads. Green dot-dashed: ideal conversion; Blue dashed: low-Q load; Red dotted: high-Q load; Cyan solid: 5-element dipole antenna model.

As it was already predicted for the dispersive model in section 3.2, the pole frequency is not a constant, and it depends on the modulus of the load immittance [90]. Larger modulus of the load immittance leads to a lower value of OPAMP gain, and therefore, higher frequency of the pole. Consequently, accurate conversion of low-Q loads is limited to lower frequencies than conversion of high-Q loads. Similar to the grounded version (Fig. 4.4), relatively low input impedance of the OPAMP causes high positive values of the input conductance for high-Q loads at low frequencies. However, the dispersive model from section 3.2 could not predict such large offset of the real part of the admittance (around 50 times) in the high-Q case. Moreover, the depth of the notch in the curve of conductance ratio, which occurs when the influence of OPAMP pole becomes significant, is somewhat larger than predicted. The reason for such discrepancy may lie in the use of a single pole model of the OPAMP, especially because it

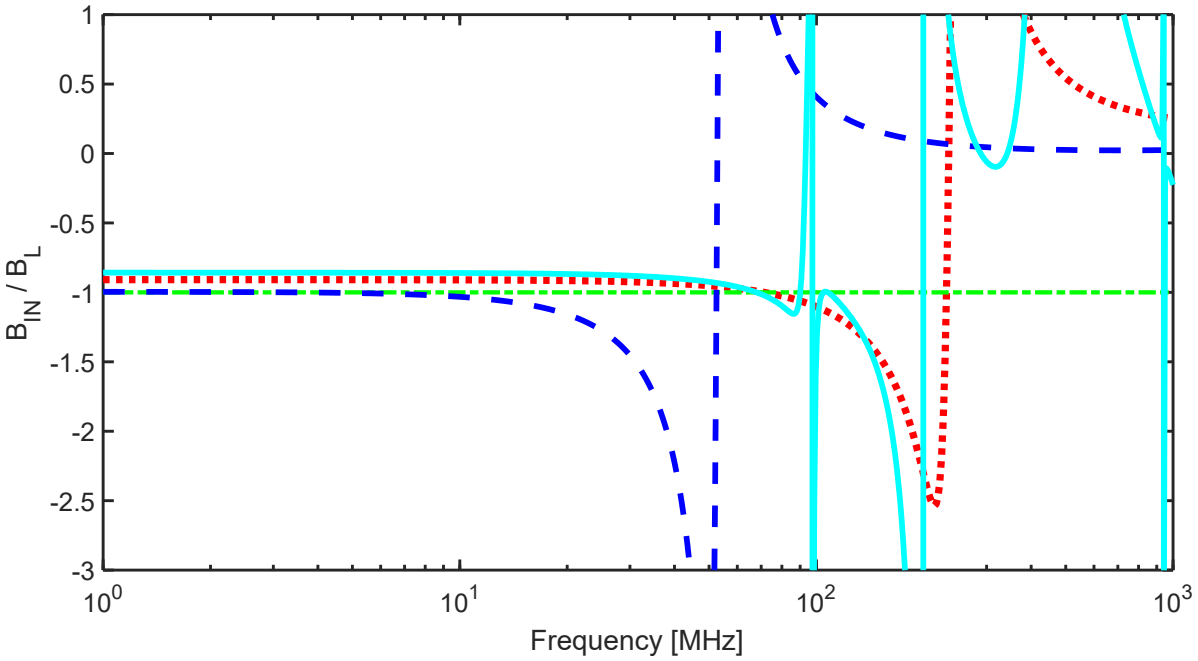

Figure 4.7: Simulated susceptance conversion ratio of floating NIC based on SPICE model of THS4304 OPAMP for three different loads. Green dot-dashed: ideal conversion; Blue dashed: low-Q load; Red dotted: high-Q load; Cyan solid: 5-element dipole antenna model.

is a floating NIC with variable pole frequencies. For better prediction accuracy of NIC input conductance one should use three or more poles in the model.

Regarding the imaginary part of the input admittance, conversion ratio is very similar to the predicted one, for all three loads. Conversion ratios of equivalent dipole model and high-Q load are much more broadband than the conversion ratio of low-Q load. However, even for those cases, the upper operating frequency is around 100MHz, which is close to $\frac{f_{POLE}}{10}$ of the grounded version of NIC. Altogether, the S-parameter simulations in circuit theory simulator gave results which were very close to ones predicted using derived theoretical models, making them useful for future investigation.

The following simulations in this part dealt with the non-linear behaviour of NICs based on THS4304 SPICE model [109]. Both the grounded and floating versions were tested and compared. Simulations were made in ADS^{TM} in Large Signal S-parameter (LSSP) simulator. Voltage magnitude of the input signal was taken as parameter, while figures of merit were conversion ratio of the harmonic input conductance and susceptance. In this case, the load of interest was only equivalent model of dipole antenna.

The simulation results are shown in Figs. 4.8, 4.9. The source of the signal in simulations was a single frequency (CW) power generator with a low internal impedance ($Z_G = 0.01\Omega$) connected in series. Low external impedance is necessary to ensure stable operation of used NIC configurations (Short circuit stable or SCS NIC [53]). From the input power (P_{IN}) and internal impedance (Z_G) it was simple to derive the effective input voltage (V_{IN}) as $V_{IN} = \sqrt{P_{IN} \cdot |Z_G|}$,

and use it as a simulation parameter. Furthermore, it is worth mentioning that the peak value of output saturation voltage for THS4304 OPAMP is approximately 1.5V, meaning that the effective output saturation voltage is approximately 1.06V.

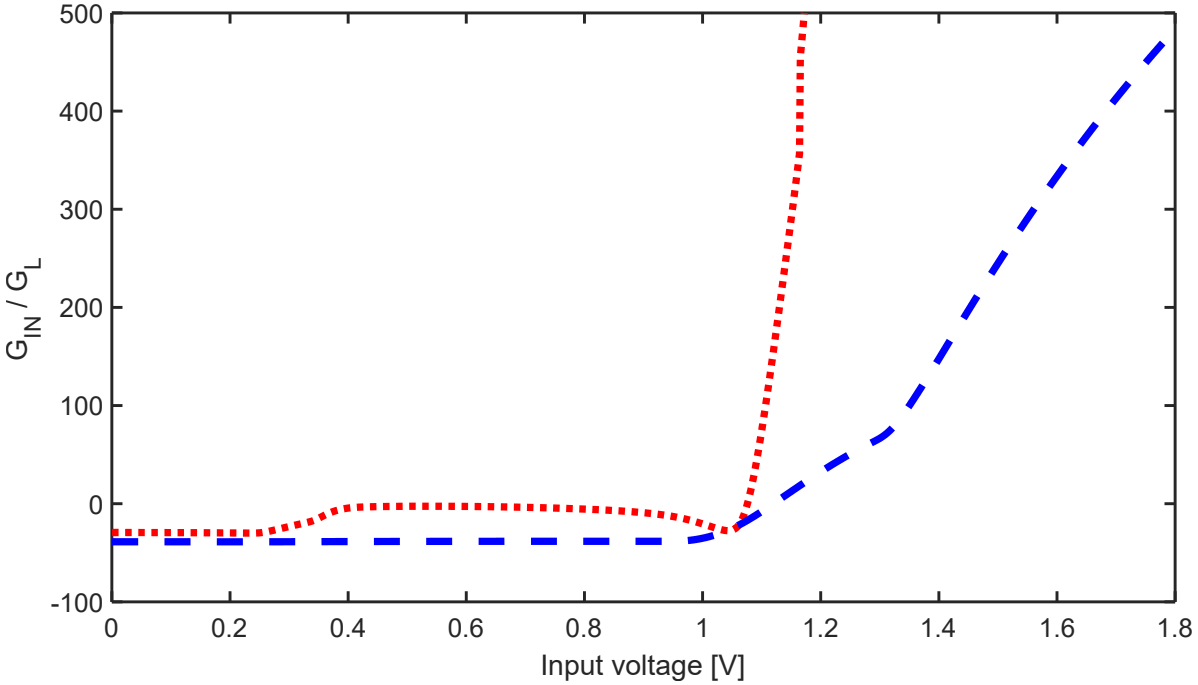

Figure 4.8: Comparison of simulated conductance conversion ratio with respect to the input voltage magnitude between the grounded and floating NIC based on SPICE model of THS4304 OPAMP. Red dotted: grounded NIC; Blue dashed: floating NIC.

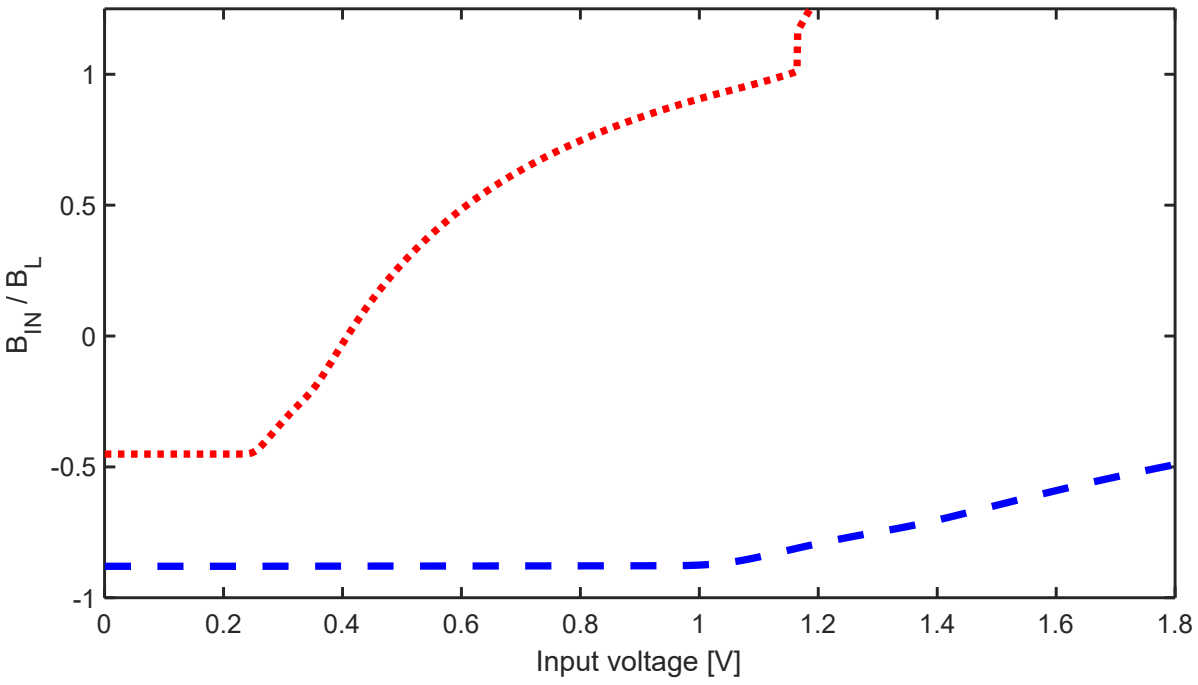

Figure 4.9: Comparison of simulated susceptance conversion ratio with respect to the input voltage magnitude between the grounded and floating NIC based on SPICE model of THS4304 OPAMP. Red dotted: grounded NIC; Blue dashed: floating NIC.

In Figs. 4.8 and 4.9, non-linear behaviour of grounded type NIC is represented with dotted red curves, while dashed blue curves illustrate the non-linearity of floating type NIC. From both real and imaginary parts of the admittance, it is evident that floating type NIC is much less sensitive to the change of the input signal than grounded NIC. Consequently, voltage swing in the quasi-linear operating region is approximately twice as large for the floating NIC. This is due to the fact that floating NIC consists of two OPAMPs connected in differential configuration, which enable twice as large voltage magnitude at the load. Even though the behaviour of real and imaginary parts of the admittance are not identical to the expected ones, tendencies of the curves are similar to those from the model in Chapter 3.3. All curves have positive derivative, and conversion ratios gradually reach positive values. The reason for difference in real and imaginary parts may lie in the large offset of the input conductance at the frequency of interest (conversion ratio starts with -40 instead of -1), where seemingly real part of the admittance increases much faster than the imaginary part.

Certainly, one should take into account these simulation results, both for dispersion and non-linearity. Regarding dispersive behaviour, grounded NIC based on THS4304 offers somewhat better results, especially for conversion of low-Q loads. However, floating type NIC deals with non-linearity much better than grounded NIC does.

4.2 Testing of device with antenna equivalent network

To get a glimpse, in the first set of simulations of a complete self-oscillating system, the antennas were replaced with two simple RC equivalent networks (with high-Q and low-Q behaviour, similarly to the analytical discussion in Chapter 2.2) and connected to a grounded NIC [24, 91, 93]. Values of the elements of the equivalent circuit for the high-Q model are $R = 2\Omega$, $C = 4$pF, giving the Q$\approx$2000 at the frequency 10 MHz. For the low-Q model values are $R = 100\Omega$, $C = 50$pF, giving the Q$\approx$1.6 at the frequency 20 MHz. The electronic part of the unit cell was designed using the circuit-theory simulator (ADS^{TM}) and manufacturer's OPAMP SPICE model (THS4304, [109]). For this analysis, only grounded version of NIC was used (Fig. 4.2). The simulations showed expected self-oscillatory behaviour with the dependence of tuning bandwidth on a load type. The error of negative conversion was also investigated. It was done by the extraction of the NIC input admittance from the simulations.

A sample of generated self-oscillating signal and associated spectrum of self-oscillating antenna with high-Q antenna emulating network, simulated in circuit theory simulator, are shown in Fig. 4.10. Waveform of the signal was taken from the growing stage of oscillations, while spectrum was calculated using Fourier transform over a segment of signal with stable frequency and amplitude. Frequency of oscillations was set by changing the parameters of the tank circuit (C_0=30pF, L_0=1μH) to value 29.1 MHz, which is close to the upper limit of obtainable

self-oscillations.

It can be seen in Fig. 4.10 that simulated network generates signal with fundamental frequency of 26.23 MHz, which is somewhat lower than expected. This frequency shift of 10% is caused by NIC conversion error due to dispersion. Voltage magnitude at the NIC input was limited to approximately 200 mV by the use of diode limiters. It results in suppression of higher harmonics as high as 65 dB (right part of Fig. 4.10).

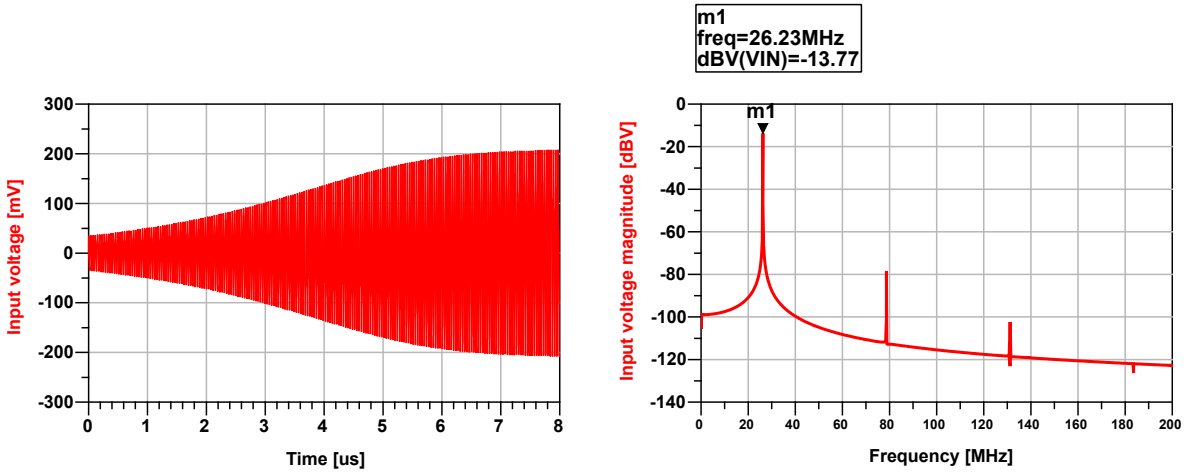

Figure 4.10: Waveform (left graph) and spectrum (right graph) of generated signal of self-oscillating antenna with high-Q RC equivalent antenna network.

After these initial simulations, several NIC prototypes were assembled using standard SMD components mounted on a small (25x25 mm) FR4 PCB (designed in $Altium^{TM}$ environment). The prototyped NICs were equipped with tuning LC tank circuit and antenna emulating RC networks [93]. The photo of the constructed demonstrator circuit board is shown in Fig. 4.11

The experiments were performed as follows. At first, the oscillating frequency was adjusted using the LC circuit. Then, the passive network (LC circuit with external antenna emulating network) was dismounted and its admittance was measured by a VNA. The NIC input admittance was calculated by flipping the sign of the measured admittance (in accordance with the basic oscillation condition derived in (2.2)). This procedure was repeated at a number of discrete frequency points, and obtained results were compared with simulations [93]. A sample of obtained results are shown in Figs. 4.12, 4.13, 4.14, 4.15.

In the above figures, blue solid curves represents simulation results without a limiter network, black dot-dash curves simulation results with a limiter network, and red dashed curves measurements with a limiter network. Generally, the results for high-Q antenna emulating network (Figs. 4.12, 4.13), show more pronounced conversion error than those for low-Q network (Figs. 4.14, 4.15), which is in agreement with theoretical predictions.

However, there are two unexpected results. First, the error of the real part of the input admittance (Fig. 4.12) of the prototype is significantly higher than predicted. Secondly, the imaginary part of the input admittance has a flipped sign for frequencies above 15 MHz (Fig.

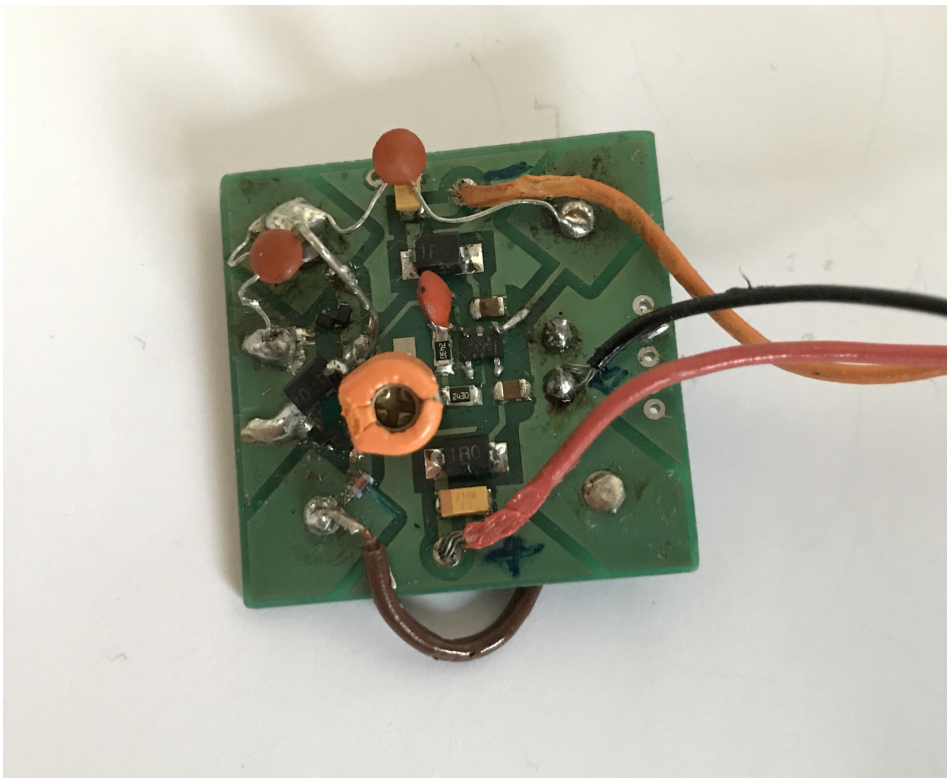

Figure 4.11: Photograph of the developed self-oscillating antenna circuit board with embedded antenna equivalent networks.

4.13) in the case without limiter. Thus, the inverted dispersive behaviour (negative derivative of susceptance regarding to the frequency) is lost. The reason for these inconsistencies lies in highly non-linear operation of the device. Due to the high quality factor of the antenna emulating network, the conversion error caused by the amplifier's dispersion was significant. The negated curve of the active element ($-Y_{ACT,REAL}(V,\omega)$) is located at the right side of the load curve ($Y_{ANT}(\omega)$), but far away from it (Fig. 3.22). Thus, the amplitude of oscillations should grow significantly before the intersection with a load curve ($Y_{ANT}(\omega)$) is reached. It moves the operating point into a non-linear region of the N curve with gain lower than one (Fig.

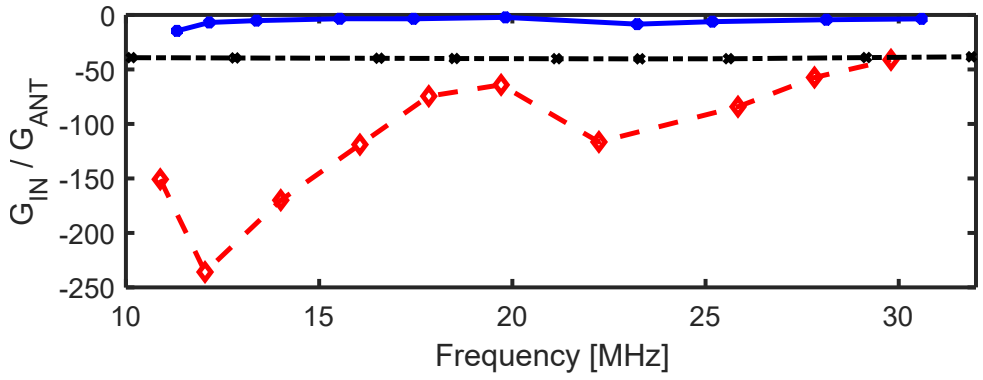

Figure 4.12: Conversion ratio of simulated and measured input conductance of a self-oscillating antenna with high-Q antenna equivalent network. Blue solid: simulation without a limiter; Black dot-dashed: simulation with a limiter; Red dashed: measurements with a limiter.

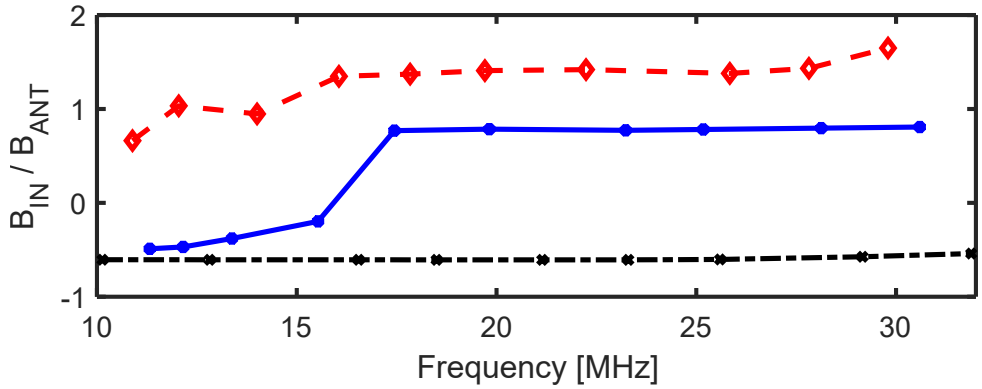

Figure 4.13: Conversion ratio of simulated and measured input susceptance of a self-oscillating antenna with high-Q antenna equivalent network. Blue solid: simulation without a limiter; Black dot-dashed: simulation with a limiter; Red dashed: measurements with a limiter.

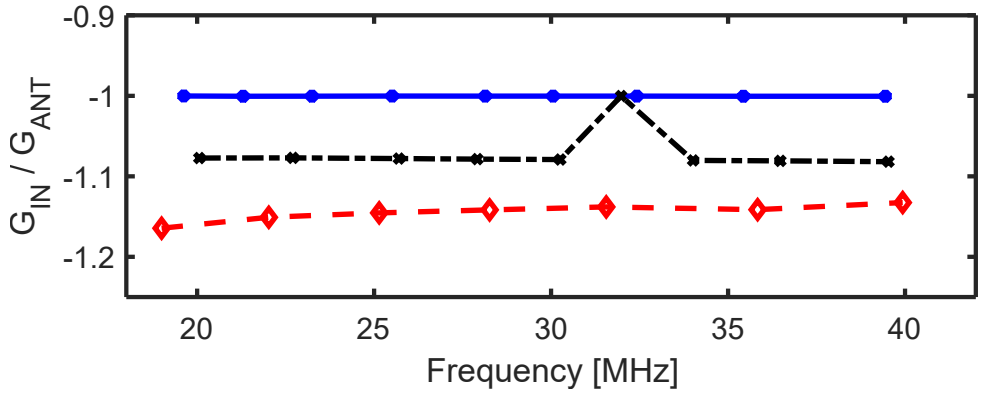

Figure 4.14: Conversion ratio of simulated and measured input conductance of a self-oscillating antenna with low-Q antenna equivalent network. Blue solid: simulation without a limiter; Black dot-dashed: simulation with a limiter; Red dashed: measurements with a limiter.

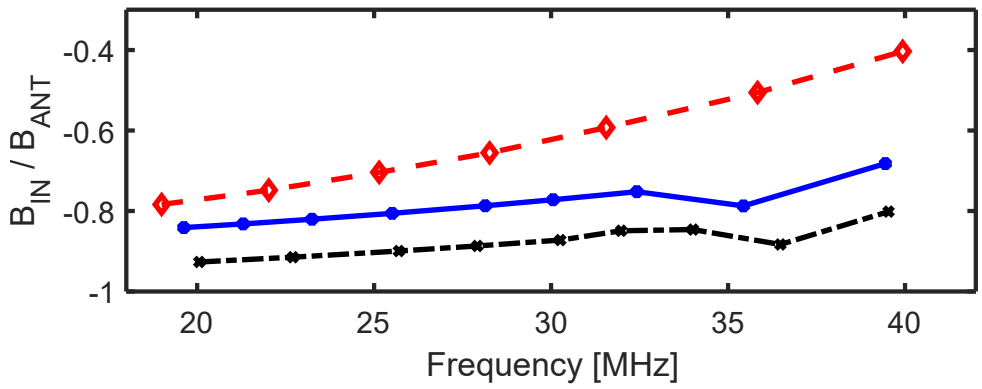

Figure 4.15: Conversion ratio of simulated and measured input susceptance of a self-oscillating antenna with low-Q antenna equivalent network. Blue solid: simulation without a limiter; Black dot-dashed: simulation with a limiter; Red dashed: measurements with a limiter.

3.18).

Because of such large gain compression negative conversion ceased, initiated relaxation oscillations, and deteriorated dispersive cancellation. This problem was overcome by adding a simple diode-based limiter network (dot-dashed curve) that limited signal at the NIC input

and did not allow the value of gain to drop below unity [93]. It can be seen (Fig. 4.13) that the incorporation of the limiter indeed assured required oscillations which included dispersion cancellation, within a tuning range of approximately 1:3 (10MHz-30MHz).

A case with a low-Q antenna emulating network (Figs. 4.14, 4.15) showed better results, as expected. There, the conversion errors in real and imaginary parts of the input admittance are 15-20% and 20-60%, respectively. Those results were obtained without any optimization and they are acceptable for practical purposes. It is interesting that the difference between the results with and without limiter network is not very pronounced. This is a consequence of a low quality factor of the load network, which does not contribute significantly to the error caused by dispersion and finite length of used OPAMP (Fig. 3.9, 3.10). Hereof, it is not necessary to use a limiter network at all in the case of a low-Q antenna. Finally, it should be mentioned that the tuning range for a low-Q load was 1:2 (20 MHz to 40 MHz), limited by the available tuning elements.

4.3 Testing of device with dipole-like antennas

Previous discussion has shown that the use of a high-Q antenna as a load of NIC causes a relatively large error in NIC conversion, a shift of the operating frequency, and the deterioration of matching properties. One could use resonant low-Q antennas, but this would require a very large size of the antenna (approximately one half of a wavelength), which then could not be used for possible application in metasurfaces. A better option would be to use some design of a miniaturized dipole antenna, which could lead to a smaller size of the device [111]. We decided to concentrate on those designs that maintain a radiator symmetry, essential for a low cross-polarization (and low mutual coupling) of orthogonal elements.

Therefore, we selected a capacitively loaded dipole (Fig. 4.17) [112], and a bow-tie antenna (Fig. 4.18) [113], as possible candidates. These radiators are considered to have the same physical footprint as the original cross-dipole sketched in Fig. 2.1. They were fitted within a square with the same base length l. Numerical models were designed and calculated in the CST^{TM} Microwave Studio full-wave simulation environment. Antennas were calculated using time domain solver with following simulation parameters. Mesh type was hexahedral with 8,903,396 cells. Boundary conditions were open (add space) in all directions, while background type was normal (bounding box was a cube with side length of 2 meters). Frequency range of interest was from 1 MHz to 200 MHz. Two discrete S-parameter type ports (with internal impedance of 50Ω) were used for the excitation of antenna structure. Accuracy of simulation was set to -40 dB (simulation lasted until the level of injected energy dropped by 40 dB), which gave the average simulation time of 150 ns.

For the sake of experiment, antennas were also constructed using conventional simplistic

materials, aluminum foil over styrofoam supstrate. Both of the antennas were compared to the initial basic dipole antenna, both in simulations and measurements [93]. We also simulated a surface current distribution at all three unit cells at the frequency 30MHz, assuming idealized excitation by two in-phase currents with unit magnitude ($1\angle 0°$). As expected, surface currents flow predominantly along the line of symmetry at 45°. A superposition of associated electric fields results with vertical linear polarization. In reality, the currents flowing in the radiators will not be perfectly in phase (due to NIC conversion error), causing a change of a polarization angle. Designs, calculated surface currents and photos of the constructed antennas are shown in Figs. 4.16, 4.17 and 4.18.

The width of the capacitive loading arm of a cross-dipole (a) and the width of a bow-tie arm (a) were taken as design parameters. The antennas were made of aluminum and the thickness of such planar dipole-like antennas was equal to the dipole rod diameter used in [24]. One of the output simulation results are scattering parameters of the antenna. This scattering matrix was imported into the circuit theory simulator (ADS^{TM}) and all the tests done previously for the RC antenna emulating networks, were repeated. For the sake of generalization, simulation results are normalized to the frequency at which the unit cell has a size of $\frac{\lambda}{2}$x$\frac{\lambda}{2}$. Magnitudes of S_{11} for all three designed antennas are shown in Fig. 4.19.

In Fig. 4.19, $|S_{11}|$ of dipole antennas is represented with black curves, $|S_{11}|$ of capacitively loaded dipole antennas with red curves, and $|S_{11}|$ of bow tie antennas with blue curves. Solid and dashed stand for simulations and measurements, respectively. As expected, a simple cross-dipole has the poorest miniaturization potential. Return loss is very good (16dB) when a cross-dipole is resonant ($l = \frac{\lambda}{2}$). However, for the unit cell of moderate subwavelength size ($\frac{\lambda}{5}x\frac{\lambda}{5}$), obtained return loss is close to 0 dB due to the highly capacitive input reactance and a very low radiation resistance. This high-Q behaviour introduces a significant error in NIC conversion ratio [93].

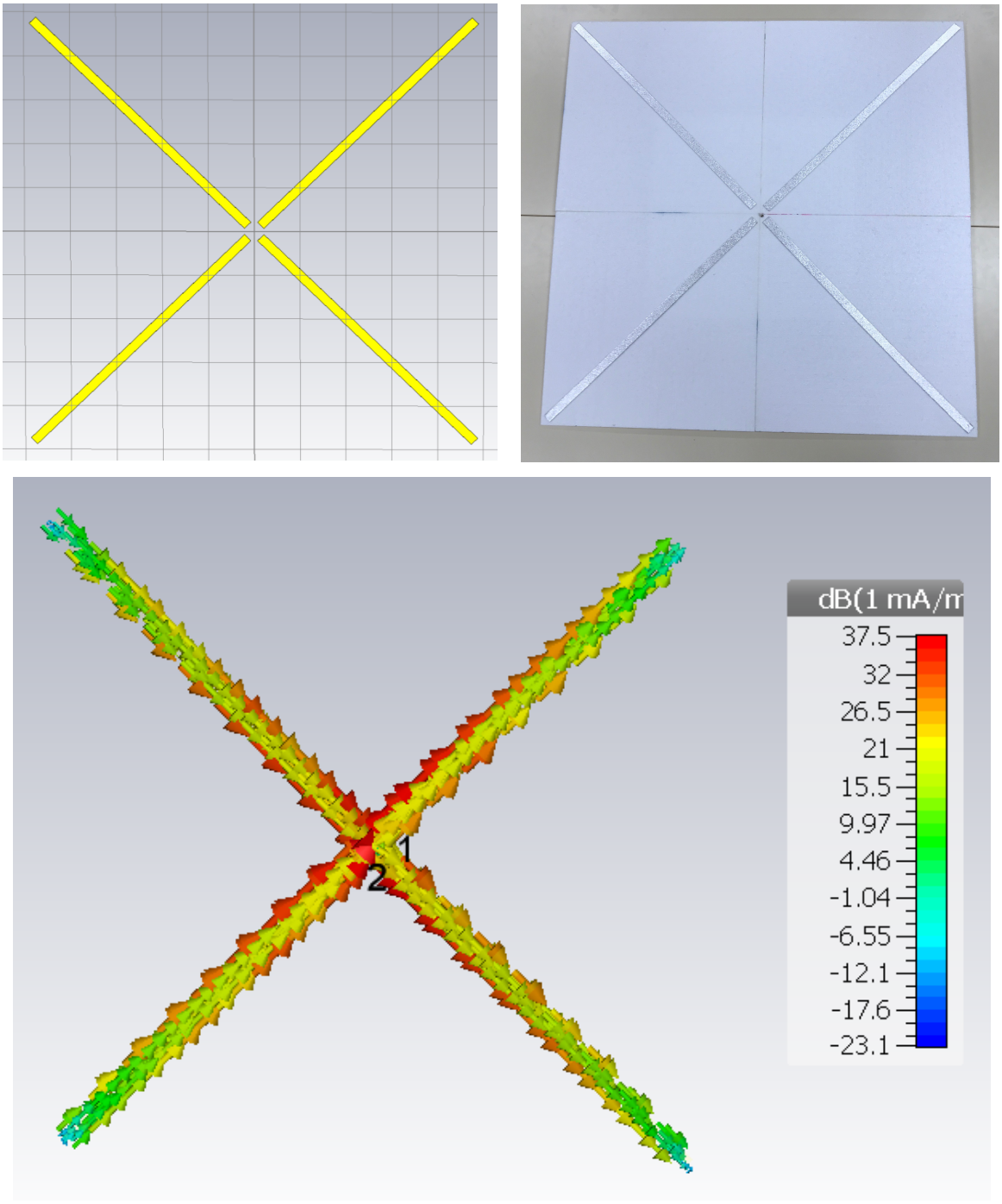

Figure 4.16: Design (upper left), calculated surface currents (bottom) in CST^{TM} Microwave studio, and photo (upper right) of the constructed crossed dipole antenna. Dipole length: 1.414m; Dipole width: 0.02m; Dipole thickness: 10^{-4}m.

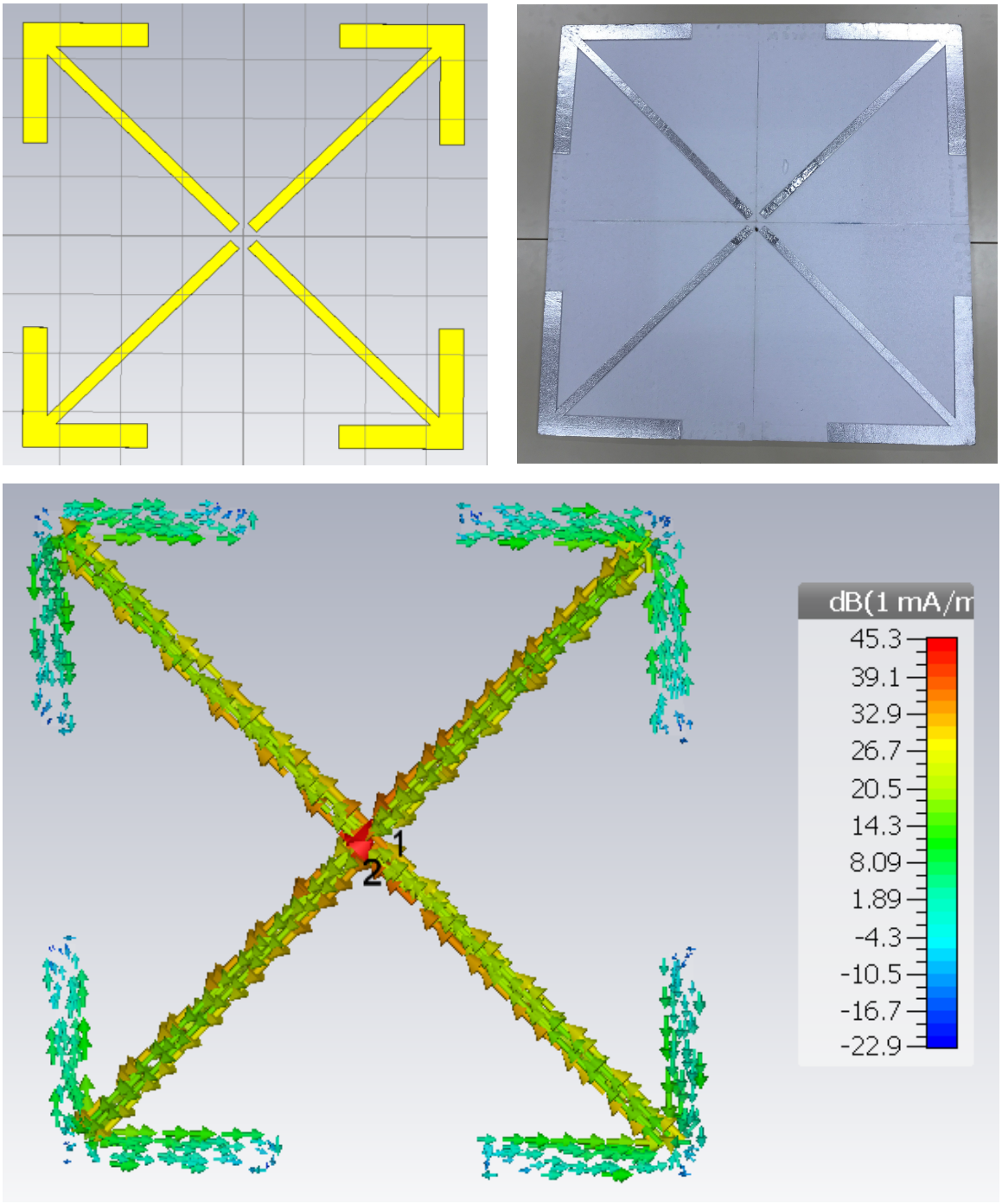

Figure 4.17: Design (upper left), calculated surface currents (bottom) in CST^{TM} Microwave studio, and photo (upper right) of the constructed capacitively loaded dipole antenna. Dipole length: 1.414m; Dipole width: 0.02m; Capacitive arm length: 0.4m; Capacitive arm width: 0.04m; Antenna thickness: 10^{-4}m.

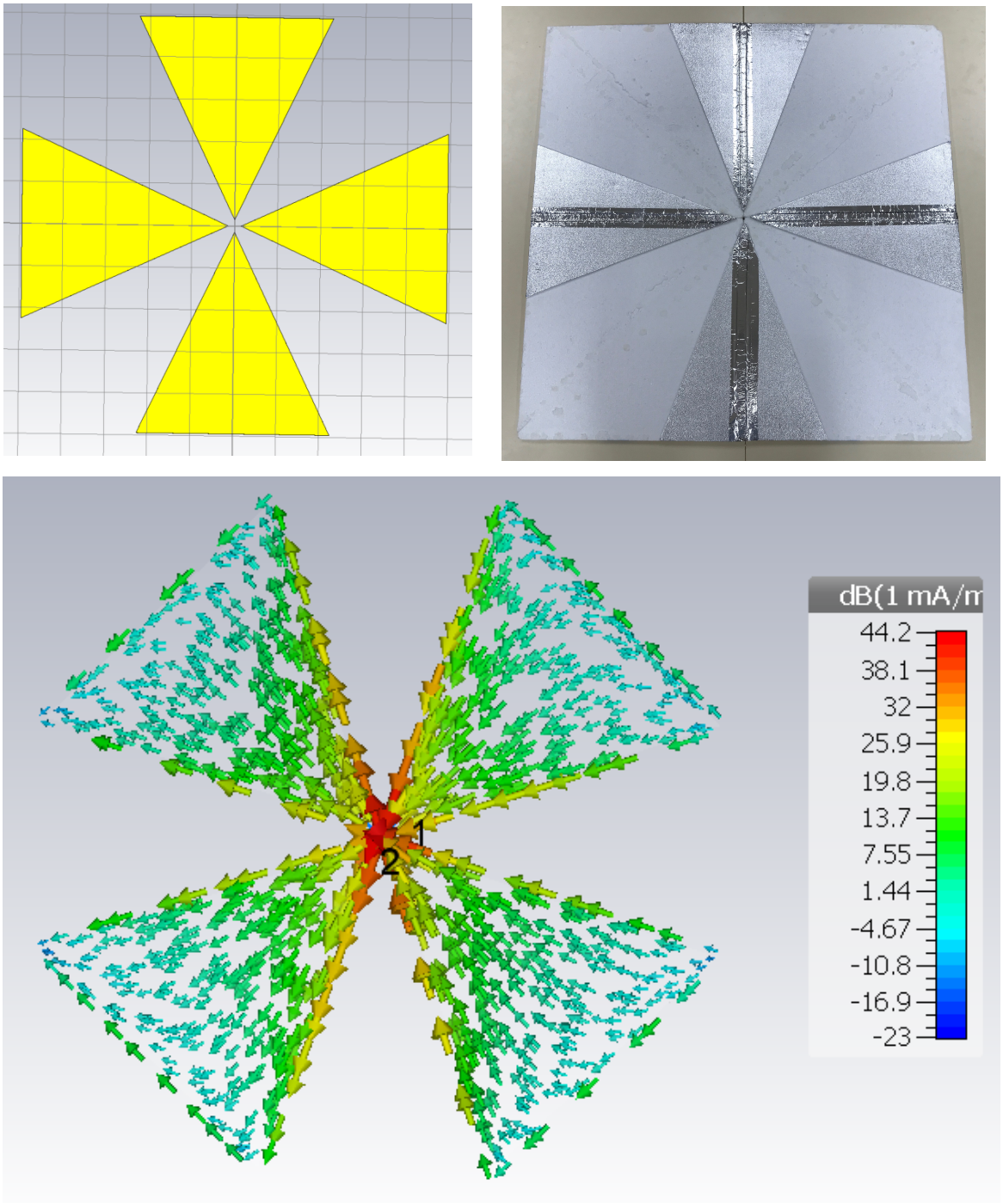

Figure 4.18: Design (upper left), calculated surface currents (bottom) in CST^{TM} Microwave studio, and photo (upper right) of the constructed bow-tie antenna. Bow-tie length: 1.414m; Bow-tie arm width: 0.365m; Bow-tie thickness: 10^{-4}m.

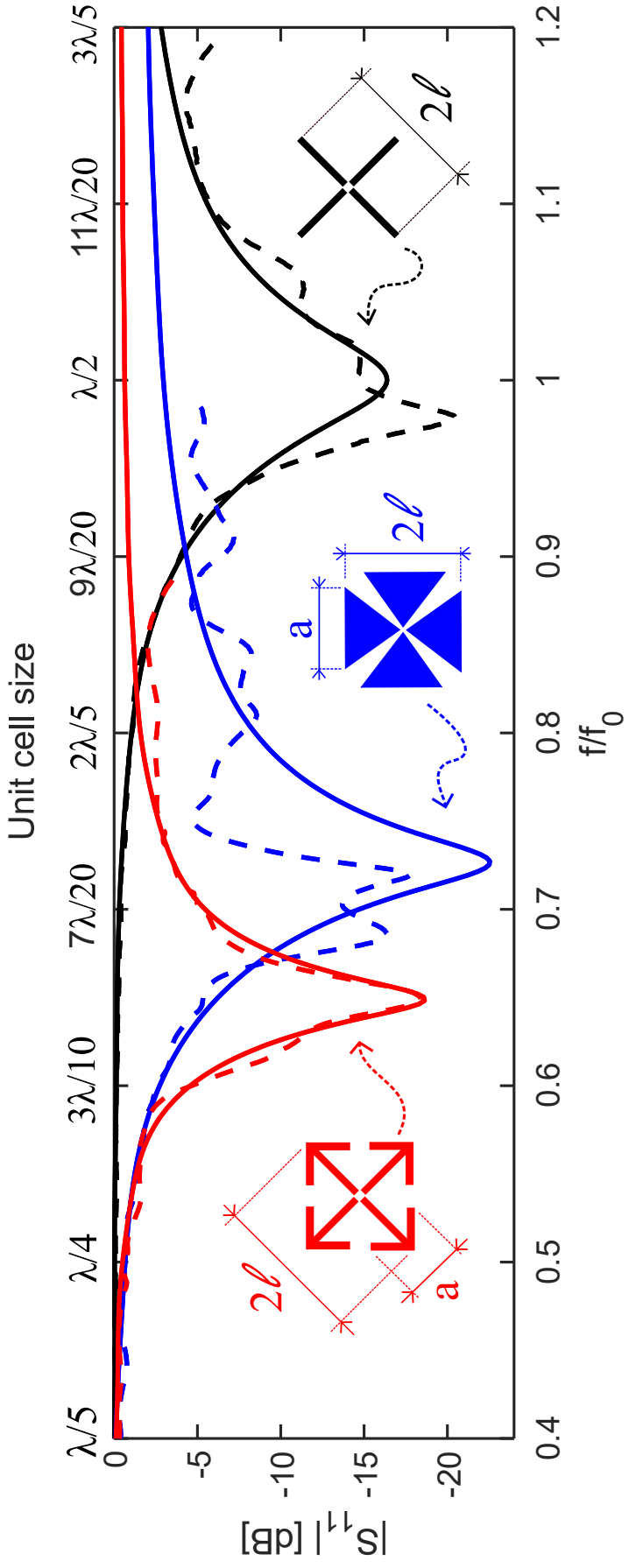

Figure 4.19: Comparison of $|S_{11}|$ for dipole (black), capacitively loaded dipole (red) and bow-tie antenna (blue). Solid curves: simulations; Dashed curves: measurements.

Adding a simple 'arrow-shaped' capacitive loading ($a = 0.6 \cdot l$) [112], decreases the unit cell size down to 65% of the original size with a return loss of 18dB. Further miniaturization to a $\frac{\lambda}{5} x \frac{\lambda}{5}$ unit cell size deteriorates the return loss to 1 dB, which is slightly better than the original case of a cross-dipole. The case with two orthogonal bow-tie radiators ($a = 0.5 \cdot l$) shows very good return loss (22dB) with the unit cell, whose size is 75% of that from the original design. Miniaturization down to a $\frac{\lambda}{5} x \frac{\lambda}{5}$ unit cell exhibits a return loss of 0.5 dB, but with a rather broad 10 dB matching bandwidth.

Next data which was calculated using CST^{TM} are directivity patterns of all three antennas. Results are shown in Figs. 4.20, 4.21, 4.22, and they represent far-field directivity in polar diagram in the case when both of the antennas are excited. Solid blue curves represent directivity in E-plane (electric field plane) for constant value of angle Φ (cut angle of 90°), while dashed red curves represent directivity in H-plane (magnetic field plane) for constant value of angle Θ (cut angle of 0°).

All three radiation patterns are of familiar 'doughnut-like' shape. It is evident that all three antennas behave as (modified) small dipoles. Therefore, the associated simulated directivities are found to be very similar (they vary from 1.59 dBi to 1.79 dBi across the range 10MHz to 50MHz [93]).

The next step was to extract the scattering parameter matrix obtained by the full wave electromagnetic simulator, and insert it into circuit theory simulator (ADS^{TM}) in the place of the antenna admittances. All of the following simulations were based on SPICE model of the OPAMP. A series of transient (time domain) simulations revealed NIC conversion error of real and imaginary parts of the input admittance at several operating frequencies, waveform of generated signal, signal spectrum and simulated radiated power. From gathered results it was possible to

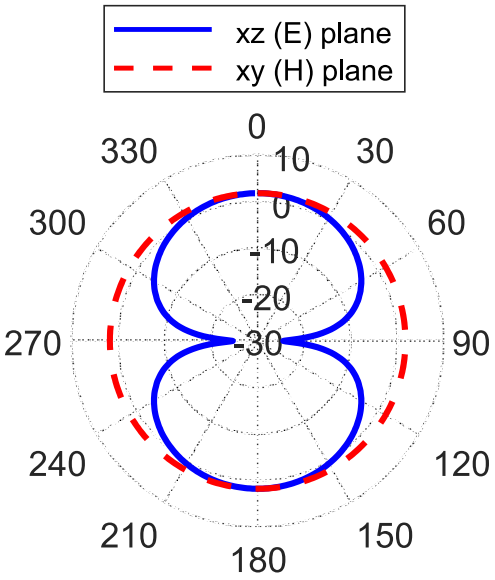

Figure 4.20: Simulated radiation pattern of designed crossed dipoles from Fig. 4.16 at the frequency of 30 MHz, obtained by CST^{TM} Microwave Studio.

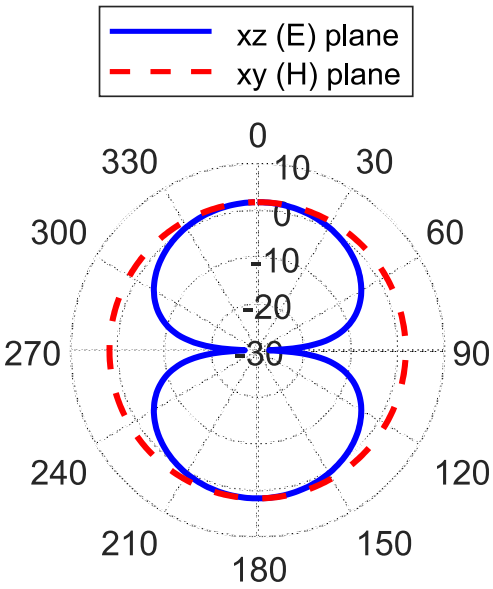

Figure 4.21: Simulated radiation pattern of designed capacitively loaded dipoles from Fig. 4.17 at the frequency of 30 MHz, obtained by CST^{TM} Microwave Studio.

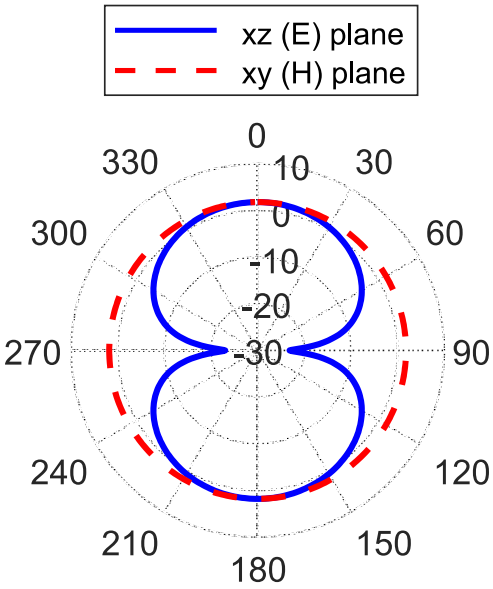

Figure 4.22: Simulated radiation pattern of designed bow-tie antennas from Fig. 4.18 at the frequency of 30 MHz, obtained by CST^{TM} Microwave Studio.

extract the achievable tuning bandwidth for each antenna.

A sample of waveform and spectrum of simulated self-oscillating bow-tie antenna is shown in Fig. 4.23, as an example. Ideally, fundamental frequency would be 30.1 MHz (parameters of the tank circuit were set to C_0=28pF, L_0=1μH). However, simulations predicted the frequency of 27.79 MHz, which is 7.6% lower than the expected. Magnitude of the input voltage is limited to approximately 350 mV (left part of Fig. 4.23) by the use of diode limiters, which were connected as in Fig. 4.3. Suppression of higher harmonics is as high as 45 dB. Chosen fundamental frequency is in the middle of the obtainable tuning range of with bow-tie antennas.

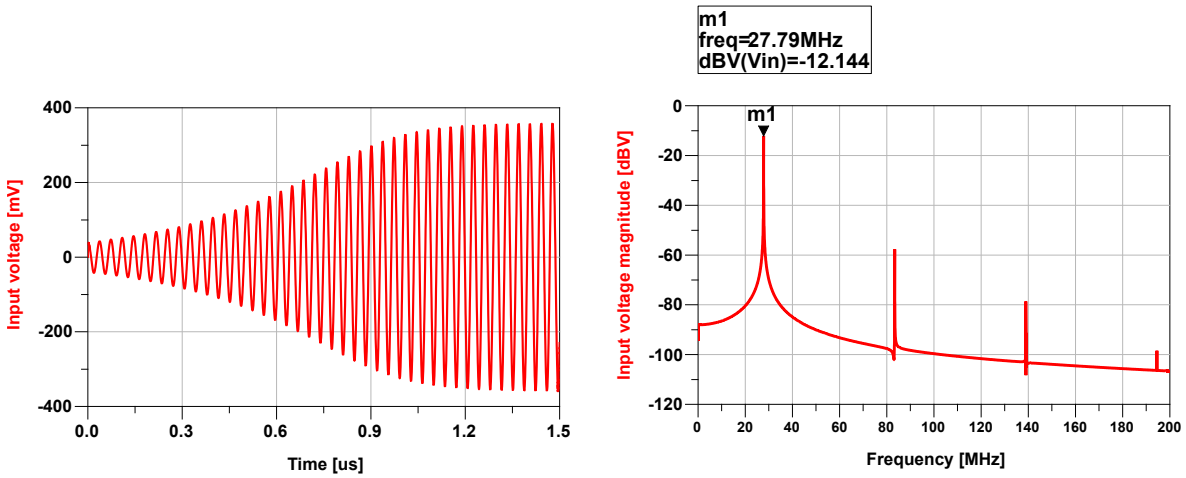

Figure 4.23: Sample of waveform (left graph) and spectrum (right graph) of generated signal of simulated self-oscillating bow-tie antenna from Fig. 4.18.

Conversion ratios of real and imaginary parts of the admittance are shown in Figs. 4.24, 4.25. Solid black curves represent conversion ratio for dipoles, dotted red curves for capacitively loaded dipoles, and dashed blue curves for bow tie antenna. At first, it can clearly be seen that both capacitively loaded cross dipole and cross bow-tie radiators offer approximately one order of magnitude lower conversion error comparing to the original crossed dipoles. Secondly, the error in the real part of the admittance is more pronounced than the error of the imaginary part. Again, this is a direct consequence of a high-Q factor of the load (antenna) [93].

The most important observation deals with the tuning bandwidth. Original crossed dipoles span the cell sizes from $\frac{\lambda}{20}$ to $\frac{2\lambda}{5}$ (1:8 bandwidth). Meanwhile, capacitively loaded crossed dipoles span sizes from $\frac{\lambda}{25}$ to $\frac{\lambda}{5}$ (1:5 bandwidth), and bow tie antennas span the sizes from $\frac{\lambda}{36}$ to $\frac{\lambda}{6}$ (1:6 bandwidth). These bandwidths presume that the LC tuning network can be set arbitrarily. As it was the case in testing of RC equivalent networks, one could expect the tuning range of oscillations from 1:2 to 1:3, using a single tuning circuit comprising commercial inductors and capacitors.

The next step was to retrieve the information about the individual currents at the antennas at the operating frequency points and import those results in CST^{TM} Microwave Studio. The goal was to calculate the polarization angle offset using the calculated currents as excitation. Polarization angle offset is here defined as a difference between the polarization angle in the case of identical currents at the antennas, and polarization angle which is achieved with numerically obtained currents in ADS^{TM}. In the ideal case, polarization of the self-oscillating antenna system is linear with 45° angle with respect to both of the radiators (vertical polarization) [92].

Simulated currents at both antennas are approximately the same in magnitudes as well as in angles, which can be seen in Figs. 4.26, 4.27. The only noticeable discrepancy occurs regarding the current angle difference in the case of a bow tie antenna. This can be attributed to shifted resonant frequency of bow tie radiators which then results in relatively large conversion error

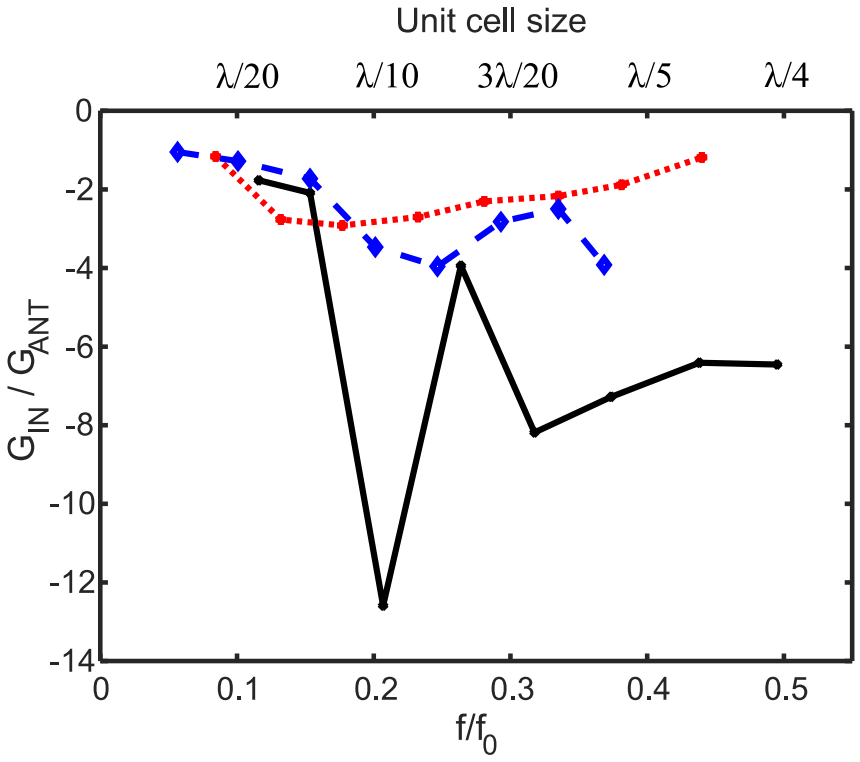

Figure 4.24: Comparison of conductance conversion ratios for self-oscillating antenna with dipoles (Fig. 4.16), capacitively loaded dipoles (Fig. 4.17) and bow-tie antenna (Fig. 4.18). Black solid: dipoles; Blue dashed: bow-tie; Red dotted: capacitively loaded dipoles.

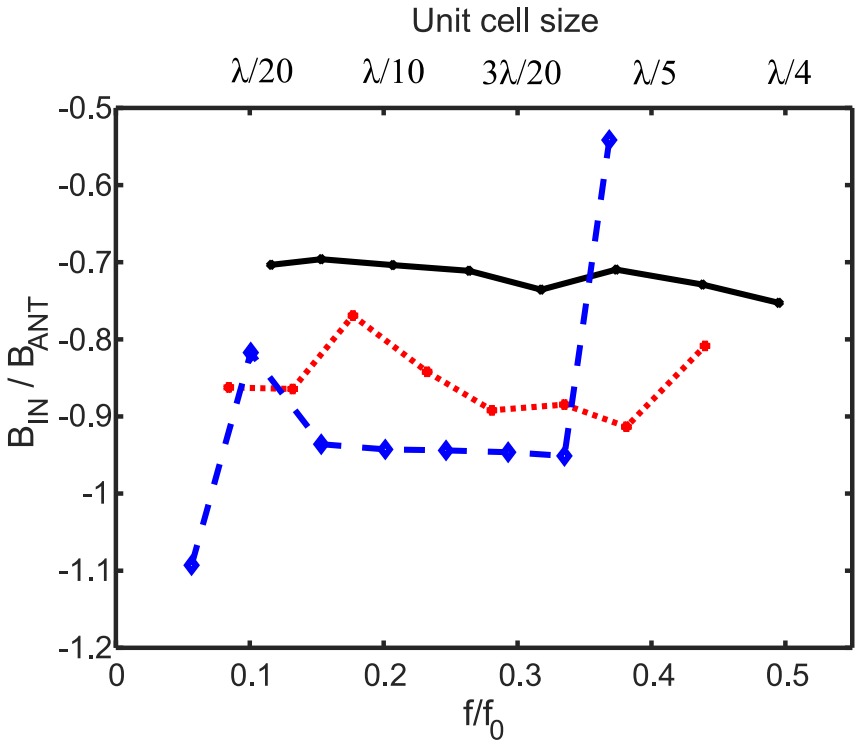

Figure 4.25: Comparison of susceptance conversion ratios for self-oscillating antenna with dipoles (Fig. 4.16), capacitively loaded dipoles (Fig. 4.17) and bow-tie antenna (Fig. 4.18). Black solid: dipoles; Blue dashed: bow-tie; Red dotted: capacitively loaded dipoles.

of imaginary part of the admittance (Fig. 4.25). In general, small difference in antenna currents results in relatively small polarization angle offset across the whole operating frequency band (Fig. 4.28).

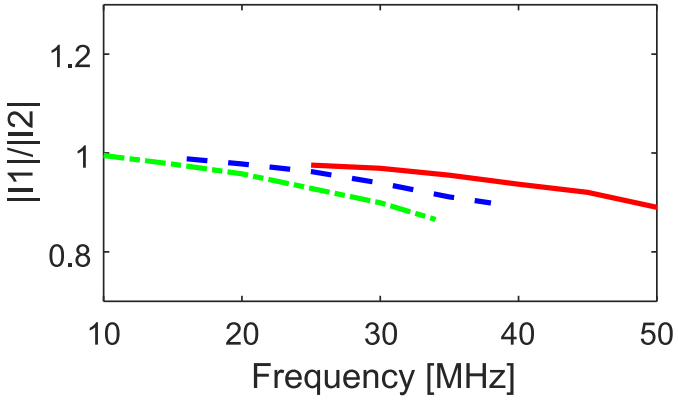

Figure 4.26: Ratio of current magnitudes across the antennas as a result of SPICE based simulations. Red solid: dipoles; Blue dashed: bow-tie; Green dot-dashed: capacitively loaded dipoles.

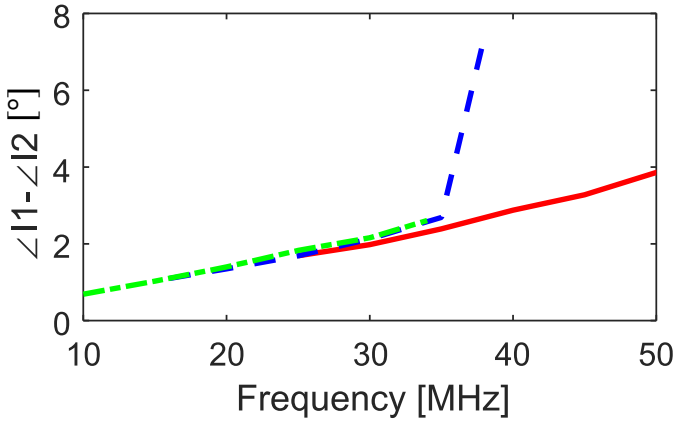

Figure 4.27: Difference in angle of currents across the antennas as a result of SPICE based simulations. Red solid: dipoles; Blue dashed: bow-tie; Green dot-dashed: capacitively loaded dipoles.

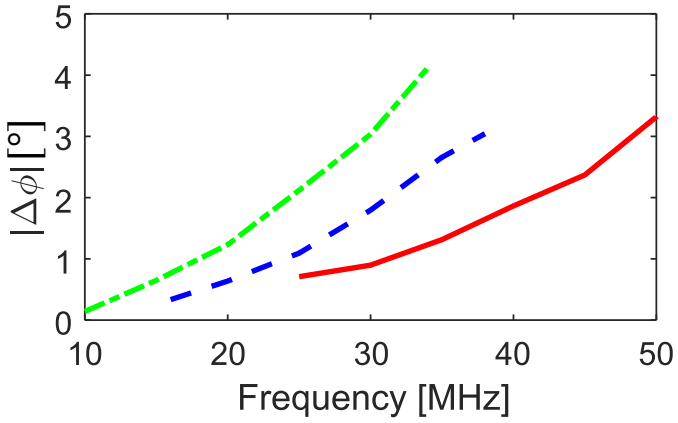

Figure 4.28: Simulated polarization angle offset of self-oscillating antenna with three different types of antennas. Red solid: dipoles; Blue dashed: bow-tie; Green dot-dashed: capacitively loaded dipoles.

In the above figures, crossed dipoles are represented with solid red curves, capacitively loaded dipoles with dot dashed green curves, and bow tie antennas with dashed blue curves. The curves representing all three antennas have approximately the same tendency, polarization angle offset slightly increases with frequency with a maximal shift of approximately 4° [93].

The prototyped NIC with a tuning network was connected to antenna feeding points, finalizing the unit cell fabrication (Fig. 4.29) [93].

Due to the very low frequency of operation of the scaled prototype (i.e. large near-field zone) it is not possible to directly measure the radiation pattern and radiated power. Thus, we have performed a series of indirect qualitative tests in the near-field (Fig. 4.30). A prototype of the scaled unit cell (powered by a battery pack) was hung from the ceiling of a lecture hall. The receiving signal was monitored by a spectrum analyser connected to a short dipole, at the distance of 3m [93]. In the first group of experiments, it was verified that all three unit cells indeed radiate signals produced by self-oscillations. Although the testing was done in the near field, rotation of the receiving dipole proved predominantly vertical polarization (approximately 45° shift with respect to individual radiators), which is consistent with the simulations.

A sample of measured spectrum (Fig. 4.31) showed suppression of a second harmonic better than 20 dB. The level of received power varied from approximately -60 dBm to -80

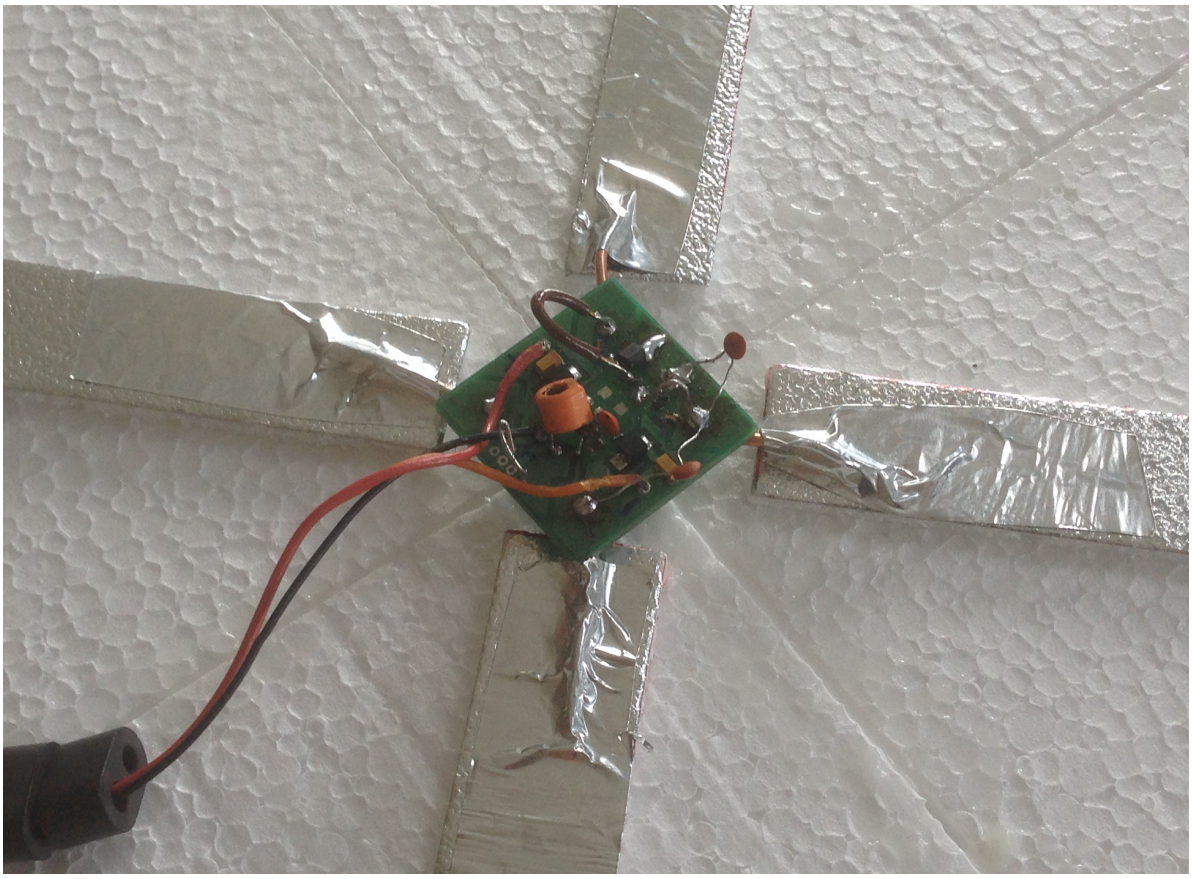

Figure 4.29: NIC electronic circuit board connected to crossed dipole antenna.

Figure 4.30: Photo of the measurement setup of self-oscillating antenna with crossed capacitively loaded dipoles.

dBm. Reasons for such low received power are related to the prototype, receiving antenna, and also very reflective environment in which measurements were made [93]. As explained before, OPAMPs in general are limited with a relatively low voltage swing, resulting in a low output power. NIC used in experiments was based on a THS4304 OPAMP with 2.5V DC power supply and the output signal swing of approximately 1.5V. Therefore, maximal voltage swing at the NIC input is approximately $\pm$0.75V and $\pm$1.5V for NICs in Fig. 4.2 and Fig. 4.3, respectively. These voltage levels directly limit maximal achievable output power to approximately 0 dBm. On the other hand, receiving antenna for frequencies around 30MHz ($\lambda = 10$m) should have the length of at least few meters for good reception, which was not practical for preliminary measurements.

In order to reduce the influence of reflective near-field environment on power level estimation, a simple calibration was performed. Each antenna unit cell (with dismounted NIC) was fed from the RF signal generator and the signal received by a spectrum analyser was recorded. Then, the RF signal generator was replaced by NIC and receiving signal was recorded again [93]. Using that data and a reflection coefficient (obtained from measured antenna scattering

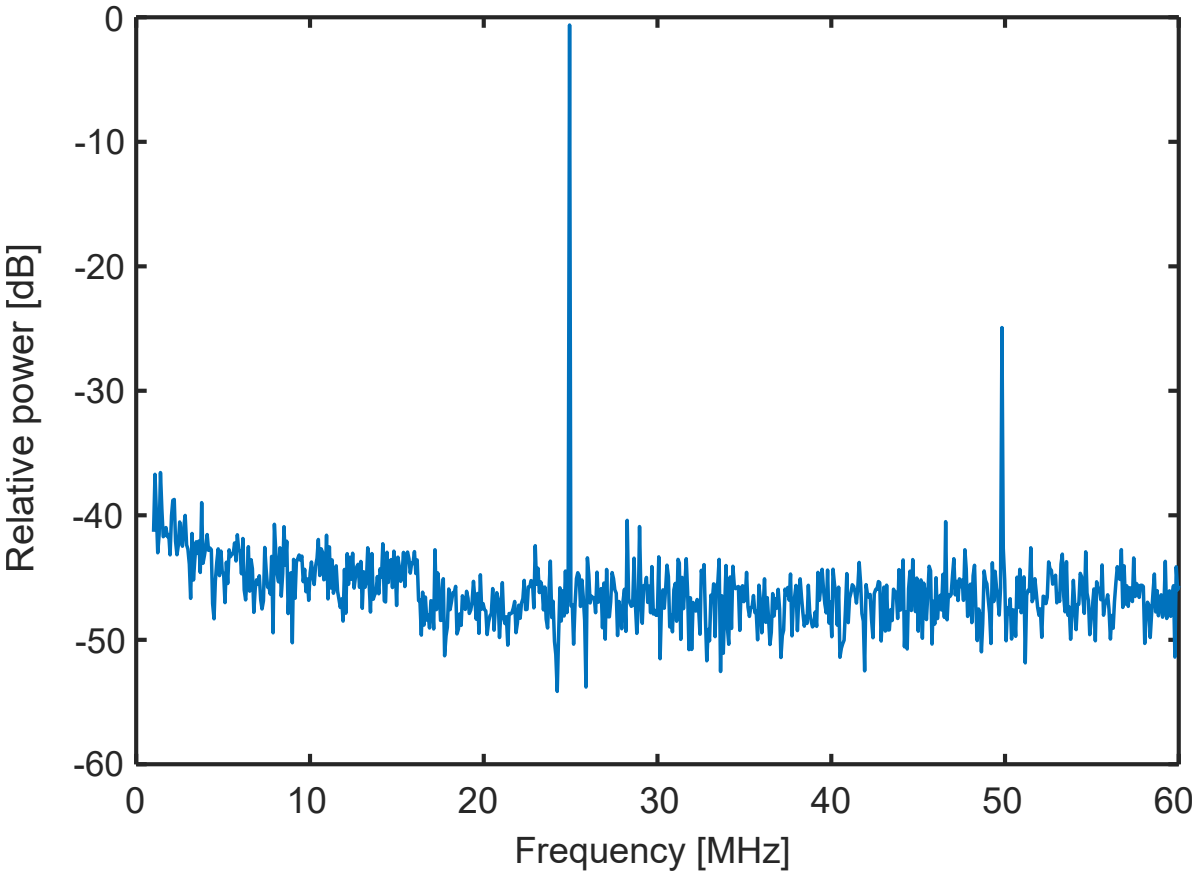

Figure 4.31: Sample of measured spectrum of self-oscillating antenna with crossed dipole radiators. Fundamental frequency set to 24 MHz.

matrix, Fig. 4.19), the output power was calculated. The obtained levels varied from –10 dBm for the unit cell with bow-tie radiators up to –3 dBm for the unit cell with capacitively loaded dipoles. It is consistent with the ADS simulations with imported scattering matrix (simulated maximum was around 0 dBm) [93].

Using active elements with higher DC voltage supply it is certainly possible to construct a NIC that would enable output power in range of +10 dBm to +20 dBm (as shown, for the case of discrete transistors, in [88]). However, the main purpose of this PhD study is a demonstration of proposed basic principles, instead of some specific design.

Furthermore, measured phase noise level was -65 dBc at 10kHz offset from the carrier (Fig. 4.32). This is a rather good result, particularly taking into account that prototyped NIC is based on a commercial OPAMP with a noise figure of 15 dB. Phase noise level was measured for transmitter with capacitively loaded dipole antenna at the lowest operating frequency, which was around 16 MHz [93].

In the next test, tuning range obtained using a single tuning element (a trimmer capacitor) was measured. Achieved results varied from 1:2 (16 to 32 MHz in the case of a unit cell with capacitively loaded dipoles) to 1:3 (14-42 MHz for the unit cell with bow tie radiators). Measured spectrum at several operating frequency for both capacitively loaded dipoles and bow

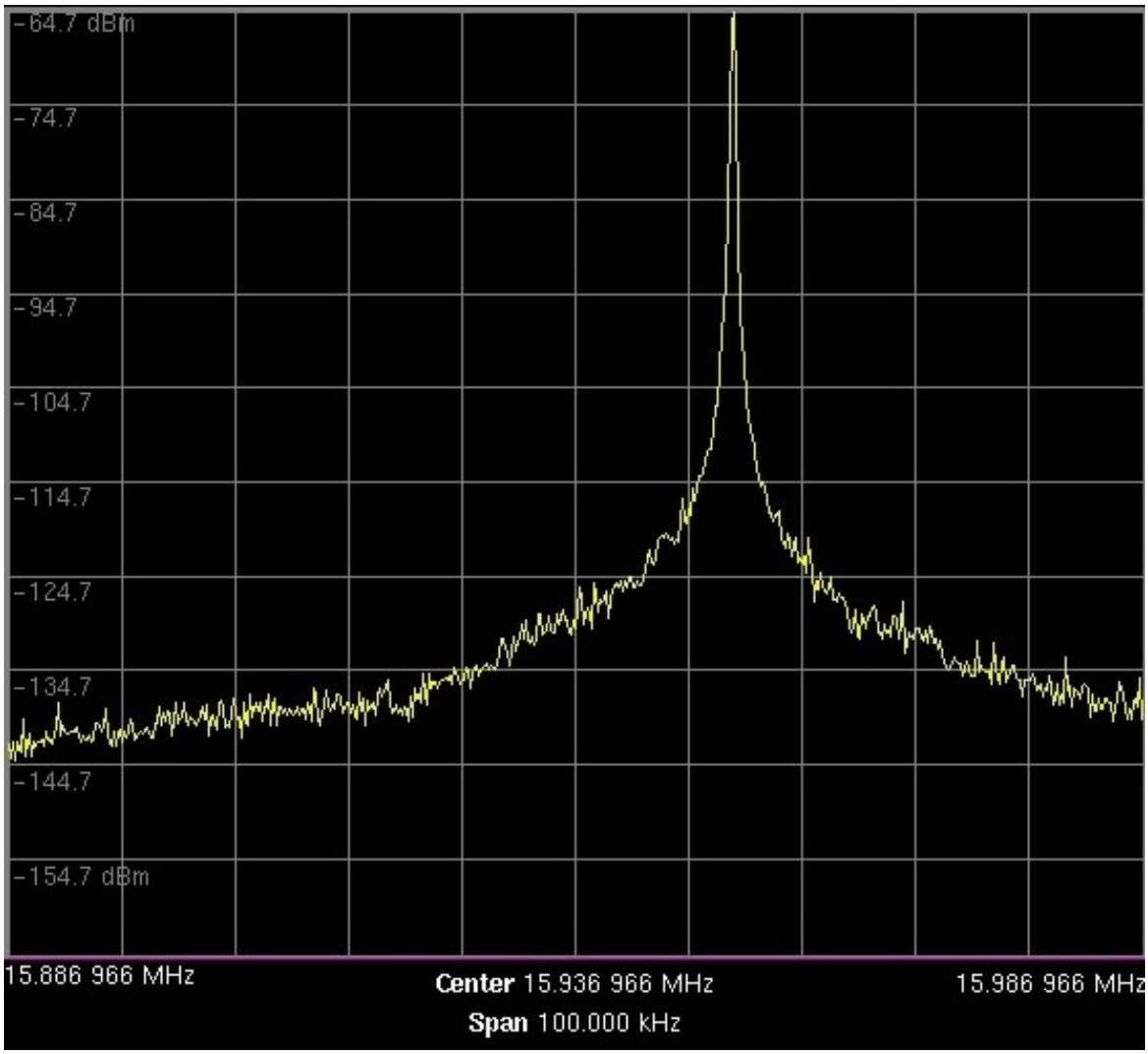

Figure 4.32: Sample of measured spectrum revealing phase noise for self-oscillating antenna (measured with a spectrum analyser). Fundamental frequency set to 15.945 MHz.

tie antennas is shown in Fig. 4.33. Those spectra reveal the information about the tuning range as well as suppression of higher harmonics. All the results are comparable with the simulations which predict a tuning range from 1:2 to 1:3 [93].

Moreover, we attempted to estimate the radiation pattern and radiated power using a combination of experiments, CST full-wave simulations, and ADS circuit-theory simulations. At first, the NIC circuits were dismounted and the full 2x2 scattering matrix of all three pairs of radiators was measured by a network analyser. Extracted $|S_{11}|$ was compared with the results from CST full-wave simulations and a qualitative agreement was satisfactory (dashed versus solid curves in Fig. 4.19) [93].

Observed differences are caused by the fact that measurements were done in a highly reflective environment (a lecture hall). $|S_{21}|$ and $|S_{12}|$ of the pair of antennas varied from -40 dB at 10 MHz up to -20 dB at 40 MHz, which was again similar to the values from simulations. Those results validate an assumption of negligible coupling used in theoretical analysis.

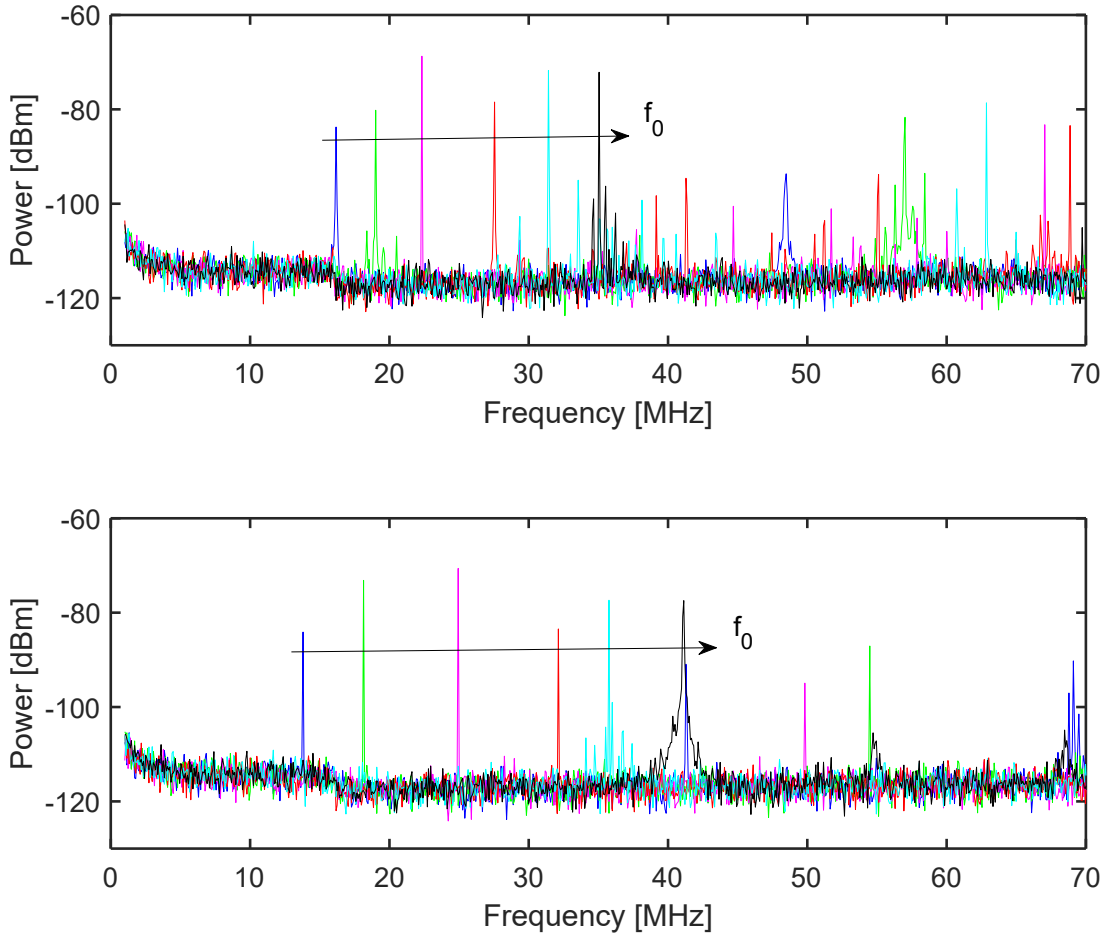

Figure 4.33: Measured spectrum at several operating frequencies for capacitively loaded dipoles (upper graph) and bow-tie antennas (lower graph), revealing measured tuning range.

From all the above results one can conclude that the proposed idea of self-oscillating antenna based on negative immittance conversion is feasible, and therefore, could compete with similar devices in practice.

Chapter 5

Experimental demonstration of self-oscillating antenna with unidirectional radiation pattern

In this chapter, previously analysed self-oscillating antenna based on negative immittance conversion will be implemented using a radiator with unidirectional radiation pattern. For such matter, a so-called Huygens' antenna represents a convenient choice. Part of the research in this chapter was made in collaboration with professor Richard W. Ziolkowski from The University of Technology, Sydney, Australia.

5.1 What is Huygens' source?

Huygens' principle in physics deals with the observation of wave propagation. It states that each point on a wavefront may be considered as a source of new spherical waves expanding from that point forward [114]. The secondary expanding waves can be demonstrated by sending a plane wave toward a barrier with small openings or apertures. If a plane wave approaches a barrier with small apertures, the waves may be seen to expand from the aperture (Fig. 5.1). In that sense, the Huygens' principle allows a visualization of how electromagnetic wave penetrates into the geometric shadow, in a way that could not be explained with a particle theory point of view [114].

Furthermore, the idea of a so-called Huygens' source or Huygens' antenna arises from the Huygens' principle. The main point is to achieve radiation in forward direction from the point of secondary source (antenna aperture) onwards. Huygens' source enables twice as large directivity (4.77 dBi) comparing to the elementary radiators (electric or magnetic dipoles) alone. If two elementary (electric and magnetic) modes are combined in such a way that their magnitudes are equal, with a phase shift of 90°, and with the same polarization, then the Huygens' source is

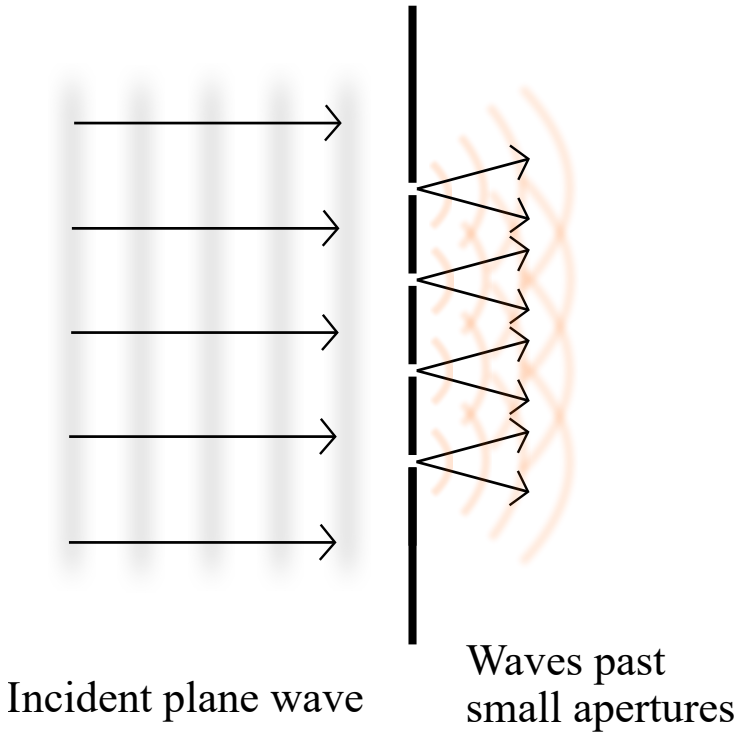

Figure 5.1: Demonstration of Huygens' principle by visualization of wave expansion through small apertures.

created [33]. Consequently, a Huygens' source can be viewed as a coupled pair of electric and magnetic radiating elements.

Let us imagine an antenna comprised of an infinitesimal electric dipole of length dl, and a magnetic dipole (small loop) with cross-sectional area dS. It is easier to analyse this problem in spherical coordinate system with coordinates (r, ϕ, θ), followed by transformation to orthogonal coordinate system (x, y, z), if needed [115]. Since both dipole and loop are electrically small, the currents through dipole and along the loop can be approximated as being constant with magnitude I_0 [116]. Using Maxwell's equations, one finds the value of electric field in the far-field zone that contributes to radiation of the electric dipole [115]:

$$E_\theta = j\frac{\eta I_0}{2}\left(\frac{dl}{\lambda}\right)\sin\theta\frac{e^{-jkr}}{r}, \tag{5.1}$$

and of the small loop, respectively [115]:

$$E_\phi = \eta I_0 \pi\left(\frac{dS}{\lambda^2}\right)\sin\theta\frac{e^{-jkr}}{r}. \tag{5.2}$$

Here, η stands for wave impedance, while λ represents the operating wavelength. From (5.1) and (5.2) it can be concluded that radiation patterns of elemental dipole and loop have the same shape, but their polarizations are orthogonal. Associated angles of directivity are Θ_D=90° and Φ_D=360°, respectively [115]. If one of the elemental radiators is rotated by 90°, polarizations

of dipole and loop will be identical, but superposition of their electric fields in the far field zone will yield cardioid radiation pattern. However, due to a different dependence of generated electric and magnetic fields by dipoles and loops on the frequency, a unidirectional radiation is achieved only across a narrow frequency band [32], usually in the vicinity of the resonance.

An example of realization of a Huygens' source is illustrated in Fig. 5.2. It consists of two elemental radiators, an electric dipole and an orthogonal loop. When combined together in such a way that currents flowing through them are equal in magnitudes but shifted 90° in phase, a cardioid radiation pattern is obtained. Again, such condition can be satisfied only across a limited frequency band.

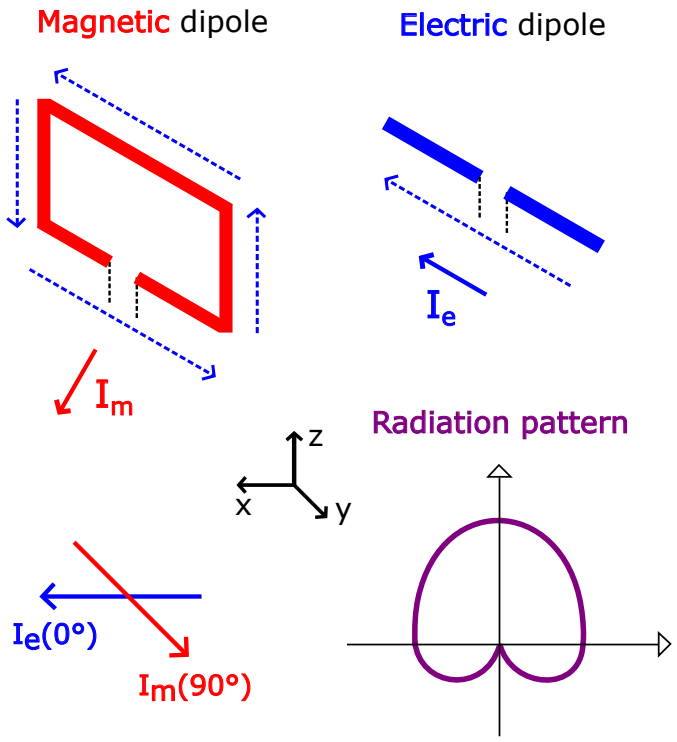

Figure 5.2: Illustration of realization of Huygens' radiator with cardioid radiation pattern, using the combination od elementary electric and magnetic radiator.

Antennas with Huygens' radiation pattern, especially electrically small, have been of the particular interest in the electromagnetic community for the last couple of years [32, 33, 117]. There were even some attempts of construction of low-profile Huygens' sources for applications as wireless energy transfer and IoT, with additional capabilities of circular polarization or pattern configurability [37, 117–119]. Some of the designs are also augmented with internal negative elements to increase the operational bandwidth [9], and near field resonant parasitic (NFRP) elements to increase the antenna efficiency [8].

An electrically small antenna with a higher directivity than what is available from an elemental radiator could be rather appealing and useful for some applications as active metasurfaces. In fact, Huygens' metasurfaces are nowadays engineered even more than Huygens' antennas alone, due to the possibility of controlling the wavefronts of an impinging electro-

magnetic field to an arbitrary distribution [32, 33, 37]. It occurs by induction of electric and magnetic currents along the surface required by the equivalence principle [10]. Briefly, the equivalence principle states that a physical structure can be replaced with equivalent electric and magnetic current densities radiating in free space, as long as sources are retained in the region of interest [120]. For the external equivalence, equivalent current densities yield effective fields in the external region, and null fields within the equivalent surface [120]. Along with that, active Huygens' metasurface also comprise negative elements to increase the bandwidth [121].

In the thesis, we deal with the design of an electrically small planar Huygens' source using the recently introduced near-field resonant parasitic paradigm. The idea is to incorporate an electrically small parasitic structure, essentially one unit cell, into the near field of the radiator. By manipulation of characteristics of parasitic structure, it is possible to achieve effective material properties that lead to matching of the input impedance of the obtained antenna system, without external matching network [9]. Moreover, resulting electrically small resonant antennas ought to have high overall efficiencies [9]. Afterwards, we used our designed Huygens' source as a radiating element connected with a NIC circuit, to obtain a self-oscillating Huygens' source based on negative immittance conversion [122].

5.2 Design of Huygens' antenna

As explained earlier, a Huygens' source comprises of at least a pair of coupled loop and dipole antenna [117]. Unfortunately, such radiating structure does not contain a single feeding port and, as a consequence, cannot be used to realize a self-oscillating system. Namely, envisioned transmitting system, illustrated in Fig. 2.1, comprises two identical antennas which are connected via two pairs of terminals. One of the antennas is connected in the feedback loop of the NIC, while the other one is connected at the NIC input. On the other hand, two basic Huygens' sources would require four different feeding ports in order to ensure proper excitation (90° phase shift between currents through dipoles and loops for each radiator).

Therefore, it was decided to modify a recently introduced miniaturized planar Huygens antenna from [118] to achieve this functionality. The system is comprised of two orthogonal pairs of electric and magnetic near-field parasitic radiators, each of which is driven by a small electric dipole [123]. The input ports of driving dipoles are connected to a floating negative impedance converter. Exploded view of the proposed modified design is shown in Fig. 5.3 [123].

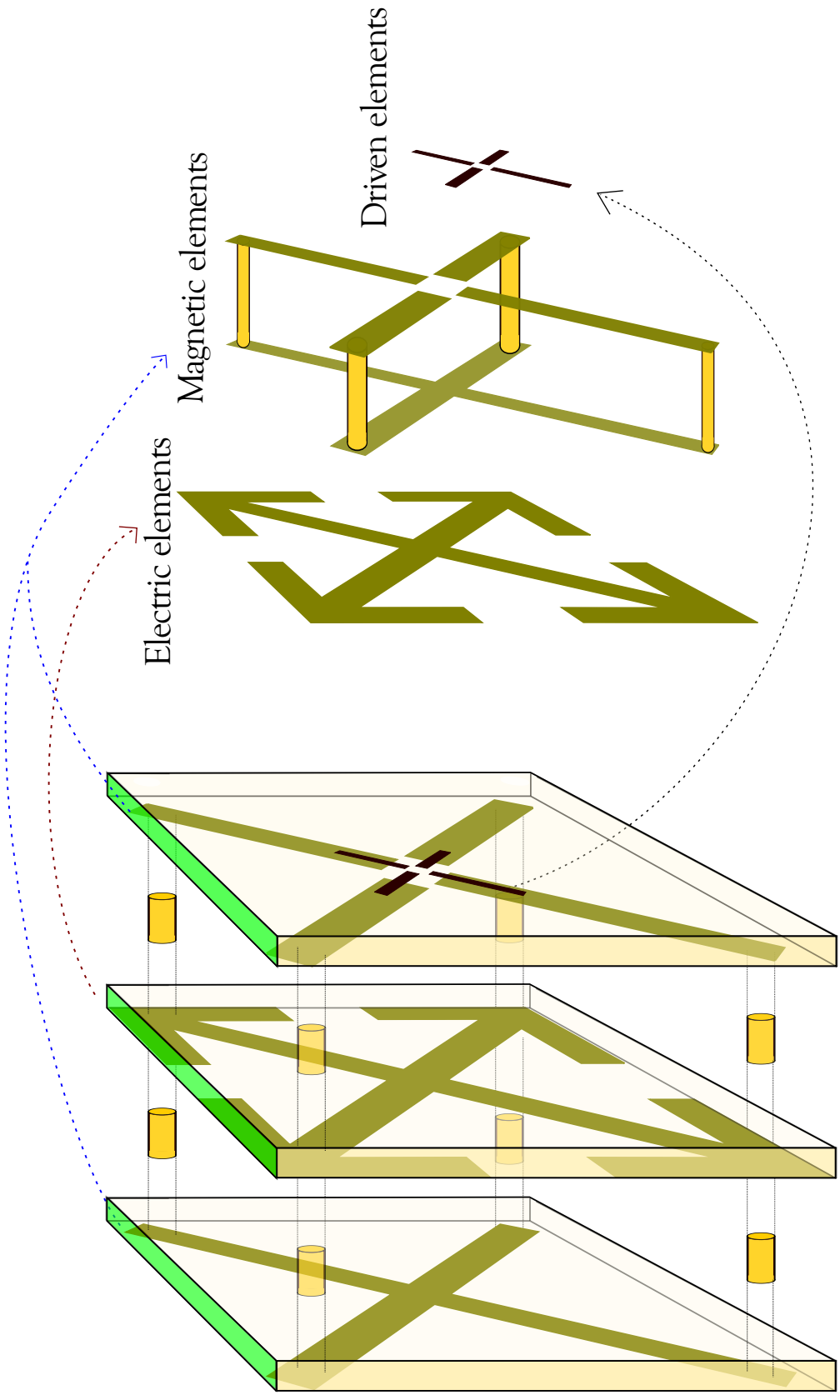

Figure 5.3: Exploded view of a designed planar, low-profile Huygens' antenna with two orthogonal pairs of loops and dipoles. Layer 1 (top): electrically small dipoles; Layer 1 (bottom): upper part of orthogonal loops; Layer 2 (bottom): capacitively loaded dipoles; Layer 3 (bottom): bottom part of orthogonal loops.

On the bottom of the first layer, there are two orthogonal, electrically small dipoles, each equipped with an independent feeding port. These dipoles are electromagnetically coupled to two pairs of near field resonant parasitic (NFRP) elements. The first pair of NFRP elements is comprised of orthogonal, capacitively loaded magnetic dipoles, i.e., rectangular loops. Loops are formed by horizontal conductors lying on Layers 1 and 3, connected by four vertical vias which act as their end conductors. Loops are strongly capacitively coupled to two orthogonal electric dipoles. Electric dipoles are also capacitively loaded which decreases their resonant frequency, and are located on the middle layer (layer 2). From the miniaturization point of view, it would be desirable to use dielectric substrates for all of the layers [118]. Miniaturization though, would be of interest for microwave applications. However, for low frequency prototypes, which are sufficient for testing of the basic principle, it is quite enough to print the antenna elements on simple styrofoam supstrate ($\varepsilon_r = 1$).

5.3 Numerical analysis and measurements

A design based on a pattern from Fig. 5.3 was developed for the 60 MHz RF band using metallic (aluminum) foil over styrofoam layers [123], analogously to the antennas from the previous chapter. The antenna's footprint was 1m x 1m x 0.09m in size ($\frac{\lambda}{5}$x$\frac{\lambda}{5}$x$\frac{\lambda}{50}$). Electrically small dipoles that excited Huygens' radiators were connected to the floating type NIC. Simplified block schematic of the system is the same as shown in Fig. 2.1, with driving dipoles in the place of the first and second antenna. Such excitation is slightly different than the excitation of dipole-like antennas. Electrically small driven elements are not used as loads, but rather for energy transfer. Huygens' sources are resonantly matched by tuning the electromagnetic near-field couplings, and their self-admittances are cancelled by NIC. Utilised Floating NIC is based on two THS4304 operational amplifiers and is equipped with optional diode limiters to prevent very high non-linear operation (4.3).

The electromagnetic (EM) part of the self-oscillating Huygens' radiator was simulated in the CST^{TM} environment. Electric dipoles and magnetic loops were initially simulated separately. They were driven by simple voltage generators and their dimensions were adjusted until the same resonant frequency (66.2 MHz) was achieved. These radiators were then integrated into the proposed configuration (Fig. 5.3) and all of their dimensions, together with distances between the radiators and driven dipoles, were optimized [123]. Radiator dimensions and properties of used materials are given in table 5.1.

The optimized design was calculated and series of relevant numerical results were gathered in the CST^{TM} simulator. For start, calculated surface currents at the resonant frequency (66.2 MHz) are shown in Fig. 5.4. It can be seen that, at the resonant frequency, the currents are approximately equally distributed across capacitively loaded dipoles (middle layer) and both

Design Parameter List			
Material property	**Value**	**Material property**	**Value in S/m**
Relative permittivity of styrofoam (ε_r)	1.1	Conductivity of aluminum (σ_{Al})	$3.5\text{x}10^7$
Parameter Name	**Value in mm**	**Parameter Name**	**Value in mm**
Length of the supstrate side	1000	Length of the loop	866.7
Thickness of layer 1 supstrate	2.5	Width of the loop	62.5
Thickness of layer 2 supstrate	44.64	Thickness of the loop	0.1
Thickness of layer 3 supstrate	44.64	Length of the cap. dipole	1160
Length of the driving dipole	302.8	Width of the dipole	62.5
Width of the driving dipole	8.333	Thickness of the dipole	0.1
Thickness of the driving dipole	0.1	Length of the cap. leg of dipole	291.7
Radius of vias connecting loops	19.4	Width of the cap. leg of dipole	61.1

Table 5.1: List of design parameters from CST^{TM} of developed Huygens' radiator.

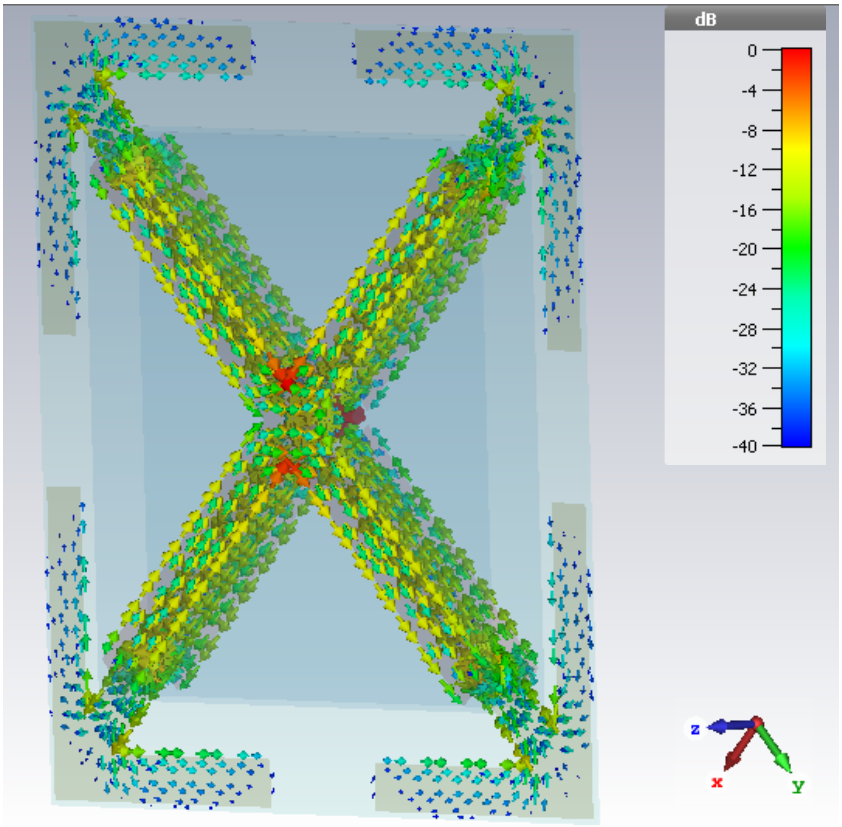

Figure 5.4: Simulated surface currents in CST^{TM} of designed Huygens' radiator.

parts of the loops (layers 1 and 3). Currents somewhat lower in magnitude are distributed across capacitive endings of dipoles. Such distribution indicates that the condition for cardioid pattern is most likely satisfied at the resonant frequency.

After the initial numerical tests, designed Huygens' antenna was constructed using thin aluminum layers over a styrofoam supstrate and the NIC circuit was connected to driving dipoles, which were made of copper. The dimensions are given in the table 5.1 and they match those used in CST^{TM} simulations. Photographs of the each layer of prototyped antenna, as well as the electronic circuit board are shown in Fig. 5.5. Upper left photo displays layer 1 or the bottom sides of the NFRP loops with driving electrically small dipoles. In the upper right photo, front side of the NFRP dipoles on layer 2 is shown. Lower left photo displays upper sides of the NFRP loops on layer 3, while lower right photo provides close-up view of the electronic circuit board and driving dipoles [123].

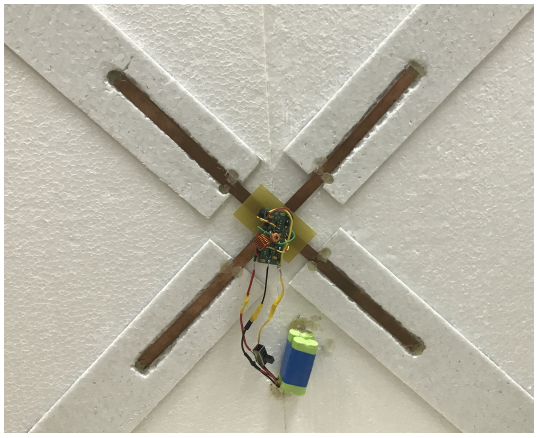

Layer 1

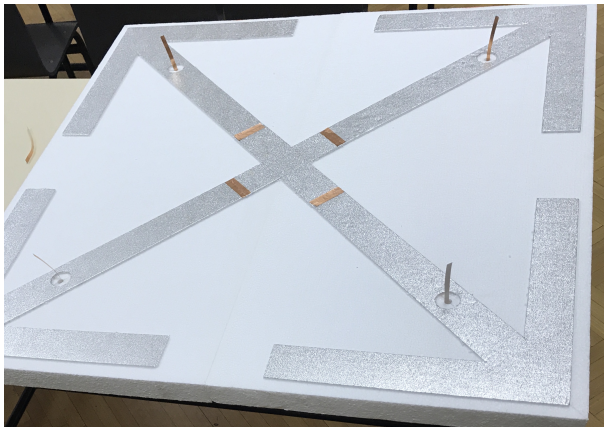

Layer 2

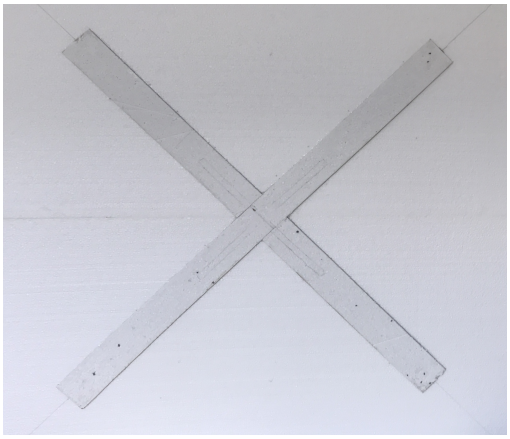

Layer 3

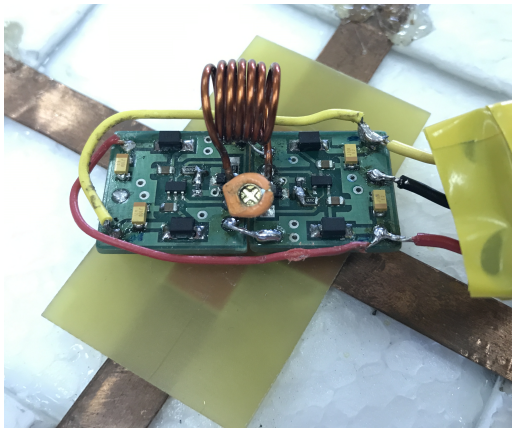

NIC circuit board

Figure 5.5: Photographs of the each layer of the constructed self-oscillating Huygens' radiator prototype. Upper left: bottom part of layer 1; Upper right: layer 2 (capacitively loaded dipoles); Bottom left: top part of layer 3; Bottom right: NIC circuit board connected to electrically small dipoles.

A sample of simulation results for the modulus of S_{11} and S_{22} is compared with the measurement results of the developed prototype and shown in Fig. 5.6. Simulated results are rep-

resented with solid curves, while measurements on the constructed prototype are represented with dashed curves. One can notice that the prototyped antenna is reasonably matched at both ports (return loss of 26 dB and 17 dB, respectively) within a narrow frequency band (1.0 MHz bandwidth, 2.6% fractional bandwidth). However, there are two prominent differences between the measured and simulated results. Resonant frequencies of both antennas are shifted towards slightly higher frequencies (72 and 75 MHz, respectively), and there is an occurrence of resonant notches in the curves of modulus of S_{11} and S_{22} around 40 MHz. Notch depths are 5 dB and 9 dB, respectively. Both of these discrepancies can be attributed to fabrication errors and relatively reflective test chamber.

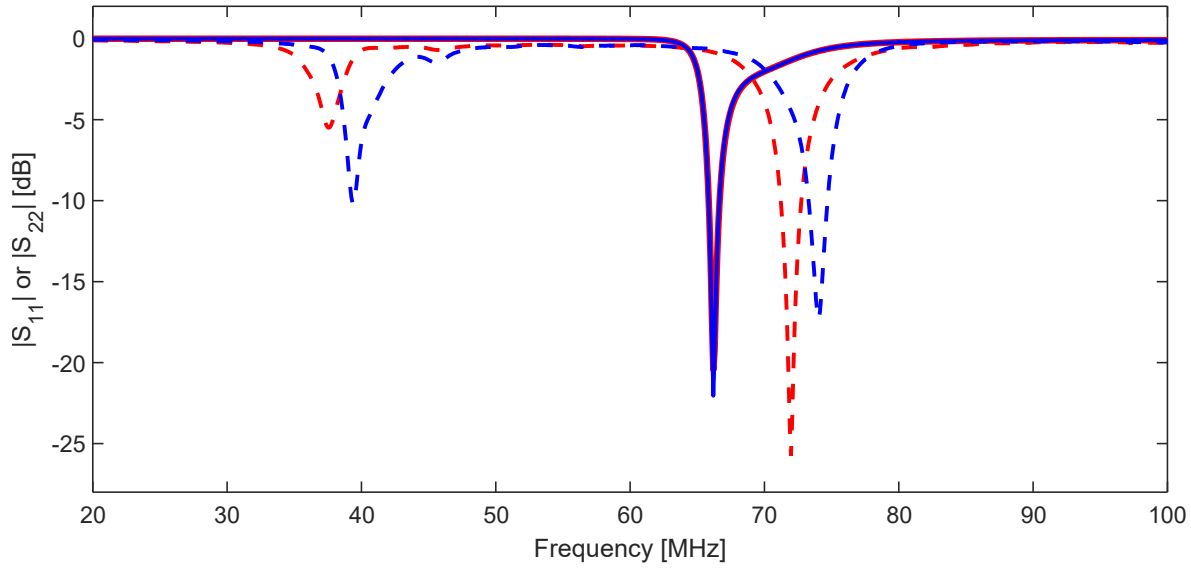

Figure 5.6: Comparison of simulated (solid) and measured (dashed) $|S_{11}|$ (blue) and $|S_{22}|$ (red) of Huygens' radiator.

Furthermore, the results for modulus of S_{12} and S_{21} are also compared with the measurements, and given in Fig. 5.7. The simulation results predict cross coupling between the orthogonal radiators lower than -100 dB. Such a low coupling will contribute to an accurate 'negation' of the antenna's admittance by NIC and ensure stable self-oscillations over a broad tuning range. However, measurement results (dashed curves) display cross coupling of only -10 dB. Again, such a difference between measured and simulated results is caused by non-ideal measurement setup (low frequency measurements demand large anechoic chamber) and unexpected fabrication errors or misalignments. However, the cross coupling of -10 dB is still enough for proper operation of designed system.

The familiar cardioid radiation patterns were obtained in CST^{TM} with a peak broadside directivity of 3.9 dBi. Such value of directivity is somewhat less than the theoretical maximum of 4.77 dBi [117], but it is still noticeably greater than directivity of dipoles or loops. As expected, the frequency bandwidth of the cardioid (unidirectional) pattern is rather narrow. Approximately 15% around the resonant frequency the pattern reminds of a cardioid, whereas

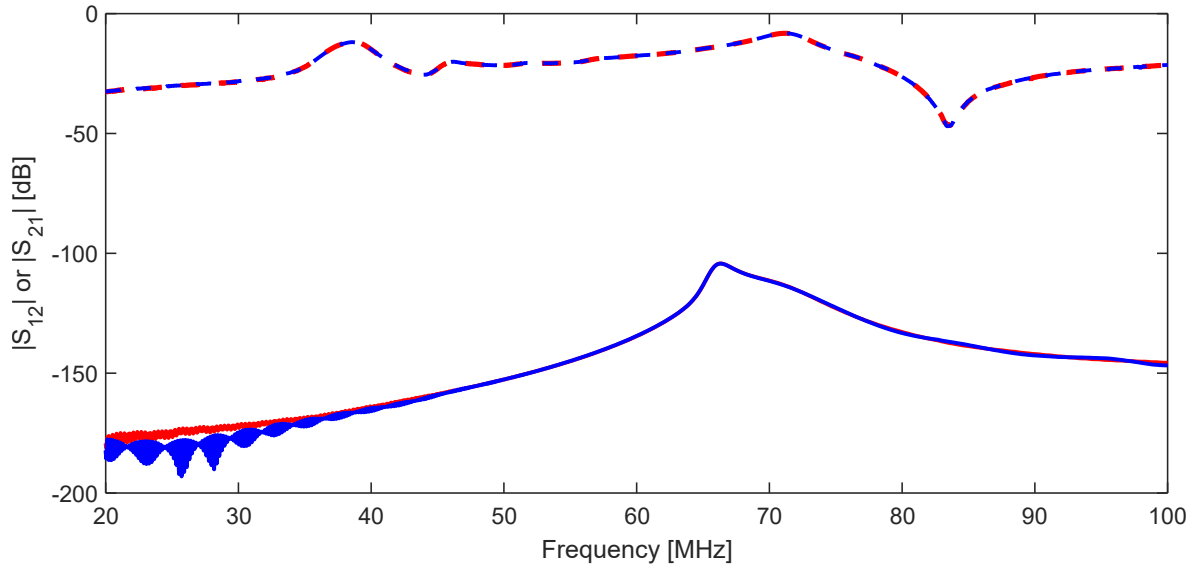

Figure 5.7: Comparison of simulated (solid) and measured (dashed) $|S_{12}|$ (red) and $|S_{21}|$ (blue) of Huygens' radiator. Upper curves: measured cross coupling; Lower curves: simulated cross coupling.

away from that range, pattern is more similar to 'doughnut-like' pattern of dipoles and loops alone. This is related to the necessity of equal magnitudes and 90° phase shift between the excitation currents of loops and dipoles. Due to physical constraints, such condition can be met only at the narrow frequency band [3]. Directivity patterns at three different operating frequencies (resonant frequency or 66.2 MHz, 63 MHz and 60 MHz) are shown in Figs. 5.8, 5.9 and 5.10.

It is important to mention that all of the following directivity patterns are plotted in Θ-plane (electric field plane) for the constant value of Φ, which is 45°. Such angle is chosen due to the orientation of designed antenna in CST^{TM}. Plotted quantity is absolute value of directivity in

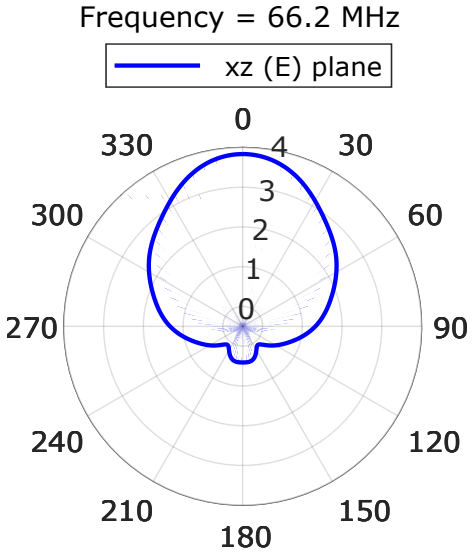

Figure 5.8: Simulated far field directivity pattern of designed Huygens' radiator in CST^{TM} Microwave studio at frequency of 66.2 MHz.

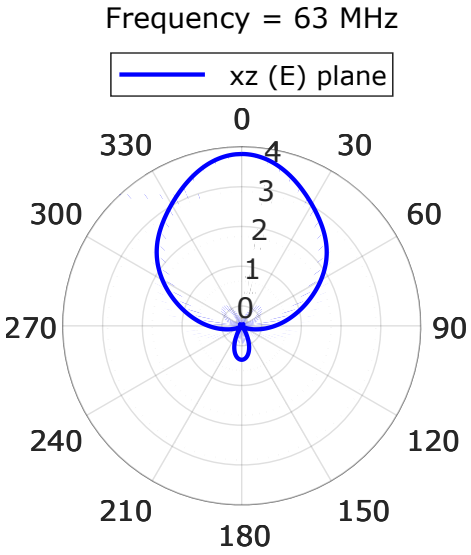

Figure 5.9: Simulated far field directivity pattern of designed Huygens' radiator in CST^{TM} Microwave studio at frequency of 63 MHz.

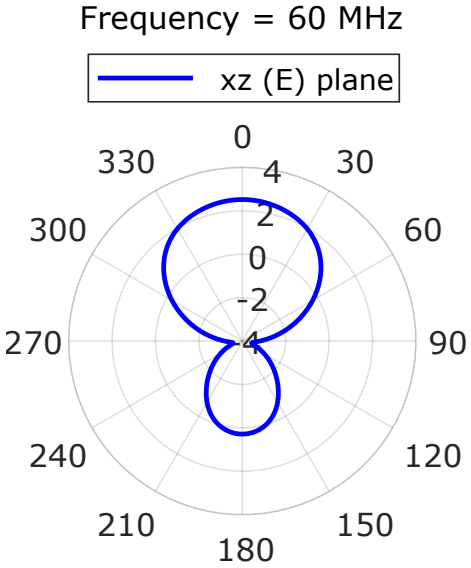

Figure 5.10: Simulated far field directivity pattern of designed Huygens' radiator in CST^{TM} Microwave studio at frequency of 60 MHz.

dBi. Very similar results also occur for frequencies higher than the resonant frequency.

Following series of simulations were made in ADS^{TM} circuit theory simulator. Obtained S-parameter matrix of Huygens' antenna was extracted from CST^{TM} and imported as a *Touchstone file* [124], into S-parameter data block in ADS^{TM}. Data block was connected in the place of loads in the circuit diagram of floating type NIC (Fig. 4.3). Firstly, the system was simulated in transient domain solver for several different parameters of the tuning circuit in order to predict wether oscillations may occur, and at which fundamental frequency. Using Fourier transform it was possible to calculate the signal spectrum, input harmonic admittance, expected radiated power and polarization angle offset. From the obtained results one could extract the information about the simulated tuning range and matching properties [123].

Firstly, in Fig. 5.11, a sample of voltage signal across one of the antennas, and its spectrum, are represented for the central fundamental frequency (46.96 MHz). Obtained frequency is 6.6% shifted downwards from the resonant frequency of the tuning circuit. (C_0=20pF, L_0=500nH, f_0=50.3MHz). Contrary to the case with dipole-like antennas, where grounded NICs with diode limiters were used, magnitude of generated input voltage is as high as 3.1V (maximum for THS4304 OPAMP [108]), thus enabling higher radiated power. In addition, suppression of spurious components is close to 30 dB, which is still a very good result.

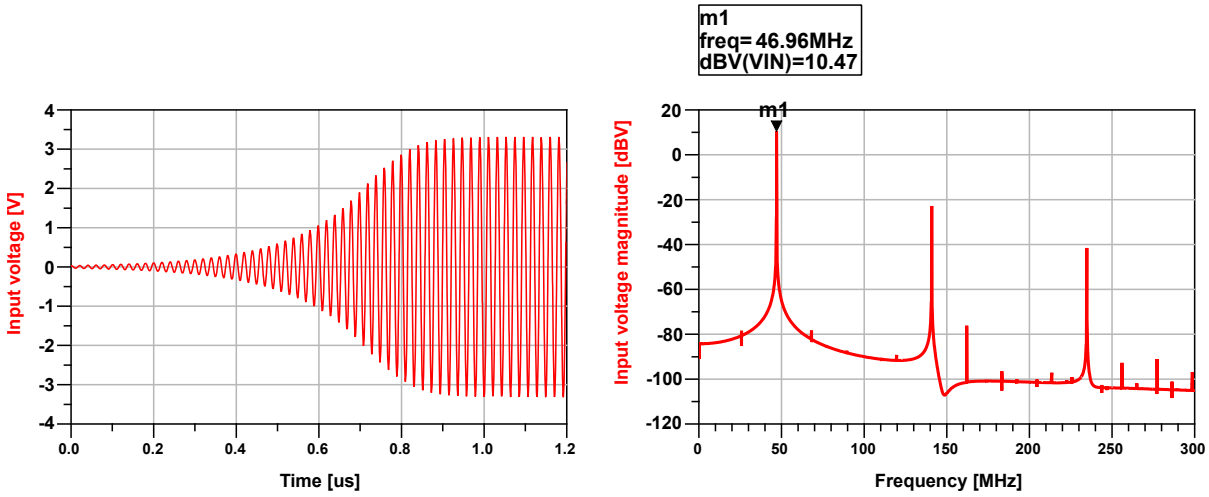

Figure 5.11: A sample of waveform (left graph) and spectrum (right graph) of generated signal of simulated self-oscillating Huygens' radiator.

The results for the conversion ratio of the input conductance and susceptance indicating the NIC conversion error and tuning range are shown in Figs. 5.12, 5.13. Simulated tuning range was around 1:2.3 (28 to 64 MHz). It was found that the NIC conversion errors of the real part of the input admittance are most pronounced at frequencies far below the resonance, where the antenna Q factor is high. The antenna Q factor is lowered in the vicinity of the resonance, which decreases the NIC conversion error. Regarding the imaginary part of the input admittance, conversion ratio is very close to the ideal value of -1 across the whole operating range [123].

However, large conversion error of the input conductance does not disable the occurrence of self-oscillations. The tank circuit corrects the difference between the admittance of active and passive elements, and therefore enables oscillations by shifting the operating point of oscillations. Still, the error does effect the radiated power balance between the two orthogonal Huygens' radiators. Consequently, the polarization angle offset is present. Polarization angle offset was calculated using both circuit theory simulator and EM simulator, in the same way as for the dipole-like antennas in Section 4.3. The antenna was designed and simulated in CST^{TM} and the S-parameter matrix was extracted. Extracted S-matrix of Huygens' antenna was then inserted (as a two-port NIC loading network) in ADS^{TM} model. The Fourier transform was performed for the self-oscillating signal obtained in transient simulation, so magnitudes

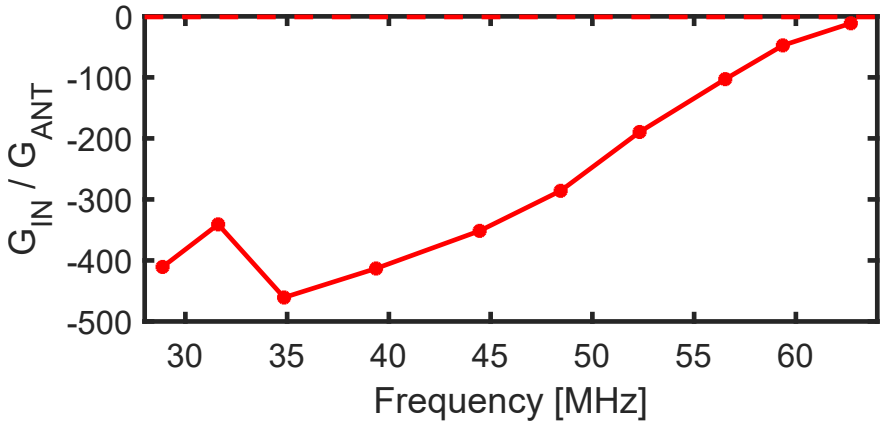

Figure 5.12: Conversion ratio of simulated input conductance of a self-oscillating Huygens' radiator. Dashed: ideal conversion; Solid: simulated conversion.

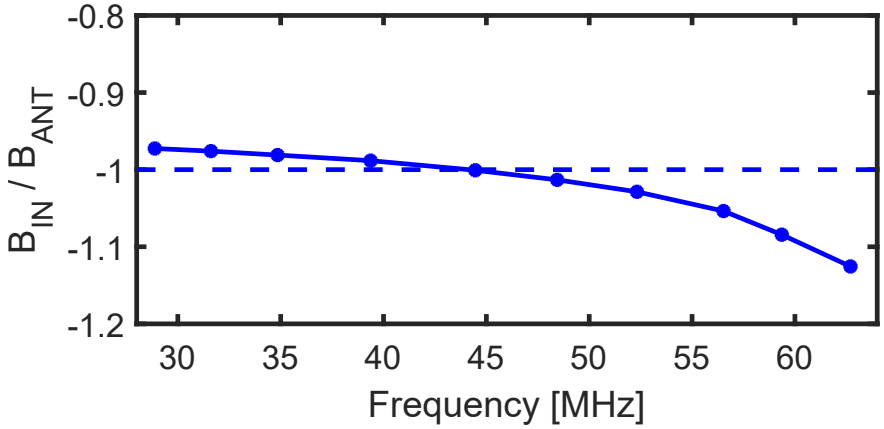

Figure 5.13: Conversion ratio of simulated input susceptance of a self-oscillating Huygens' radiator. Dashed: ideal conversion; Solid: simulated conversion.

($|I_1|$and$|I_2|$) and phases of currents along both of the antennas could be collected. The information about the magnitudes of currents could then be connected with polarization angle offset by a simple equation [123]:

$$\Delta\phi = 45^\circ - \arctan\left(\frac{|I_1|}{|I_2|}\right). \tag{5.3}$$

In an ideal case, polarization is linear with 45° angle, due to the identical influence of both orthogonal radiators. In the realistic case, magnitudes of currents will differ, which results in the angle offset. Simulated antenna power balance as well as calculated polarization angle offset at each operating frequency are presented in Fig. 5.14.

Power difference in decibels is shown with blue curve, while the polarization angle offset (in degrees) is shown with red curve. The maximal imbalance of the power radiated by the HP and VP elements was around 5 dB, while the associated polarization angle imbalance was smaller than 5°. These imperfections are not crucial since they are within arbitrarily set limits (6 dB and 10°, respectively), in which they do not change the total net radiated power significantly.

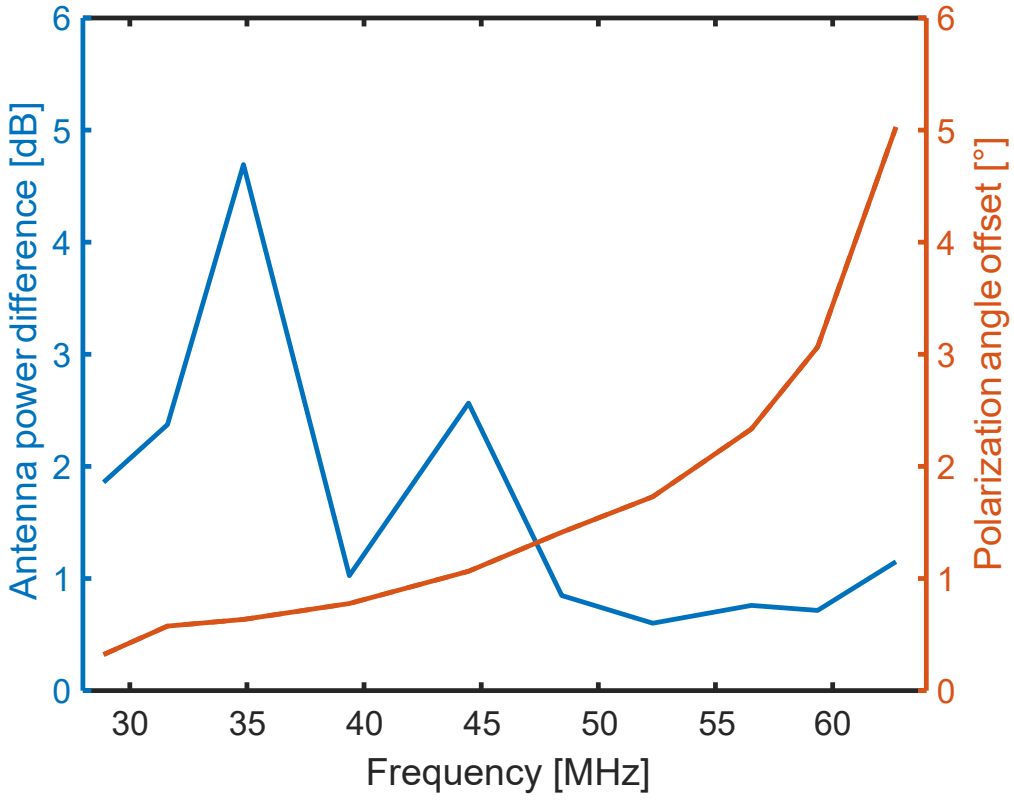

Figure 5.14: Simulated difference between the radiated power of first and second Huygens' radiator (blue solid), and polarization angle offset (red solid).

Finally, the spectrum of generated self-oscillating signal was measured using a spectrum analyser. Self-oscillating Huygens' radiator was placed at the distance of 2m from the receiving antenna and spectrum was obtained at several different operating frequencies (for several different positions of tunable capacitance). Photo of the preliminary measurements setup is shown in Fig. 5.15.

A log-periodic antenna was used for the receiving of radiating signal as it can be seen in the left part of Fig. 5.15. Spectra at lowest and highest operating frequency are shown in Figs. 5.16 and 5.17, respectively.

It can be seen that the measured tuning range is from 29 to 59 MHz or 1:2, which is reasonably close to the simulated one (28 to 64 MHz). However, in that range the received power varies from -75 dBm to -55 dBm. Such power difference may be partly attributed to frequency dependence of the receiving antenna gain. Other part of the problem inevitably relates to the NIC operation and associated NIC conversion error. Concerns of relatively high variation of radiated power will be addressed in the Chapter 6 in more details. The suppression of spurious components is within acceptable limits, varying from 15 to 20 dB. One can notice that measured results are consistent with their simulated values, thus indicating the correctness of the idea.

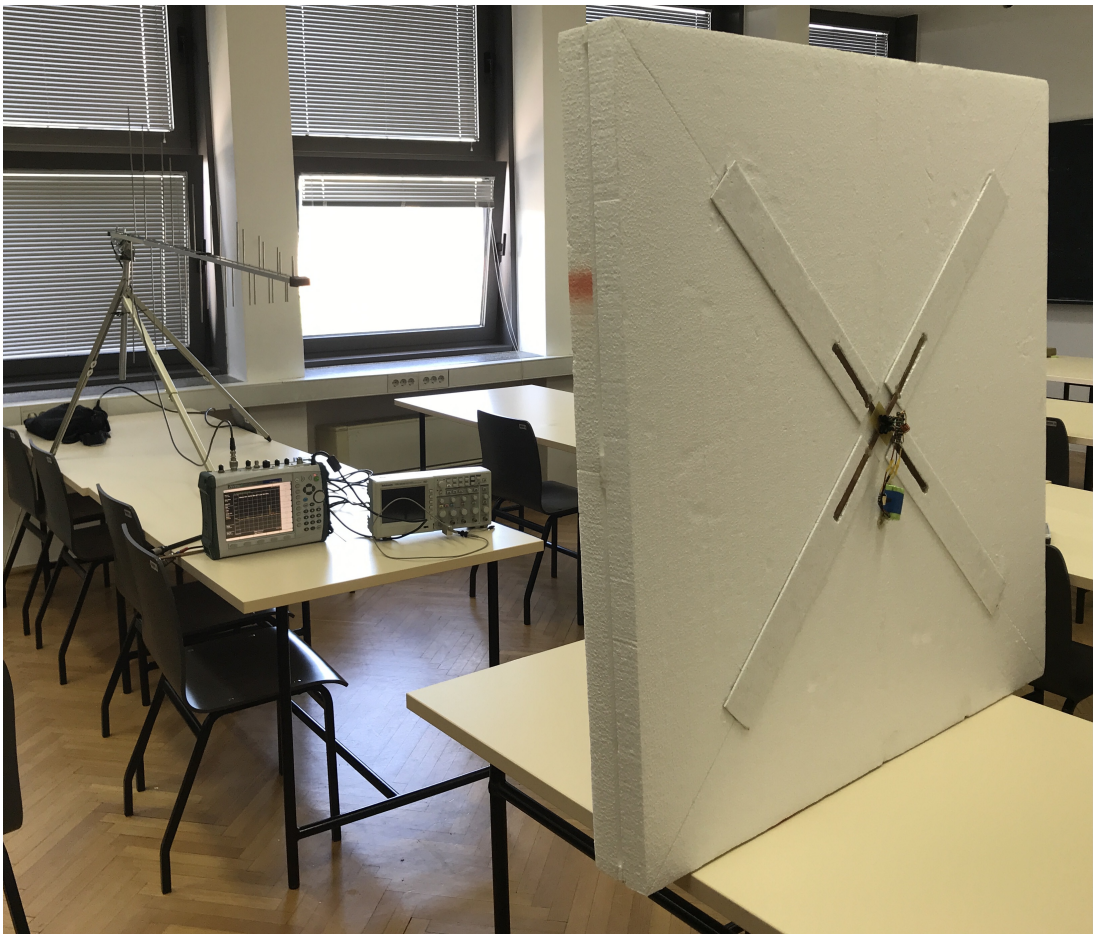

Figure 5.15: Photo of the setup for preliminary measurements of self-oscillating Huygens' antenna.

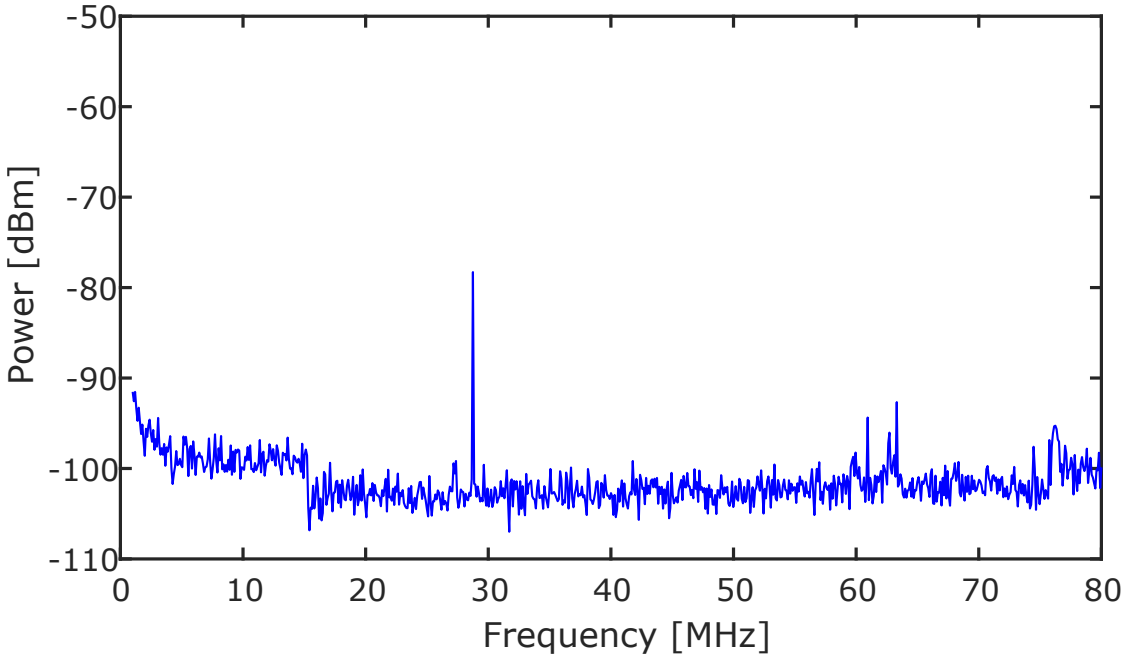

Figure 5.16: Measured spectrum of prototyped self-oscillating Huygens' radiator at lowest operating frequency (29 MHz).

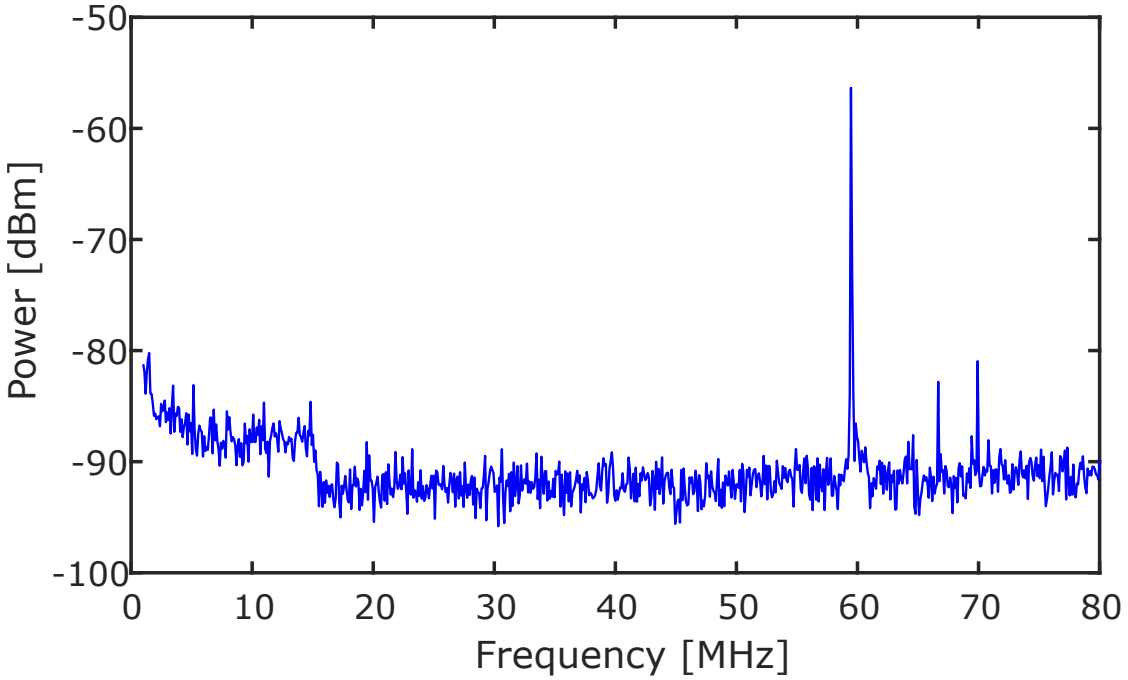

Figure 5.17: Measured spectrum of prototyped self-oscillating Huygens' radiator at highest operating frequency (59 MHz).

5.4 Increasing the tuning range of self-oscillating Huygens' radiator

Even though a developed self-oscillating Huygens' source revealed broadly tunable behaviour (1:2 tuning range) both in simulations and measurements, it is legitimate to wonder why oscillations cease in the vicinity of the resonant frequency of an antenna. The same effect occurs with dipole-like antennas, and any other resonant load. Self-oscillating dipole-like antennas, which were previously analysed in the thesis, operated at frequencies much lower than the antenna resonance in order to ensure the sub-wavelength size of elements. However, in the case of Huygens' radiators, operation around the resonant frequency becomes important because of the unidirectional radiation pattern. As explained previously, due to fundamental physical constraints, it is possible to achieve cardioid radiation pattern with Huygens' source only across a limited frequency band [3]. The necessary condition is to have equal magnitudes, and 90° phase shift between the currents across electric and magnetic radiating elements. In our design, such condition is met at approximately 15% relative bandwidth around the antenna resonance (61 to 71 MHz). Therefore, it would be preferred to ensure oscillatory behaviour in that range.

Careful investigation revealed that the problem lies in dispersive behaviour of NIC and its dependence on the quality factor of the load to be negated. For a better explanation, conversion ratios of real and imaginary parts of NIC input admittance are plotted in Fig. 5.18, for frequencies around the resonance of designed Huygens' antenna (around 66.2 MHz). Conversion of conductance is represented with red curve, and conversion of susceptance with blue curve.

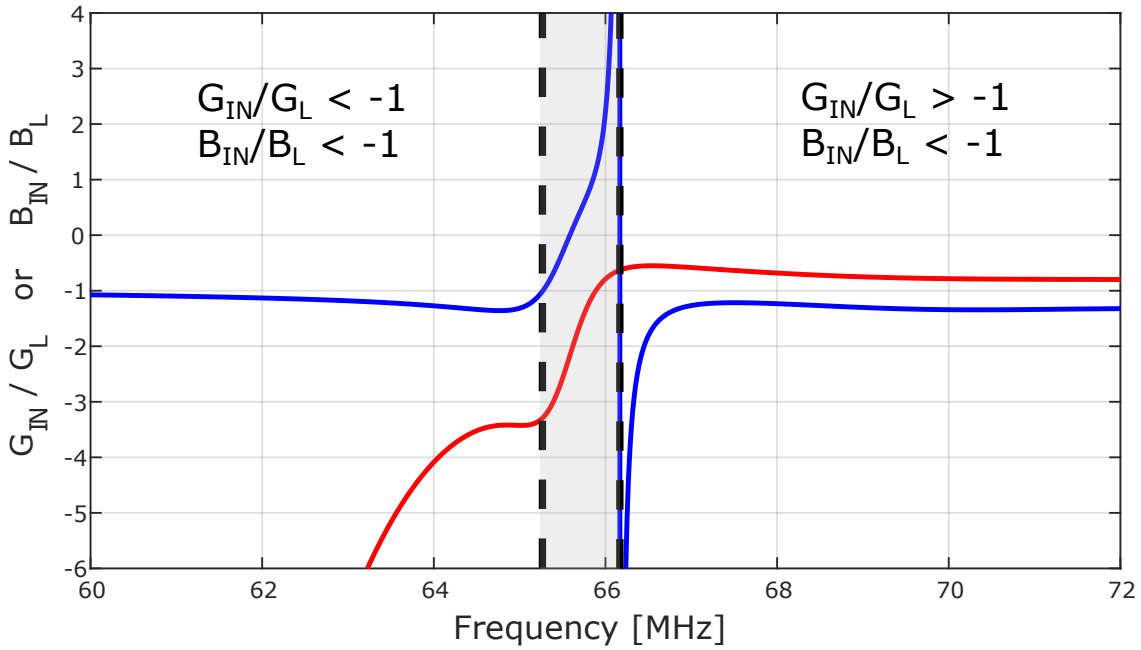

Figure 5.18: Conversion ratios of real (red) and imaginary (blue) parts of NIC input admittance with Huygens' antenna as load, around the antenna resonance (f_{RES}=66.2 MHz).

NIC is again based on a THS4304 OPAMP, while the load in the positive feedback loop is modelled with S-matrix of Huygens' radiator extracted from CST^{TM}. It can be seen that below 65.5 MHz conversion ratios of both real and imaginary parts of the admittance have values smaller than -1. In the region between 65.5 MHz and 66.2 MHz (shaded with grey colour) the conversion ratio of imaginary part diverges. Ratio of conductance shows more gentle variation but it approaches positive values. Finally, at frequencies above resonance, ratio of conductance becomes greater than -1, while ratio of susceptance contains values less than -1.

In order to meet the oscillating condition, a negated admittance of the active element has to be equal to the admittance of the passive element. That means that the value of admittance conversion ratio should be exactly -1 at the operating frequency. However, due to the large conversion error of input conductance two effects occur. Frequency is shifted away from the resonance of the tank circuit, and, consequently the magnitude of generated self-oscillating signal rises (amplifier enters non-linear regime). The shift of frequency causes the change of susceptance of the active element. The effect of non-linearity on harmonic NIC input admittance was discussed in Chapters 3 and 4, and it was concluded that it affects both conductance and susceptance in the same manner. It results in shifting input admittance toward positive values. From there, it can be concluded that self-oscillations would require values of conversion ratios at least more negative than -1, before the occurence of non-linearity. Such conclusion is in accordance with the results from section 5.3, and from Fig. 5.18.

To overcome the above challenge, two modifications are proposed. The first modification involves a capacitance connected in series with both of Huygens' antennas. Series capacitance

shifts the antenna resonance toward higher frequencies, and therefore allows us to avoid grey region from Fig. 5.18. The second modification consists in increasing the NIC conversion ratio by changing the amplifier gain. This is done by increasing the values of resistors R_2 and R_4 in the floating NIC configuration (Fig. 3.2). In order to maintain the symmetry, values of resistors R_2 and R_4, as well as R_1 and R_3 should remain identical. For the specific case of self-oscillating Huygens' radiator we simulated a series connection of 3.3pF capacitance with the antenna, and changed the values of resistors R_2 and R_4 to 300Ω, while resistors R_1 and R_3 were 250Ω. Such values cause the change of conversion ratio to -1.2. Newly obtained conductance and susceptance ratios are shown in Fig. 5.19. Conductance ratio is represented with red curve, and susceptance ratio with blue curve.

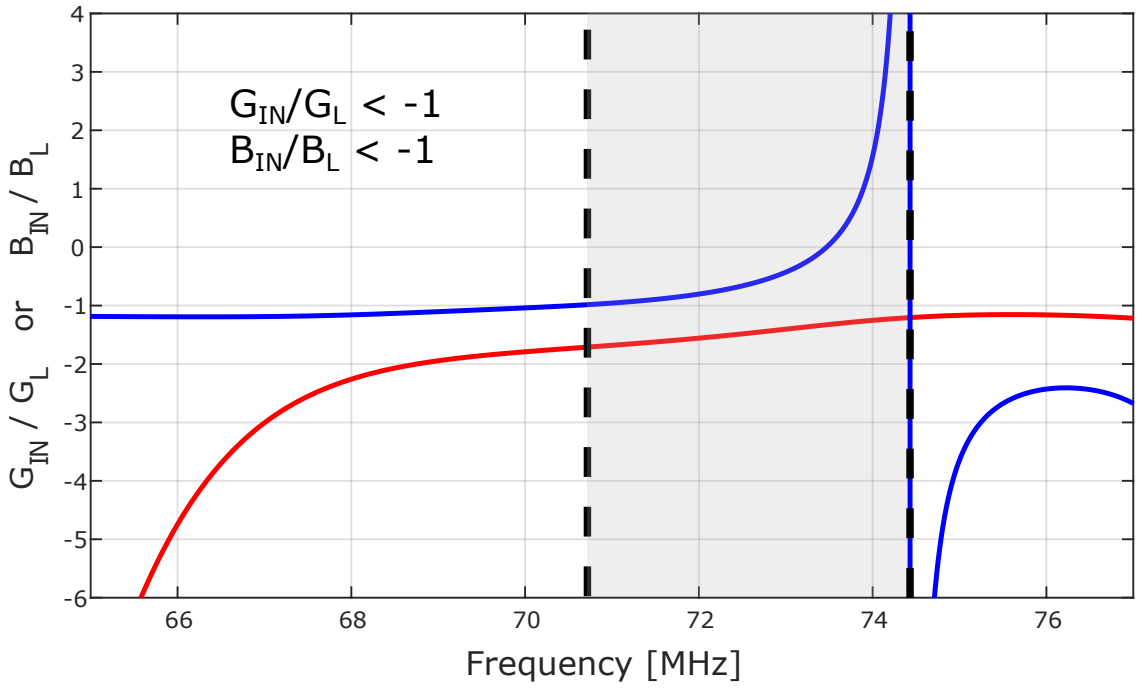

Figure 5.19: Influence of series capacitance and modified NIC gain on the admittance conversion of Huygens' antenna. Red solid: conductance conversion ratio; Blue solid: susceptance conversion ratio.

It is evident that the antenna resonance is successfully shifted toward higher frequencies. Also, by changing resistors in the feedback loop of floating NIC, the values of conversion ratios of real and imaginary parts were maintained below -1, up to the frequency 70.5 MHz. However, grey area ($\frac{B_{IN}}{B_L} > -1$) has now become broader, which limits the oscillations at higher frequencies. For our purpose, it is desirable to enable self-oscillations up to frequency 71 MHz, so characteristics at higher frequencies do not represent a concern. In order to test the performance of modified self-oscillating Huygens' source, a time domain simulation in ADS^{TM} was performed. Waveform of generated self-oscillating signal as well as signal spectrum are shown in Fig. 5.20.

It can be seen that frequency of the signal was successfully set to the Huygens' antenna resonance. Some time is needed for the amplitude of self-oscillating signal to stabilize (300

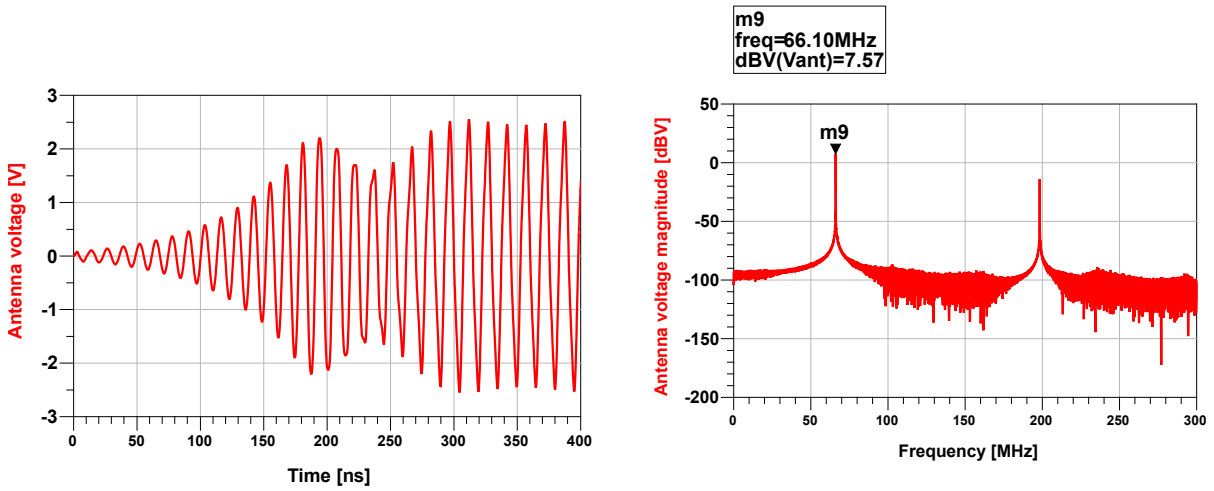

Figure 5.20: Waveform (left graph) and spectrum (right graph) of generated signal of self-oscillating Huygens' radiator, near the antenna resonance (f_0=66.1 MHz).

ns), after which the waveform reaches steady state. Suppression of spurious components is 20 dB. By tuning the resonant LC circuit, changing the values of series capacitance, as well as feedback resistances, it should be possible to obtain the tuning range from 28 to 71 MHz (1:2.54). Most importantly, it is possible to cover the whole frequency band in which cardioid pattern is generated.

Chapter 6

Matching properties and possible applications of self-oscillating antenna based on negative immittance conversion

So far, a proposed device has shown great potential as being a standalone oscillator that feeds an antenna, enabling radiation of generated electromagnetic energy. Thus, it can be considered as a special kind of broadly tunable active antenna, which can operate without additional antennas or sources. Measured tuning range varied from 1:2 to 1:3, depending on the antenna type. Such results certainly indicate that the envisioned system is frequency agile.

On the other hand, some transmitting properties as relative bandwidth, antenna efficiency (η_{RAD}), and total radiation efficiency (ratio of the radiated power to the power incident from the network) of self-oscillating antenna have not yet been thoroughly investigated. In this chapter, those problems are discussed, some of the possible solutions are proposed and briefly validated by numerical analysis.

Moreover, in real-world applications, a self-oscillating antenna would have limited utility as an individual integrated system radiating just a CW electromagnetic wave. Therefore, it is also important to investigate means of connection of the proposed device with other parts of the communication system, and ways to modulate the self-oscillating signal for transmission of the useful information.

6.1 Radiated power and matching properties

When it comes to the evaluation of a radiating device, one can introduce a wide variety of criteria, depending on the application. Usually, the most important parameters are bandwidth (absolute or relative), return loss, radiation pattern, directivity, polarization and antenna efficiency. Most of the parameters can be well manipulated by a careful design and choice of

materials. However, due to physical limitations, there is always a certain trade-off.

We have already analysed the return loss, radiation pattern, directivity and polarization of our antenna designs. Here, more will be said about the relative bandwidth, antenna efficiency and radiated power.

All of the antenna designs presented in this thesis had the same footprint. They were fitted into a square of dimensions 1m x 1m. Because of the need of an orthogonally crossed pair of radiators, antennas were arranged across the diagonal of a square. It means that the antenna length was l=$\sqrt{2}$m, and accordingly, parameter a (smallest radius of a sphere containing the whole antenna) was $\frac{\sqrt{2}}{2}$m.

Knowing the parameter a, one can calculate the theoretically minimal quality factor (Q) of an antenna using the equation (1.5). Frequency dependence of minimal achievable Q for designed antennas with a=$\frac{\sqrt{2}}{2}$m is shown in Fig. 6.1.

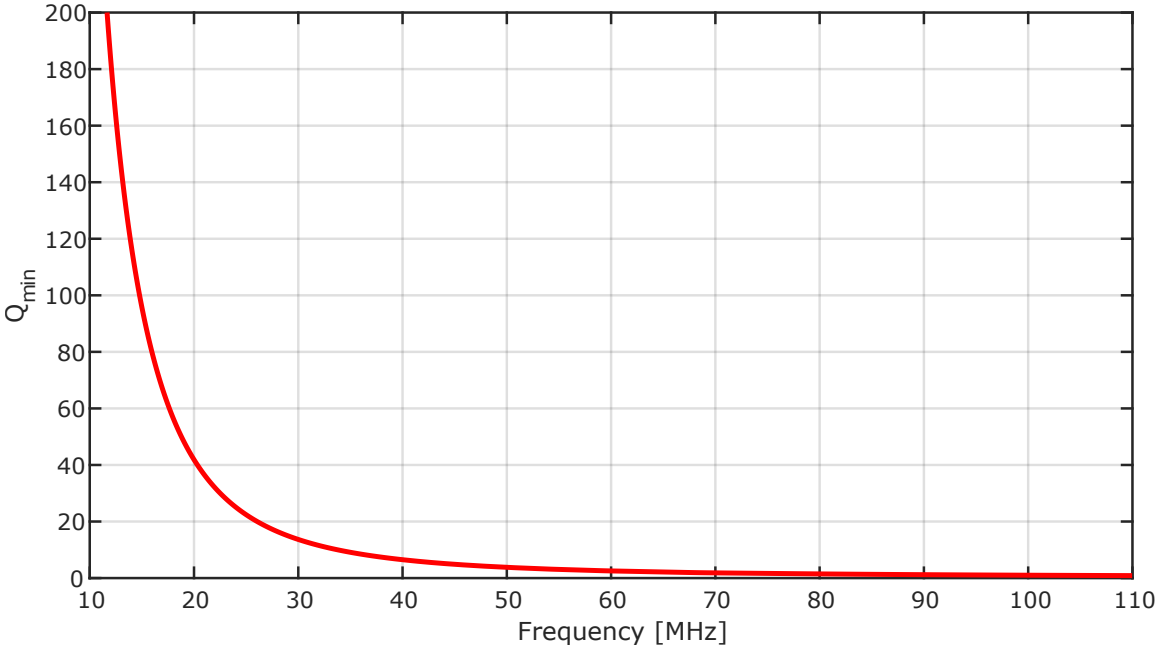

Figure 6.1: Theoretically minimal quality factor of an antenna with associated radius of a radiating sphere a =0.707m.

Frequency range of interest is from 10 to 110 MHz, where all of the antenna resonances and tuning ranges of self-oscillating systems are contained. For the evaluation of developed antennas regarding quality factor, we calculated Q at the resonant frequency of each antenna, using simulation results from CST^{TM}, and compared them with theoretically minimal ones. Instead of using (1.4), which is often complicated, one can estimate Q at the central frequency (f_0) using frequency points at which the maximal return loss decreases by 3dB (f_{high} and f_{low}) [12]:

$$Q = \frac{f_0}{f_{high} - f_{low}}. \tag{6.1}$$

The denominator is also known as the absolute bandwidth (B_{3dB}=$f_{high} - f_{low}$). An illustration of determining antenna bandwidth and quality factor, using associated 3dB points of the $|S_{11}|$ curve, is shown in Fig. 6.2 From the estimated quality factor, it is easy to calculate the relative bandwidth using (1.7). Calculated values of Q factor and relative bandwidth for all the antennas designed in this thesis are presented in Table 6.1.

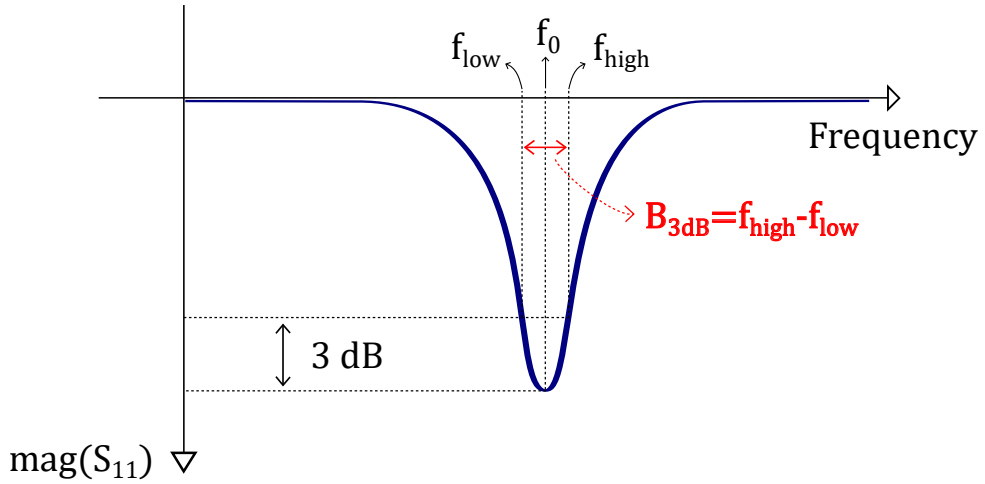

Figure 6.2: An example of magnitude of S_{11} of an antenna with associated 3 dB points.

Q & relative bandwidth			
Antenna	Resonant frequency	Quality factor (Q)	Relative bandwidth
Dipoles	108.11 MHz	18.7	5.35%
Cap. loaded dipoles	66.27 MHz	17.8	5.61%
Bow-tie	75.07 MHz	6.8	14.6%
Huygens' source	66.13 MHz	423.9	0.24%

Table 6.1: Quality factors and relative bandwidths of designed antennas, estimated from simulated $|S_{11}|$ curves.

Firstly, it can be seen that capacitively loaded dipole, bow-tie and Huygens' radiator brought significant improvement regarding the antenna miniaturization. The antenna resonance was successfully shifted down to 40% lower frequencies (miniaturization down to 60% of the original size). The lowest quality factor was achieved with a bow-tie antenna (Q=6.8), giving the relative bandwidth of 14.6%. This indicates that the best potential for possible modulating applications offers a bow-tie antenna. Theoretically minimal values of Q though, varied between 0.9 and 2, for all of the given antennas (Fig. 6.1). The best miniaturization was achieved with a Huygens' source (f_0=66.13MHz), which besides that is the only one that supports unidirectional radiation. However, due to its very resonant nature (caused by the near-field resonant parasitic paradigm), its simulated quality factor reaches the value of 423.9, thus giving the relative bandwidth of

only 0.24%.

On the other hand, one should bear in mind that in the proposed self-oscillating system, effective quality factor is mostly determined by the quality factor of the tank circuit. Another point is that the antenna is not used only at the central frequency, but also across the wide frequency range where it can be considered electrically small. Therefore, the abovementioned deficiencies could be aided by the use of active elements.

The following antenna characteristic of interest is the efficiency. Basically, efficiency can be defined as a ratio between the radiated and total accepted power by the antenna, as derived in (1.2) [3]. Antenna efficiency is dependent on the used material, and it varies with the operating frequency. There can be two types of losses in the antenna that affect the efficiency, conduction losses and dielectric losses (if a dielectric is present). Electrically small antennas usually have relatively low efficiency due to the high surface current density associated with predominantly reactive behaviour.

As an example, efficiency of designed Huygens' antenna regarding to frequency is plotted in Fig. 6.3. Antenna was simulated in the full-wave EM simulator (CST^{TM}), and corresponding powers were monitored at multiple frequencies within the achievable tuning range. Then, the efficiency was calculated using (1.2) at every frequency point, and the graph was fitted with the basic fitting option (shape-preserving interpolant) in $MATLAB^{TM}$.

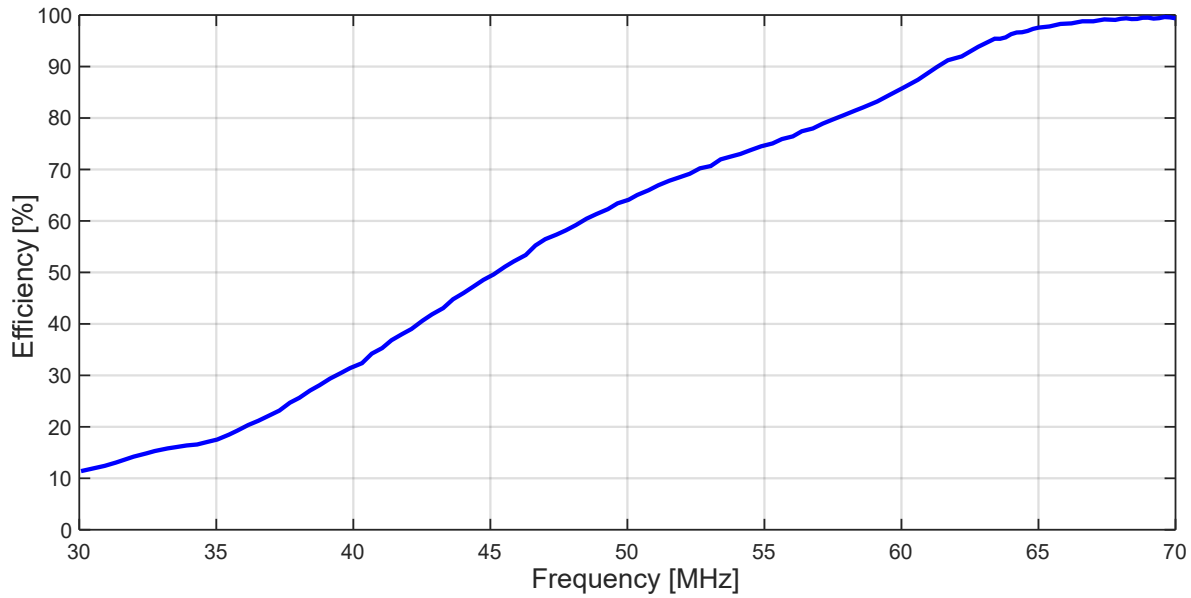

Figure 6.3: Simulated radiation efficiency with regards to frequency for designed Huygens' antenna.

It can be seen that for frequencies below 45 MHz, efficiency is rather low (below 50%). However, in the region between 60 and 70 MHz (where cardioid radiation pattern is generated), efficiency varies between 85% and 99%, which is a very promising result for a miniaturized, low-profile antenna. The reason for increased efficiency lies in the use of NFRP elements [8].

The last figure of merit in this section deals with the active power (power accepted by the

antennas) of the whole self-oscillating transmitting system. Frequency distribution of active power indicates the effectiveness of the matching network.

Let us assume that transmitting system consists of an RF source with voltage amplitude V_G, internal impedance Z_G, which is connected to a load Z_L via transmission line of length l and characteristic impedance Z_0 (upper part of Fig. 1.3). There are a few different matching concepts known in the microwave engineering community, load matched to the line, generator matched to loaded line, and conjugate matching [2]. In the case where $Z_L = Z_0$ (load matched to transmission line), reflection coefficient of the load (Γ_L) will be zero, and power delivered to the load is [2]:

$$P_L = \frac{1}{2}|V_G|^2 \frac{Z_0}{(Z_0 + R_G)^2 + {X_G}^2}. \tag{6.2}$$

Second type of matching is probably most commonly used, and it ensures maximum power transfer from the source to the load [2]. It occurs when the input impedance of the transmission line is $Z_{IN} = {Z_G}^*$. This condition is also known as conjugate matching [2]. In this case, power at the load will be [2]:

$$P_L = \frac{1}{2}|V_G|^2 \frac{1}{4R_G}. \tag{6.3}$$

There still may be reflections at the transmission line because reflection coefficients (Γ_L, Γ_{IN}, Γ_G) may not be zero. Physically, this means that in some cases the power in the multiple reflections on a mismatched line may add in phase to deliver more power to the load than it would be delivered in the case with no reflections on the line [2]. Moreover, conjugate matching is not the most efficient one. 50% of the power produced by the generator is inevitably lost in Z_G. In general, power efficiency can only be improved by making Z_G as small as possible. Nevertheless, conjugate matching is the most common one, due to greater importance of maximum power transfer comparing to power efficiency in the majority of transmitting systems [2].

Finally, there is a configuration where the generator is matched to loaded line (source-load matching). It means that from some point at the transmission line (l') toward the load, overall reflection coefficient (regarding to the generator) will be zero [2]:

$$\Gamma = \frac{{Z_{IN}}' - Z_G}{{Z_{IN}}' + Z_G} = 0. \tag{6.4}$$

This type of matching ensures that there will be no reflected wave back to the generator. However, there still may be standing wave on the line since Γ_L may not be zero. Active power at the load is then [2]:

$$P_L = \frac{1}{2}|V_G|^2 \frac{R_G}{4({R_G}^2 + {X_G}^2)}. \tag{6.5}$$

Even though the line is matched to the generator, power delivered to the load may not be maximal as in the case of conjugate matching [2]. The only way to achieve maximum power transfer with source-load matching is to ensure $Z_G = Z_{IN} = Z_0$ (which is most often equal to 50Ω).

Type of matching inherently present in our self-oscillating antenna from Fig. 2.1, is source-load matching. Analysis is simplified at low frequencies (up to 100 MHz) due to negligible influence of transmission lines (wires connecting NIC with the antennas), so matching properties can be examined from the circuit theory point of view. Theoretically, admittance cancellation can occur at any frequency due to connection of two identical antennas, positive antenna and its negated image. The equivalent circuit can then be comprised of a voltage (or current) source, and two identical impedances or admittances (Fig. 2.2). The biggest advantage of such configuration comparing to existing transmitting systems is that both of those two impedances (admittances) are useful loads (antennas). Consequently, no power is lost on the internal impedance (Z_G), but rather radiated into free space. In an ideal case, power efficiency of such system is maximal (100%).

On the other hand, the proposed device does not necessarily ensure maximum power transfer at any frequency. Voltage (current) amplitude of generated self-oscillating signal will depend on the total impedance (admittance) in the circuit, and on the available voltage swing of the active element. For instance, low-impedance antennas could influence generation of self-oscillating signal with higher amplitudes of current, and therefore higher available power. As the operating frequency changes, the antenna impedance changes, which causes variable amplitude of self-oscillating signal, as well as the available power. An example of power distribution with frequency is shown in Fig. 6.4.

The graph displays simulated active power (power accepted at the antennas) for a designed self-oscillating Huygens' radiator, based on THS4304 OPAMP. Solid black curve represents actual active power generated at the antennas, while dashed black curve represents active power in the case with no mismatch between the antennas (no difference between the active powers at the antennas). Active powers at the antennas are the same when there is no NIC conversion error (the case with dispersion-less NIC).

It can be seen that power difference at two different frequencies can be as high as 40 dB. Power efficiency though, should be high because none of the available power is lost on the internal impedance. However, high variations in the impedance of the antenna cause high variations in the available power. The same effect can be noticed observing the measured spectra of prototyped self-oscillating Huygens' radiator at lowest and highest operating frequency (Figs. 5.16, 5.17), where difference in power reaches approximately 20 dB.

For some applications where power efficiency is more appreciated than maximum power transfer, self-oscillating antenna would be a great competitor. For others, where maximum

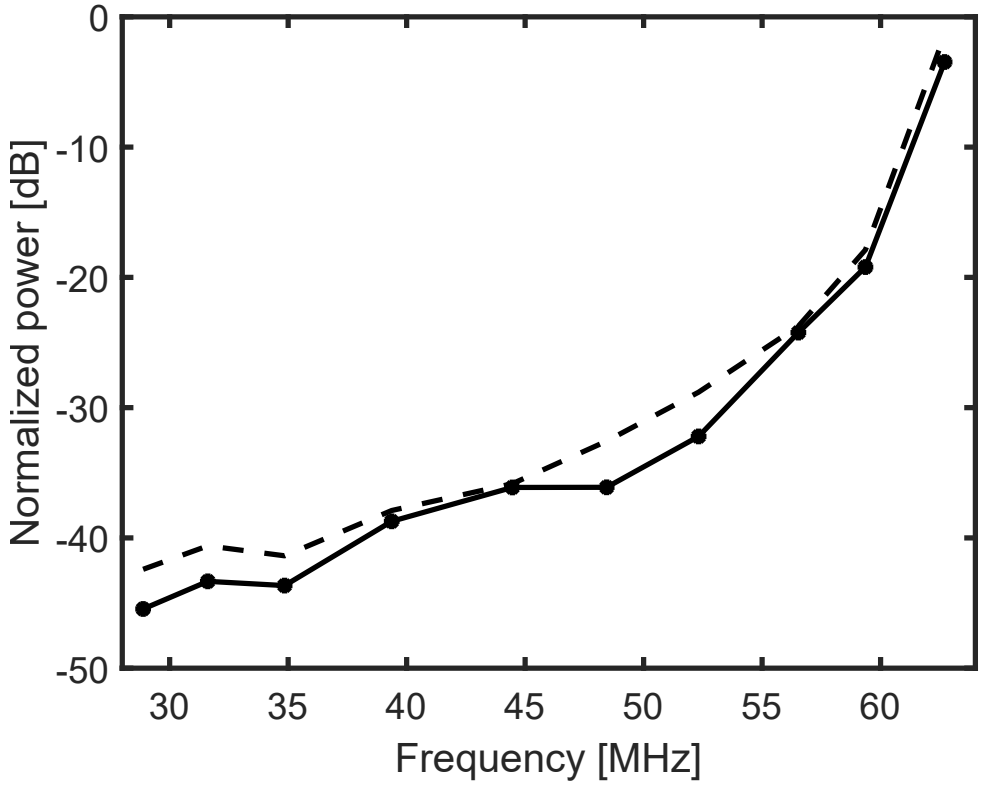

Figure 6.4: Normalized accepted power regarding to frequency by simulated self-oscillating Huygens' radiator. Dashed: case with no mismatch between the antennas (ideal NIC conversion); Solid: actual accepted power.

power transfer is mandatory, or where a 'flat' power characteristic is needed (maximal swing of 3 dB), additional improvements should be made. However, it should be stressed that broadband or broadly tunable devices which enable maximum power transfer at various frequencies, are extremely rare or even non-existing, and due to fundamental physical constraints, they are difficult to realize in practice.

Possible solutions which could improve the 'flatness' of power characteristic and increase the output power are following. First, one could use active elements which enable larger voltage swing, and therefore, allow higher available power (high-power transistors). Secondly, radiating element should be used in a frequency region where its impedance does not significantly change.

Those two proposals where implemented and tested in circuit theory simulator. NIC was of floating type (Fig. 4.3), and based on two operational amplifiers with a voltage swing of $\pm$15V. As in Fig. 6.4, loads were Huygens' radiators, but they were used in a frequency range where the variation of the magnitude of antenna impedance is relatively small (size of the antenna was approximately between $\frac{\lambda}{8}$ and $\frac{\lambda}{4}$). In that range, maximal variation of radiation resistance of the antenna is around 50%. Simulation results of obtained active power with optimized self-oscillating antenna are shown in Fig. 6.5.

It can be seen that it was possible to obtain 5dB 'flatness' of power characteristic in the frequency range from 25 to 52 MHz (tuning range of 1:2). With the frequency increase, magni-

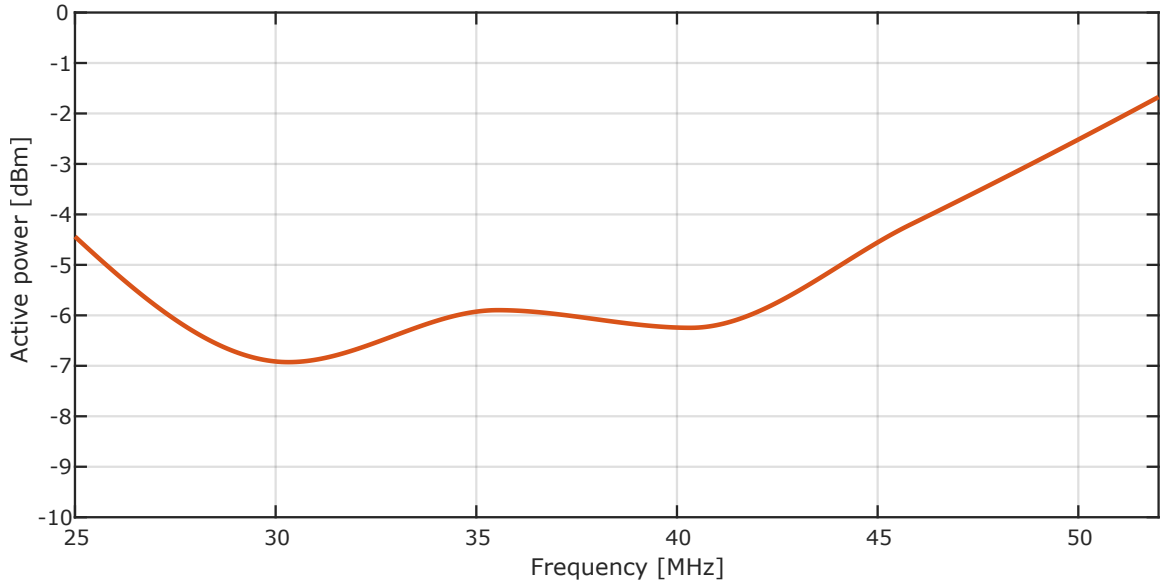

Figure 6.5: Active power regarding to frequency of optimized self-oscillating Huygens' radiator.

tude of the antenna impedance decreases (antenna becomes electrically longer), and the active power gradually increases. Using active elements with a voltage swing of ±15V, generated active power reached values up to -2 dBm in the obtained frequency range. With a larger than ±15V voltage swing of the OPAMPs, it may be possible to achieve even better results.

6.2 Synchronization with external source

One interesting application of a proposed self-oscillating antenna is synchronization with an external RF source. That possibility was already briefly mentioned in section 2.3. In such case, LC tuning network is no longer needed for frequency selection. The system is tuned to the frequency of external signal. Synchronization can be realized either by directly connecting an RF source through a buffer amplifier, or via injection locking [102]. When the source is directly connected to the circuit, negated antenna behaves similarly to a reflection amplifier [125], and positive antenna as a second load.

An example of a three-port network comprising reflection amplifier is shown in Fig. 6.6. Signal is generated via voltage generator of magnitude V_G with internal impedance Z_G. Electromagnetic wave travels from the source to the port 1 of circulator, where it is directed toward the reflection amplifier at port 2. Let us assume that the input impedance of the reflection amplifier consists of real and imaginary part ($Z_{IN} = R_{IN} + jX_{IN}$). We can then define the amplifier input reflection coefficient as:

$$\Gamma_{IN} = \frac{Z_{IN} - Z_0}{Z_{IN} + Z_0}, \tag{6.6}$$

where Z_0 stands for the characteristic impedance of the system. In the case where the real part

of the amplifier input impedance is negative, modulus of the input reflection coefficient ($|\Gamma_{IN}|$) becomes greater than one.

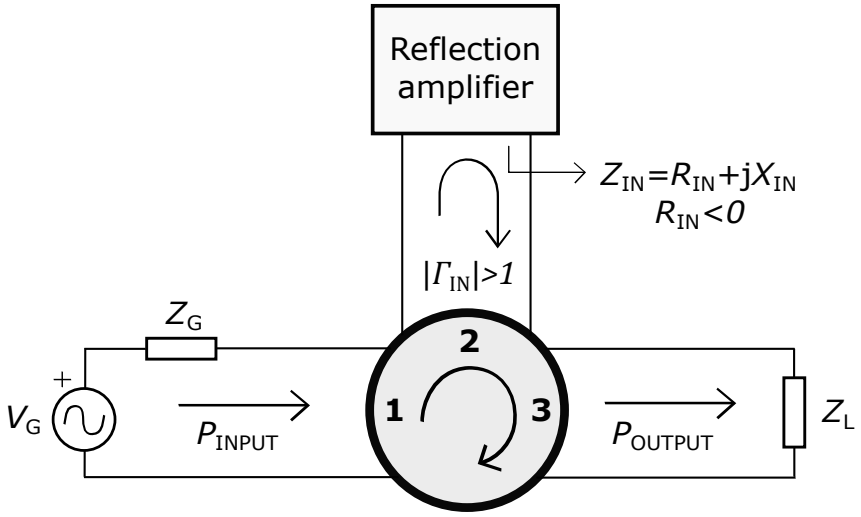

Figure 6.6: Block diagram of a 3-port network comprising RF source, reflection amplifier and a load. Components are connected via 3-port circulator.

For example, let us suppose that Z_0 = 50Ω and Z_{IN} = (-10 + j20)Ω. By insertion in (6.6), we obtain the amplifier input reflection coefficient $\Gamma_{IN} = \sqrt{2}\angle 135°$. Magnitude of reflection coefficient greater than unity means that the power reflected from the reflection amplifier, which can be calculated as [2]:

$$P_{OUTPUT} = P_{INPUT} \cdot |\Gamma_{IN}|^2, \tag{6.7}$$

is greater than the input power generated by RF source (P_{INPUT}). In another words, negative input resistance of a one-port network leads to an amplification of the input signal via reflection.

On the other hand, the idea of injection locking is to stabilize the frequency of a high-power free-running oscillator with another low-power oscillator of stable frequency, using a non-linear effect of synchronization [102]. A process of injection locking is illustrated in Fig. 6.7. Free-running oscillator can be separated into passive and active part, which are represented with their admittance loci ($Y_{RES}(\omega)$ and $Y_{ACT}(A)$). For the sake of simplicity, we will consider that the admittance of the passive element of the oscillator (resonant circuit) depends only on the operating frequency (ω), while the admittance of the active element changes only with the amplitude of oscillating signal (A).

Following the analysis from Chapter 2, stable operating point is achieved at the intersection between the negated locus of the active element (-$Y_{ACT}(A)$) and locus of the passive element ($Y_{RES}(\omega)$), defining the frequency of oscillations (ω_0). Furthermore, with the introduction of a small synchronizing signal of normalized magnitude $\frac{|E_i|}{A_0}$ (green solid curve in Fig. 6.7), it is possible to achieve a frequency range ($\Delta\omega$) in which two oscillators behave as one, with better characteristics (high-power and stable frequency). Two oscillators are locked, i.e. the second

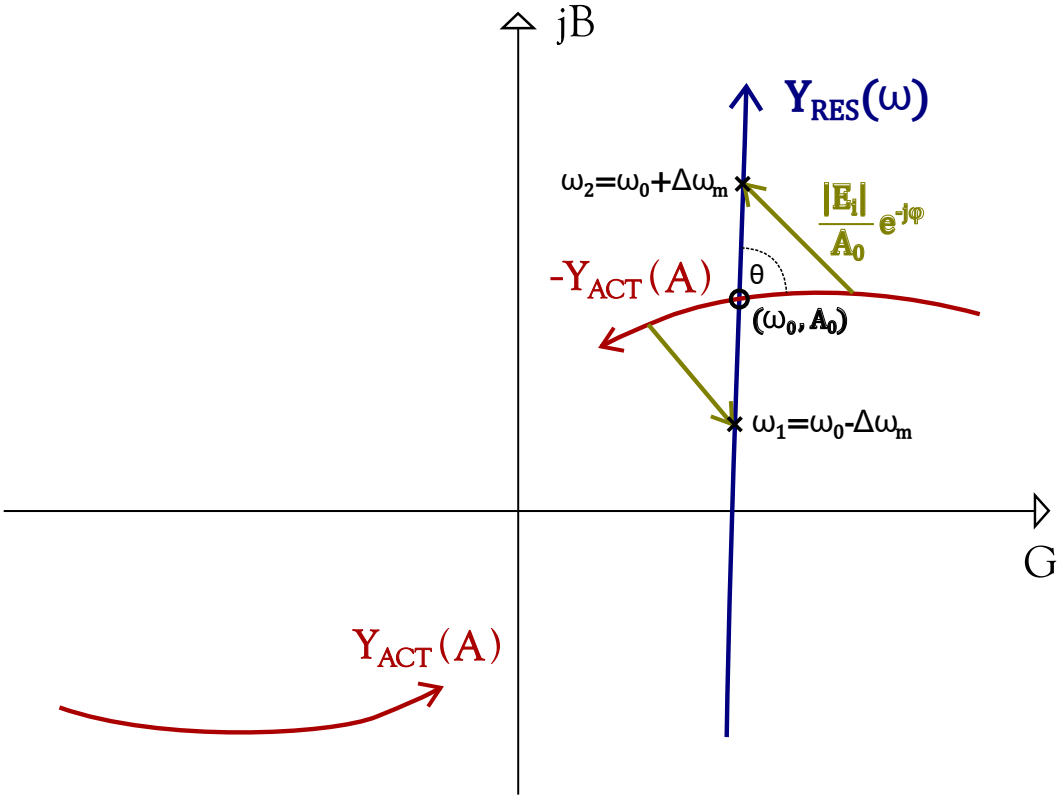

Figure 6.7: Illustration of injection locking of a free-running oscillator with associated admittance loci. Red solid: active element; Blue solid: resonator circuit (passive element); Green solid: normalized synchronizing signal.

oscillator captured the first oscillator causing them to have identical frequencies and phases, when the coupling between the oscillators is strong enough, and when their frequencies are near enough. The lock-in range is then determined by a well-known Adler's equation [126]:

$$\Delta\omega = \frac{2\omega_0}{Q_{ext}}\sqrt{\frac{P_i}{P_0}}\frac{1}{\sin\theta}, \tag{6.8}$$

where Q_{ext} and P_0 stand for the external quality factor of the resonator and output power of free-running oscillator, respectively. Moreover, P_i represents power of the injected signal, while θ stands for the angle between loci of active and passive element (Fig. 6.7). Basically, (6.8) states that the lock-in range is greater for larger ratios between the power of injected and free-running oscillations, but it is inversely proportional to the quality factor of the resonator.

Similar implementations of injection locking were already attempted in oscillator circuits many years back [103, 104, 127]. However, our approach offers improvements regarding frequency agility. Namely, in the case of synchronization, self-oscillating antenna operates without the tank circuit, which means that external quality factor (Q_{ext}) is theoretically zero. Insertion of null quality factor in equation (6.8) leads to a theoretically infinite lock-in range. Furthermore, proposed system consists of two identical antennas, which inherently radiate generated signal, so the synchronized transmitting system does not require additional radiators.

Possible circuit configuration for synchronization of self-oscillating antenna with an external source is shown in Fig. 6.8. Circuit can be separated into three main parts. Firstly, low power signal is generated with an RF source, which is here presented with a sinusoidal voltage source comprising internal impedance Z_G. In order to minimize the influence of source on the self-oscillating antenna, one should insert a current buffer due to its low input, and high output impedance. In our case current buffer was realized with an ideal current-controlled current source. Third part of the circuit is of course a self-oscillating antenna, but without the tank circuit. Oscillating frequency should depend only on the external source.

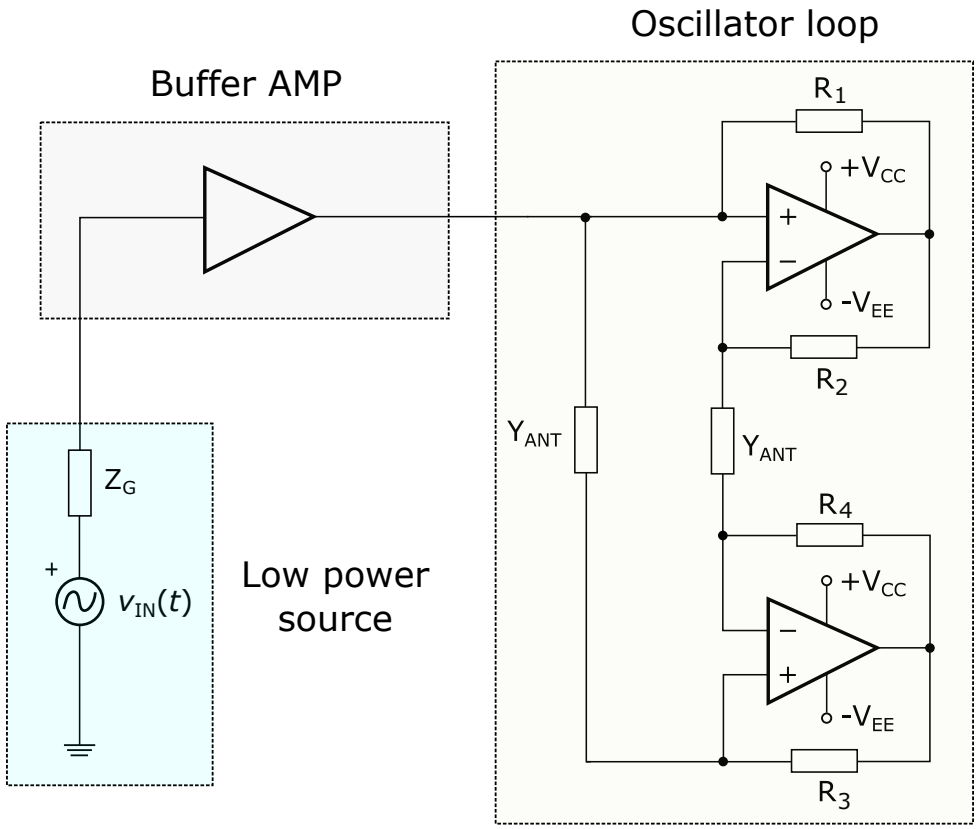

Figure 6.8: Schematic of a self-oscillating antenna based on negative immittance conversion synchronized with low power source.

Simulation parameters were following. Source voltage amplitude was set to 111.6 μV, while internal impedance Z_G was 50Ω. Those values set the input synchronizing current to a constant value of 2.23μA. However, due to the presence of current buffer, voltage was amplified to a magnitude of approximately 1V at the NIC input terminals. Such values ensured the avoidance of high non-linearity in the operation of self-oscillating antenna, but also kept the level of radiated power sufficiently high. Antenna was modelled as a simple series RC circuit with R=2Ω and C=4pF, while operational amplifiers were almost ideal (f_{POLE}=100GHz, A_{OL}=70dB, R_{IN}=1TΩ,R_{OUT}=0). Frequency of the source was varied in relatively small steps (step size was 2 MHz), from 30 to 60 MHz. A sample of waveform of voltage across the antenna, and its spectrum at the central operating frequency (f_0=45MHz), are shown in Fig. 6.9.

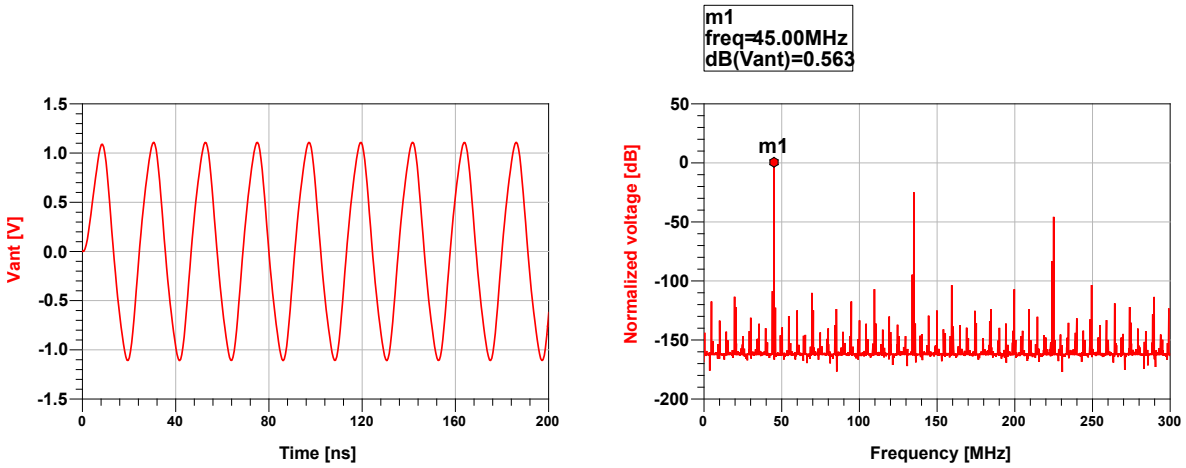

Figure 6.9: Onset of oscillations (left graph) and sample of spectrum (right graph) at central operating frequency (f_0=45MHz) for synchronized self-oscillating antenna.

It should be stressed that operating range of 1:2 (30 MHz to 60 MHz) was chosen solely for the purpose of demonstration. It depends only on the characteristics of operational amplifiers, while theoretically it can be infinite. From Fig. 6.9 it can be seen that the signal is quite clean with the suppression of higher harmonics as high as 25 dB.

Across the chosen frequency range active power at the antennas varied from -24.8 to -21.1 dBm (power swing of 3.7 dB, Fig. 6.10). Comparing the radiated power with total input power from the external source (also taking into account the current buffer), self-oscillating system enables power gain of at least 4.5 dB across the whole bandwidth.

The results demonstrate that in direct synchronizing mode self-oscillating antenna indeed

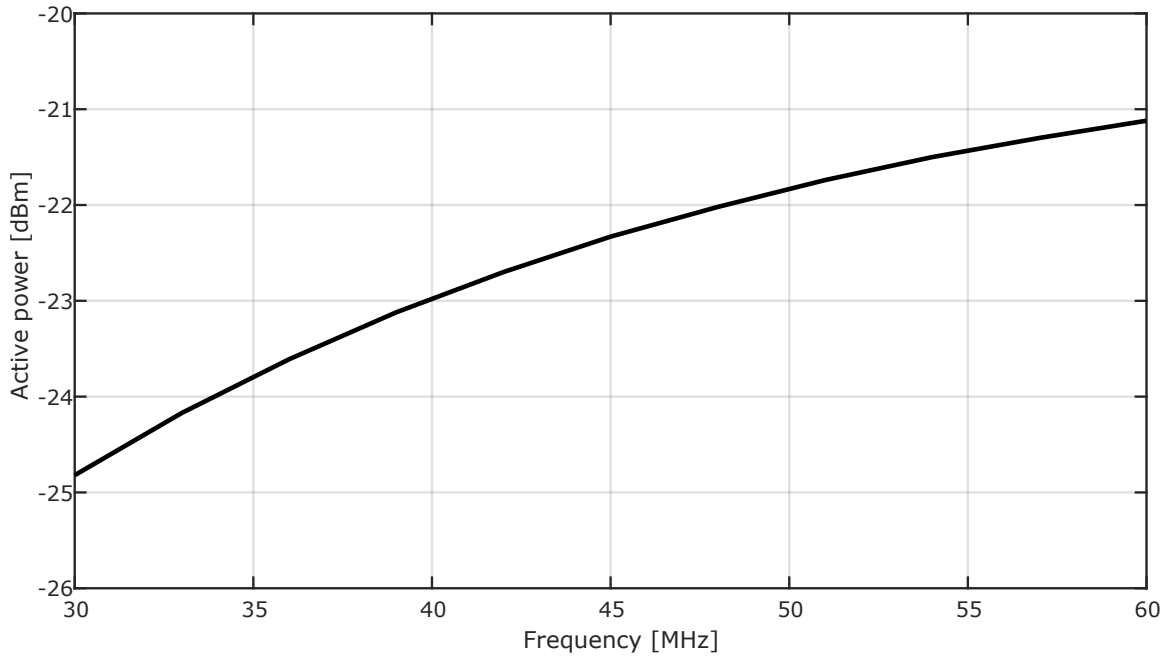

Figure 6.10: Active power at the antennas regarding to the frequency of a self-oscillating antenna synchronized with external low power source.

behaves as a reflection amplifier. NIC input immittance is negative, which means that the input signal from the source will be amplified and reflected back to feed the second 'positive' antenna. Due to the flow of current through NIC, antenna in the feedback loop also radiates, increasing the output active power by approximately 3 dB.

Regarding the experimental part, so far there have not been any successful experiments of injection locking without the tank circuit. Verification of directly connected synchronized RF source via buffer, as displayed in the simulations, has not yet been performed either. Experiments of wireless injection locking were attempted on a self-oscillating antenna based on grounded version of NIC. Unfortunately, it was not possible to achieve injection locking, probably due to problems with DC biasing of OPAMP [24]. Namely, in the case with tank circuit, the DC return path was ensured via inductor, which was no longer present for the synchronization purpose [24]. It is hoped that the use of floating type NIC could lead to successful results.

However, classical wireless injection locking with the tank circuit was successfully demonstrated [24]. The experiments were made with the help of small external dipole antenna, fed by the synthesized RF generator. Self-oscillating antenna with crossed dipoles was locked within the fractional bandwidth of 2%. Central frequency was set to 17.75 MHz with the tuning elements. Obtained lock-in range was inherently mostly defined by the Q factor of the tank circuit. A sample of obtained spectra of locked signal, as well as the low and high frequency boundary of lock-in range are presented in Figs. 6.11, 6.12 and 6.13 [24].

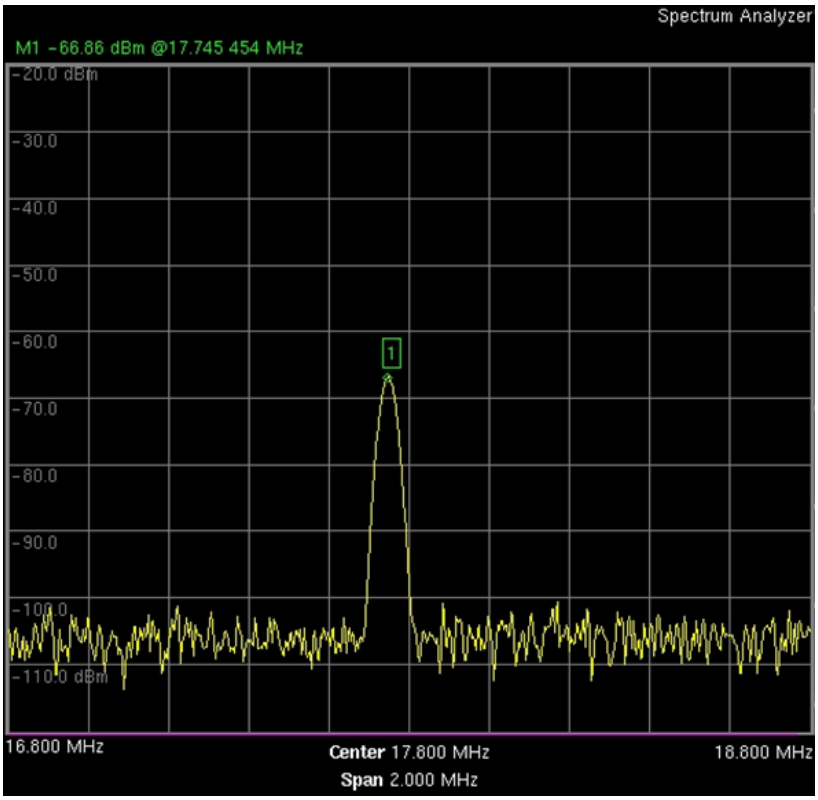

Figure 6.11: Measured spectrum of injection-locked self-oscillating antenna with crossed dipoles, f_0=17.75MHz.

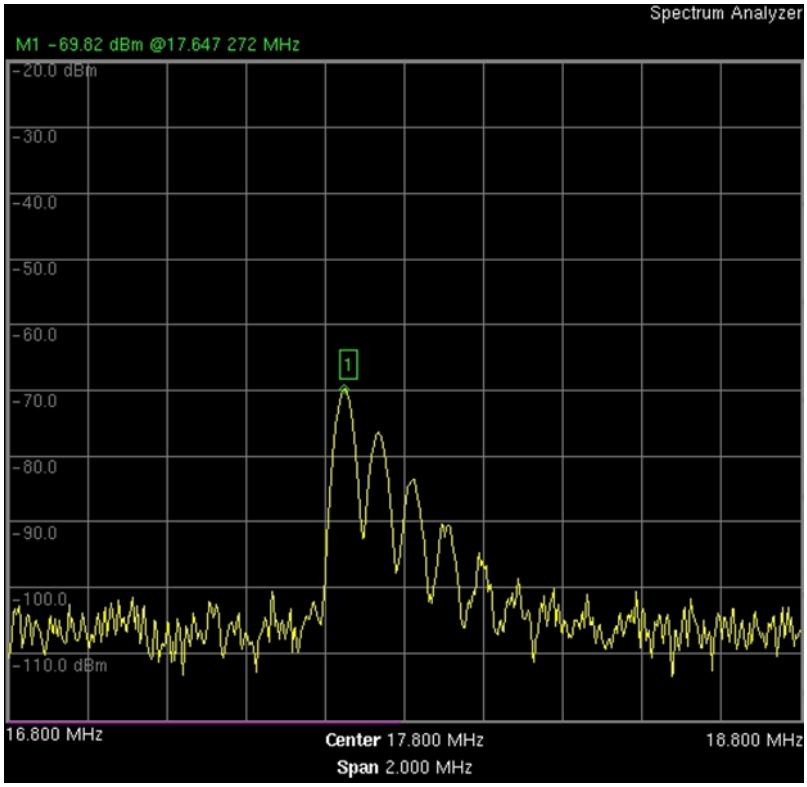

Figure 6.12: Injection locking of a self-oscillating antenna with crossed dipoles, lower lock-in boundary, f_{LOW}=17.65 MHz.

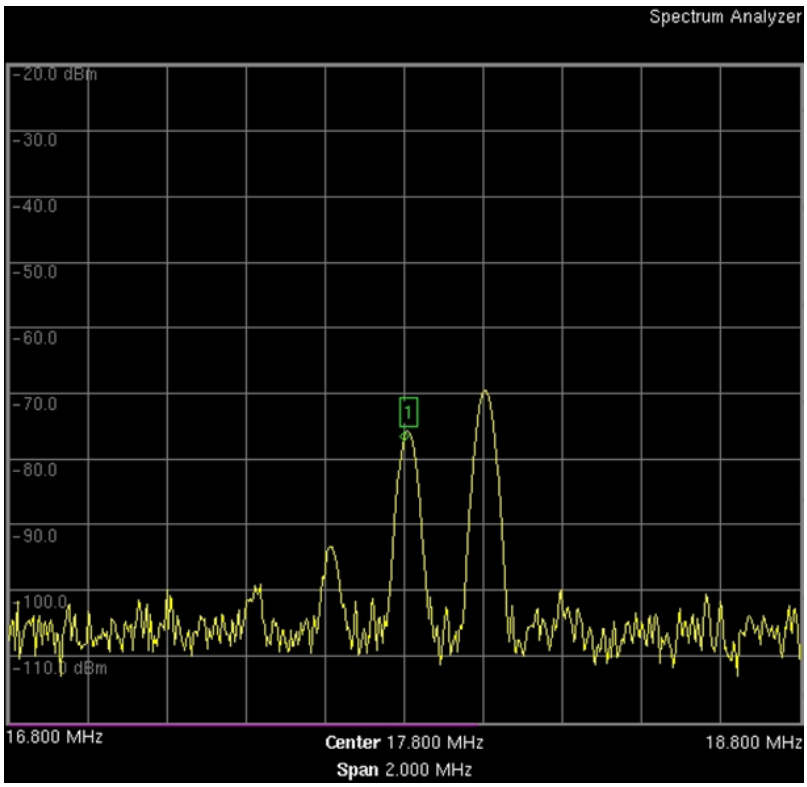

Figure 6.13: Injection locking of a self-oscillating antenna with crossed dipoles, upper lock-in boundary, f_{HIGH}=18 MHz.

6.3 FSK modulation

Another improvement of the properties of self-oscillating antenna could be managing of NIC non-linearities and associated implementation of modulation feature. It was already shown possible to maintain the influence of non-linearity at the acceptable level by the use of appropriate limiter. The modulation feature could be implemented either directly, or by injection locking of modulated signal.

We have performed preliminary simulations in circuit theory solver (ADS^{TM}). In direct mode, we simulated a simple binary frequency-shift keying (BFSK) implementation, based on additional varactor diode embedded into the tank circuit. Simplified schematic diagram used in circuit theory simulations is given in Fig. 6.14.

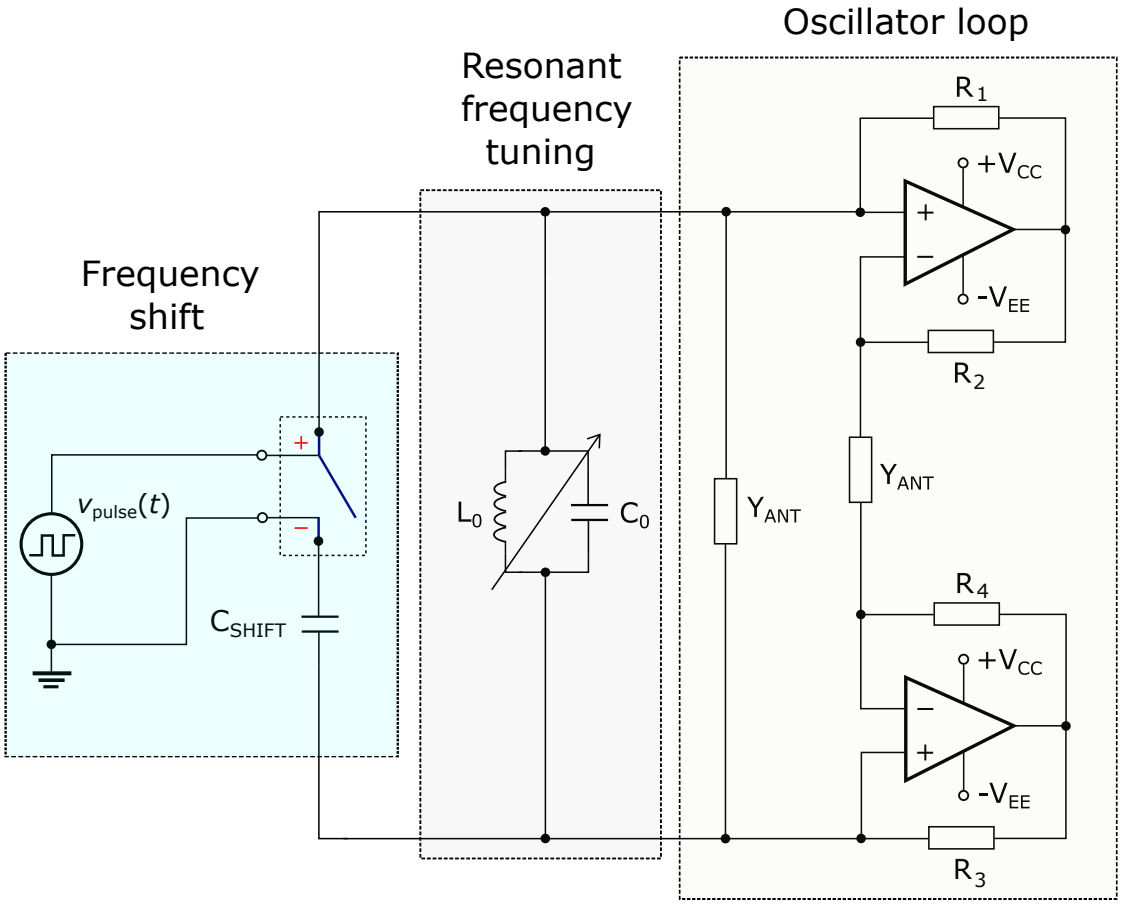

Figure 6.14: Schematic diagram of test environment for FSK modulation of self-oscillating Huygens' radiator.

In the simulator, varactor diode was modelled with a capacitance (C_{SHIFT}) connected in series to an 'almost ideal' voltage controlled switch (R_{ON}=1mΩ, R_{OFF}=1TΩ). Switch was controlled via voltage pulse generator, that defined the frequency of shifting. When the switch is on, capacitance C_{SHIFT} connects in parallel to the capacitance of the tank circuit (C_0), thus increasing the total capacitance and decreasing the operating frequency. C_0+C_{SHIFT} define the first frequency (named mark frequency in BFSK), which symbolizes binary "1". When the

switch is off, capacitance C_{SHIFT} is disconnected, and operating frequency is defined only by the tank circuit. It means that C_0 defines the second frequency (named space frequency in BFSK), which symbolizes binary "0".

As an example, we used designed Huygens' antennas as radiators, and performed transient simulations for two different shifting frequencies, 10 kHz, and 20 kHz, respectively. Mark frequency was set to 48.84 MHz (with L_0=500nH, C_0=20.3pF, C_{SHIFT}=0.8pF), while space frequency was 49.8 MHz. Spectrum for the case of shifting frequency of 10 kHz is shown in the left part of Fig. 6.15, and spectrum for the shifting frequency of 20 kHz in the right part of Fig. 6.15. Both results are quite satisfying, and it is possible to detect shifting frequencies, as well as mark and space frequencies. However, it can be noticed that for the higher shifting frequency, levels of generated parasitic components in the spectrum become higher.

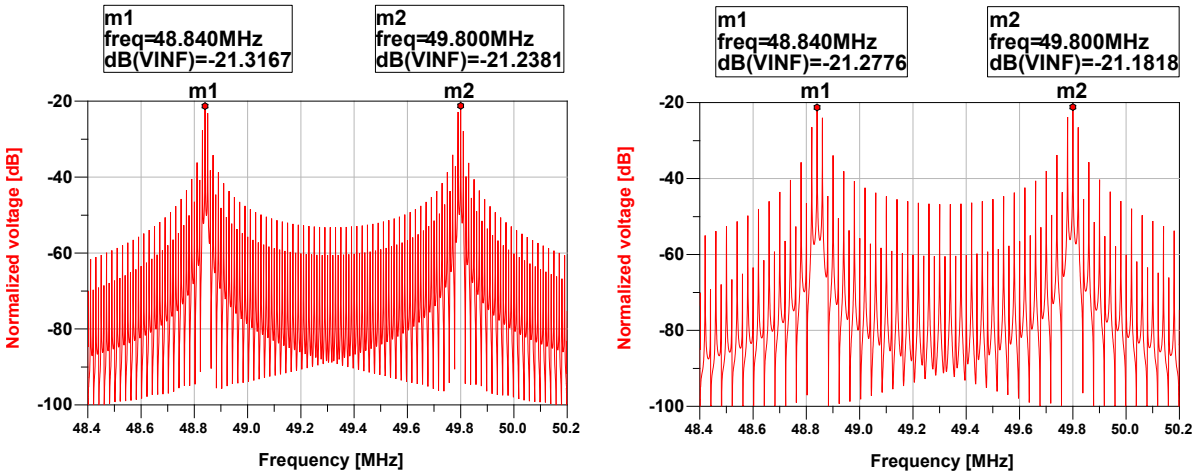

Figure 6.15: Sample of spectra of generated signal obtained via BFSK modulation of self-oscillating Huygens' radiator. Mark frequency set to 48.84 MHz, and space frequency to 49.8 MHz. Left graph: shifting frequency of 10 kHz; Right graph: shifting frequency of 20 kHz.

It is interesting that (at least in the idealized case) the instantaneous bandwidth appears not to be limited by the Q factor of used antennas, since the admittance of the first antenna is completely cancelled by its negative image. Therefore, the instantaneous bandwidth is limited solely by the Q factor of the resonant circuit. Since this Q factor can be lower than the Q factor of an electrically small antenna, a higher instantaneous bandwidth becomes possible. On the contrary, there are no limitations on the instantaneous bandwidth in (idealized) injection locking mode. These modulation properties are similar to, or in some cases even better, than the properties of direct antenna modulation systems [128].

Chapter 7

Conclusions and recommendation for future work

The concept of a self-oscillating antenna based on negative immittance conversion has been proposed and investigated analytically, numerically, and experimentally. Presented concept makes use of a well-known inherent instability of networks with negative elements, which is in most applications considered as a serious drawback.

The proposed device is based on two orthogonally polarized electrically small radiators, connected via negative impedance converter (NIC). Due to cancellation of the antenna admittances, the system is source-load matched and it supports generation and radiation of the EM signal within theoretically infinite bandwidth. Such self-oscillating system behaves as a sub-wavelength widely tunable transmitting active antenna. Frequency tuning of self-oscillating signal can be achieved either by inclusion of a resonant circuit or by injection locking from an external source.

The basic idea was discussed and compared with a well-known concept of active antenna from microwave engineering. It was be concluded, that in order to increase the tunability of active antennas, one should use negative elements in the immittance transformation network. Therefore, a self-oscillating antenna based on negative immittance conversion can be seen as an extension of the concept of active antenna.

Two mathematical models of negative impedance converter were derived separately, for grounded and floating configuration, in order to predict the behaviour of self-oscillating antenna. Finite-length single-pole model of the amplifier was derived, and analysis of the NIC conversion for a complex load in the positive feedback loop was performed. The results revealed that the conversion error depends not only on the amplifier characteristics, but also on the quality factor of the load admittance. Secondly, a simple non-linear model of a negative impedance converter was presented, which can be used regardless of the actual implementation. It was noticed that non-linearity affects conversion of both real and imaginary part of the load harmonic admittance

in the same manner. Finally, dispersive and non-linear models of NIC were combined, and oscillations' dynamics was investigated theoretically. Three-dimensional graphical tool for the prediction of amplitude and frequency of generated self-oscillations was proposed, and its use was illustrated by a numerical example.

Several scaled experimental demonstrators of self-oscillating antenna based on negative immittance conversion, operating in the lower RF range (up to 50 MHz), were designed, manufactured, and tested. First set of prototypes incorporated dipole-like antennas with a doughnut-shaped radiation pattern. Experimental results were found to be similar to the results from theoretical analysis and numerical simulations. Measured tuning range was 1:2 in the case of capacitively loaded dipole antennas, and 1:3 in the case of bow-tie antennas.

The basic concept was further extended to self-oscillating Huygens' radiator, with a unidirectional (cardioid-shaped) radiation pattern. Design of Huygens' antenna comprised of two pairs of capacitively loaded dipoles, and orthogonal loops, excited by an orthogonal pair of electrically small dipoles. The advantage of unidirectional radiation lies in the possible application in reflective active metasurfaces. Self-oscillating Huygens' radiator was constructed, and measured demonstrator results were consistent with their simulated values. It was possible to achieve the tuning range of 1:2.

The future research efforts could be devoted to better understanding of the background physics of resonator-free injection locking and its experimental verification. In addition, it would be interesting to investigate if the use of microelectronic technology could enable extension of the proposed concept into microwave regime. This could lead to realization of a self-oscillating metasurface, which may incorporate modulation feature, external tuning based on injection locking and, possibly, beam-steering functionality.

Literature

[1] Lakhtakia, A., Furse, C. M., “The world of applied electromagnetics”, Springer, 2018.

[2] Pozar, D. M., Microwave engineering. John Wiley & Sons, 2009.

[3] Balanis, C. A., Antenna Theory: Analysis and Design. Wiley, 2015.

[4] Wheeler, H. A., “Fundamental limitations of small antennas”, Proceedings of the IRE, Vol. 35, No. 12, 1947, pp. 1479-1484.

[5] Hansen, R. C., “Fundamental limitations in antennas”, Proceedings of the IEEE, Vol. 69, No. 2, 1981, pp. 170-182.

[6] Chu, L. J., “Physical limitations of omni-directional antennas”, Journal of Applied Physics, Vol. 19, No. 12, 1948, pp. 1163-1175.

[7] Sohrabi, A., Dashti, H., Ahmadi-Shokouh, J., “Design and analysis of a broadband electrically small antenna using characteristic mode theory”, AEU - International Journal of Electronics and Communications, Vol. 113, 2020, pp. 152991.

[8] Tang, M., Ziolkowski, R. W., “Electrically small metamaterial-inspired antennas with active near field resonant parasitic elements: From theory to practice”, in 2017 11th European Conference on Antennas and Propagation (EUCAP), 2017, pp. 1559-1563.

[9] Jin, P., Ziolkowski, R. W., “Metamaterial-inspired, electrically small huygens sources”, IEEE Antennas and Wireless Propagation Letters, Vol. 9, 2010, pp. 501-505.

[10] O’Donnell, T. H., Yaghjian, A. D., “Electrically small superdirective arrays using parasitic elements”, in 2006 IEEE Antennas and Propagation Society International Symposium, 2006, pp. 3111-3114.

[11] Yaghjian, A. D., “Increasing the supergain of electrically small antennas using metamaterials”, in 2009 3rd European Conference on Antennas and Propagation, 2009, pp. 858-860.

[12] Gustafsson, M., Nordebo, S., “Bandwidth, q factor, and resonance models of antennas”, in Technical Report LUTEDX/(TEAT-7138)/1-16/(2005), Vol. TEAT-7138, 2005.

[13] Harrington, R., “Effect of antenna size on gain, bandwidth, and efficiency”, Journal of Research of the National Bureau of Standards, Section D: Radio Propagation, 1960, pp. 1.

[14] Bartolić, J., Mikrovalna elektronika. Graphis Zagreb, 2011.

[15] Fano, R. M., “Theoretical limitations on the broadband matching of arbitrary impedances”, Journal of the Franklin Institute, Vol. 249, No. 1, 1950, pp. 57-83.

[16] Foster, R. M., “A reactance theorem”, Bell Labs Technical Journal, Vol. 3, No. 2, 1924, pp. 259–267.

[17] van der Pol, B., “A new transformation in alternating-current theory with an application to the theory of audition”, Proceedings of the Institute of Radio Engineers, Vol. 18, No. 2, 1930, pp. 220-230.

[18] Verman, L. C., “Negative circuit constants”, Proceedings of the Institute of Radio Engineers, Vol. 19, No. 4, 1931, pp. 676-681.

[19] Hrabar, S., “First ten years of active metamaterial structures with “negative” elements”, EPJ Applied Metamaterials, Vol. 5, 01 2018, pp. 9.

[20] Sussman-Fort, S. E., Rudish, R. M., “Non-foster impedance matching of electrically-small antennas”, IEEE Transactions on Antennas and Propagation, Vol. 57, No. 8, 2009, pp. 2230-2241.

[21] Mehdizadeh, M., “Chapter 1 - the impact of fields on materials at rf/microwave frequencies”, in Microwave/RF Applicators and Probes for Material Heating, Sensing, and Plasma Generation, Mehdizadeh, M., (ur.). Boston: William Andrew Publishing, 2010, pp. 1-34.

[22] Kshetrimayum, R., “A brief intro to metamaterials”, IEEE Potentials, Vol. 23, No. 5, 2004, pp. 44-46.

[23] Engheta, N., R.W., Z., “Metamaterials: physics and engineering explorations”, 2006, pp. 3-30, wiley and Sons.

[24] Hrabar, S., Krois, I., Loncar, J., Vincelj, L., “Non-foster source-load networks and metasurfaces”, in EOARD/AFRL, Wright-Patterson Air Force Base, OH, USA, Final Rep., FA 9550-15-1-0120, 2018.

[25] Tretyakov, S., “Meta-materials with wideband negative permittivity and permeability”, Microwave and Optical Technology Letters, Vol. 31, 11 2001, pp. 163 - 165.

[26] Engheta, N., “Metamaterials with negative permittivity and permeability: background, salient features, and new trends”, in IEEE MTT-S International Microwave Symposium Digest, 2003, Vol. 1, 2003, pp. 187-190 vol.1.

[27] Iyer, A. K., Eleftheriades, G. V., “A multilayer negative-refractive-index transmission-line (nri-tl) metamaterial free-space lens at x-band”, IEEE Transactions on Antennas and Propagation, Vol. 55, No. 10, 2007, pp. 2746-2753.

[28] Bilotti, F., Tricarico, S., Vegni, L., “Plasmonic metamaterial cloaking at optical frequencies”, IEEE Transactions on Nanotechnology, Vol. 9, No. 1, 2010, pp. 55-61.

[29] Ivsic, B., Sipus, Z., Hrabar, S., “Analysis of uniaxial multilayer cylinders used for invisible cloak realization”, IEEE Transactions on Antennas and Propagation, Vol. 57, No. 5, 2009, pp. 1521-1527.

[30] Hrabar, S., Krois, I., Bonic, I., Kiricenko, A., Munoz, E. U., “Broadband epsilon-near-zero (enz) and mu-near-zero (mnz) active metamaterial”, 2011.

[31] Chen, H.-T., Taylor, A., yu, N., “A review of metasurfaces: Physics and applications”, Reports on Progress in Physics, Vol. 79, 05 2016.

[32] Epstein, A., Eleftheriades, G. V., “Passive lossless huygens metasurfaces for conversion of arbitrary source field to directive radiation”, IEEE Transactions on Antennas and Propagation, Vol. 62, No. 11, 2014, pp. 5680-5695.

[33] Pfeiffer, C., Grbic, A., “Metamaterial huygens’ surfaces”, in 2013 IEEE MTT-S International Microwave Symposium Digest (MTT), 2013, pp. 1-4.

[34] Lončar, J., Grbic, A., Hrabar, S., “A reflective polarization converting metasurface at *X* -band frequencies”, IEEE Transactions on Antennas and Propagation, Vol. 66, No. 6, 2018, pp. 3213-3218.

[35] Tierney, B. B., “Advances in emerging electromagnetics topics: Metamaterials and wireless power transfer”, PhD Thesis, The University of Michigan, 2016.

[36] Pfeiffer, C., Grbic, A., “Millimeter-wave transmitarrays for wavefront and polarization control”, IEEE Transactions on Microwave Theory and Techniques, Vol. 61, No. 12, 2013, pp. 4407–4417.

[37] Xu, M. Y., Hum, S. V., “Realization of low-complexity reconfigurable huygens’ metasurfaces”, in 2019 13th European Conference on Antennas and Propagation (EuCAP), 2019, pp. 1-4.

[38] Pfeiffer, C., Grbic, A., “Emulating nonreciprocity with spatially dispersive metasurfaces excited at oblique incidence”, Physical Review Letters, Vol. 117, No. 7, 2016, pp. 077401.

[39] Kishor, K. K., Hum, S. V., “An amplifying reconfigurable reflectarray antenna”, Antennas and Propagation, IEEE Transactions on, Vol. 60, No. 1, 2012, pp. 197–205.

[40] Merrill, J., “Theory of the negative impedance converter”, Bell System Technical Journal, Vol. 30, No. 1, 1951, pp. 88–109.

[41] Linvill, J. G., “Transistor negative impedance converters”, Proceedings of the IRE, Vol. 41, 1953, pp. 725–729.

[42] Larky, A., “Negative-impedance converters”, IRE Transactions on Circuit Theory, Vol. 4, No. 3, 1957, pp. 124–131.

[43] Su, K. L., “A method for realizing the negative-impedance inverter”, IEEE Journal of Solid-State Circuits, Vol. 2, No. 1, 1967, pp. 22-25.

[44] “Linear Mode of Voltage Inversion NIC”, Available: https://en.wikibooks.org/wiki/Circuit_Idea/Linear_Mode_of_Voltage_Inversion_NIC, [Online] (2020, January 20).

[45] “Linear Mode of Current Inversion NIC”, Available: https://en.wikibooks.org/wiki/Circuit_Idea/Linear_Mode_of_Current_Inversion_NIC, [Online] (2021, January 20).

[46] Carter, B., Huelsman, L., “Handbook of operational amplifier active rc networks”, Texas Instruments, Dallas, TX, Application Report SBOA093A, 2001.

[47] White, C. R., May, J. W., Colburn, J. S., “A variable negative-inductance integrated circuit at uhf frequencies”, IEEE Microwave and Wireless Components Letters, Vol. 22, No. 1, 2012, pp. 35-37.

[48] Hrabar, S., Krois, I., Bonic, I., Kiricenko, A., “Negative capacitor paves the way to ultra-broadband metamaterials”, Applied physics letters, Vol. 99, No. 25, 2011, pp. 254103.

[49] Hrabar, S., Krois, I., Bonić, I., Kiricenko, A., Muha, D., “Active reconfigurable metamaterial unit cell based on non-foster elements”, in EOARD/AFRL, Wright-Patterson Air Force Base, OH, USA, Final Rep. FA 8655-12-1-2081, 2013.

[50] Hrabar, S., Kiricenko, A., “Towards broadband tunable non-foster radiating systems”, in 2016 10th International Congress on Advanced Electromagnetic Materials in Microwaves and Optics (METAMATERIALS), 2016, pp. 133-135.

[51] Baraniuk, R., “Signals and systems”, OpenStax CNX, 2015.

[52] Brownlie, J., “On the stability properties of a negative impedance converter”, IEEE Transactions on Circuit Theory, Vol. 13, No. 1, 1966, pp. 98–99.

[53] Hoskins, R., “Stability of negative-impedance convertors”, Electronics Letters, Vol. 2, September 1966, pp. 341-341.

[54] Schwarz, A., “On the stability properties of a negative-immittance converter”, IEEE Transactions on Circuit Theory, Vol. 14, No. 1, 1967, pp. 77–77.

[55] Davies, A., “Stability properties of a negative immittance converter”, IEEE Transactions on Circuit Theory, Vol. 15, No. 1, 1968, pp. 80–81.

[56] Tang, Q., Xin, H., “Stability analysis of non-foster circuit using normalized determinant function”, IEEE Transactions on Microwave Theory and Techniques, Vol. 65, No. 9, 2017, pp. 3269-3277.

[57] Ugarte-Munoz, E., Hrabar, S., Segovia-Vargas, D., Kiricenko, A., “Stability of non-foster reactive elements for use in active metamaterials and antennas”, IEEE transactions on antennas and propagation, Vol. 60, No. 7, 2012, pp. 3490–3494.

[58] Stearns, S. D., “Circuit stability theory for non-foster circuits”, in Microwave Symposium Digest (IMS), 2013 IEEE MTT-S International. IEEE, 2013, pp. 1–3.

[59] Loncar, J., Hrabar, S., Muha, D., “Stability of simple lumped-distributed networks with negative capacitors”, IEEE Transactions on Antennas and Propagation, Vol. 65, No. 1, 2017, pp. 390–395.

[60] Loncar, J., Muha, D., Hrabar, S., “Influence of transmission line on stability of networks containing ideal negative capacitors”, in 2015 IEEE International Symposium on Antennas and Propagation & USNC/URSI National Radio Science Meeting. IEEE, 2015, pp. 73–74.

[61] Stearns, S. D., “Non-foster circuits and stability theory”, in Antennas and Propagation (APSURSI), 2011 IEEE International Symposium on. IEEE, 2011, pp. 1942–1945.

[62] Stearns, S. D., “Incorrect stability criteria for non-foster circuits”, in Antennas and Propagation Society International Symposium (APSURSI), 2012 IEEE. IEEE, 2012, pp. 1–2.

[63] Perry, K., Albert, “Broadband antenna systems realized from active circuit conjugate impedance matching”, dostupno na: https://calhoun.nps.edu/handle/10945/16511 1973.

[64] Ziolkowski, R. W., Zhu, N., “Broad bandwidth, efficient, metamaterial-inspired, electrically small antennas augmented with internal non-foster elements”, in 2012 6th European Conference on Antennas and Propagation (EUCAP), 2012, pp. 123-125.

[65] Zhu, N., Ziolkowski, R. W., “Active metamaterial-inspired broad-bandwidth, efficient, electrically small antennas”, IEEE Antennas and Wireless Propagation Letters, Vol. 10, 2011, pp. 1582-1585.

[66] Mirzaei, H., Eleftheriades, G. V., “A wideband metamaterial-inspired compact antenna using embedded non-foster matching”, in Antennas and Propagation (APSURSI), 2011 IEEE International Symposium on. IEEE, 2011, pp. 1950–1953.

[67] Zhu, N., Ziolkowski, R. W., “Design and measurements of an electrically small, broad bandwidth, non-foster circuit-augmented protractor antenna”, Applied Physics Letters, Vol. 101, No. 2, 2012, pp. 024107.

[68] Albarracin-Vargas, F., Gonzalez, V., Herraiz-Martínez, F. J., Segovia-Vargas, D., “Design method for actively matched antennas with non-foster elements”, IEEE Transactions on Antennas and Propagation, Vol. 64, 09 2016, pp. 1-1.

[69] Jacob, M. M., Long, J., Sievenpiper, D. F., “Broadband non-foster matching of an electrically small loop antenna”, in Antennas and Propagation Society International Symposium (APSURSI), 2012 IEEE. IEEE, 2012, pp. 1–2.

[70] Shih, T., Behdad, N., “Wideband, non-foster impedance matching of electrically small transmitting antennas”, IEEE Transactions on Antennas and Propagation, Vol. 66, No. 11, 2018, pp. 5687-5697.

[71] Yang, H., Kim, I., Kim, K., “Non-foster matching of a resistively loaded vee dipole antenna using operational amplifiers”, IEEE Transactions on Antennas and Propagation, Vol. 64, No. 4, 2016, pp. 1477-1482.

[72] Song, K., Rojas, R. G., “Electrically small wire monopole antenna with non-foster impedance element”, in Proceedings of the Fourth European Conference on Antennas and Propagation, 2010, pp. 1-4.

[73] Long, J., Jacob, M. M., Sievenpiper, D. F., “Broadband fast-wave propagation in a non-foster circuit loaded waveguide”, IEEE Transactions on Microwave Theory and Techniques, Vol. 62, No. 4, 2014, pp. 789–798.

[74] Sievenpiper, D. F., “Superluminal waveguides based on non-foster circuits for broadband leaky-wave antennas”, IEEE Antennas and Wireless Propagation Letters, Vol. 10, 2011, pp. 231–234.

[75] Gao, F., Zhang, F., Long, J., Jacob, M., Sievenpiper, D., “Non-dispersive tunable reflection phase shifter based on non-foster circuits”, Electronics Letters, Vol. 50, No. 22, 2014, pp. 1616–1618.

[76] Weldon, T. P., Miehle, K., Adams, R. S., Daneshvar, K., “A wideband microwave double-negative metamaterial with non-foster loading”, in Southeastcon, 2012 Proceedings of IEEE. IEEE, 2012, pp. 1–5.

[77] Miehle, K., Weldon, T. P., Adams, R. S., Daneshvar, K., “Wideband negative permeability metamaterial with non-foster compensation of parasitic capacitance”, in Antennas and Propagation Society International Symposium (APSURSI), 2012 IEEE. IEEE, 2012, pp. 1–2.

[78] Long, J., Sievenpiper, D. F., “Low-profile and low-dispersion artificial impedance surface in the uhf band based on non-foster circuit loading”, IEEE Transactions on Antennas and Propagation, Vol. 64, No. 7, 2016, pp. 3003-3010.

[79] Hrabar, S., Krois, I., Bonic, I., Kiricenko, A., “Ultra-broadband simultaneous superluminal phase and group velocities in non-foster epsilon-near-zero metamaterial”, Applied physics letters, Vol. 102, No. 5, 2013, pp. 054108.

[80] Ghadiri, A., Moez, K., “Gain-enhanced distributed amplifier using negative capacitance”, IEEE Transactions on Circuits and Systems I: Regular Papers, Vol. 57, No. 11, 2010, pp. 2834-2843.

[81] Chen, P.-Y., Argyropoulos, C., Alù, A., “Broadening the cloaking bandwidth with non-foster metasurfaces”, Physical review letters, Vol. 111, No. 23, 2013, pp. 233001.

[82] Hrabar, S., Krois, I., Kiricenko, A., “Towards active dispersionless enz metamaterial for cloaking applications”, Metamaterials, Vol. 4, No. 2, 2010, pp. 89-97, metamaterials-2009 Congress in London.

[83] Gregoire, D. J., White, C. R., Colburn, J. S., “Wideband artificial magnetic conductors loaded with non-foster negative inductors”, IEEE Antennas and Wireless Propagation Letters, Vol. 10, 2011, pp. 1586–1589.

[84] Mou, J., Shen, Z., “Design and experimental demonstration of non-foster active absorber”, IEEE Transactions on Antennas and Propagation, 2016.

[85] Auzanneau, F., Ziolkowski, R., “Theoretical study of synthetic bianisotropic materials”, Journal of Electromagnetic Waves and Applications, Vol. 12, 1998, pp. 353-370.

[86] Auzanneau, F., Ziolkowski, R. W., “Artificial composite materials consisting of nonlinearly loaded electrically small antennas: operational-amplifier-based circuits with applications to smart skins”, IEEE Transactions on Antennas and Propagation, Vol. 47, No. 8, 1999, pp. 1330-1339.

[87] Jacob, M. M., Sievenpiper, D. F., “Non-foster matched antennas for high-power applications”, IEEE Transactions on Antennas and Propagation, Vol. 65, No. 9, 2017, pp. 4461-4469.

[88] Lee, S., Park, H., Kim, J., Kwon, Y., “A 6–18 ghz gan phemt power amplifier using non-foster matching”, in 2015 IEEE MTT-S International Microwave Symposium, 2015, pp. 1-4.

[89] Weldon, T. P., Covington, J. M. C., Smith, K. L., Adams, R. S., “Performance of digital discrete-time implementations of non-foster circuit elements”, in 2015 IEEE International Symposium on Circuits and Systems (ISCAS), 2015, pp. 2169-2172.

[90] Vincelj, L., Hrabar, S., Krois, I., “Non-ideal ’negation’ of complex load in self-oscillating non-foster structures”, Metamaterials congress, 2019, rome, Italy.

[91] Hrabar, S., Kiricenko, A., Krois, I., “Antenna-transmitter based on non-foster source”, in 2017 IEEE International Symposium on Antennas and Propagation USNC/URSI National Radio Science Meeting, 2017, pp. 875-876.

[92] Hrabar, S., Krois, I., Vincelj, L., “Two-element non-foster antenna-transmitter array”, IEEE Int. Symp. on Antennas and Prop. (APS / URSI), 2018.

[93] Vincelj, L., Krois, I., Hrabar, S., “Toward self-oscillating non-foster unit cell for future active metasurfaces”, IEEE Tran. on Ant. and Prop., Vol. 68, No. 3, 2020, pp. 1665-1679.

[94] Chang, K., York, R. A., Hall, P. S., Itoh, T., “Active integrated antennas”, IEEE Transactions on Microwave Theory and Techniques, Vol. 50, No. 3, 2002, pp. 937-944.

[95] Modlic, B., Modlic, I., Titranje i Oscilatori. Školska knjiga - Zagreb, 1991.

[96] Barkhausen, H., Lehrbuch der Elektronen-Röhren und ihrer technischen Anwendungen [Textbook of Electron Tubes and their Technical Applications]. Leipzig: S. Hirzel, 1935.

[97] Kurokawa, K., “Some basic characteristics of broadband negative resistance oscillator circuits”, The Bell System Technical Journal, Vol. 48, No. 6, 1969, pp. 1937-1955.

[98] Jacob, M. M., Long, J., Sievenpiper, D. F., “Nonlinear effects of non-foster matching networks”, in 2015 IEEE International Symposium on Antennas and Propagation USNC/URSI National Radio Science Meeting, 2015, pp. 1248-1249.

[99] Vincelj, L., Hrabar, S., Krois, I., “Non-linear model of negative impedance converter for use in non-foster circuitry”, ICECOM 2019, 2019, dubrovnik, Croatia.

[100] Stearns, S., “Counterintuitive aspects of non-foster networks”, in Adelphi Antenna Workshop on Electrically Small Antennas, 2010, pp. 8–9.

[101] Vincelj, L., Hrabar, S., “Dynamical behavior of non-foster self-oscillating antenna”, in 2020 International Symposium ELMAR, 2020, pp. 17-20.

[102] Kurokawa, K., “Injection locking of microwave solid-state oscillators”, Proceedings of the IEEE, Vol. 61, No. 10, 1973, pp. 1386-1410.

[103] Popovic, Z. B., Weikle, R. M., Kim, M., Potter, K. A., Rutledge, D. B., “Bar-grid oscillators”, IEEE Transactions on Microwave Theory and Techniques, Vol. 38, No. 3, 1990, pp. 225-230.

[104] Weikle, R. M., Kim, M., Hacker, J. B., De Lisio, M. P., Popovic, Z. B., Rutledge, D. B., “Transistor oscillator and amplifier grids”, Proceedings of the IEEE, Vol. 80, No. 11, 1992, pp. 1800-1809.

[105] Arthur, J. W., “Microelectronics: Digital and analog circuits and systems”, Electronics and Power, Vol. 25, No. 10, 1979, pp. 729-.

[106] Schwarz, A. F., “Negative resistors and negative conductors”, PhD Thesis, Technische Hogeschool Delft, 1969.

[107] Antoniou, A., “Floating negative-impedance converters”, IEEE Transactions on Circuit Theory, Vol. 19, No. 2, 1972, pp. 209-212.

[108] Texas Instruments, “Wideband Operational Amplifier THS4304”, Available: https://www.ti.com/lit/ds/symlink/ths4304.pdf, [Online] (2020, December 15).

[109] Texas Intruments, “THS4304 SPICE model”, Available: https://www.ti.com/lit/zip/sloj170, [Online] (2018, April 4).

[110] ElectronicsNotes, “What is a Balun: RF Antenna Balun”, Available: https://www.electronics-notes.com/articles/antennas-propagation/balun-unun/what-is-rf-antenna-balun.php, [Online] (2021, February 21).

[111] Hrabar, S., Cavar, K., Miksic, M., Tomic, L., Vincelj, L., "Miniaturization of unit cell of self-oscillating non-foster metasurface", in 2019 Thirteenth International Congress on Artificial Materials for Novel Wave Phenomena (Metamaterials), 2019, pp. X-161-X-163.

[112] Ta, S. X., Park, I., Ziolkowski, R. W., "Crossed dipole antennas: A review.", IEEE Antennas and Propagation Magazine, Vol. 57, No. 5, 2015, pp. 107-122.

[113] Tawk, Y., Kabalan, K. Y., El-Hajj, A., Christodoulou, C. G., Costantine, J., "A simple multiband printed bowtie antenna", IEEE Antennas and Wireless Propagation Letters, Vol. 7, 2008, pp. 557-560.

[114] R Nave, "Huygens' Principle", Available: http://hyperphysics.phy-astr.gsu.edu/hbase/phyopt/huygen.html, [Online] (2021, January 27).

[115] Zentner, E., Antene i radiosustavi. Graphis Zagreb, 2001.

[116] Bevelacqua, P. J., "Antenna types", Available: antenna-theory.com/antennas/smallLoop.php, [Online] (2021, February 23).

[117] Ziolkowski, R. W., "Low profile, broadside radiating, electrically small huygens source antennas", IEEE Access, Vol. 3, 2015, pp. 2644-2651.

[118] Lin, W., Ziolkowski, R. W., "Electrically small, low-profile, huygens circularly polarized antenna", IEEE Transactions on Antennas and Propagation, Vol. 66, No. 2, 2018, pp. 636-643.

[119] Lin, W., Ziolkowski, R. W., Huang, J., "Electrically small, low-profile, highly efficient, huygens dipole rectennas for wirelessly powering internet-of-things devices", IEEE Transactions on Antennas and Propagation, Vol. 67, No. 6, 2019, pp. 3670-3679.

[120] Booysen, A. J., "Aperture theory and the equivalence principle", IEEE Antennas and Propagation Magazine, Vol. 45, No. 3, 2003, pp. 29-40.

[121] Wong, A. M. H., Eleftheriades, G. V., "A simple active huygens source for studying waveform synthesis with huygens metasurfaces and antenna arrays", in 2015 IEEE International Symposium on Antennas and Propagation USNC/URSI National Radio Science Meeting, 2015, pp. 1092-1093.

[122] Vincelj, L., Hrabar, S., Ziolkowski, R., "Non-foster self-oscillating huygens radiator", in 2020 IEEE International Symposium on Antennas and Propagation and North American Radio Science Meeting, 2020, pp. 521-522.

[123] Vincelj, L., Ziolkowski, R. W., Hrabar, S., “Experimental demonstration of non-foster self-oscillating huygens radiator”, in 2020 Fourteenth International Congress on Artificial Materials for Novel Wave Phenomena (Metamaterials), 2020, pp. 508-510.

[124] Keysight, “Touchstone format”, Available: http://literature.cdn.keysight.com/litweb/pdf/genesys200801/sim/linear_sim/sparams/touchstone_file_format.htm, [Online] (2021, February 4).

[125] Tohyama, H., Mizuno, H., “23-ghz band gaas mesfet reflection-type amplifier”, IEEE Transactions on Microwave Theory and Techniques, Vol. 27, No. 5, 1979, pp. 408-415.

[126] Adler, R., “A study of locking phenomena in oscillators”, Proceedings of the IRE, Vol. 34, No. 6, 1946, pp. 351-357.

[127] York, R. A., Compton, R. C., “Quasi-optical power combining using mutually synchronized oscillator arrays”, IEEE Transactions on Microwave Theory and Techniques, Vol. 39, No. 6, 1991, pp. 1000-1009.

[128] Manteghi, M., “Fundamental limits, bandwidth, and information rate of electrically small antennas: Increasing the throughput of an antenna without violating the thermodynamic q-factor”, IEEE Antennas and Propagation Magazine, Vol. 61, No. 3, 2019, pp. 14-26.

Biography

Leo Vincelj was born in Zagreb, Croatia in 1993. He received B.Sc. and Mag.Ing. degrees in electrical engineering from the University of Zagreb, Faculty of electrical engineering and computing, Croatia, in 2015. and 2017., respectively. After graduation, he was employed at Ericsson Nikola Tesla, Zagreb, Croatia, where he worked on a software improvement for 2G and 3G mobile networks. He started pursuing a Ph.D. degree at Department of Communication and Space Technologies, Faculty of electrical engineering and computing, Zagreb, Croatia, in February 2018. There he does research as well as participates in teaching of five different courses in the field of wireless communication technology and electromagnetics. Since 2018, he was involved in two scientific projects including "Non-Foster Source-load Networks and Metasurfaces", and "Electromagnetic Structures for Emerging Communication Systems". In 2020 he started a collaboration with the University of Technology, Sydney, Australia, and with Saint-Petersburg Electrotechnical University ETU "LETI", Russia. He is (co)author of one international refereed journal paper, twelve conference papers and one scientific report. He was awarded with scholarship of Zagreb City for excellence in high school achievements from 2011 to 2012. His scientific research interests include analog, high frequency electronics, and metamaterial-inspired antennas, focusing on analysis and synthesis of active electromagnetic structures.

List of publications

Journal paper

1. Vincelj, L., Krois, I., Hrabar, S., “Toward self-oscillating non-Foster unit cell for future active metasurfaces”, IEEE Tran. on Ant. and Prop., Vol. 68, No. 3, March 2020, pp. 1665-1679.

Conference papers

1. Hrabar, S., Krois, I., Vincelj, L., “Two-element non-Foster antenna-transmitter array”, IEEE Int. Symp. on Antennas and Prop. (APS / URSI), 2018.

2. Hrabar, S., Vincelj, L., Krois, I., “Analysis of Metamaterial-inspired N-type Non-Foster Oscillator”, 12th International Congress on Artificial Materials for Novel Wave Phenomena (Metamaterials), 2018, pp. 179-181.
3. Hrabar, S., Krois, I., Vincelj, L., “An Update on Use of Unstable Non-Foster Networks in Metamaterial-inspired EM Structures”, International Symposium on Antennas and Propagation (ISAP), 2018, pp. 1-2.
4. Hrabar, S., Cavar, K., Miksic, M., Tomic, L., Vincelj, L., “Miniaturization of Unit Cell of Self-oscillating Non-Foster Metasurface”, Thirteenth International Congress on Artificial Materials for Novel Wave Phenomena (Metamaterials), 2019, pp. X-161-X-163.
5. Vincelj, L., Hrabar, S., Krois, I., “Non-ideal ’negation’ of complex load in self-oscillating non-Foster structures”, Thirteenth International Congress on Artificial Materials for Novel Wave Phenomena (Metamaterials), 2019.
6. Vincelj, L., Hrabar, S., Krois, I., “Non-linear model of negative impedance converter for use in non-Foster circuitry”, ICECOM, Dubrovnik, Croatia, 2019.
7. Vincelj, L., Hrabar, S., Basic, I., “Influence of NIC Accuracy on Properties of Self-oscillating Antennas and Metasurfaces”, IEEE Int. Symp. on Antennas and Prop. (APS / URSI), 2019.
8. Buiantuev, B., Vincelj, L., Kholodnyak, D., Hrabar, S., “A Novel Design Methodology for Non-Foster Elements with Application in Broadband Self-oscillating Antennas”, 14th European Conference on Antennas and Propagation (EuCAP), 2020.
9. Buiantuev, B., Kalmykov, N., Kholodnyak, D., Vincelj, L., Brizic, A., Hrabar, S., “Design of Non-Foster Negative Capacitances by Using Decomposition of Linvill’s Circuit”, IEEE Asia-Pacific Microwave Conference (APMC), 2020, pp. 272-274.
10. Vincelj, L., Hrabar, S., “Dynamical Behavior of Non-Foster Self-oscillating Antenna”, International Symposium ELMAR, 2020, pp. 17-20.
11. Vincelj, L., Hrabar, S., Ziolkowski, Richard W., “Non-Foster Self-Oscillating Huygens Radiator”, IEEE International Symposium on Antennas and Propagation and North American Radio Science Meeting, 2020, pp. 521-522.
12. Vincelj, L., Ziolkowski, Richard W., Hrabar, S., “Experimental Demonstration of Non-Foster Self-oscillating Huygens Radiator”, Fourteenth International Congress on Artificial Materials for Novel Wave Phenomena (Metamaterials), 2020, pp. 508-510.

Scientific report

1. Hrabar, S., Krois, I., Loncar, J., Vincelj, L., “Non-Foster Source-load Networks and Metasurfaces”, EOARD/AFRL, Wright-Patterson Air Force Base, OH, USA, Final Rep., FA 9550-15-1-0120, 2018.

Životopis

Leo Vincelj rođen je 1993. godine u Zagrebu, Hrvatska. Završio je preddiplomski i diplomski studij elektrotehnike i informacijske tehnologije na Sveučilištu u Zagrebu Fakultetu Elektrotehnike i Računarstva, 2015., odnosno 2017. godine. Nakon obrane diplomskog rada zaposlio se u poduzeću Ericsson Nikola Tesla, Zagreb, Hrvatska, gdje je radio na programskom unaprijeđenju za 2G i 3G mobilne mreže. Doktorski studij započeo je u veljači 2018. godine na Zavodu za Komunikacijske i Svemirske Tehnologije, Sveučilište u Zagrebu Fakultet Elektrotehnike i Računarstva. Tamo radi na istraživanjima te sudjeluje u nastavi na pet kolegija iz područja komunikacijskih tehnologija i elektromagnetizma. Od 2018. godine sudjelovao je u dva znanstvena projekta uključujući "Non-Foster Source-load Networks and Metasurfaces", te "Electromagnetic Structures for Emerging Communication Systems". 2020. godine započeo je suradnju s University of Technology, Sydney, Australija i Saint-Petersburg Electrotechnical University ETU "LETI", Rusija. Autor i koautor je jednog rada u znanstvenom časopisu s međunarodnom recenzijom, 12 radova na međunarodnim konferencijama te jednog znanstvenog izvješća. Nagrađen je stipendijom Grada Zagreba za uspjeh u školovanju od 2011. do 2012. godine. Njegovo područje interesa uključuje analognu, visokofrekvencijsku elektroniku te antene inspirirane metamaterijalima, s naglaskom na analizu i sintezu aktivnih elektromagnetskih struktura.